Universidad de Granada

Facultad de Ciencias

Departamento de Física Aplicada

Programa de Doctorado de

Física y Ciencias del Espacio

TESIS DOCTORAL

Dynamics of Magnetorheological Fluids at the Microscale

Autor: Keshvad Shahrivar

Director: Juan de Vicente Alvarez-Manzaneda

2017

Editor: Universidad de Granada. Tesis Doctorales
Autor: Keshvad Shahrivar
ISBN: 978-84-9163-265-8
URI: http://hdl.handle.net/10481/47125

El doctorando / The *doctoral candidate* **[Keshvad Shahrivar]** y los directores de la tesis / and the thesis supervisor/s: **[Juan de Vicente Álvarez-Manzaneda]**

Garantizamos, al firmar esta tesis doctoral, que el trabajo ha sido realizado por el doctorando bajo la dirección de los directores de la tesis y hasta donde nuestro conocimiento alcanza, en la realización del trabajo, se han respetado los derechos de otros autores a ser citados, cuando se han utilizado sus resultados o publicaciones.

/

Guarantee, by signing this doctoral thesis, that the work has been done by the doctoral candidate under the direction of the thesis supervisor/s and, as far as our knowledge reaches, in the performance of the work, the rights of other authors to be cited (when their results or publications have been used) have been respected.

Lugar y fecha / Place and date:

Granada, 6 de Marzo de 2017

Director/es de la Tesis / *Thesis supervisor/s;*

Firma / Signed

Doctorando / *Doctoral candidate*:

KESHVAD SHAHRIVAR

Firma / Signed

Table of Contents

ABSTRACT

Materials whose properties change in the presence of an external stimulus are known as smart materials. Magnetic fluids are smart colloidal suspensions of ferromagnetic/ferrimagnetic particles whose rheological properties can be tuned by a magnetic field. Generally speaking, magnetic fluids can be divided in two categories: ferrofluids (FFs) and magnetorheological fluids (MRFs). MRFs are suspensions of magnetizable micron-sized particles suspended in a non-magnetic medium and FFs are dispersions of nano-sized particles in a non-magnetic carrier fluid. Under the application of a magnetic field, in the case of MRFs, magnetized particles form aggregates along the field direction and the apparent viscosity changes in several orders of magnitude. If the magnetic field is large enough, a minimum force is needed to make the suspension flow (i.e. yield stress). Under external magnetic fields, MRFs acquire viscoelastic properties and exhibit a strongly shear-thinning behavior.

Being field responsive suspensions, MRFs and FFs have received considerable attention in the field of mechanical engineering for actuation and motion control. Some examples are shock absorbers, dampers, clutches and rotary brakes. However, interest from other research areas such as thermal energy transfer, precision polishing, chemical sensing and biomedical applications shows the potential of these materials to be employed in many other different disciplines.

In this dissertation, we investigated a new class of MRFs that bridges the gap between conventional MRFs and MR elastomers. In a novel approach, a thermoresponsive polymer-based suspending medium, whose rheological properties can be externally controlled through changes in the temperature, was used in the formulation of the MRFs. We used, particularly, Poly (ethylene oxide)–poly (propylene oxide)–poly (ethylene oxide) triblock copolymers and Poly(N-isopropylacrylamide) microgels. Thus, we found a feasible way to prevent particle sedimentation in MRFs but at the same time retaining a very large MR effect in the excited state.

The study of the creep flow behavior of MRFs is of valuable help in understanding the yielding behavior of these materials. A direct comparative study on the creep-recovery behavior of conventional MR fluids was carried out using magnetorheometry and particle-level simulations. We show that the recovery behavior strongly depends on the stress level. For low stress levels, below the bifurcation value, the MRF is capable to recover part of the strain. For stresses larger than the bifurcation value, the recovery is negligible as a result of irreversible structural rearrangements.

From a practical point of view, it is interesting to study the thin-film rheological and tribological properties of FFs. Recently, it has been shown that by using FFs in mechanical contacts it is possible to actively control the frictional behavior. In this dissertation, we explored a new route to control friction in the isoviscous-elastic

lubrication regime between compliant point contacts. By superposition of non-homogeneous magnetic fields in FFs lubricated contacts, a friction reduction was achieved. Also, we compared the tribological performance of FFs and MRFs using the same tribological conditions and tribopairs. In the case of FFs lubrication the sliding wear occurs mainly by two-body abrasion and in the case of MRFs lubrication the sliding wear occurs by two-body and three-body abrasion.

Finally, the study of the growing rate of the field-driven structure formation is also important, in particular, for the prediction of the response time of MRFs since their practical applications depend on the rate of change in their properties. The irreversible two-dimensional aggregation kinetics of dilute non-Brownian magnetic suspensions was investigated in rectangular microchannels using video-microscopy, image analysis and particle-level dynamic simulations. Especial emphasis was given to carbonyl iron suspensions that are of interest in the formulation of MRFs; carrier fluid viscosity, particle/wall interactions, and confinement effect was investigated. On the one hand, the carrier fluid viscosity determines the time scale for aggregation. On the other hand, particle/wall interactions strongly determine the aggregation rate and therefore the kinetic exponent. It was found that aggregation kinetics follow a deterministic aggregation process. Furthermore, experimental and simulation aggregation curves can be collapsed in a master curve when using the appropriate scaling time. The effect of channel width is found to be crucial in the dynamic exponent and in the saturation of cluster formation at long times. On the contrary, it has no effect in the onset of the tip-to-tip aggregation process.

RESUMEN

Aquellos materiales cuyas propiedades cambian en presencia de un estímulo externo se conocen como materiales inteligentes. Los fluidos magnéticos son suspensiones coloidales de partículas ferromagnéticas/ferrimagnéticas cuyas propiedades reológicas pueden ser modificadas a voluntad mediante un campo magnético externo. En términos generales, los fluidos magnéticos pueden dividirse en dos categorías: ferrofluidos (FFs) y fluidos magneto-reológicos (FMRs). Los FMRs son suspensiones de partículas magnetizables de tamaño micrométrico en un medio no magnético mientras que los FFs son dispersiones de nanopartículas magnéticas en un fluido portador no magnético. Bajo la aplicación de un campo magnético, las partículas dispersas en un FMR se magnetizan y agregan formando estructuras alineadas con el campo. En consecuencia, la viscosidad aparente se incrementa en varios órdenes de magnitud. Si el campo magnético es lo suficientemente intenso, será necesaria una fuerza mínima (un esfuerzo umbral) para hacer que la suspensión fluya. Bajo campos magnéticos externos, los FMR exhiben un comportamiento viscoelástico y pseudoplasticidad.

Al poder controlar sus propiedades externamente, los FMRs y FFs han recibido una considerable atención en el ámbito de la ingeniería mecánica para el accionamiento y control de movimiento. Algunos ejemplos son los amortiguadores, los embragues y los frenos rotativos. Sin embargo, el interés de otras áreas de investigación tales como la transferencia de energía térmica, pulido de alta precisión, detección química y aplicaciones biomédicas, demuestran el potencial de estos materiales para ser utilizados en otras muchas disciplinas diferentes.

En esta tesis, se describe una nueva clase de FMR que salva la brecha existente entre los FMR convencionales y los elastómeros MR. Para ello, se hace uso de polímeros termosensibles cuyas propiedades reológicas pueden ser controladas externamente a través de cambios en la temperatura. En particular, se utilizan Poly (ethylene oxide)–poly (propylene oxide)–poly (ethylene oxide) y Poly(N-isopropylacrylamide). Se demuestra que la formulación en base a un medio continuo termosensible permite evitar la sedimentación de las partículas en el FMR, y al mismo tiempo retener un efecto MR muy grande en el estado excitado.

El estudio en profundidad del flujo “Creep-recovery” en FMR es de valiosa ayuda en la comprensión del comportamiento reológico de estos materiales. En esta tesis se lleva a cabo un estudio comparativo del comportamiento en régimen estacionario y dinámico para FMR convencionales utilizando magnetoreometría y simulaciones de dinámica molecular a nivel de partícula. Se demuestra que el “recovery” depende en gran medida del nivel de esfuerzo. Para niveles de esfuerzo pequeños, por debajo de la bifurcación, el FMR es capaz de recuperar parte de la deformación. Sin embargo, para esfuerzos

mayores la recuperación es despreciable como resultado de reordenamientos estructurales irreversibles.

Desde un punto de vista práctico, resulta interesante estudiar las propiedades reológicas y tribológicas de FFs en película delgada. En esta tesis, se demuestra que es posible minimizar la fricción empleando campos magnéticos no homogéneos en el régimen de lubricación isoviscosa-elástica en "point contacts". También se compara el rendimiento tribológico de FFs y FMRs utilizando las mismas condiciones tribológicas y tribopares.

Por último, con miras a entender y mejorar el tiempo de respuesta de los FMRs, resulta de capital importancia estudiar la cinética de agregación de las partículas en suspensión al aplicar un campo magnético externo. En esta tesis se estudia la cinética de agregación irreversible en 2D de suspensiones diluidas no Brownianas en canales de sección rectangular mediante video-microscopía, análisis de imagen y simulaciones de dinámica molecular. El estudio se centra en el caso de suspensiones de hierro carbonilo, por su interés en la formulación de FMR, y describe el efecto de la viscosidad del fluido portador, las interacciones partícula-pared y el efecto del confinamiento. Por un lado, la viscosidad del fluido portador determina la escala de tiempo para la agregación. Por otro lado, las interacciones partícula-partícula y partícula-pared determinan la tasa de agregación y por lo tanto el exponente cinético. Se encuentra que la agregación es puramente determinista. Además, tanto las curvas experimentales como las de simulación colapsan en una curva maestra al usar la escala de tiempo apropiada. El efecto de la anchura del microcanal resulta ser crucial en el exponente dinámico y en la saturación de la formación de agregados a tiempo largo. Por el contrario, el confinamiento no tiene efecto en el tiempo de inicio del proceso de agregación.

INTRODUCTION

Since Rabinow [1] and Winslow [2] discoveries in 1940's, magnetorheology and electrorheology have emerged as multidisciplinary disciplines covering fields such as Physics, Chemistry and Materials Science. They are often called "Smart Materials" since their rheological response can be altered by external fields. The most striking property of these fluids, over conventional materials, is that their viscosity can be increased several orders of magnitude in a fraction of millisecond, in some cases becoming a solid-like material. Thus, under the application of an external stimuli, it is necessary to overcome a minimum stress value, the so-called yield stress, to induce the flow [3]–[5]. The rheological controllability of these fluids provides an efficient way to design simple and fast electromechanical systems. Research and development have demonstrated that the performance of magnetorheological fluids may inherently be better suited to meet the design requirements of most devices over electrorheological fluids [5]. These advantages include a higher yield stress for the same energy consumption, a wide range of operating temperatures and activation using electromagnets driven by low-voltage power [6]–[9]. In recent years, magnetorheological fluids have received considerable attention in the field of mechanical engineering for actuation and motion control [10]–[12]. Some examples are shock absorbers, dampers, clutches and rotary brakes [13], [14]. However, interest from other research areas such as thermal energy transfer [15], [16], precision polishing [17]–[19], chemical sensing [20] and biomedical applications [21] demonstrates the potential of these materials to be employed in many other different disciplines.

For a nonprofessional person the term magnetism brings to mind pieces of iron being attracted across a distance by magnets. All materials are affected by magnetic field, although most only weakly so. The nature of interaction with magnetic field allows us to roughly categorize the phenomena into three major magnetics orders: diamagnetism, paramagnetism, and ferromagnetism. Ferromagnetic and paramagnetic materials are attracted towards a magnetic pole while diamagnetic material interaction is weakly repulsive [22]. Ferromagnetism is exhibited by iron, nickel, cobalt, and some alloys; some rare earth, such as gadolinium; and some metallic compounds, such as gold-vanadium. Examples of paramagnetic materials are platinum, aluminum, various salts of the transition metals such as chlorides, sulphates, and carbonates of manganese, chromium, and copper. Diamagnetism is exhibited by materials such as mercury, silver, carbon, and water [23].

From an atomic scale perspective, the exchange energy can align neighboring atomic moments so that they may cooperatively yield to a macroscopic total moment. In paramagnetic materials in the presence of a field, there is a *partial alignment* of the atomic magnetic moments in the direction of the field, resulting in a net positive magnetization in the material. In the absence of magnetic field magnetic, however,

moments do not interact and the net magnetic moment of the material is zero. Unlike paramagnetic materials, the atomic moments of ferromagnetic materials exhibit very strong interactions. Interactions produced by electronic exchange forces result in a *parallel alignment* of atomic moments and very large exchange forces. Therefore, magnetic interaction in ferromagnetic materials is stronger than paramagnetic materials. Parallel alignment of moments results in a large net magnetization even in the absence of a magnetic field [24].

It is well known that a piece of iron in the absence of a magnetic field exhibits no net magnetization. This observation is, *a priori*, in conflict with our expectation that the above referred atomic exchange energy between aligned moments should result in a net moment in a ferromagnetic material. An explanation for this was provided by Weiss (1906) who postulated the existence of macroscopic regions within the bulk material, so-called magnetic domains, containing magnetic moments aligned in such a manner as to minimize the total effective moment of material. In each magnetic domain a large number of atomic moments, typically 10^{12} to 10^{15}, are perfectly aligned (independently of the field). However, the orientation of the domains magnetization varies randomly from domain to domain. In practice, the bulk material divides itself into regions by creating domain walls of finite thickness; along the domain wall, the moment rotates coherently from the direction in one domain to that in the next domain [22]. However, the exchange energy at the boundary between oppositely aligned domains competes against antialignment. Therefore, the competition between the magnetostatic energy of the domains and domains walls limits the break-up of materials to domains of a finite size [24].

In classical electromagnetism, magnetization or magnetic polarization is the vector field that expresses the density of permanent or induced magnetic dipole moments in a magnetic material. Magnetization also describes how a material responds to an applied magnetic field as well as the way the material changes the magnetic field, and can be used to calculate the forces that result from those interactions. Net magnetization results from the response of a material to an external magnetic field, together with any unbalanced magnetic dipole moments that may be inherent in the material itself; for example in ferromagnets. The process of magnetization in ferromagnetic materials happens at three stages: domain growth, domain rotation, and magnetization rotation. The first process occurs at low fields and consists in the growth of the domains which are favorably aligned with the field. At moderate fields, domain rotation becomes significant and the magnetization process is determined principally by the magnetocrystalline anisotropy [24]. At this stage unfavorably aligned domains overcome the anisotropy energy and suddenly rotate from their original direction of magnetization into one of the crystallographic easy axes which is nearest to the field direction. The final process occurs at high fields in which magnetic moments, which are all aligned along the preferred magnetic crystallographic easy axes, are gradually rotated into the field direction. When all domains are aligned in the direction of external field no further increase in magnetization occurs, thus the material gets saturated [25]. The

saturation process is not reversible for ferromagnetic materials since they show a hysteresis loop.

In the particular case of ferromagnetic materials at the nanoscale (e.g. sufficiently small nanoparticles), the thermal energy can disrupt the orientation of the magnetic moment, hence, resulting in a superparamagnetic behavior. Superparamagnetic particles share with paramagnetic particles the absence of magnetization when the external magnetic field is removed, and with ferromagnetic materials the high levels of magnetization reached under the influence of a low magnetic fields [26].

The magnetic field inside magnetic material (H) is different from the external field (H_0). This is so because the induced magnetization in matter acts as source of another field. This field is called demagnetization field, H_D, opposes to the external field and depends on the shape and permeability of material. The demagnetization field for a uniformly magnetized matter is calculated as $-N_D M$ where N_D is the demagnetization tensor. Thus, the field inside matter is obtained from $H = H_0 + H_D = H_0 - N_D M$. For the particular case of a sphere, the tensor N_D is diagonal with components equal to 1/3 [22].

Magnetic Colloids

Generally speaking, magnetic suspensions can be divided into three groups: Ferrofluids (FF), Inverse Ferrofluids (IFF), and Magnetorheological fluids (MRF) [4].

FFs are colloidal suspensions made of nanoscale ferromagnetic, or ferrimagnetic, particles suspended in a non-magnetic carrier fluid. The carrier liquids can be polar or nonpolar liquids. The particles are usually made from magnetite (Fe_3O_4) or maghemite ($\gamma - Fe_2O_3$) and have a mean diameter of about 3-15 nm [27]. In this size the particles can be treated as superparamagnetic single-domain particles. FFs are used in applications ranging from dynamic sealing [28], [29], heat dissipation [15], [30], and drug delivery agents [31], to magnetic resonance imaging [32]. Functionalized superparamagnetic particles and their recovery have made them good candidates for biotechnological applications [33]–[40].

IFFs (or magnetic holes) are a class of magnetic fluids formed by dispersing micronsized non-magnetizable particles in a ferrofluid. IFFs are not currently used in commercial applications. Instead, they serve as model systems for theoretical and simulation studies. The reason for this is that there are many synthesis routes available for the fabrication of non-magnetic particles with well-defined shapes and sizes.

Finally, MRFs are dispersions of magnetizable particles (typically carbonyl iron) in non-magnetic liquid carriers (typically non polar liquids). MRFs are currently used in torque transfer applications involving clutches, brakes and dampers. Clearly, the major difference between FFs and MRFs originates in the size of the particles. Particles constituting MRFs primarily consist of micronsized particles which behave as magnetic

multidomains. Because of this large size and the inherent density mismatch between the particles and the carrier fluid, the dispersed particles in a MRF tend to settle. Another difference in the properties of MRFs and FFs underlies in the saturation magnetization. While in a MRF, particles typically have a large saturation magnetization, in a FF, the saturation magnetization is smaller because it is limited by the nanoparticles concentration and the saturation magnetization of the iron oxides employed. MRFs may exhibit a solid-to-liquid transition in presence of a large enough magnetic field, but FFs remain always liquid. Therefore, the mechanical properties of a FF can be described as Newtonian whatever the field.

Obviously, the long-term stability is one of the major challenges in the formulation of magnetic suspensions. Different approaches have been followed to minimize the settling of particles such as introducing additives and surface chemical functionalization [41], [42]. For example, in surfactant-coated ferrofluids each tiny particle is thoroughly coated with a polymeric surfactant to inhibit clumping. In non-polar media, one layer of surfactant is needed; however in polar media a double surfactation of particles is needed to form a hydrophilic layer around them [27]. The use of viscoplastic materials [43] as carrier fluids and mixtures of different size particles have also been shown to inhibit sedimentation [44], [45]. Also, the incorporation of elongated magnetic particles have been reported to enhance the kinetic stability [46], [47]. Previous approaches to hinder sedimentation resulted in higher viscosity levels when the field was absent (off-state). However, in practical applications a low off-state viscosity is more desirable. In a recent attempt, thermosensible carrier fluids were employed in the formulation of MRFs to overcome this problem [48], [49]. On one hand, in liquid state the thermoresponsive MR composite behaved as a conventional MRF. On the other hand, upon changing the temperature, the transition to a gelled state inhibited the sedimentation of the particles.

Rheology

The word Rheology originates from the Greek word "Rheo" which means flow of streams. Thus, rheology is the study of the deformation and flow of matter. This field is dominated by inquiry into the flow behavior of complex fluids such as polymers, foods, biological systems, slurries, suspensions, emulsions, pastes, and other compounds. The relationship between the stress and the deformation for these types of materials differs from the Newton's law of viscosity. Complex fluids also do not follow Hooke's law of elasticity; the relationship between stress and deformation that is used for metals and other elastic materials. To find constitutive equations, experiments are performed on materials using the so-called standard flows. There are numerous standard flows that may be constructed from two sets of flows; shear and shear-free flows. Next, we will describe the most relevant ones for this PhD Thesis.

Standard Flows

A fluid element may undergo four fundamental types of motion; translation, rotation, linear strain, and shear strain. The combination of different fluid element motions defines the velocity field ($\underline{v}$). The constitutive equation for a compressible Newtonian fluid is:

$$\underline{\underline{\tau}} = -\eta\left[\nabla\underline{v} + (\nabla\underline{v})^T\right] + \left(\frac{2}{3}\eta - k\right)(\nabla.\,\underline{v})\underline{\underline{I}} \qquad \text{In.1}$$

where η and k are shear and bulk viscosity, respectively. The shear viscosity is the coefficient that describes the resistance of a fluid to sliding motion. The dilatational or bulk viscosity κ is the coefficient that describes an isotropic contribution to stress that is generated when the density of a fluid changes upon deformation. The first term within the brackets in the constitutive equation, $\nabla\underline{v} + (\nabla\underline{v})^T$, is known as shear rate tensor. Diagonal elements in the tensor represent the deformation in the principal directions and off-diagonal elements correspond to the shear deformation on different planes. Figure In.1 shows a schematic representation of the velocity field, and shear rate, as well as the corresponding analytical solution for the flow kinematics of shear and elongation flow assuming a constant viscosity fluid.

MRFs under external magnetic fields acquire viscoelastic properties, and commonly exhibit a shear-thinning behavior [4], [50]. Therefore, MRFs under external fields cannot be described by the Newtonian constitutive equation. In order to describe non-Newtonian fluids, additional material functions are needed. When the flow field is established, three stress-related quantities are measured in shear flow ($\tau_{21}, N_1 \equiv \tau_{11} -$

τ_{22} , $N_2 \equiv \tau_{22} - \tau_{33}$), and two stress differences are measured in elongational flow ($\tau_{33} - \tau_{11}$ and $\tau_{22} - \tau_{11}$).

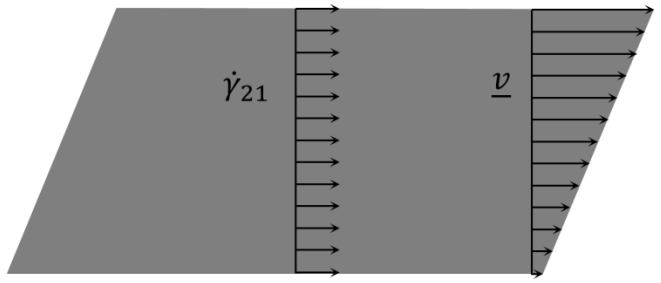

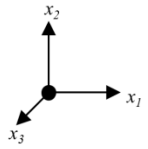

$$\dot{\gamma} = \begin{pmatrix} 0 & \dot{\varsigma}(t) & 0 \\ \dot{\varsigma}(t) & 0 & 0 \\ 0 & 0 & 0 \end{pmatrix} \qquad \underline{v} = \begin{bmatrix} v_1 \\ v_2 \\ v_3 \end{bmatrix} = \begin{bmatrix} \frac{\partial v_1}{\partial x_2} x_2 \\ 0 \\ 0 \end{bmatrix}$$

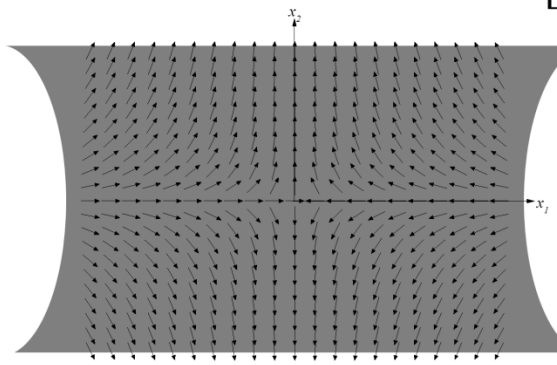

$$\dot{\gamma} = \begin{pmatrix} -\dot{\epsilon}(t) & 0 & 0 \\ 0 & 2\dot{\epsilon}(t) & 0 \\ 0 & 0 & -\dot{\epsilon}(t) \end{pmatrix} \qquad \underline{v} = \begin{bmatrix} v_1 \\ v_2 \\ v_3 \end{bmatrix} = \begin{bmatrix} \frac{-\dot{\epsilon}(t)}{2} x_1 \\ \dot{\epsilon}(t) x_2 \\ \frac{-\dot{\epsilon}(t)}{2} x_3 \end{bmatrix}$$

Figure In.1 Two-dimensional representations of the velocity field in a) shear flow b) uniaxial elongational flow.

Steady Shear Flow

Shear flow is the most common kinematics used in rheology. In this flow, layers of fluid slide past each other and do not mix. The flow is unidirectional, and the velocity only varies in one direction. In the case of steady shear flow, the shear rate function $\dot{\varsigma}(t)$ is

constant (see Figure In.2a). Thus $\dot{\varsigma}(t) = \dot{\gamma}_{21} = \dot{\gamma}_0$ where $\dot{\gamma}_0$ is a constant shear rate. Using the stress quantities three material functions are defined for shear flow, namely:

$$\text{Shear viscosity: } \eta(\dot{\gamma}) = \frac{-\tau_{21}}{\dot{\gamma}_0^2} \qquad \text{In.2}$$

$$\text{First normal stress coefficient: } \psi_1(\dot{\gamma}) = \frac{-(\tau_{11}-\tau_{22})}{\dot{\gamma}_0^2} \qquad \text{In.3}$$

$$\text{Second normal stress coefficient: } \psi_2(\dot{\gamma}) = \frac{-(\tau_{22}-\tau_{33})}{\dot{\gamma}_0^2} \qquad \text{In.4}$$

The constitutive equation that is found to predict the material functions most closely is the most appropriate constitutive equation to be used when modeling the flow behavior of that material. The material functions $\psi_1(\dot{\gamma})$ and $\psi_2(\dot{\gamma})$ are zero for Newtonian fluids.

Shear Creep

An alternative kinematics is to drive the flow at a constant stress level τ_0, rather than at constant shear rate $\dot{\gamma}_0$ (Figure In.2b). This can be done, for instance, driving one confining surfaces with a constant-torque motor. In MRFs the plate-plate geometry is preferred for a creep test since in cone-plate geometry the aggregates' length is not constant. Usually, creep tests are performed together with recovery tests. In a typical essay, a constant shear stress is applied while the resulting strain is measured. Then in the recovery test, which starts instantly after the creep test, the stress is removed and the recovered strain is measured. The main material function is called compliance, and is defined as: $J(t) = \frac{\gamma(t)}{\tau_0}$ where $\gamma(t)$ is the total strain as a function of time.

Small Amplitude Oscillatory Shear (SAOS)

In an oscillatory shear test, a sinusoidal strain is typically applied with a constant angular frequency and amplitude (Figure In.2c). If the amplitude is sufficiently small, the stress will be oscillatory but delayed by an angle; δ.

For example for a sinusoidal strain $\gamma(t) = \gamma_0 \sin(\omega t)$ stress can be expressed as:

$$\tau = \tau_0 \sin(\omega t + \delta) = \tau_0 \cos(\delta) \sin(\omega t) + \tau_0 \cos(\omega t) \sin(\delta). \qquad \text{In.5}$$

Conventionally two material functions, *viscoelastic moduli*, are derived by relating the stress to the shear strain; *storage modulus* and *loss modulus*. The storage modulus is

defined as $G' = \frac{\tau_0 \cos(\delta)}{\gamma_0}$ and measures the stored energy, hence representing the elastic contribution. The loss modulus $G'' = \frac{\tau_0 \sin(\delta)}{\gamma_0}$ measures the energy dissipated as heat, hence representing the viscous contribution.

If the amplitude of the oscillatory strain is small, the material stays in linear viscoelastic region in which storage and loss moduli remain constant and are not a function of the strain amplitude. Normally, in linear region the strain amplitude is below 0.1%. However, if the strain amplitude is large enough to operate on non-linear interval, the viscoelastic moduli start to decrease.

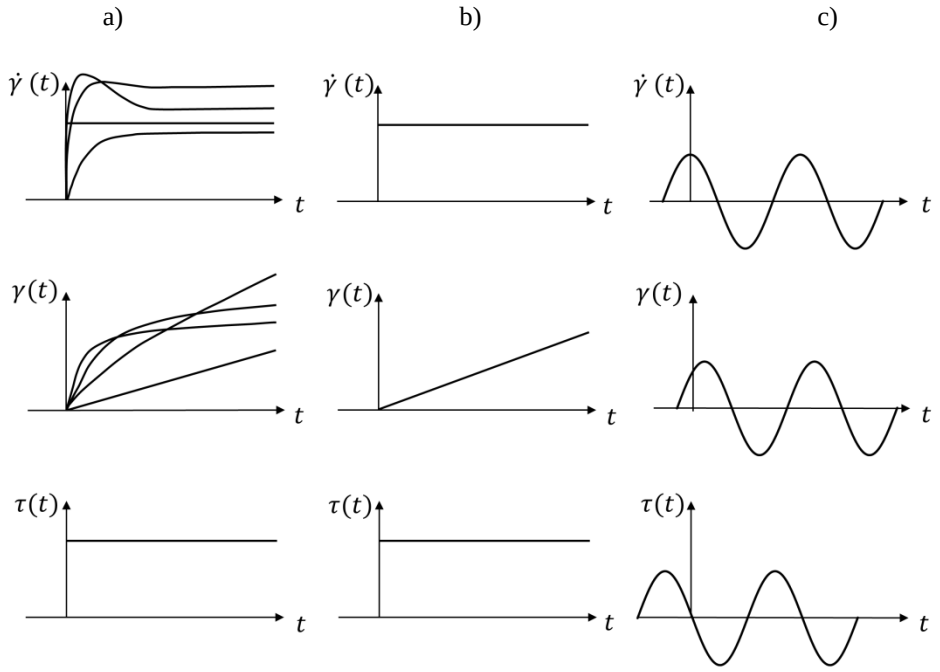

Figure In.2 Prescribed shear rate, strain, and shear stress. a) Simple shear b) Creep c) SAOS

Tribology and Lubrication

Lubrication Regimes

The word tribology is defined as the science and technology of interacting surfaces in relative motion [51]. The tribological interactions of a solid with interfacing materials may result in the loss of material from the surface. The process resulting in the loss of material is called wear. Main forms of wear are abrasion, friction (adhesion and cohesion), erosion, and corrosion. A lubricant is any material that reduces friction and wear and provides smooth running and a satisfactory life for machine elements. Most lubricants are liquids (such as mineral oils, synthetic esters, silicone fluids, and water), but they may be also solids (such as polytetrafluoroethylene, or PTFE) for use in dry bearings, greases for use in rolling-element bearings, or gases (such as air) for use in gas bearings. Hence, a better definition for tribology might be the lubrication, friction, and wear of moving or stationary parts. Wear can be minimized by modifying the surface properties of the solids by surface finishing processes or by the use of lubricants (for frictional or adhesive wear) [52]. Contacting surfaces failure is the most prominent mode in mechanical component breakdown. In conformal surfaces the load is carried over a relatively large area bur for non-conformal surfaces the full burden of the load must then be carried by a small lubrication area. Fluid film journal bearings and slider bearings have conformal surfaces. Examples of non-conformal surfaces are mating gear teeth, cams and followers, and rolling-element bearings.

Generally speaking, two distinct lubrication regimes are recognized: hydrodynamic lubrication and boundary lubrication [51]. The understanding of hydrodynamic lubrication began with the classic experiments of Tower [53], in which the existence of a fluid film was detected from measurements of pressure within the lubricant, and of Petrov [54], who reached the same conclusion from friction measurements. Two years later Osborne Reynolds [55], closely following the Tower and Petrov works, published a paper in which he used a reduced form of the Navier-Stokes equations in association with the continuity equation to derive a second-order differential equation for the pressure build up in a narrow and converging gap between bearing surfaces. This pressure enables a load to be transmitted between the surfaces with extremely low friction, since the surfaces are completely separated by a fluid film. The relative motion and the viscosity of the fluid contribute to separate the surfaces. In such a situation the physical properties of the lubricant, notably the dynamic viscosity, dictate the behavior in the conjunction.

The understanding of the boundary lubrication regime is attributed to Hardy and Doubleday [56], [57], who found that extremely thin films adhering to surfaces were often sufficient to assist relative sliding. They concluded that under such circumstances the chemical composition of the fluid is important, and they introduced the term boundary lubrication. Boundary lubrication is at the opposite end of the lubrication

spectrum from hydrodynamic lubrication. In boundary lubrication the physical and chemical properties of thin films of molecular proportions and the surfaces to which they are attached determine the contact behavior. The lubricant viscosity is not an influential parameter in this regime.

It has been recognized that between fluid film and boundary lubrication regimes, some combined mode of action can occur. This mode is generally termed partial lubrication or is sometimes referred to as mixed lubrication. Partial or mixed lubrication regime deals with the condition when the speed is low, the load is high or the temperature is sufficiently large to significantly reduce lubricant viscosity. When any of these conditions occur, the highest asperities of the bounding surfaces will protrude through the film and occasionally come in contact.

A useful concept for the understanding of the role of the different lubrication regimes is the so-called Stribeck curve as shown in Figure In.3. Historically, the Stribeck curve was first widely disseminated because of Stribeck's systematic and definitive experiments that explained friction in journal bearings. In Figure In.3 x-axis is the so-called Gumbel number [58], $\eta\omega/P$, where η is the dynamic viscosity, ω is the rotational speed and P is the bearing load projected on to the geometrical surface. A high Gumbel number means a relatively thick lubricant film, whereas a small number results in a very thin film. At an extremely low Gumbel number, no real lubricant film can develop and there is significant asperity contact, resulting in high friction. This represents the dominance of boundary lubrication in determining load transfer and friction between surfaces. This high friction value continues constantly with increasing Gumbel number until a first threshold value is reached. As the Gumbel number increases, a noticeable and rapid decrease in friction values is observed. This is explained by an increasing lubricant film thickness and shared load support between the surface asperities and the pressurized liquid lubricant present in the conjunction. In this mixed lubrication regime, widely varying friction values can be measured and are strongly dependent on operating conditions. With a further increase in Gumbel number, friction reaches a lower minimum value, corresponding to the onset of hydrodynamic lubrication. At this point, the surfaces are effectively separated by the liquid lubricant, and asperity contact has negligible effect on load support and friction. When sliding speed or viscosity further increase, the rise in friction coefficient owes to increase in viscous resistance.

Reynolds equation

The differential equation governing the pressure distribution in fluid film lubrication is known as the Reynolds equation. This equation was first derived in a remarkable paper by Reynolds (1886). Reynolds' classical paper contained not only the basic differential equation of fluid film lubrication, but also a direct comparison between his theoretical predictions and the experimental results obtained by Tower (1883). Reynolds, however, restricted his analysis to an incompressible fluid.

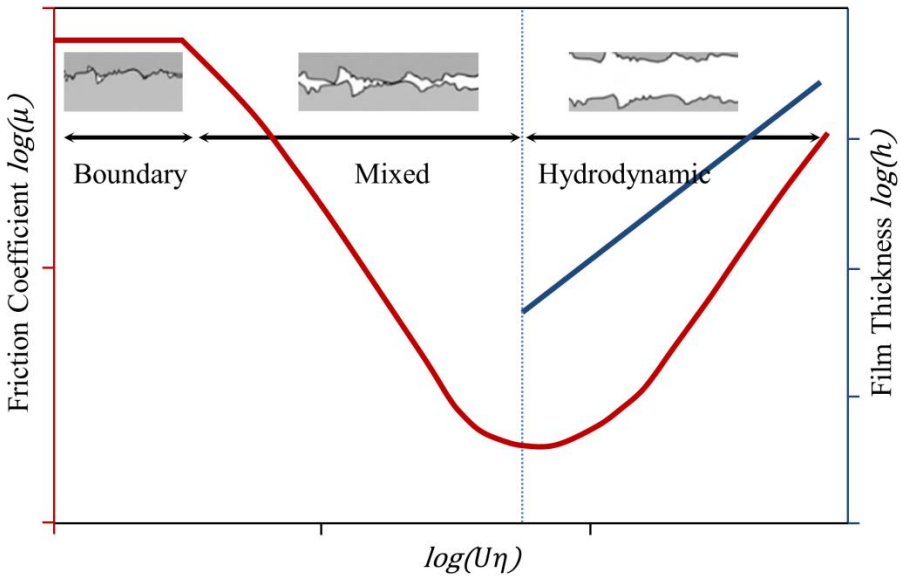

Figure In.3 A typical Stribeck curve illustrating lubrication regimes, variation in friction, and film thickness.

In its more general form, Reynolds equation for a compressible fluid is written as follows:

$$\frac{\partial}{\partial x}\left(\frac{\rho h^3}{12\eta}\frac{\partial P}{\partial x} - \rho h u_m\right) + \frac{\partial}{\partial y}\left(\frac{\rho h^3}{12\eta}\frac{\partial P}{\partial y} - \rho h v_m\right) = \frac{\partial}{\partial t}(\rho h). \qquad \text{In.6}$$

Here $u_m = \frac{u_A + u_B}{2}$ and $v_m = \frac{v_A + v_B}{2}$ where u and v are velocity components of the mating surfaces in x and y-direction. η and ρ represent viscosity and density of lubricant, respectively.

Figure In.4 shows, schematically, how the elastic deformation of the solids contributes to the film thickness. The film thickness can be expressed as:

$$h(x, y) = h_0 + s(x, y) + \delta(x, y) \qquad \text{In.7}$$

where $s(x, y)$ is the separation due to the undeformed geometry of two ellipsoids, and $\delta(x, y)$ is the deformation due to the pressure developed in the contact zone.

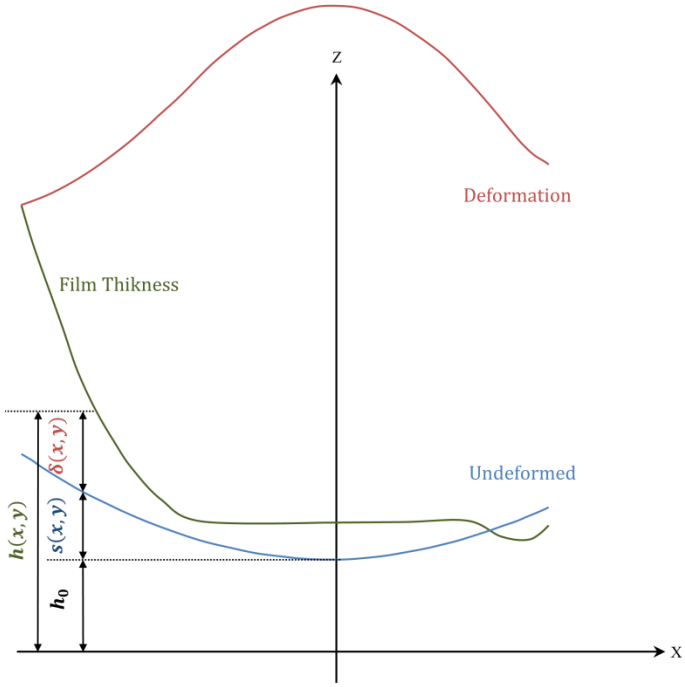

Figure In.4 Schematic illustration of parameters defining the film thickness.

When two elastic solids are brought together under a load, a contact area develops whose shape and size depend on the applied load, the elastic properties of the materials, and the curvatures of the surfaces. The theory was first developed by Hertz in 1986 for dry contacts [59]. When the two solids, shown in Figure In.**5**, are subjected to a normal load W, the contact area becomes elliptical. The separation s of two undeformed surfaces and their deformation δ due to pressure generation reads as follows [51]:

$$s(x,y) = \frac{x^2}{2R_x} + \frac{y^2}{2R_y} \qquad \text{In.8}$$

$$\delta(x',y') = \frac{2}{\pi E'} \int_{-\infty}^{+\infty} \int_{-\infty}^{+\infty} \frac{P(x,y)dxdy}{\sqrt{(x'-x)^2 + (y'-y)^2}} \qquad \text{In.9}$$

where $\frac{1}{R_x} = \frac{1}{R_{Ax}} + \frac{1}{R_{Bx}}$ and $\frac{1}{R_y} = \frac{1}{R_{Ay}} + \frac{1}{R_{By}}$. Here $E' \equiv 2\left(\frac{1-{v_A}^2}{E_A} + \frac{1-{v_B}^2}{E_B}\right)^{-1}$ and v and E are Poisson's and the modulus of elasticity of the contacting solids, respectively. The major and minor axes of the contact ellipse are proportional to $\left(\frac{W}{E'}\right)^{1/3}$. For the special case where $r_{Ax} = r_{Ay}$ and $r_{Bx} = r_{By}$ the resulting contact is a circle rather than an ellipse. This so-called dry contact model is used in tribology as a reference and for scaling purposes. In equation In.9 the limits of integration extend the computational domain far enough from the contact point, free boundary limit. Other common parameters used in the lubrication theory of two solids in contact are given in Table In.1.

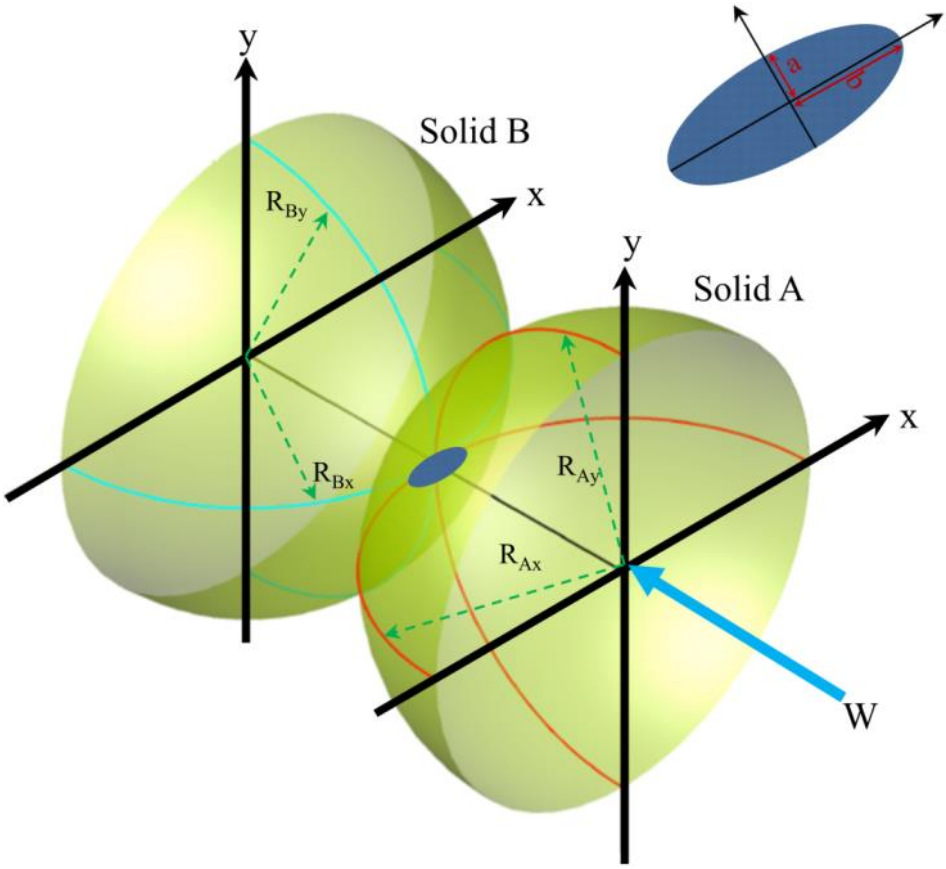

Figure In.5 Geometry of contacting elastic solids.

Table In.1. Common parameters defined for ellipsoidal bodies in contact [51]. $\mathcal{E}$ and $\mathcal{F}$ are first and second kind complete elliptic integral. Ellipticity parameter can be approximated by $\bar{k} = \left(\frac{R_y}{R_x}\right)^{2/\pi}$.

Property	Description	Expression
R	Curvature sum	$\left(\frac{1}{R_x}+\frac{1}{R_y}\right)^{-1}$
a	Minor semi-axis	$\sqrt[3]{\frac{6k^2\mathcal{E}WR}{\pi E'}}$
b	Major semi-axis	$\sqrt[3]{\frac{6\mathcal{E}WR}{\pi k E'}}$
k	Ellipticity parameter	b/a
δ_{max}	Maximum deformation	$\sqrt[3]{\frac{9\mathcal{F}^3}{2\mathcal{E}R}\left(\frac{W}{\pi k E'}\right)}$
P_H	Maximum Hertzian contact pressure	$\frac{3W}{2\pi ab}$
P_D	Hertzian pressure distribution	$P_H\sqrt{1-\left(\frac{x}{R_x}\right)^2-\left(\frac{y}{R_y}\right)^2}$

The lubricant viscosity is sensitive to both pressure and temperature. This sensitivity constitutes a considerable obstacle to the analytical description. For the isothermal hydrodynamic problem, the effect of temperature may be ignored but the behavior of a lubricant under high pressure is much different than that at the atmospheric pressure. One of the most widely used viscosity pressure relationships is the exponential Barus (1893) equation [60]:

$$\eta(P) = \eta_0 \exp^{(\alpha P)}. \qquad \text{In.10}$$

where α is the pressure viscosity coefficient, dependent on temperature.

Another widely used and accurate pressure-viscosity relationship was introduced by Roelands (1966) [61], who undertook a wide-ranging study of the effect of pressure on the viscosity of the lubricants. For isothermal conditions, the Roelands formula can be written as:

$$\eta(P) = \eta_0 exp\left\{[\ln(\eta_0) + 9.67]\left[-1 + \left(1 + \frac{P}{P_0}\right)^{\hat{z}}\right]\right\} \qquad \text{In.11}$$

where $\hat{z}$ is the pressure-viscosity index typically $0.5 < \hat{z} < 0.7$ and $P_0 = 1.98 \times 10^8$ Pa. Equation In.11 is accurate for pressures up to 1 GPa. Here η_0 is the viscosity at ambient pressure ($P = 0$) and at a constant temperature. The main advantage of this model is its simplicity, but it is only valid and applicable for relatively low pressures.

The compressibility of the lubricant in the analysis of gas lubricated bearings is an important parameter. However, in those cases where the lubricant is a liquid, the variation of the density with the pressure is usually negligible. One of the most widely used relationships for density pressure dependence was introduced by Dowson and Higginson (1966) [62]:

$$\rho(P) = \rho_0\left(1 + \frac{0.6P}{1 + 1.7P}\right) \qquad \text{In.12}$$

where ρ_0 is density at atmospheric condition.

The entire contact load, W, exerted on the contacting bodies is carried by the lubricant film in the elastohydrodynamic lubrication regime (EHL). Thus the integral of the pressure over the surface must balance the externally applied load. This condition is generally known as the force balance equation and reads as follows:

$$\int_{-\infty}^{+\infty}\int_{-\infty}^{+\infty} P(x,y)dxdy = W\,. \qquad \text{In.13}$$

Elastohydrodynamic Lubrication

The hydrodynamic lubrication regimes for non-conformal surfaces are based on two major physical effects. The first effect is the elastic deformation of the solid surfaces under an applied load which in turn alters the film shape. The second effect is the fluid viscosity change with the fluid-film pressure (see equation In.11). Therefore, four

regimes of fluid-film lubrication exist, depending on the magnitude of these effects, namely: isoviscous-rigid, piezoviscous-rigid, isoviscous-elastic, and piezoviscous-elastic. These lubrication subregimes can be visualized in terms of the following dimensionless parameters $g_E = \bar{W}^{8/3}/\bar{U}^2$ and $g_V = G\bar{W}^3/\bar{U}^2$[63], as shown in Figure In.6.

Traditionally isoviscous-elastic and piezoviscous-elastic regimes are recognized as a subclass of the elastohydrodynamic lubrication regime (EHL). The first work in field of elastohydrodynamics started with the work of Reynolds in 1886. The elastic deformation of the surfaces was next incorporated to Reynolds' equation by Meldahl [64]. Then Ertel [65] included a pressure-viscosity effect on film thickness and finally a full film could be predicted. Thereafter this type of lubrication has been called elastohydrodynamic lubrication.

Piezoviscous-elastic (Hard EHL) relates to materials of high elastic modulus such as metals. In this form of lubrication, the elastic deformation and the pressure-viscosity effects are equally important. The maximum pressure is typically between 0.5 and 3 GPa and the minimum film thickness normally exceeds 0.1 μm. In isoviscous-elastic (soft EHL) the elastic distortions are large, even with light loads, and the fluid viscosityremains constant.

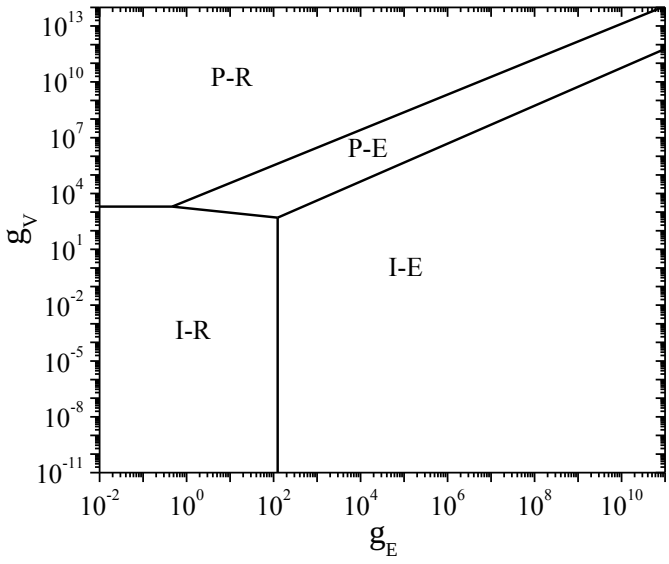

Figure In.6 Operation regimes in elastohydrodynamic lubrication.

Soft EHL relates to materials of low elastic modulus such as rubber. The maximum pressure for soft EHL is typically1 MPa, in contrast to 1 GPa for hard EHL. The minimum film thickness for soft EHL is typically above 1 μm. The common features of hard and soft EHL are that the local elastic deformation of the solids provides coherent fluid films and that asperity interaction is largely prevented. This implies that the frictional resistance to motion is due to lubricant shearing.

The most widely used film thickness formula in EHL was introduced by Hamrock and Dowson [66]–[68]. Their curve fitting to numerical solution is still broadly used. Calculating the elastic deformation is the most time consuming part in solving Reynolds equation. Multilevel-Multigrid integration technique was introduced by [69], which made it possible to numerically solve the equation with very dense grids. Venner further improved the technique to perform transient calculations. A comprehensive book has been written on this subject [70].

Magnetic body forces on ferrofluids

The total magnetic body force density acting on a ferrofluid in the presence of a magnetic field distribution is [26], [71].

$$f_m = -\nabla\left[\mu_0 \int_0^H \left(\frac{\partial M v_f}{\partial v_f}\right)_{H,T} dH\right] + \mu_0 M \nabla H. \qquad \text{In.14}$$

Here v_f and T are the volume and temperature of the fluid, respectively. The first term in equation In.14 is a magnetostrictive term related to the changes of the fluid density due to the applied magnetic field. If the fluid is considered incompressible, this term is neglected and equation In.14 simplifies to:

$$f_m = \mu_0 M \nabla H. \qquad \text{In.15}$$

As it was said before a ferrofluid can be thought as a Newtonian fluid in which an additional force appears when it is placed in the presence of a magnetic field distribution. Equation In.15 implies that in order to provoke the appearance of magnetic forces in an incompressible ferrofluid, it is necessary to place it under a non-uniform magnetic field distribution.

The motion of an incompressible magnetic ferrofluid can be described by the modified Navier-Stokes equation and reads as follows:

$$\rho\left[\frac{\partial V}{\partial t}+V\cdot\nabla V\right]=-\nabla P+\eta\nabla^2 V+\rho g+\mu_0 M\nabla H. \qquad \text{In.16}$$

In this dissertation we are interested in first obtaining and second solving the Reynolds equation for ferrofluids. It is derived by integrating the continuity and the modified Navier-Stokes equations under the lubrication approximation. In order to retain a problem where the pressure does not vary through the lubricant film, it will be supposed that the gradient of the magnetic field distribution has non-vanishing components only in the shearing plane.

Appling the same boundary conditions and assumptions as in the previous section we can obtain Reynolds equation for a Newtonian ferrofluid as follows:

$$\begin{aligned}&\frac{\partial}{\partial x}\left(\frac{\rho h^3}{12\eta}\left[\frac{\partial P}{\partial x}-\mu_0 M\frac{\partial H}{\partial x}\right]-\rho h U_x\right)\\&+\frac{\partial}{\partial y}\left(\frac{\rho h^3}{12\eta}\left[\frac{\partial P}{\partial y}-\mu_0 M\frac{\partial H}{\partial y}\right]-\rho h U_y\right)=\frac{\partial}{\partial t}(\rho h)\end{aligned} \qquad \text{In.17}$$

The modified Reynolds equation for a ferrofluid differs from the one for a Newtonian fluid only in the terms corresponding to the magnetic body forces. Obviously, in the absence of a magnetic field or in the case where the magnetic field distribution is uniform, equation In.17 reduces to equation In.6**.**

Interactions in Magnetic Suspensions

Inter-particle Interactions

The interaction energy between two magnetic dipoles with magnetic moments $m = m_i = m_j$ is given by:

$$U^{dip} = U_0 \left(\frac{1}{r_{ij}}\right)^3 \left[1 - 3cos^2\theta_{ij}\right]. \qquad \text{In.18}$$

Here $U_0 = \frac{m^2}{4\pi\mu_0}$ and $r_{ij} = \left|\vec{r}_{ij}\right| = \left|\vec{r}_j - \vec{r}_i\right|$ is the center-to-center distance between two dipoles and θ_{ij} is the angle formed between the direction of the external magnetic field and the line joining the centers of the two dipoles, as shown in Figure In.7. Here $\mu_0 = 4\pi \cdot 10^{-7}$is the vacuum permeability and U_0 represents the repulsive potential value for two dipoles that stand side by side ($\theta_{ij} = 90$ °). Consequently, the magnetic force on dipole "i" caused by dipole "j" is given by $F_{ij}^{dip} = -\nabla_i U_{ij}$ and reads as follows:

$$F_{ij}^{dip} = F_0 \left(\frac{1}{r_{ij}}\right)^4 \left[\left(3cos^2\theta_{ij} - 1\right)\hat{e}_r + \sin(2\theta_{ij})\hat{e}_\theta\right] \qquad \text{In.19}$$

where $F_0 = \frac{3U_0}{2R}$.

Determining the true magnetization of the particles in a magnetic suspension containing millions of particles is challenging. However, it is well known that a uniformly polarized/magnetized sphere generates the same electric/magnetic field outside the sphere as that produced by a single point dipole [72]. As a first approximation we suppose that the particles interact like magnetic dipoles in a carrier fluid. This is only strictly valid in the case of dilute suspensions. When a single sphere of radius R and volume V_p is placed within a uniform magnetic field, $\vec{H}_0$, it acquires a magnetic moment $\vec{m}_i = \mu_0 V_p 3\beta\vec{H}_0$ in which $\beta \equiv \frac{\mu_{pr}-\mu_{cr}}{\mu_{pr}+2\mu_{cr}}$ is the so-called contrast factor [26]. Here μ_{pr} and μ_{cr} are relative permeability of particle and carrier fluid, respectively. The field inside the particle is $\vec{H} = (1-\beta)\vec{H}_0$ [22].

The expression $\vec{m}_i = \mu_0 V_p 3\beta\vec{H}_0$ is valid for low magnetic fields, well in the linear regime, and dilute suspensions. However, the particle permeability, and subsequently the contrast factor, may vary nonlinearly with the magnetic field (e.g. ferromagnetic

materials). Usually field-dependent permeability is described by the Frohlich–Kennelly constitutive equation [73]:

$$\mu_{pr} = 1 + \frac{(\mu_{pr}^0 - 1)\frac{M_S}{H}}{(\mu_{pr}^0 - 1) + \frac{M_S}{H}} \qquad \text{In.20}$$

where M_S is the saturation magnetization and μ_{pr}^0 is the initial permeability.

EquationIn.19 is valid just for two isolated dipoles. Hence multi-body interactions are neglected. Frequently local field theory is used to calculate the magnetic field in a suspension of many particles [74], [75]. The local field, $\vec{H}_i^{\,loc}$, at center of particle "i" is calculated as a summation of external magnetic field and the magnetic field generated by other particles:

$$\vec{H}_i^{\,loc} = \vec{H}_0 + \sum_{j \neq i} \vec{H}_j^{\,\vec{m}_j} = \vec{H}_0 + \sum_{j \neq i} \frac{1}{4\pi\mu_0\mu_{cr}} \frac{3(\vec{m}_j \cdot \hat{e}_r)\hat{e}_r - \vec{m}_j}{r_{ij}^3} \qquad \text{In.21}$$

According to this, the moment of particle i is $\vec{m}_i = \mu_0 V_p 3\beta(H)\vec{H}_i^{\,loc}$ and the field inside the particle is $\vec{H} = (1-\beta)\vec{H}^{loc}$. The local field depends on the magnetic moments of the particles, but also the magnetic moments of the particles depend on the local field. Therefore the solution of these equations should be done following a self-consistent process.

The force in equation In.19 has two important features. Firstly, it is a long-range force decaying as a power law with the distance to the power of four. Secondly, it is anisotropic since the magnetic force depends on the angle formed between the center-to-center line between two particles and the direction of the magnetic field. The angle corresponding to $U_{ij}(\theta_m) = 0$ is called the magic angle $\theta_m = arcos(\frac{1}{\sqrt{3}}) \cong 54.7°$. The normal and perpendicular forces to $\vec{H}_0$, denoted by $F_{\perp}^{mag}$ and $F_{\parallel}^{mag}$ respectively, are merely given by:

$$F_{\perp}^{mag} = F_0 \left(\frac{2R}{r_{ij}}\right)^4 \sin(\theta_{ij})\left[5\cos^2(\theta_{ij}) - 1\right]$$
$$F_{\parallel}^{mag} = F_0 \left(\frac{2R}{r_{ij}}\right)^4 \cos(\theta_{ij})\left[5\cos^2(\theta_{ij}) - 3\right] \qquad \text{In.22}$$

The critical angles $\theta_\perp$and $\theta_\parallel$ for which normal and parallel forces are zero are given by $\theta_\perp = 63.4°$ and $\theta_\parallel = 39.2°$. Figure In.7a shows the interaction energy of two particles as a function of the parallel and perpendicular separation. The arrows indicate the direction of magnetic force. When approaching (say from infinity) two dipoles at prescribed shift $r_\perp$, one switch from repulsion in perpendicular direction to attraction at $\theta_\perp$. The same applies to the parallel direction (switch at $\theta_\parallel$).

The anisotropy of the particles interaction may induce the formation of anisotropic structures or assemblies, as those illustrated in Figure In.7b. Applying the principle of superposition to pairs of magnetic particles the same analysis can be performed to determine the interaction energy of an ensemble of particles. The interaction of two facing chains U_0^{cc} ($r_\parallel = 0$, $r_\perp = 2R$) consisting of N particles and length $L = 2RN$, is always repulsive. Figure In.7b illustrates the interaction energy of two chains of 9 particles U^{cc}, normalized by interaction energy of two facing chains. Similar to interaction energy of two particles (Figure In.7a), two chains of particles either repel or attract each other according to their longitudinal and transverse shift. On the one hand, for large relative separation distances ($r_\perp/L \gg 1$) the interaction energy of two facing chains retain the $1/R^3$ behavior of two point-dipole like particles. On the other hand, for short separation distances ($r_\perp/L \ll 1$) the interaction decays as $1/R$. This results in considerable softening due to long-range screening mediated by attractive pairs compensating the repulsion arising from neighboring pairs [76]. Moreover, chains shift from repulsive to attractive interaction when they are shifted longitudinally at least half of their length.

Hydrodynamic Interaction

Magnetostatic interactions are not the only forces acting on the particles. Since any magnetic fluid of interest in this PhD Thesis is truly a colloidal suspension, the interaction between the particles and the continuum phase is important. Different models for the hydrodynamic drag law are employed in simulations of MRFs; such as, one-way coupling discrete element and two-way coupled smoothed hydrodynamics [77]–[79]. The discrete element method has a higher computational efficiency but the incorporation of the hydrodynamic drag force involves some rough approximations. Furthermore, often a one-way coupling is used for the simulations, i.e. the velocity of the fluid phase is not influenced by the presence of the particles in the suspension.

In many particle-based simulations of MRFs, the Stokes drag law is used to treat the interaction between the fluid and the particles [80]–[83]. Hence, the hydrodynamic interaction is assimilated as the drag force exerted by the flow on a particle of radius R as follows: $F_d = -6\pi\eta R(u - u^\infty)$. Here, u^∞ is the velocity of continuous phase at position of particle, u is the particle's velocity, and η is viscosity of fluid. Recently, a comprehensive simulation study was done on the different hydrodynamic models applicable in MRFs [79]. They used a discrete element method with Stokes drag law for the hydrodynamic interactions and two-coupled discrete element-smoothed particle

hydrodynamics models with drag laws from Stokes and Dallavalle/Di Felice, respectively.

a) b)

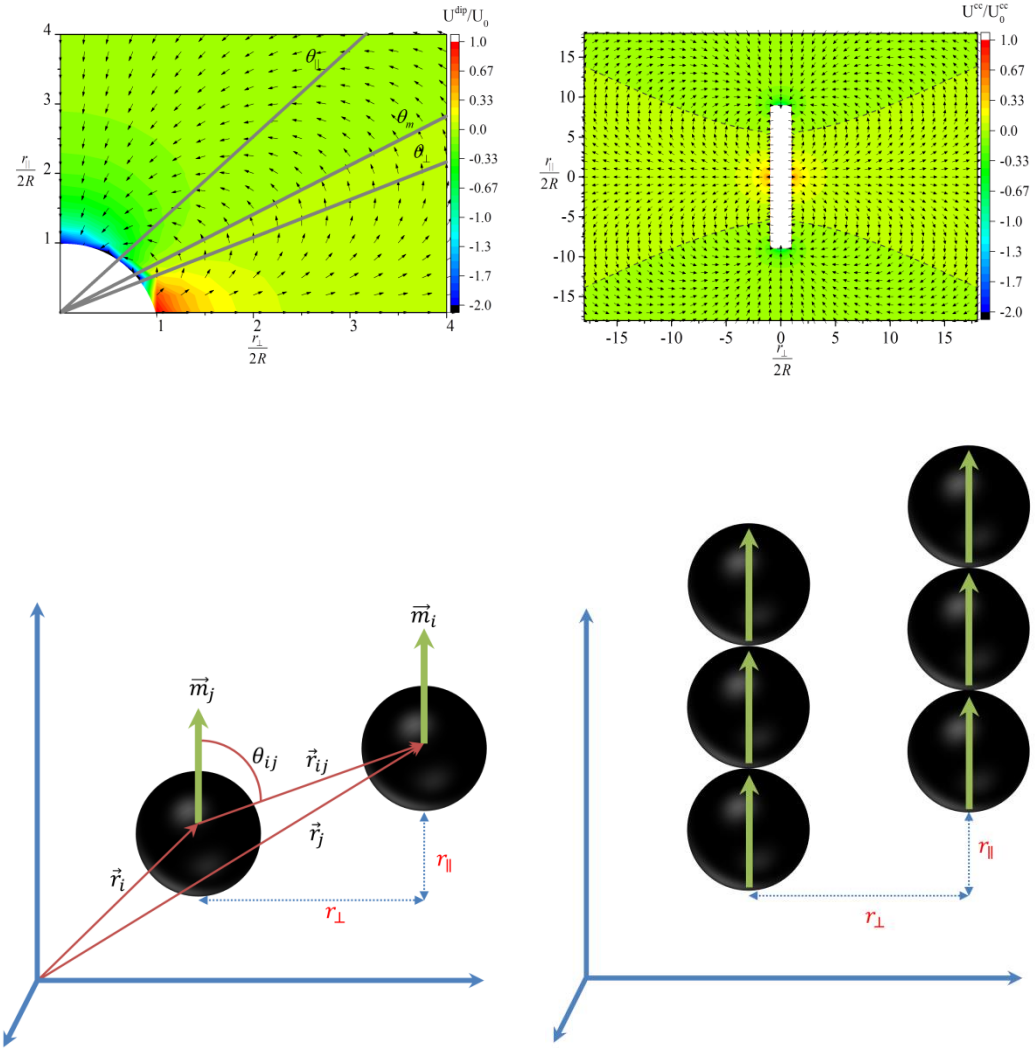

Figure In.7 Interaction energy of magnetic particles. a) Two point-dipole particles. b) assemble of 9 particles. Arrows show direction of magnetic force.

It was demonstrated that if the main stress contribution comes from other forces like wall contact forces or viscous forces, all models give similar shear stress results. Therefore, in our simulations and experiments, mostly working in the limit of creeping flow and dilute suspensions, the Stokes' drag law approximation is valid.

Brownian Motion

The Brownian motion was first reported by Robert Brown in 1827, while he was observing the movement of pollen particle in water. Brownian motion is related to thermal fluctuation of atoms and molecules and collisions between these particles. Generally speaking, a continuum medium is composed of atoms at thermal equilibrium. When particles are suspended in a fluid there are collisions between the fluid and the particles and as a result particles move randomly. Pioneering works by Albert Einstein in 1905 and Marian Smoluchowski in 1906, mathematically, related displacement of a particle to the diffusion coefficient and time. Einstein argued that displacement of a Brownian particle is proportional to the squared root of the elapsed time and diffusion coefficient. This famous equation reads as:$\langle \Delta s^2 \rangle = 2D\Delta t$. Here, D is the diffusion coefficient for an isolated particle: $D = \frac{k_B T}{6\pi\eta R}$. Due to the large sizes of dispersed particles, Brownian forces are usually neglected in the simulation of MRFs.

Dimensionless Groups

Brownian motion prevents particles from settling but also from forming aggregates, hence reducing the yield stress. In magnetorheology the Lambda ratio (also called coupling coefficient) is defined as the ratio between magnetic interparticle forces and Brownian forces [4], [26].

$$\lambda \equiv \frac{U_0}{k_B T} = \frac{\pi \mu_0 \mu_{cr} R^3 (3\beta H_0)^2}{18 k_B T} \qquad \text{In.23}$$

The Lambda ratio provides a very important criterion in defining the aggregation process. For $\lambda \sim 1$ the structure formation is reversible but for $\lambda \gg 1$ magnetostatic interaction predominates and particles attract strongly and follow a ballistic movement [84]. In the case of MRFs, the Brownian motion is negligible as compared to magnetostatic forces; thermal fluctuations play little role in breaking the chains as happens to be the case for FFs. The dimensionless group (λ) is typically of the order 10^6 for iron-based MRFs.

The so-called Mason number (Mn) is relevant when the MRF is subjected to flow. Mn is basically a dimensionless shear rate that can be defined as the ratio between hydrodynamic drag and magnetostatic forces acting on the particles [85]. If Mn is low,

magnetostatic interactions prevail and chain-like structures form. But if Mn is high the hydrodynamic interaction predominates and structures break. In the limit of linear magnetization regime, the Mason number reads as follows [4]:

$$Mn \equiv \frac{72\eta\dot{\gamma}}{\mu_0\mu_{cr}(3\beta H_0)^2} \qquad \text{In.24}$$

The utility of this dimensional analysis is that the shear rate and field strength dependence of the suspension viscosity can be described in terms of a single independent variable Mn [86]. The transition from magnetization to hydrodynamic control of the suspension structure is determined by a critical Mason number Mn* that solely depends on the particle volume fraction. Interestingly, shear viscosity measurements of MRFs at different magnetic fields and concentrations collapse reasonably well on a master curve as a function of a reduced Mason number (Mn/Mn*). The Bingham model is the most widely used model to describe the shear flow of MRFs [86], [87]. However, deviations from Bingham model have been reported [88]. A structural viscosity model was recently proposed which predicts a smoother transition between magnetostatic and hydrodynamic dominated regimes to better explain the discrepancies between the Bingham model and experimental data [89].

Aggregation Phenomena

The formation of large clusters by non-equilibrium growth processes such as, aggregation, coagulation flocculation and polymerization is ubiquitous in a wide range of applications. Hence, the formation of particulate structures and the kinetics of the phenomena are of interest for both theoretical and technological reasons. Although systems with short range-interactions are fairly understood [90], our knowledge of processes dominated by long-range interactions is far from complete. The diffusion-limited cluster-cluster aggregation models [91], [92], and the scaling theory [93] explain well the scaling properties of short-range systems. These two models have been shown to be able to explain the kinetics of aggregation of magnetic colloidal suspensions interacting via long-range forces [94]. However, some discrepancies have been observed for systems of non-Brownian particle suspensions which is the case of interest in magnetorheology [95], [96].

During the application of an external magnetic field to a MRF the particles self-assemble into chain-like structures aligned in the field direction. Because energy is required to deform and break the chains, this microstructural transition is responsible for the onset of a large –tunable- yield stress. There are many available experimental results dealing with the rheology and properties of MRFs [82], [89], [97], [98]. However, their aggregation kinetics is still not well understood. In biomedical applications, the self-assembly often reduces the biocompatibility because of the formation of aggregates. For

example, in magnetic resonance imaging (MRI) the transversal relaxation time changes with time if the magnetic interaction gives rise to the formation of chains of particles [32], [99], [100]. The formation of linear aggregates also has important consequences in hyperthermia applications of superparamagnetic particles [101].

Understanding the aggregation phenomena in the absence of flow is a rich field and has been the focus of numerous studies [84], [102]–[105]. In the quiescent state, the structure formation is determined by the interplay of three forces, namely, *thermal fluctuation*, *hydrodynamic drag forces* and *magnetic interactions*. Field-induced microstructure formation of magnetic suspensions depends on particles concentration, the dimensions of the container in the direction of the magnetic field, and more importantly, the ratio of dipolar energy to thermal energy (i.e. the Lambda ratio). If the interparticle distance r_c is below a critical distance, the initially random motion of particles due to thermal energy changes into a ballistic motion. This critical distance is known as capture radius and is defined by the surface where $U^{dip} = k_B T$.

$$r_c = R[4\lambda(3\,cos^2(\theta) - 1)]^{\frac{1}{3}} \qquad \text{In.25}$$

where r_c is the threshold separation for spherical particles and is a function of θ since U^{dip} is anisotropic. θ is the angle formed between the direction of external magnetic field and the line joining the centers of the two particles. As the Lambda ratio increases the r_c increases and more particles are attracted to the target particle; hence; the aggregation kinetics becomes faster and truly deterministic.

The irreversible aggregation of particles and the subsequent formation of complex structures have been investigated theoretically and experimentally using different materials and methods. Microparticle aggregation studies have been performed in a variety of physical systems, such as electrorheological fluids [106], nonmagnetic particles immersed in a ferrofluid [95], [107] and superparamagnetic latexes [103], [104], [108], [109]. In experiments, researchers have used a variety of methods such as video-microscopy [95], [103], [107], [110], small-angle light scattering [111], scattering dichroism [112], and optical trapping [113]–[115] among them. Theoretical models and computer aided molecular dynamic simulations have also been used to explain self-assembly process [94], [116]–[119].

When the dipolar interaction strength greatly exceeds thermal energy, $\lambda \gg 1$, particles experience an attractive dipolar interaction and form linear chains. The aggregation process happens at different time scales and form complex structures depending on packing fraction (area fraction or volume fraction). Figure In.8 shows a snapshot of the structure obtained from molecular dynamic simulations at different area fractions in a 2D rectangular confinement. For short times, during the aggregation process, tip-to-tip

aggregation results in the formation of clusters of particles elongated in the direction of the field forming single-particle cross section aggregates (Figure In.8a, b).

For surface fractions above a few percent, a transition from tip-to-tip aggregation is observed. When the surface fraction is such that long parallel chains are close enough, a sideways coalescence of the chains through a zippering motion is observed [104]. This phenomenon results in a thickening of the chains (Figure In.8c, d). Lateral interaction is observed only at sufficiently high concentrations because the net attraction between chains is a short range interaction, decaying approximately as $r_{\perp}{}^{-\frac{3}{2}} exp(-\frac{r_{\perp}}{R})$ with lateral distance $r_{\perp}$. In contrast, the tip-to-tip aggregation process occurs via a long range dipolar interaction decaying as r^{-3} [120], [121]. Lateral interactions occur because of thermal fluctuations of the particles that lead to a local variation in the magnetic field nearby a dipolar chain [113]. Halsey and Toor [120], [121] showed that fluctuating chains interact more strongly than rigid chains. Without any lateral aggregation, case of dilute suspension, tip-to-tip is the main mechanism of aggregation; the linear aggregates would partition the space into strips, and restrain the motion to only one dimension [104], [106].

Lateral interaction is also responsible for the crosslinking of chains, when a long chain attaches to other chains, it leads to the formation of horizontal and vertical interconnections between chains (Figure In.8e, f). The existence of crosslinks requires the bending of chains out of the field direction. Crosslinking of individual chains results in a fully interconnected fibrous structure typically observed above a surface fraction of 50% [104].

The study of the growing rate of the structure formation is important, in particular, for the prediction of response time of MRFs since their practical applications depend on the rate of change of their properties after the application of an exciting field. The kinetics of irreversible aggregation is usually described in terms of the evolution of the probability density of clusters of size s at time t, $n_s(t)$. Several statistical measures are typically used to characterize the kinetics of an aggregation process.

For instance, average cluster size $l(t)$ and (weighted) mean cluster size $S(t)$ [122]:

$$\langle l(t) \rangle = \frac{\sum_s s n_s(t)}{\sum_s n_s(t)} \qquad \text{In.26}$$

$$\langle S(t) \rangle = \frac{\sum_s s^2 n_s(t)}{\sum_s s n_s(t)} \qquad \text{In.27}$$

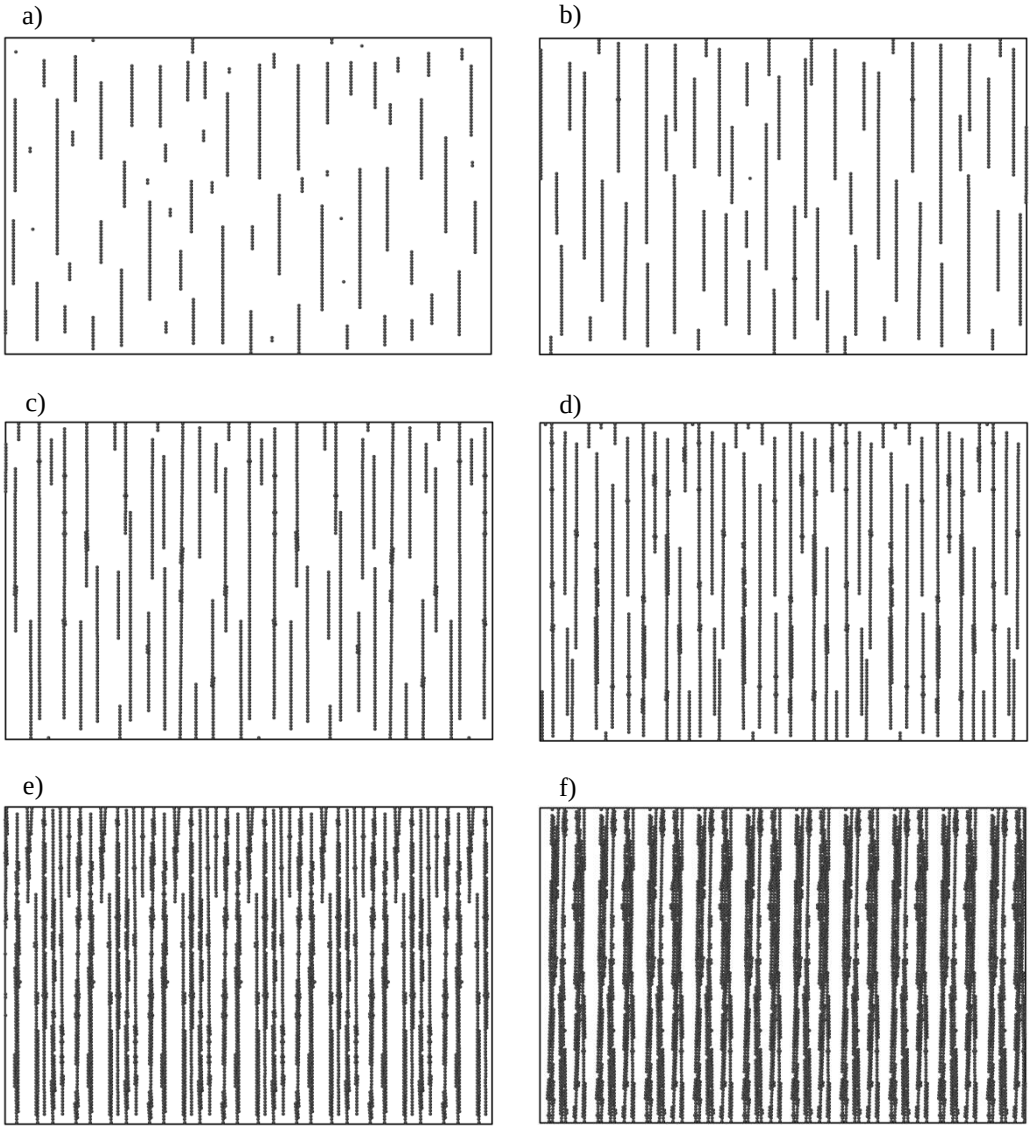

Figure In.8 Snapshot of the simulated structures for magnetic suspensions in 2D geometries at different area fractions. Obtained from molecular dynamic simulations. a) 3% b) 5% c) 7.5% d) 10% e) 20% f) 30%.

The interesting point here is that experiments and numerical simulations show that the evolution of these variables displays a power-law behavior, namely, $S(t) \sim t^{z}$, $l(t) \sim t^{z'}$.

The scaling theory [93] relationship for cluster size distribution is usually casted in the form of:

$$n_s \sim s^{-2} g(s/S(t))$$
$$n_s \sim t^{-\omega} s^{-\tau} f(s/t^z) \qquad \text{In.28}$$

with $f(x) \sim 1$ for $x \ll 1$ and $f(x) \ll 1$ for $x \gg 1$. On the other hand, $g(x) \sim x^{\Delta}$ for $x \ll 1$ and $g(x) \ll 1$ for $x \gg 1$.

Elucidating the scaling exponents z, z', and Δ has been a major objective in many previous studies on the kinetics of aggregation in magnetic suspensions [94], [95], [123], [124]. Numerical simulations of the diffusion-limited aggregation of oriented anisotropic particles suggested that $z = \frac{1}{1-\gamma}$ [116]. They assumed the diffusion coefficient D_S of a cluster of size s to be $D_S = D_0 s^{\gamma}$ where D_0 is a constant. Experimental work by Promislow *et al.* [124] found that the z exponent has a weak inverse dependence on particle volume fraction and dimensionless dipole strength. The scaling exponent was reported to be $z \in [0.48 - 0.75]$. They proposed a characteristic time scale, $t_B^* = \frac{R^2}{24[(1/3)^{1/2} - (1/3)^{3/2}] D\lambda\phi}$ which could collapse all $S(t)$ curves for different magnetic fields and volume fractions on a master curve. However, in a latter work by Dominguez *et al.* [94], in a 2D confinement, they did not observe any dependence of dynamic exponent on ϕ_{2D} and λ. They obtained an average value of dynamic exponent $\langle z \rangle = 0.57$ and $\langle \acute{z} \rangle = 0.47$ in experiments and $\langle z \rangle = 0.62$ and $\langle \acute{z} \rangle = 0.59$ via Brownian dynamic simulation. These discrepancies in the reported results for different experimental conditions, 3D geometries and quasi-2D confinement, make it hard to draw meaningful conclusions. Finally, the effect of confinement has not been sufficiently studied before. In particular, the aggregation kinetics of carbonyl iron particles (of interest in commercial MRFs) under confinement has not been reported in the literature yet.

REFERENCES

[1] J. Rabinow, "The magnetic fluid clutch," *Electrical Engineering*, 1948.

[2] W. M. Winslow, "Induced fibration of suspensions," *Journal of applied physics*, vol. 20, no. 12, pp. 1137–1140, 1949.

[3] G. Bossis, O. Volkova, S. Lacis, and A. Meunier, "Magnetorheology : Fluids , Structures and Rheology," *Ferrofluids*, pp. 202–230, 2002.

[4] J. de Vicente, D. J. Klingenberg, and R. Hidalgo-Alvarez, "Magnetorheological fluids: a review," *Soft Matter*, vol. 7, no. 8, p. 3701, 2011.

[5] X. Wang and F. Gordaninejad, “Magnetorheological materials and their applications,” *Intelligent Materials*, 2008.

[6] A.-G. Olabi and A. Grunwald, “Design and application of magneto-rheological fluid,” *Materials & design*, vol. 28, no. 10, pp. 2658–2664, 2007.

[7] A. Grunwald and A.-G. Olabi, “Design of a magnetostrictive (MS) actuator,” *Sensors and Actuators A: Physical*, vol. 144, no. 1, pp. 161–175, 2008.

[8] A. Grunwald and A.-G. Olabi, “Design of magneto-rheological (MR) valve,” *Sensors and Actuators A: Physical*, vol. 148, no. 1, pp. 211–223, 2008.

[9] R. Turczyn, M. Kciuk, F. Materials, and P. Technologies, “Preparation and study of model magnetorheological fluids,” *Journal of Achievements in Materials and Manufacturing Engineering*, vol. 27, no. 2, pp. 131–134, 2008.

[10] J.-H. Yoo and N. M. Wereley, “Design of a high-efficiency magnetorheological valve,” *Journal of Intelligent Material Systems and Structures*, vol. 13, no. 10, pp. 679–685, 2002.

[11] L. Chen, “Using magnetorheological (MR) fluid as distributed actuators for smart structures,” in *Industrial Electronics and Applications, 2009. ICIEA 2009. 4th IEEE Conference on*, 2009, pp. 1203–1208.

[12] J. Z. Chen and W. H. Liao, “Design, testing and control of a magnetorheological actuator for assistive knee braces,” *Smart Materials and Structures*, vol. 19, no. 3, p. 35029, 2010.

[13] M. R. Jolly, J. W. Bender, and J. D. Carlson, “Properties and applications of commercial magnetorheological fluids,” *Journal of Intelligent Material Systems and Structures*, vol. 10, no. 1, pp. 5–13, 1999.

[14] J. D. Carlson, “MR fluids and devices in the real world,” *International Journal of Modern Physics B*, vol. 19, no. 07n09, pp. 1463–1470, 2005.

[15] M. C. Heine, J. de Vicente, and D. J. Klingenberg, “Thermal transport in sheared electro-and magnetorheological fluids,” *Physics of Fluids*, vol. 18, no. 2, p. 23301, 2006.

[16] B. N. Reinecke, J. W. Shan, K. K. Suabedissen, and A. S. Cherkasova, “On the anisotropic thermal conductivity of magnetorheological suspensions,” *Journal of Applied Physics*, vol. 104, no. 2, p. 23507, 2008.

[17] W. I. Kordonsky, I. V Prokhorov, G. Gorodkin, S. D. Jacobs, B. Puchebner, and D. Pietrowski, “Magnetorheological finishing,” *Optics and Photonics News*, vol. 4, no. 12, pp. 16–17, 1993.

[18] S. D. Jacobs and W. I. Kordonski, “Magnetorheological finishing,” *International Journal of Modern Physics B*, vol. 10, pp. 2837–2848, 1996.

[19] S. Jha and V. K. Jain, “Design and development of the magnetorheological abrasive flow finishing (MRAFF) process,” *International Journal of Machine Tools and Manufacture*, vol. 44, no. 10, pp. 1019–1029, 2004.

[20] D. H. Read and J. E. Martin, “Field-Structured Chemiresistors,” *Advanced Functional Materials*, vol. 20, no. 10, pp. 1577–1584, 2010.

[21] J. Liu, G. A. Flores, and R. Sheng, “In-vitro investigation of blood embolization in cancer treatment using magnetorheological fluids,” *Journal of Magnetism and Magnetic Materials*, vol. 225, no. 1, pp. 209–217, 2001.

[22] D. C. Jiles, *Introduction to Magnetism and Magnetic Materials*. CRC Press, 1998.

[23] K. H. J. Buschow, *Handbook of magnetic materials*, vol. 15. Elsevier, 2003.

[24] K. J. Klabunde and R. Richards, *Nanoscale materials in chemistry*, vol. 1035. Wiley Online Library, 2001.

[25] D. C. Jiles and D. L. Atherton, "Theory of ferromagnetic hysteresis," *Journal of magnetism and magnetic materials*, vol. 61, no. 1–2, pp. 48–60, 1986.

[26] R. E. Rosensweig, *Ferrohydrodynamics*. Courier Corporation, 2013.

[27] C. Scherer and A. M. Figueiredo Neto, "Ferrofluids: properties and applications," *Brazilian Journal of Physics*, vol. 35, no. 3A, pp. 718–727, 2005.

[28] J. S. S. Walker and J. D. D. Buckmaster, "Ferrohydrodynamic thrust bearings," *International Journal of Engineering Science*, vol. 17, no. 11, pp. 1171–1182, Jan. 1979.

[29] P. Kuzhir, "Free boundary of lubricant film in ferrofluid journal bearings," *Tribology International*, vol. 41, no. 4, pp. 256–268, 2008.

[30] S. Odenbach, "Ferrofluids—magnetically controlled suspensions," *Colloids and Surfaces A: Physicochemical and Engineering Aspects*, vol. 217, no. 1, pp. 171–178, 2003.

[31] C. T. Yavuz, A. Prakash, J. T. Mayo, and V. L. Colvin, "Magnetic separations: From steel plants to biotechnology," *Chemical Engineering Science*, vol. 64, no. 10, pp. 2510–2521, 2009.

[32] D.-X. Chen, G. Via, F.-J. Xu, C. Navau, A. Sanchez, H.-C. Gu, J. S. Andreu, C. Calero, J. Camacho, and J. Faraudo, "Waiting time dependence of T 2 of protons in water suspensions of iron-oxide nanoparticles: Measurements and simulations," *Journal of Applied Physics*, vol. 110, no. 7, p. 73917, 2011.

[33] I. J. Bruce and T. Sen, "Surface modification of magnetic nanoparticles with alkoxysilanes and their application in magnetic bioseparations," *Langmuir*, vol. 21, no. 15, pp. 7029–7035, 2005.

[34] S. Bucak, D. A. Jones, P. E. Laibinis, and T. A. Hatton, "Protein separations using colloidal magnetic nanoparticles," *Biotechnology progress*, vol. 19, no. 2, pp. 477–484, 2003.

[35] C.-L. Chiang, C.-S. Sung, T.-F. Wu, C.-Y. Chen, and C.-Y. Hsu, "Application of superparamagnetic nanoparticles in purification of plasmid DNA from bacterial cells," *Journal of Chromatography B*, vol. 822, no. 1, pp. 54–60, 2005.

[36] B. Kozissnik, A. C. Bohorquez, J. Dobson, and C. Rinaldi, "Magnetic fluid hyperthermia: advances, challenges, and opportunity," *International Journal of Hyperthermia*, vol. 29, no. 8, pp. 706–714, 2013.

[37] J. T. Mayo, C. Yavuz, S. Yean, L. Cong, H. Shipley, W. Yu, J. Falkner, A. Kan, M. Tomson, and V. L. Colvin, "The effect of nanocrystalline magnetite size on arsenic removal," *Science and Technology of Advanced Materials*, vol. 8, no. 1–2, p. 71, 2007.

[38] A. Funes, J. de Vicente, and I. de Vicente, "Synthesis and characterization of magnetic chitosan microspheres as low-density and low-biotoxicity adsorbents for lake restoration," *Chemosphere*, vol. 171, pp. 571–579, 2017.

[39] A. Funes, A. Del Arco, I. Álvarez-Manzaneda, J. de Vicente, and I. de Vicente, "A microcosm experiment to determine the consequences of magnetic microparticles application on water quality and sediment phosphorus pools," *Science of The Total Environment*, vol. 579, pp. 245–253, 2017.

[40] J. K. Lim, D. C. J. Chieh, S. A. Jalak, P. Y. Toh, N. H. M. Yasin, B. W. Ng, and A. L. Ahmad, "Rapid magnetophoretic separation of microalgae," *Small*, vol. 8, no. 11, pp. 1683–1692, 2012.

[41] J. De Vicente, M. T. López-López, F. González-Caballero, and J. D. G. Durán, "Rheological study of the stabilization of magnetizable colloidal suspensions by addition of silica nanoparticles," *Journal of rheology*, vol. 47, no. 5, pp. 1093–1109, 2003.

[42] S. T. Lim, M. S. Cho, I. B. Jang, and H. J. Choi, "Magnetorheological characterization of carbonyl iron based suspension stabilized by fumed silica," *Journal of magnetism and magnetic materials*, vol. 282, pp. 170–173, 2004.

[43] P. J. Rankin, A. T. Horvath, and D. J. Klingenberg, "Magnetorheology in viscoplastic media," *Rheologica Acta*, vol. 38, no. 5, pp. 471–477, 1999.

[44] A.-M. Trendler and H. Böse, "Influence of particle size on the rheological properties of magnetorheological suspensions," *International Journal of Modern Physics B*, vol. 19, no. 07n09, pp. 1416–1422, 2005.

[45] K. H. Song, B. J. Park, and H. J. Choi, "Effect of magnetic nanoparticle additive on characteristics of magnetorheological fluid," *IEEE Transactions on Magnetics*, vol. 45, no. 10, pp. 4045–4048, 2009.

[46] J. De Vicente, J. P. Segovia-Gutiérrez, E. Andablo-Reyes, F. Vereda, and R. Hidalgo-Álvarez, "Dynamic rheology of sphere-and rod-based magnetorheological fluids," *The Journal of chemical physics*, vol. 131, no. 19, p. 194902, 2009.

[47] R. C. Bell, J. O. Karli, A. N. Vavreck, D. T. Zimmerman, G. T. Ngatu, and N. M. Wereley, "Magnetorheology of submicron diameter iron microwires dispersed in silicone oil," *Smart Materials and Structures*, vol. 17, no. 1, p. 15028, 2008.

[48] K. Shahrivar and J. De Vicente, "Thermogelling magnetorheological fluids," *Smart Materials and Structures*, vol. 23, no. 2, p. 25012, 2013.

[49] K. Shahrivar and J. de Vicente, "Thermoresponsive polymer-based magneto-rheological (MR) composites as a bridge between MR fluids and MR elastomers," *Soft Matter*, vol. 9, no. 48, pp. 11451–11456, 2013.

[50] P. J. Rankin, A. T. Horvath, and D. J. Klingenberg, "Magnetorheology in viscoplastic media," *Rheologica Acta*, vol. 38, no. 5, pp. 471–477, 1999.

[51] B. J. Hamrock, S. R. Schmid, and B. O. Jacobson, *Fundamentals of fluid film lubrication*. CRC press, 2004.

[52] G. W. Stachowiak, *Wear: materials, mechanisms and practice*. John Wiley & Sons, 2006.

[53] B. Tower, "Research committee on friction: second report on friction experiments," *Proceedings of the institution of mechanical engineers*, vol. 36, no. 1, pp. 58–70, 1885.

[54] N. P. Petrov, "Friction in Machines and the Effect of the Lubricant," *Inzherernii Zhurnal*, vol. 1, pp. 71–140, 1883.

[55] O. Reynolds, "On the Theory of lubrication and its application to mr. beauchamp tower's experiments, including an experimental determination of the viscosity of olive oil.," *Proceedings of the Royal Society of London*, vol. 40, no. 242–245, pp. 191–203, 1886.

[56] W. B. Hardy and I. Doubleday, "Boundary lubrication. The paraffin series," *Proceedings of the Royal Society of London. Series A, Containing Papers of a Mathematical and Physical Character*, vol. 100, no. 707, pp. 550–574, 1922.

[57] W. B. Hardy and I. Doubleday, "Boundary lubrication. The temperature coefficient," *Proceedings of the Royal Society of London. Series A, Containing Papers of a Mathematical and Physical Character*, vol. 101, no. 713, pp. 487–492, 1922.

[58] Y. Wang and Q. J. Wang, "Stribeck curves," in *Encyclopedia of Tribology*, Springer, 2013, pp. 3365–3370.

[59] H. Hertz, "Hertz's Miscellaneous Papers; Chapters 5 and 6," *ed: Macmillan, London, UK*, 1896.

[60] C. Barus, "Isothermals, isopiestics and isometrics relative to viscosity," *American journal of science*, no. 266, pp. 87–96, 1893.

[61] C. J. A. Roelands, "Correlational aspects of the viscosity-temperature-pressure relationship of lubricating oils," TU Delft, Delft University of Technology, 1966.

[62] D. Dowson and G. R. Higginson, *Elasto-hydrodynamic lubrication: the fundamentals of roller and gear lubrication*, vol. 23. Pergamon Press, 1966.

[63] M. Esfahanian and B. J. Hamrock, "Fluid-film lubrication regimes revisited," *Tribology Transactions*, vol. 34, no. 4, pp. 628–632, 1991.

[64] A. Meldahl, "Contribution to theory of lubrication of gears and of stressing of lubricated flanks of gear teeth," *Brown Boveri Review*, vol. 28, no. 11, 1941.

[65] H. Ertel and C.-G. Rossby, "A new conservation-theorem of hydrodynamics," *Geofisica pura e applicata*, vol. 14, no. 3–4, pp. 189–193, 1949.

[66] B. J. Hamrock and D. Dowson, "Isothermal elastohydrodynamic lubrication of point contacts: Part III—Fully flooded results," *Journal of Tribology*, vol. 99, no. 2, pp. 264–275, 1977.

[67] B. J. Hamrock and D. Dowson, "Isothermal elastohydrodynamic lubrication of point contacts: part 1—theoretical formulation," *Journal of Lubrication Technology*, vol. 98, no. 2, pp. 223–228, Apr. 1976.

[68] B. J. Hamrock and D. Dowson, "Isothermal elastohydrodynamic lubrication of point contacts: part ii—ellipticity parameter results," *Journal of Lubrication Technology*, vol. 98, no. 3, pp. 375–381, Jul. 1976.

[69] A. A. Lubrecht, C. H. Venner, W. E. Ten Napel, and R. Bosma, "Film thickness calculations in elastohydrodynamically lubricated circular contacts, using a multigrid method," *Trans. ASME, Journal of Tribology*, vol. 110, pp. 503–507, 1988.

[70] C. . Venner and A. . Lubrecht, *Multilevel Methods in Lubrication*, vol. 37. Elsevier, 2000.

[71] S. Odenbach and S. Thurm, "Magnetoviscous effects in ferrofluids," in *Ferrofluids*, Springer, 2002, pp. 185–201.

[72] J. D. Jackson, *Electrodynamics*. Wiley Online Library, 1975.

[73] R. M. Bozorth, "Ferromagnetism," *Ferromagnetism, by Richard M. Bozorth, pp. 992. ISBN 0-7803-1032-2. Wiley-VCH, August 1993.*, vol. 1, 1993.

[74] H. J. H. Clercx and G. Bossis, "Many-body electrostatic interactions in electrorheological fluids," *Physical Review E*, vol. 48, no. 4, p. 2721, 1993.

[75] Z. Wang, Z. Lin, and R. Tao, "many-body effect in electrorheological responses," *International Journal of Modern Physics B*, vol. 10, no. 10, pp. 1153–1166, 1996.

[76] R. Messina and L. Spiteri, "On the interaction of dipolar filaments," *The European Physical Journal E*, vol. 39, no. 81, 2016.

[77] Y. Pappas and D. J. Klingenberg, "Simulations of magnetorheological suspensions in Poiseuille flow," *Rheologica Acta*, vol. 45, no. 5, pp. 621–629, 2006.

[78] A. Ghaffari, S. H. Hashemabadi, and M. Ashtiani, "A review on the simulation and modeling of magnetorheological fluids," *Journal of Intelligent Material Systems and Structures*, vol. 26, no. 8, pp. 881–904, 2015.

[79] H. G. Lagger, T. Breinlinger, J. G. Korvink, M. Moseler, A. Di Renzo, F. Di Maio, and C. Bierwisch, "Influence of hydrodynamic drag model on shear stress in the simulation of magnetorheological fluids," *Journal of Non-Newtonian Fluid Mechanics*, vol. 218, pp. 16–26, 2015.

[80] D. Kittipoomwong, D. J. Klingenberg, and J. C. Ulicny, "Simulation of bidisperse magnetorheological fluids," *International Journal of Modern Physics B*, vol. 16, no. 17n18, pp. 2732–2738, Jul. 2002.

[81] J. C. Fernández-Toledano, J. A. Ruiz-López, R. Hidalgo-Álvarez, and J. de Vicente, "Simulations of polydisperse magnetorheological fluids: A structural and kinetic investigation," *Journal of Rheology*, vol. 59, no. 2, pp. 475–498, 2015.

[82] J. de Vicente, J. A. Ruiz-López, E. Andablo-Reyes, J. P. Segovia-Gutiérrez, and R. Hidalgo-Alvarez, "Squeeze flow magnetorheology," *Journal of Rheology*, vol. 55, no. 4, p. 753, 2011.

[83] J. C. Fernández-Toledano, J. Rodríguez-López, K. Shahrivar, R. Hidalgo-Álvarez, L. Elvira, F. Montero de Espinosa, and J. de Vicente, "Two-step yielding in magnetorheology," *Journal of Rheology*, vol. 58, no. 5, pp. 1507–1534, Sep. 2014.

[84] H. See and M. Doi, "Aggregation kinetics in electro-rheological fluids," *J. Phys. Soc. Jpn.*, vol. 60, no. 8, p. 2778, 1991.

[85] J. de Vicente, D. J. Klingenberg, and R. Hidalgo-Alvarez, "Magnetorheological fluids: a review," *Soft Matter*, vol. 7, no. 8, pp. 3701–3710, 2011.

[86] L. Marshall, C. F. Zukoski, and J. W. Goodwin, "Effects of electric fields on the rheology of non-aqueous concentrated suspensions," *Journal of the Chemical Society, Faraday Transactions 1: Physical Chemistry in Condensed Phases*, vol. 85, no. 9, pp. 2785–2795, 1989.

[87] D. J. Klingenberg, J. C. Ulicny, and M. A. Golden, "Mason numbers for magnetorheology," *Journal of Rheology*, vol. 51, no. 5, pp. 883–893, 2007.

[88] J. Ramos, D. J. Klingenberg, R. Hidalgo-Alvarez, and J. de Vicente, "Steady shear magnetorheology of inverse ferrofluids," *Journal of Rheology*, vol. 55, no. 1, p. 127, 2011.

[89] C. L. A. Berli and J. de Vicente, "A structural viscosity model for magnetorheology," *Applied Physics Letters*, vol. 101, no. 2, p. 21903, 2012.

[90] V. J. Anderson and H. N. W. Lekkerkerker, "Insights into phase transition kinetics from colloid science," *Nature*, vol. 416, no. 6883, pp. 811–815, 2002.

[91] P. Meakin, "Formation of fractal clusters and networks by irreversibleirreversible diffusion-limited aggregation," *Physical Review Letters*, vol. 51, no. 13, pp. 1119–1122, 1983.

[92] M. Kolb, R. Botet, and R. Jullien, "Scaling of kinetically growing clusters," *Physical Review Letters*, vol. 51, no. 13, p. 1123, 1983.

[93] T. Vicsek and F. Family, "Dynamic scaling for aggregation of clusters," *Physical Review Letters*, vol. 52, no. 19, p. 1669, 1984.

[94] P. Dominguez-Garcia, S. Melle, J. M. Pastor, and M. A. Rubio, "Scaling in the aggregation dynamics of a magnetorheological fluid," *Physical Review E - Statistical, Nonlinear, and Soft Matter Physics*, vol. 76, no. 5, pp. 1–13, 2007.

[95] J. Černák, G. Helgesen, and A. T. Skjeltorp, "Aggregation dynamics of nonmagnetic particles in a ferrofluid," *Physical Review E - Statistical, Nonlinear, and Soft Matter Physics*, vol. 70, no. 31, 2004.

[96] R. M. Erb, M. D. Krebs, E. Alsberg, B. Samanta, V. M. Rotello, and B. B. Yellen, "Beyond diffusion-limited aggregation kinetics in microparticle suspensions," *Physical Review E - Statistical, Nonlinear, and Soft Matter Physics*, vol. 80, no. 5, pp. 1–7, 2009.

[97] Z. Wang, K. Shahrivar, and J. de Vicente, "Creep and recovery of magnetorheological fluids: Experiments and simulations," *Journal of Rheology*, vol. 58, no. 6, pp. 1725–1750, 2014.

[98] Y. Grasselli, G. Bossis, and E. Lemaire, "Structure induced in suspensions by a magnetic field," *Journal de Physique II*, vol. 4, no. 2, pp. 253–263, 1994.

[99] S. L. Saville, R. C. Woodward, M. J. House, A. Tokarev, J. Hammers, B. Qi, J. Shaw, M. Saunders, R. R. Varsani, T. G. St Pierre, and others, "The effect of magnetically induced linear aggregates on proton transverse relaxation rates of aqueous suspensions of polymer coated magnetic nanoparticles," *Nanoscale*, vol. 5, no. 5, pp. 2152–2163, 2013.

[100] J. S. Andreu, C. Calero, J. Camacho, and J. Faraudo, "On-the-fly coarse-graining methodology for the simulation of chain formation of superparamagnetic colloids in strong magnetic fields," *Physical Review E*, vol. 85, no. 3, p. 36709, 2012.

[101] S. L. Saville, B. Qi, J. Baker, R. Stone, R. E. Camley, K. L. Livesey, L. Ye, T. M. Crawford, and O. T. Mefford, "The formation of linear aggregates in magnetic hyperthermia: Implications on specific absorption rate and magnetic anisotropy," *Journal of colloid and interface science*, vol. 424, pp. 141–151, 2014.

[102] J. Černák, G. Helgesen, and A. T. Skjeltorp, "Aggregation dynamics of nonmagnetic particles in a ferrofluid," *Physical Review E*, vol. 70, no. 3, p. 31504, 2004.

[103] J. H. E. Promislow, A. P. Gast, and M. Fermigier, "Aggregation kinetics of paramagnetic colloidal particles," *The Journal of Chemical Physics*, vol. 102, no. 13, p. 5492, 1995.

[104] M. Fermigier, A. P. Gast, and A. P. Gast, "Structure evolution in a paramagnetic latex suspension," *Journal of Magnetism and Magnetic Materials*, vol. 122, no. 1–3, pp. 46–50, Dec. 1993.

[105] Y. Grasselli, G. Bossis, E. Lemaire, E. L. Structure, and S. Antipolis, "Structure induced in suspensions by a magnetic field," *Journal de Physique II, EDP Sciences*, vol. 4, no. 2, pp. 253–263, 1994.

[106] S. Fraden, A. J. Hurd, and R. B. Meyer, "Electric-field-induced association of colloidal particles," *Physical review letters*, vol. 63, no. 21, p. 2373, 1989.

[107] J. Černák and G. Helgesen, "Aggregation of magnetic holes in a rotating magnetic field," *Physical Review E - Statistical, Nonlinear, and Soft Matter Physics*, vol. 78, no. 6, pp. 1–6, 2008.

[108] G. Bossis, C. Mathis, Z. Mimouni, and C. Paparoditis, "Magnetoviscosity of micronic suspensions," *EPL (Europhysics Letters)*, vol. 11, no. 2, p. 133, 1990.

[109] J.-C. Bacri, K. Djerfi, S. Neveu, and R. Perzynski, "Ferrofluid viscometer: transient magnetic birefringence in crossed fields," *Journal of magnetism and magnetic materials*, vol. 123, no. 1–2, pp. 67–73, 1993.

[110] C. P. Reynolds, K. E. Klop, F. A. Lavergne, S. M. Morrow, D. G. A. L. Aarts, and R. P. A. Dullens, "Deterministic aggregation kinetics of superparamagnetic colloidal particles," *The Journal of chemical physics*, vol. 143, no. 21, p. 214903, 2015.

[111] J. E. Martin, J. Odinek, and T. C. Halsey, “Evolution of structure in a quiescent electrorheological fluid,” *Physical Review Letters*, vol. 69, no. 10, pp. 1524–1527, 1992.

[112] S. Melle, M. A. Rubio, and G. G. Fuller, “Time Scaling Regimes in Aggregation of Magnetic Dipolar Particles: Scattering Dichroism Results,” *Physical Review Letters*, vol. 87, no. 11, p. 115501, 2001.

[113] E. M. Furst and A. P. Gast, “Dynamics and lateral interactions of dipolar chains,” *Physical Review E*, vol. 62, no. 5, p. 6916, 2000.

[114] E. M. Furst and A. P. Gast, “Micromechanics of magnetorheological suspensions,” *Physical Review E*, vol. 61, no. 6, p. 6732, 2000.

[115] E. M. Furst and A. P. Gast, “Micromechanics of dipolar chains using optical tweezers,” *Physical Review Letters*, vol. 82, no. 20, p. 4130, 1999.

[116] S. Miyazima, P. Meakin, and F. Family, “Aggregation of oriented anisotropic particles,” *Physical Review A*, vol. 36, no. 3, p. 1421, 1987.

[117] M.-C. Miguel and R. Pastor-Satorras, “Kinetic growth of field-oriented chains in dipolar colloidal solutions,” *Physical Review E*, vol. 59, no. 1, p. 826, 1999.

[118] D. Liu, M. R. Maxey, and G. E. Karniadakis, “Simulations of dynamic self-assembly of paramagnetic microspheres in confined microgeometries,” *Journal of Micromechanics and Microengineering*, vol. 15, no. 12, pp. 2298–2308, 2005.

[119] E. Climent, M. R. Maxey, and G. E. Karniadakis, “Dynamics of self-assembled chaining in magnetorheological fluids,” *Langmuir*, vol. 20, no. 2, pp. 507–513, 2004.

[120] T. C. Halsey and W. Toor, “Fluctuation-induced couplings between defect lines or particle chains,” *Journal of statistical physics*, vol. 61, no. 5, pp. 1257–1281, 1990.

[121] T. C. Halsey and W. Toor, “Structure of electrorheological fluids,” *Physical review letters*, vol. 65, no. 22, p. 2820, 1990.

[122] D. Sohn, “Kinetic studies of magnetic latex particles’ self-assembly under applied magnetic field,” *Journal of magnetism and magnetic materials*, vol. 173, no. 3, pp. 305–313, 1997.

[123] M. Fermigier and A. P. Gast, “Structure evolution in a paramagnetic latex suspension,” *Journal of Colloid and Interface Science*, vol. 154, no. 2, pp. 522–539, 1992.

[124] J. H. E. Promislow, A. P. Gast, and M. Fermigier, “Aggregation kinetics of paramagnetic colloidal particles,” *The Journal of chemical physics*, vol. 102, no. 13, pp. 5492–5498, 1995.

METHODOLOGY

In the scope of this dissertation rheological and tribological properties of magnetic suspension were determined in a torsional rheometer (Anton Paar MCR 302). Three different geometries were used for different test conditions. In rheology tests plate-plate and cone-plate configurations were used, mainly to ascertain the viscosity and the viscoelastic moduli of the suspensions. In tribology tests, friction essays were carried out in a non-conforming ball-on-three-plates contact. Finally, aggregation kinetics experiments were performed using video-microscopy techniques. In these tests we captured snapshots of the aggregation phenomena in a modified inverted microscope in the presence of uniaxial magnetic fields.

Materials

Magnetic particles used in this thesis are carbonyl iron microparticles and magnetic latexes. Carbonyl iron particles were obtained from thermal decomposition of iron pentacarbonyl and purchased from BASF SE (grades HQ and EW). They are quasi-spherical in shape and polydisperse in size with density of $\rho = 7.86\ \frac{g}{cm^3}$. The average particle diameter of the HQ grade has been reported in the literature to be around $d_{50} \cong 1.1\ \mu m$ [1], [2]. According to the manufacturer, EW grade particles have an average diameter $d_{50} \cong 3.0 - 4.0\ \mu m$. The iron purity is greater than 96.8%. Other impurities are carbon, nitrogen and oxygen. In the EW grade carbonyl iron particles a very thin surface layer of silica exists that facilitates their re-dispersibility in suspension. Magnetic latex particles used in this thesis have a diameter of approx. ~ 5 μm with a magnetic content of 5.72 wt% (density of ~ 1.1 g/cm^3). These particles were prepared by Nanogetic by first coating a layer of magnetic iron oxide onto a polystyrene core. Then an additional second polymer coating was applied to fully encapsulate the iron oxide shell. These latexes were functionalized with amino groups on their surface to minimize interparticle aggregation and particle/wall adhesion. The hysteresis loops of carbonyl iron particles (grade HQ and EW) and magnetic latexes are shown in Figure Mt.1.

In this thesis, the tribological characteristics of different lubricants in contact with a variety of surfaces have been investigated. In particular, we used three different types of lubricants: namely a ferrofluids, a commercial MRF and silicone oils. Silicone oils of different viscosities, in the range from 0.1 $Pa.s$ to 10 $Pa.s$ were used (Sigma-Aldrich). The commercial MRF used in this dissertation was a gift from Lord Corporation (MRF-132, US). Finally, the ferrofluid used in this work was purchased from Ferrotec (APG series). This particular series consists in magnetite nanoparticles dispersions in a synthetic hydrocarbon carrier typically used in audio speaker applications. It has a saturation magnetization of $24.3 \pm 0.7\ kAm^{-1}$ and Newtonian shear

viscosity $560\ mPa.s$. Particle volume fraction is around 5.5 vol% and the saturation magnetization for bulk magnetite is $447\ kAm^{-1}$.

We studied three different compliant contacts always operating in the isoviscous elastic regime: Polytetrafluoroethylene (PTFE), Polyoxymethylene (POM), and polydimethylsiloxane (PDMS). PTFE was used here as a compliant material because it exhibits appreciably lower friction coefficients than most other polymers and have important applications as solid lubricant and bearing material. POM possesses high tensile strength, creep resistance and toughness. It also exhibits low moisture absorption and is chemically resistant to hydrocarbons, solvents and neutral chemicals. These properties along with its fatigue endurance make POM ideal for many industrial applications such as in the automotive, appliance, construction, hardware and electronics. The elastomer surfaces are made of PDMS; fabricated from a two-component silicone elastomer kit (Sylgard 184, Dow Corning). The plates were made by casting a 3 mm thick sheet in a homemade mould. After allowing any air bubbles to escape using a vacuum chamber, the PDMS was cured for 8 h under vacuum at 70 ºC. After cooling overnight, the PDMS sheet was removed from the mould and plates of size (3mm × 6mm × 16mm) were retrieved. In a similar way, PDMS spheres were cast with a radius of 6.35 mm. Finally, the tribological properties of the commercial MRF were studied in steel-steel contacts. The steel tribopairs were commercial plates and balls of AISI316 stainless steel.

We employed thermoresponsive materials, in a novel approach, to formulate a new class of MRFs. We used, particularly, Poly (ethylene oxide)–poly (propylene oxide)–poly (ethylene oxide) (PEO–PPO–PEO) triblock copolymers and Poly(N-isopropylacrylamide) microgels (PNIPAM).

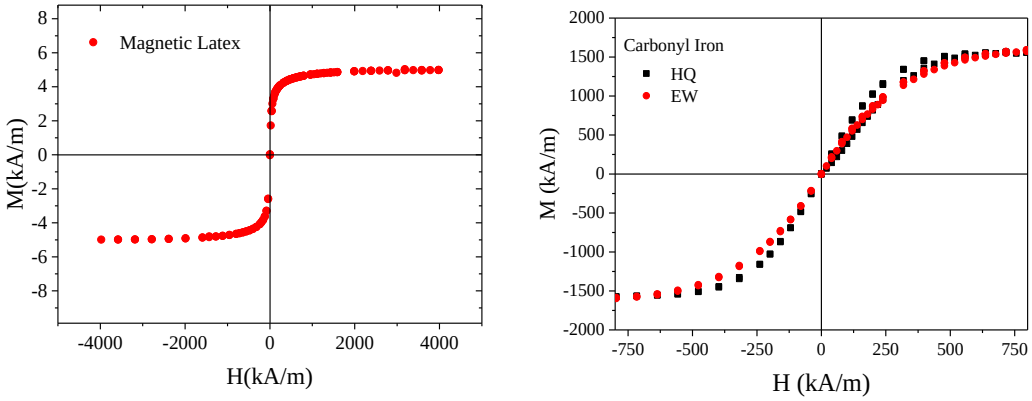

Figure Mt.1 Hysteresis loops of magnetic particles employed in this dissertation.

The triblock copolymers with a trade mark name Pluronic exhibit a temperature responsive micellization and gelation, and they are one major temperature responsive polymers based on amphiphilic balance [3], [4]. The hydrophilic and hydrophobic blocks in the molecular structure of Pluronic copolymers asset them the temperature responsive properties.

On the other hand, Poly(N-isopropylacrylamide) microgel (PNIPAM) is one of the most studied microgels known for its thermosensitivity properties. PNIPAM is hydrophilic at room temperature, and the microgel particles are highly swollen. When heated above a critical temperature, ~32°, the PNIPAM microgel becomes hydrophobic, so the particles shrink [5]. Recently, PINIPAM microgels sensitive to metal cations, pH, and light have also been synthesized [6]. Because of these unique properties, PNIPAM microgels has found numerous applications, especially in biomedical areas.

The Triblock copolymers, known as Pluronics F127, were purchased from Sigma-Aldrich. On the other hand, PNIPAM microgels were fabricated from a single-step emulsion polymerization reaction.

Rheometry

We performed rheometry tests to study the mechanical properties of MRFs. In a typical shear experiment, i.e. plate-plate geometry, the upper plate of the rheometer rotates while the bottom plate remains stationary. In this geometry, the shear rate and stress are not uniform; the shear rate increases in the radial direction according to $\dot{\gamma} = \frac{\omega r}{h}$. The shear stress for any non-Newtonian fluid can be expressed as a function of the torque by the expression: $\tau = \frac{2T}{\pi R^3}\left[\frac{3}{4} + \frac{1}{4}\frac{dlnT}{dln\dot{\gamma}_R}\right]$ [7], where T stands for torque and $\dot{\gamma}_R$ is shear rate at the rim of the plate. In the case of non-Newtonian fluids, the apparent viscosity measured with plate-plate geometry at the zero-shear limit overestimates the yield stress by a factor of 4/3 [7]. In cone-plate geometry this problem can be avoided since for small angles the shear rate is constant at all radii. However, this configuration causes different length of gapspanning chains and jamming in the apex of the cone. For Newtonian fluids, the relationship between the torque and the stress can be expressed as $\tau = \frac{2T}{\pi R^3}$. The maximum and minimum torques that the rheometer can achieve are $0.23Nm$ and $0.1\mu Nm$, respectively. The minimum angular velocity the rheometer can measure is $1.7 \cdot 10^{-8}\ s^{-1}$ and the maximum is $50\ s^{-1}$.

Particle Level Simulations

Magnetic interactions along with the Brownian motion and hydrodynamic forces can be casted into the equation of motion using a Lagrangian description. Thus the equation of motion of a magnetic particle can be written as follows:

$$m_i \frac{d\vec{v}_i}{dt} + \vec{F}_i^H - \vec{F}_i^B = \sum_{j \neq i} \vec{F}_{ij}^{mag} + \vec{F}_{ij}^{rep} \qquad \text{Mt.1}$$

where m_i and v_i represent mass and velocity of the particle i, respectively. Usually the inertia term on left hand side of the equation is neglected because Reynolds number is small ($Re \ll 1$). $\vec{F}_i^B$ stands for the Brownian force and is determined by $\overrightarrow{F}_i^B = B\overrightarrow{W}_i(t)$. The stochastic force, $\overrightarrow{W}_i(t)$, follows a standard Gaussian noise distribution and the coefficient B measures the ratio between the Brownian and magnetic interaction forces. We used an exponential form for the short-range repulsive forces for inter-particle repulsion and for particles and walls interaction.

$$\sum_{j \neq i} \vec{F}_{ij}^{rep} = \begin{cases} \exp\left(-k\dfrac{(r_{ij} - 2R)}{2R}\right)(-\hat{e}_r) \\ \exp\left(-k\dfrac{(h_i - R)}{2R}\right)\hat{n} \end{cases} \qquad \text{Mt.2}$$

Here k=100, $\hat{e}_r$ is unit vector in the direction of the line joining the centers of the two particles and $\hat{n}$ is the direction of the normal vector to the rigid walls. The short-range interactions between the particles have been argued to play an important role in determining the rheological behavior of the MRFs [8], [9]. This sharp repulsive force closely imitates hard spheres repulsion interaction and so favors the formation of thick column structures observed in experiments [9], [10]. Using characteristic length, force and time scales $L_c = 2R$, $F_c = F_0$ and $t_c = \frac{12\pi\eta_{cr}R^2}{F_0}$ the equation of motion is transformed to dimensionless form:

$$\sum_j \vec{F}_{ij}^{mag*} + \sum_{j \neq i} \vec{F}_{ij}^{rep*} + \vec{F}_i^{B*} + u^{\infty*}(\vec{x}_i^*) = \frac{d\vec{x}_i^*}{dt^*} \qquad \text{Mt.3}$$

Aggregation Kinetics Simulations

Simulations were performed within a 2D simulation box with periodic boundary conditions in x-direction as shown in Figure Mt.2. In the quiescent case ambient flow was set to zero and ‘no-slip’ condition was applied to those particles located at a critical distance from the walls. Particles within a distance $\frac{h_i}{\sigma} \leq 0.55$ of a boundary surface are considered ‘stuck’ and thus their velocities in the flow direction are set to zero. Therefore these particles can only move in the direction perpendicular to the wall.

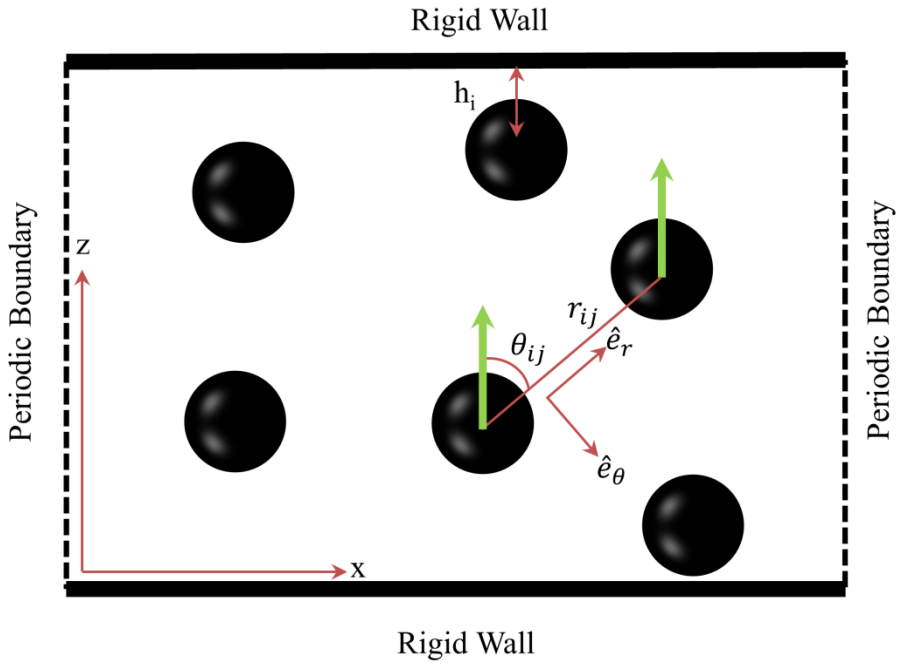

Figure Mt.2 Schematics of the simulation cell in quiescent state in 2D confinement.

A uniform external magnetic field was directed in the z-direction and the particle concentration was determined by the area fraction $\phi_{2D} = \frac{N\pi}{4L_z^* L_x^*}$. The total number of particles was chosen to be 1000 and the width of the simulation box, L_z^*, was 25, 50, and 100. Hence, to simulate different area fractions in the range $\phi_{2D} = 0.01 - 0.3$, L_x^* was changed to meet the desired area fraction.

The simulation began with the particles randomly distributed in the simulation box and the equations of motion were integrated numerically using an explicit Euler method, with time step $\Delta t^* = 1 \times 10^{-3}$up to $t^* = 10^5$. On the one hand, inter-particle exponential repulsive interactions were evaluated for separation less than a cut-off radius 2σ. On the other hand, wall-particle repulsive interactions were evaluated only for particles within distance $\frac{h_i}{\sigma} \leq 1.5$ from walls.

Creep-recovery simulation

In creep experiments, a constant step stress, τ_0, is applied to the upper wall of the confined system at time zero. The rheometer is able to instantaneously control the torque and the motion of the shaft in order to keep the stress on upper plate constant. In

the dynamic molecular simulations this is done by controlling the instantaneous strain of simulation box. The creep-recovery simulation of the MR system is performed in three steps with a constant magnetic field applied: (i) quiescent state, (ii) creep process, (ii) recovery process. The quiescent state step starts from a configuration with randomly distributed particles. Then, the system is equilibrated for a certain time to allow the formation of field-induced structures. Next, in the creep process, a stress is suddenly applied to the upper wall for a fixed duration of time. Finally, the stress is suddenly removed and the system relaxes for another prestablished period of time.

The stress, τ_0, imposed on simulation box has two components: viscous (τ_{vis}) and non-hydrodynamic contribution originating from the magnetic field (τ_H). The instantaneous strain rate is estimated as follows:

$$\dot{\gamma}(t) = \frac{[\tau_0 - \tau_H(t)]}{\eta_s} \qquad \text{Mt.4}$$

here η_s is the viscosity of the suspension in the absence of a magnetic field. For the case where the external field is imposed in the z-direction and the suspension is sheared in the x-direction, τ_H contains a pairwise contribution of the magnetic and repulsive forces in the direction of the imposed strain. This is calculated as follows:

$$\tau_{zx,H} = -\frac{1}{V}\sum_{i,j\neq i} F_{ij}^{x}\,(z_i(t) - z_j(t)) \qquad \text{Mt.5}$$

During each time step the instantaneous strain of the cell is calculated by $d\gamma = \dot{\gamma}(t)\Delta t$ and imposed on the upper surface of simulation box.

Tribometry

Experimental procedure

The tribological properties were examined on a ball-on-three plates geometry mounted on a MCR 302 Anton Paar rheometer. In the ball-on-three-plates device, a ball (radius R) is pressed at a given normal force against three plates that are mounted on a movable stage. As a result, the same load is acting evenly on all three frictional pairs. Next, the ball is commanded to rotate at an increasing sliding speed V while the plates are held stationary, at rest. This generates three sliding point contacts. In this device, the sliding speed V is related to the angular velocity (ω) through $V = R\omega/\sqrt{2}$. In this thesis, all tests were carried out at a temperature of 25 ºC and at a constant slide-to-roll ratio of

SRR = 2 (i.e., pure sliding conditions). In general, the slide-to-roll ratio is defined as the ratio of the absolute value of the sliding speed, $|V| = |U_B - U_P|$, to the entrainment speed, $U = (U_B - U_P)/2$, where U_B and U_P are the sliding speeds of the ball and plate, respectively. As a consequence, for pure sliding conditions the sliding speed is related to the entrainment speed through $|V| = 2U$). A schematic diagram of the test set-up is shown in Figure Mt.3.

The possibility of introducing a magnetic body force in the case of the ferrofluids has made these materials promising candidates for shaft sealing and lubrication in mechanical applications [11]–[13]. For example, it has been shown that by using ferrofluids in mechanical contacts it is possible to actively control frictional behavior [11]. In order to explore the tribological properties of ferrofluids in point contacts under magnetic fields, the ball-on-three-plates set-up was modified in this dissertation by placing cylindrical NdFeB magnets below each contact. For this purpose a spacer, of 1mm thickness was placed below the tribopairs that serves as a holder for the magnets. In this way we could provide a manner to superimpose an inhomogeneous magnetic field to the contact. This inhomogeneous magnetic field contributes to the appearance of an extra pressure in the contact zone. Moreover, the position of the magnets could be moved along the direction of the flow to study the effect of the magnetic field inhomogeneity on the frictional properties of ferrofluids in soft polymeric point-contacts.

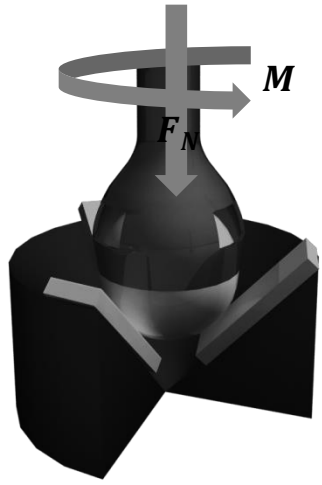

Figure Mt.3 Illustration of experimental set-up in ball-on-three-plates geometry.

Numerical Method in EHL

The understanding of the elastohydrodynamic lubrication of a point contact under combined rolling and squeeze film motion requires the simultaneous solution of the Reynolds equation, the elastic film shape, the force balance, and the lubricant state equations. By making use of the following dimensionless parameters:

$$\bar{X} = \frac{x}{a} \quad \bar{Y} = \frac{y}{b} \quad \bar{\rho} = \frac{\rho}{\rho_0} \quad \bar{\eta} = \frac{\eta}{\eta_0} \quad \bar{U} = \frac{u_m \eta_0}{E' R_x}$$
$$\bar{h} = \frac{h R_x}{b^2} \quad \bar{P} = \frac{P}{P_H} \quad \bar{t} = \frac{U_x t}{R_x} \quad \bar{W} = \frac{W}{E' R_x^2} \qquad \text{Mt.6}$$

for elastohydrodynamic conditions in a point contact the non-dimensional Reynolds equation can be written as follows:

$$\frac{\partial}{\partial \bar{X}}\left(\bar{\varepsilon}\frac{\partial \bar{P}}{\partial \bar{X}}\right) + \frac{\partial}{\partial \bar{Y}}\left(\bar{\varepsilon}\frac{\partial \bar{P}}{\partial \bar{Y}}\right) - \frac{\partial}{\partial \bar{X}}\left(\bar{\rho}\bar{h}\right) = 0 \qquad \text{Mt.7}$$

where $\bar{\varepsilon} = \frac{\bar{\rho}\bar{h}^3}{\bar{\eta}\bar{\lambda}}$ and $\bar{\lambda} = \frac{12 u_m \eta_0 R_x^2}{a^3 P_H}$. In the presence of a magnetic field, the pressure is defined as $\bar{P} = \frac{P - \mu_0 M H}{P_H}$. Generally, $\frac{\partial}{\partial \bar{X}}\left(\bar{\varepsilon}\frac{\partial \bar{P}}{\partial \bar{X}}\right)$ and $\frac{\partial}{\partial \bar{Y}}\left(\bar{\varepsilon}\frac{\partial \bar{P}}{\partial \bar{Y}}\right)$ are called Poiseuille term, and $\frac{\partial}{\partial \bar{X}}\left(\bar{\rho}\bar{h}\right)$ is called wedge term.

The first step in the numerical solution process is discretizing the Reynolds equation on a grid (Figure Mt.4). The computational domain is a rectangle of size $ma \times nb$. There are several ways to derive a discrete system of the equations from the differential problem each with their own merits for a given class of problems, e.g. Finite Element discretization, Variational Approach, Finite Difference Method and Finite Volume Approach. To this end, the continuous problem (partial differential equation(s) and boundary conditions) is transformed to a set of equations in terms of the unknown values at grid points. In this thesis we have used a classical multilevel multi-integration method that is based on finite difference discretization [14].

Before 1970s it was assumed that inlets were always fully flooded. This assumption seemed to be entirely reasonable in view of the small quantities of lubricant required to provide an adequate film. However, later it was recognized that some machine elements suffered from lubricant starvation. The lack of lubricant in the neighborhood of the

contact region is often referred to as starved lubrication and has major consequences for the performance of any EHL contact. The starved lubrication makes the boundary with the pressurized region a free boundary [15].

How partial filling of the inlet to EHL conjunction influences pressure and film thickness can readily be explored theoretically by adopting different starting points for the inlet pressure boundary. Lubricant starvation can be studied by simply changing m^*(see Figure Mt.4). A fully flooded condition is said to exist when m^* ceases to influence the minimum film thickness to any significant extent [16]:

$$m^* = 1 + 1.07\left[\frac{R_x h_{min}}{a^2}\right]^{0.16} \qquad \text{Mt.8}$$

The Reynolds equation is a non-linear partial differential equation for which a finite difference approximation is usually employed. A short central second order discretization of the Poiseuille terms, and a second order upstream discretization for the wedge term was used to discretize the Reynolds equation. This gives the following discrete Reynolds equation for the point (i, j) of the grid.

$$\begin{aligned} F = &\frac{\bar{\varepsilon}_{i-\frac{1}{2},j}\bar{P}_{i-1,j} + \bar{\varepsilon}_{i+\frac{1}{2},j}\bar{P}_{i+1,j} + (\bar{\varepsilon}_{i-\frac{1}{2},j} + \bar{\varepsilon}_{i-\frac{1}{2},j})\bar{P}_{i,j}}{d\bar{X}^2} \\ &+ \frac{\bar{\varepsilon}_{i,j-\frac{1}{2}}\bar{P}_{i,j-1} + \bar{\varepsilon}_{i,j+\frac{1}{2}}\bar{P}_{i,j+1} + (\bar{\varepsilon}_{i,j-\frac{1}{2}} + \bar{\varepsilon}_{i,j+\frac{1}{2}})\bar{P}_{i,j}}{d\bar{Y}^2} \\ &- \frac{1.5\bar{\rho}_{i,j}\bar{h}_{i,j} - 2\bar{\rho}_{i-1,j}\bar{h}_{i-1,j} + 0.5\bar{\rho}_{i-2,j}\bar{h}_{i-2,j}}{d\bar{X}} = 0 \end{aligned} \qquad \text{Mt.9}$$

where $\bar{\varepsilon}_{i\mp\frac{1}{2},j} = \frac{\bar{\varepsilon}_{i,j} + \bar{\varepsilon}_{i\mp1,j}}{2}$ and $\bar{\varepsilon}_{i,j\mp\frac{1}{2}} = \frac{\bar{\varepsilon}_{i,j} + \bar{\varepsilon}_{i,j\mp1}}{2}$.

An iterative solution method for these systems of equations starts with the Hertzian pressure distribution as an initial guess. Given an approximation to the solution of the problem, in each grid point a new approximation is computed by scanning the grid points in a prescribed order, changing the value in each grid point such that the local equation in that point is satisfied. The process comes in two flavors. If the new values are computed using only old values in the surrounding grid points it is referred to as Jacobi relaxation (Simultaneous Displacement).

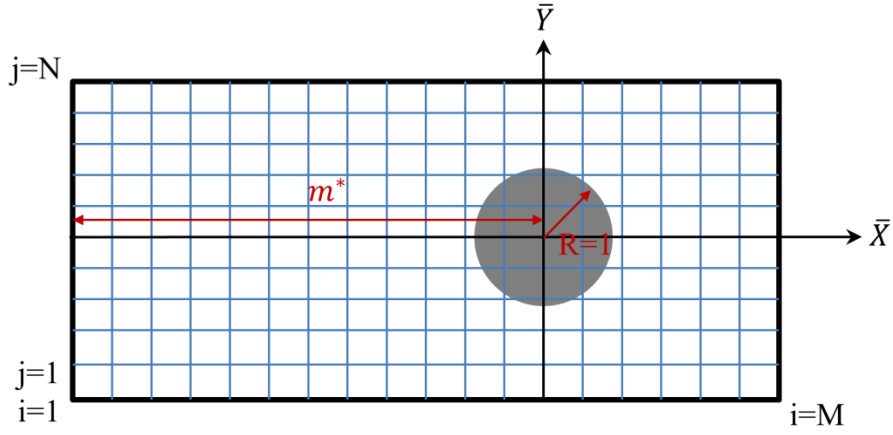

Figure Mt.4 Computational domain used in the iterative procedure.

To obtain an accurate and convergent solution the iterative procedure such as Gauss-Seidel requires heavy under relaxation. In the case of heavily loaded conditions, the under relaxation factor is usually very small, leading to a slow rate of convergence and a long computational time. One Gauss-Seidel type relaxation then consists of two steps. First compute a new approximation $\bar{P}^k$ in each grid point according to:

$$\bar{P}^k = \bar{P}^{k-1} + \omega\Delta\bar{P} \qquad \text{Mt.10}$$

where:

$$\Delta\bar{P} = F\left(\frac{\partial F}{\partial \bar{P}}\right)^{-1} \qquad \text{Mt.11}$$

Next given the new approximation for pressure in each point, a new approximation to the film thickness is computed in each point using equation In.7. The term $\frac{\partial F}{\partial \bar{P}}$ in equation Mt.11 is a full matrix.

The parameter $\bar{\varepsilon}$ changes numbers of orders of magnitude in the computational domain and this property causes a divergence in numerical solution procedures. There are two conventional approaches to get stability, convergence and lower time consumption: line relaxation and point relaxation. In a point relaxation procedure the derivative is just calculated in the grid point and the pressure is updated using the obtained value. Point

relaxation is stable when $\bar{\varepsilon}$ is high and become unstable when $\bar{\varepsilon}$ is low. In line relaxation, instead of scanning the grid point by point it is scanned line by line solving simultaneously the equations of one line. This approach helps overcome the weak points of point relaxation and is more stable for lower values of $\bar{\varepsilon}$.

In this dissertation a hybrid line relaxation method is used to have stable and converging procedure. The conventional value of $\frac{\bar{\varepsilon}}{d\bar{X}^2}$ which specifies the limit between point and line relaxation is 0.3 [14]. So in the hybrid procedure, if $\frac{\bar{\varepsilon}}{d\bar{X}^2}$ is higher than 0.3 while calculating $\frac{\partial F}{\partial \bar{P}}$ only the current grid point is considered but if $\frac{\bar{\varepsilon}}{d\bar{X}^2}$ is lower than 0.3, five neighboring points are used to construct the matrix $\frac{\partial F}{\partial \bar{P}}$. After solving a system of equations for points in a line, i.e. j, vector $\Delta\bar{P}$ is calculated and a portion of this is added to a previous pressure. This portion is decided by the under relaxation factor ω. It should be lower than 1 and in the literature values in the range $0.4 < \omega < 0.8$ are suggested [14].

At the boundaries of the rectangular computational domain, the (manometric) pressure is assumed to be zero. Therefore, when the iteration reaches the boundaries of computation domain the pressure is set to be zero. This can be written as follows:

$$\bar{P}_{i,1} = \bar{P}_{i,N} = \bar{P}_{1,j} = \bar{P}_{M,j} = 0 \qquad \text{Mt.12}$$

In the outlet region, where cavitation occurs, the Reynolds boundary condition is adopted:

$$\bar{P} = \frac{\partial \bar{P}}{\partial \bar{X}} = \frac{\partial \bar{P}}{\partial \bar{Y}} = 0 \qquad \text{Mt.13}$$

As a result of this condition the problem to be solved is a complementarity problem and the outlet boundary of the pressurized region becomes a free boundary.

Aggregation kinetics and Videomicroscopy

Many of the previous works on aggregation kinetics of magnetic suspensions have used videomicroscopy techniques [17]–[20]. In these works the confinement in the direction of field was frequently kept constant. For a precise control of the confinement geometry we used Soft Lithography techniques [21]. Hence, the magnetic suspensions were confined in a rectangular PDMS microchannel. On the one hand, using this approach, the cell depth is carefully controlled in contrast to previous works that typically used spacers. On the other hand, we fabricated microchannels of different width in order to study effect of confinement on aggregation kinetics.

The master for each rectangular cell was created on a silicon wafer using an epoxy-based photoresist (SU 8). This silicon wafer was purchased to Microliquid. Then PDMS microchannels were fabricated from a two-component silicone elastomer kit (SylgardTM 184, Dow Corning); the base and curing agent in a mass ratio of 10:1. After manually mixing the two components, the mixture was introduced in a desiccator for degassing. Then, the mixture was poured over the master, and cured at room temperature for 24 hours. The final step was to release the elastomer from the master. In this way we obtained a PDMS replica with three of the four walls necessary to form a rectangular microchannel and openings for the connections. In order to provide the fourth wall, the PDMS replica was sealed onto a plasma treated microscope glass slide. In this way we obtained rectangular microchannels with a constant $25\mu m$ depth and 6.3 cm length. The channel widths ranged from 75 to 1000 μm.

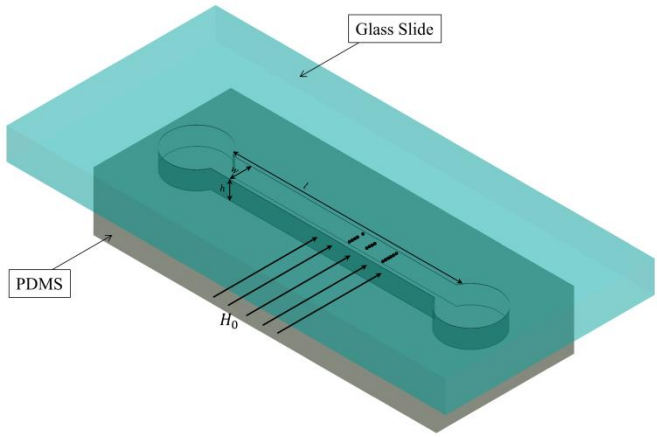

Figure Mt.5 Schematic representation of the PDMS microchannel used in videomicroscopy experiments (not to scale). The channel length is $\boldsymbol{l = 6.3\ cm}$. The depth is $\boldsymbol{h = 25\ \mu m}$. The width $\boldsymbol{w}$ ranges from $\mathbf{75}$ to $\mathbf{1000}\ \boldsymbol{\mu m}$.

The magnetic field (H_0) was generated using a homemade electromagnet adapted to an inverted microscope (Leica DMI 3000). The electromagnet provides magnetic fields up to $54\ kA/m$. The magnetic field was directed in the direction of confinement (c.f. Figure Mt.5). In this configuration the gravitation force acts in the direction of the channel depth invoking particles to settle down on the bottom of the cell. A small amount of sodium dodecyl sulphate (SDS) was also added to prevent particle aggregation and minimize particle surface interactions. Magnetic suspensions were carefully prepared by mechanical dispersion of the carbonyl iron powder (grade EW) or magnetic latex in glycerol/water mixtures. The suspension was prepared as follows. A small amount of SDS (1 wt%) was added to the water/glycerol mixture. For 3 minutes the mixture was stirred in a vortex. Then, it was introduced in a hot bath (50º) for 15 minutes in order to completely dissolve the SDS. Next, the particles were added and the suspension was stirred by implementing vortex for 1 more minute. Subsequently, the suspension was sonicated for 1 more minute. Finally, the suspension was subjected to repeated vortex and sonication 3 more times.

A typical aggregation experiment starts with the application of an external field and the acquisition of a sequence of images at a rate of 1 frame per second as shown in Figure Mt.6. The raw images were converted to a grayscale image by removing the hue and saturation values while keeping only the luminescence information. The image analysis was carried out using a pixel based cluster detection algorithm to identify clusters of particles. Then, thresholding was carried out to obtain a binary image and also to remove errors due to background noise and out-of-focus particles. The cluster detecting algorithm finds particles in neighbouring positions of every particle by detecting dark pixels around every pixel (Figure Mt.7). Clusters are then detected by tracing out neighbours of each pixel and organizing them into individual groups until the boundary, with no dark pixels surrounding it, is delimited. We discarded regions that have an area below a critical value. This critical value was considered to eliminate small regions (smaller than the particle size) that still were detected due to background noise and out-of-focus shadow of the particles.

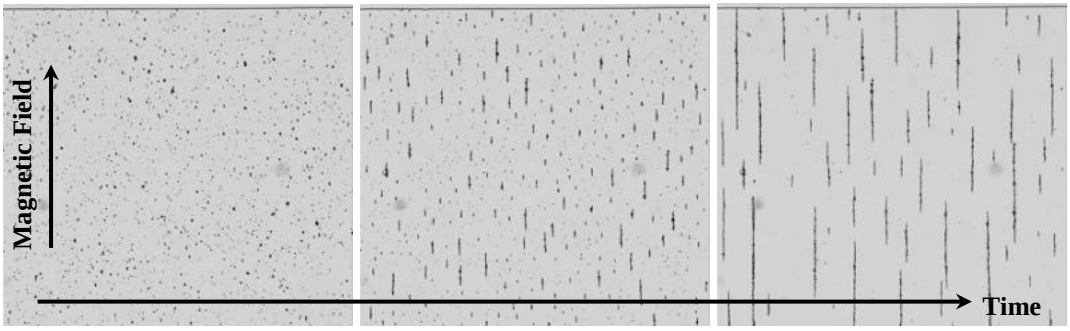

Figure Mt.6. Snapshot of the aggregation process at different times captured in a videomicroscopy experiment.

a)

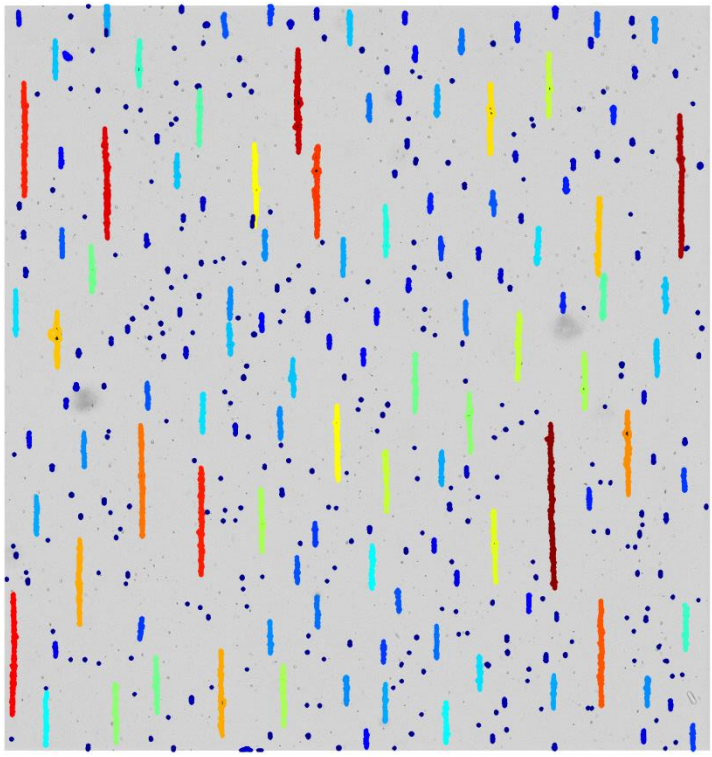

b)

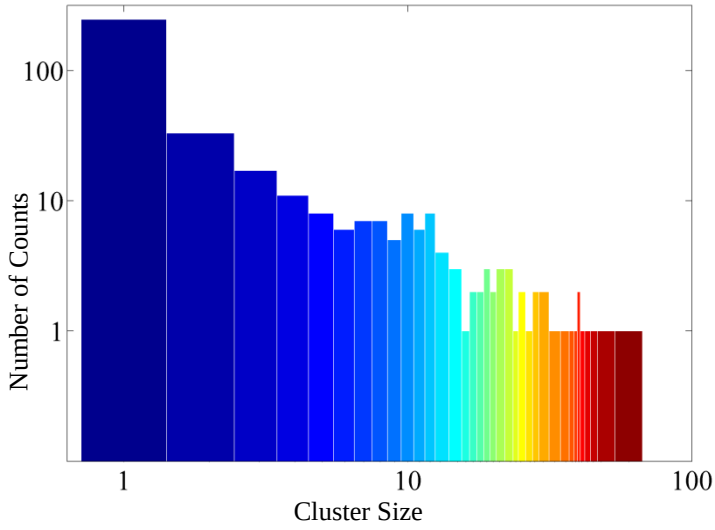

Figure Mt.7 Panels: a) Detected clusters using Matlab cluster detection subroutine b) Histogram of the cluster size.

REFERENCES

[1] A. J. F. Bombard and J. Vicente, “Thin-film rheology and tribology of magnetorheological fluids in isoviscous-ehl contacts,” *Tribology Letters*, vol. 47, no. 1, pp. 149–162, May 2012.

[2] A. J. F. Bombard and J. de Vicente, “Boundary lubrication of magnetorheological fluids in PTFE/steel point contacts,” *Wear*, vol. 296, no. 1–2, pp. 484–490, Aug. 2012.

[3] G. Wanka, H. Hoffmann, and W. Ulbricht, “The aggregation behavior of poly-(oxyethylene)-poly-(oxypropylene)-poly-(oxyethylene)-block-copolymers in aqueous solution,” *Colloid & Polymer Science*, vol. 268, no. 2, pp. 101–117, 1990.

[4] G. Wanka, H. Hoffmann, and W. Ulbricht, “Phase diagrams and aggregation behavior of Poly(oxyethylene)-Poly(oxypropylene)-Poly(oxyethylene) triblock copolymers in aqueous solutions,” *Macromolecules*, vol. 27, no. 15, pp. 4145–4159, 1994.

[5] M. J. Murray and M. J. Snowden, “The preparation, characterisation and applications of colloidal microgels,” *Advances in colloid and interface science*, vol. 54, pp. 73–91, 1995.

[6] Y. Guan and Y. Zhang, “PNIPAM microgels for biomedical applications: from dispersed particles to 3D assemblies,” *Soft Matter*, vol. 7, no. 14, pp. 6375–6384, 2011.

[7] G. Bossis, O. Volkova, S. Lacis, and A. Meunier, “Magnetorheology : Fluids , Structures and Rheology,” *Ferrofluids*, pp. 202–230, 2002.

[8] J. P. Segovia-Gutiérrez, C. L. A. Berli, and J. De Vicente, “Nonlinear viscoelasticity and two-step yielding in magnetorheology: A colloidal gel approach to understand the effect of particle concentration,” *Journal of Rheology*, vol. 56, no. 6, pp. 1429–1448, 2012.

[9] J. C. Fernández-Toledano, J. Rodriguez-López, K. Shahrivar, R. Hidalgo-Álvarez, L. Elvira, F. de Espinosa, and J. de Vicente, “Two-step yielding in magnetorheology,” *Journal of Rheology*, vol. 58, no. 5, pp. 1507–1534, 2014.

[10] D. J. Klingenberg, F. Van Swol, and C. F. Zukoski, “Dynamic simulation of electrorheological suspensions,” *The Journal of Chemical Physics*, vol. 91, no. 12, pp. 7888–7895, 1989.

[11] E. Andablo-Reyes, J. de Vicente, R. Hidalgo-Álvarez, C. Myant, T. Reddyhoff, and H. A. Spikes, “Soft elasto-hydrodynamic lubrication,” *Tribology Letters*, vol. 39, no. 1, pp. 109–114, 2010.

[12] S. Odenbach, “Ferrofluids—magnetically controlled suspensions,” *Colloids and Surfaces A: Physicochemical and Engineering Aspects*, vol. 217, no. 1, pp. 171–178, 2003.

[13] a. Chaves, C. Rinaldi, S. Elborai, X. He, and M. Zahn, “Bulk flow in ferrofluids in a uniform rotating magnetic field,” *Physical Review Letters*, vol. 96, no. 19, p. 194501, May 2006.

[14] C. . Venner and A. . Lubrecht, *Multilevel Methods in Lubrication*, vol. 37. Elsevier, 2000.

[15] B. Damiens and C. Venner, “Starved lubrication of elliptical EHD contacts,” *Journal of tribology*, vol. 126, no. January, pp. 105–111, 2004.

[16] B. J. Hamrock, S. R. Schmid, and B. O. Jacobson, *Fundamentals of fluid film lubrication*. CRC press, 2004.

[17] M. Fermigier, A. P. Gast, and A. P. Gast, “Structure evolution in a paramagnetic latex suspension,” *Journal of Magnetism and Magnetic Materials*, vol. 122, no. 1–3, pp. 46–50, Dec. 1993.

[18] J. H. E. Promislow, A. P. Gast, and M. Fermigier, “Aggregation kinetics of paramagnetic colloidal particles,” *The Journal of Chemical Physics*, vol. 102, no. 13, p. 5492, 1995.

[19] P. Dominguez-Garcia, S. Melle, J. M. Pastor, and M. A. Rubio, “Scaling in the aggregation dynamics of a magnetorheological fluid,” *Physical Review E - Statistical, Nonlinear, and Soft Matter Physics*, vol. 76, no. 5, pp. 1–13, 2007.

[20] R. M. Erb, M. D. Krebs, E. Alsberg, B. Samanta, V. M. Rotello, and B. B. Yellen, “Beyond diffusion-limited aggregation kinetics in microparticle suspensions,” *Physical Review E - Statistical, Nonlinear, and Soft Matter Physics*, vol. 80, no. 5, pp. 1–7, 2009.

[21] Y. N. Xia and G. M. Whitesides, “Soft lithography,” *Annual Review Of Materials Science*, vol. 37, no. 5, pp. 551–575, 1998.

CHAPTER 1

Thermoresponsive polymer-based magneto-rheological (MR) composites as a bridge between MR fluids and MR elastomers

Keshvad Shahrivar and Juan de Vicente

This article is published in: Soft Matter, 2013, 9, 11451.

Abstract

A new class of magnetorheological (MR) material is reported that bridges the gap between conventional MR fluids and MR elastomers. The key point is the use of a thermoresponsive polymer-based suspending medium in the formulation of the MR material whose rheological properties can be externally controlled through changes in the temperature. Under appropriate conditions, it is even possible to induce a thermally driven "liquid-to-solid" transition in the carrier medium. As a result, when the suspending medium is in the "liquid" phase, the MR composite behaves as a conventional MR fluid exhibiting a large MR effect (approx. 1000 %). On the contrary, when the suspending medium is in the "solid" phase, and exhibits an apparent yield stress, the whole material behaves as a MR elastomer where the iron microparticles are entrapped in a polymer network. Two different examples are reported in this communication; on the one hand a triblock copolymer solution is used as suspending medium that evolves towards a lyotropic liquid crystalline cubic phase upon heating. On the other hand, a concentrated microgel dispersion is used that reaches maximum packing as the temperature decreases forming a repulsive colloidal glass. The rheological properties of the materials are evaluated under dynamic oscillatory and steady simple shear to ascertain the MR effect.

Conventional magnetorheological (MR) fluids are dispersions of non-Brownian highly magnetizable carbonyl iron microparticles in a Newtonian (oily) fluid. They experience dramatic rheological changes when an external magnetic field is applied. In particular, a large stress enhancement of three or four orders of magnitude (so-called MR effect) is observed as a result of field-driven particle structuration.[1,2] In the "solid" phase, for large enough magnetic fields, the MR effect is manifested by the appearance of a apparent "yield" stress and a highly viscoelastic response.[3,4]

MR fluids are currently employed in a wide range of commercial devices for torque transfer, from automotive to optical polishing applications.[5,6] A typical example is their use in dampers for sport cars such as the case of Delphi automotive primary suspension system (MagneRide). Importantly, the large density mismatch between the iron microparticles and the suspending media used in the formulation of MR fluids results in their eventual sedimentation under gravity. In this sense, since the discovery of these fluids more than sixty years ago,[7] many efforts have been devoted to minimize sedimentation.[1,5] Unfortunately, all approaches employed up to now entail a higher off-state (i.e. no-field) viscosity and this is not desirable in applications.

MR elastomers can be thought of as solid analogs of MR fluids. They are typically fabricated by dispersing carbonyl iron particles in a polymer composite. Traditionally, a magnetic field is superimposed in the material to promote the formation of elongated particle aggregates during crosslinking such that become locked in place upon final cure.[6,8,9] The most important difference between MR fluids and elastomers is in the way the materials are intended to operate. MR elastomers are intended to operate in the pre-yield regime, while MR fluids typically operate in the post-yield regime.

MR elastomers have also found widespread commercialization. In particular, they are currently used in the fabrication of adaptive tuned vibration, mounts and automotive bushings. Also, by introduction of graphite microparticles into the elastomeric matrix composites become electroconductive. This property is currently applied in the fabrication of magnetoresistors, magnetic field sensors and transducers.[8,10] Of course, sedimentation is not an issue in the case of MR elastomers. However, the price to be paid is a much lower MR effect if compared to MR fluids. In fact, the strength of MR elastomers is typically characterized by their field dependent linear viscoelastic modulus.

In this report, we tackle a long-standing challenge facing MR fluid technology since its discovery. We pursue two objectives: i) to minimize the sedimentation of the iron microparticles in the absence of the magnetic field (off-state), ii) to enhance the MR response under the field (on-state). For this end we follow an innovative approach that involves the use of polymer-based carrier media in the fabrication of a thermoresponsive MR composite. These polymer carriers experience a "liquid-to-solid" transition by changing the temperature, and results in a thermoresponsive MR composite that behaves as a conventional MR fluid, a MR elastomer, or a complex viscoelastic material that

behaves in between these two extreme cases depending on the temperature under operation.

In general, temperature responsive polymers can be categorized into two groups.[11] One of these groups involve temperature responsive polymers based on amphiphilic balance, the other involves thermoresponsive polymers based on a lower critical solution temperature (LCST). Undoubtedly, the main representatives of these two groups are Poly (ethylene oxide)-poly (propylene oxide)-poly (ethylene oxide) (PEO-PPO-PEO) triblock copolymers and Poly (N-isopropyl acrylamide) (P-NIPA), respectively. In this note we will use these particular polymers to fabricate novel MR composites. However, the idea behind this work is applicable to other more complex thermoresponsive formulations.

The "liquid-to-solid" transition in the suspending carrier, and therefore, the kinetic arrest of the dispersed carbonyl iron microparticles, is accomplished in this note following two very different routes. On the one hand a three dimensional crystal-like (cubic) packing of PEO-PPO-PEO micelles is formed by hydrophilic-hydrophobic balance upon heating.[12] On the other hand a repulsive colloidal glass is formed by swelling P-NIPA microgels in dispersion when decreasing the temperature.[13] Independently of the route followed, a large enough apparent yield stress can be induced in the suspending medium upon heating (PEO-PPO-PEO) or cooling (P-NIPA) when the polymer content in solution is large enough.

As a first example we use a water-based amphiphilic PEO_x-PPO_y-PEO_x triblock copolymer solution with x = 100 and y = 65 (namely Pluronics F127). These copolymers form self-assembled structures as a result of the temperature-dependent solubility of the PPO block. At low concentration these copolymers behave as conventional surfactants solutions, with the peculiarity that their critical micelle concentration decreases with increasing temperature; they are present in isotropic solution below room temperature and transform into micelles at higher temperatures.[12] At high copolymer concentrations, isotropic micellar solutions form lyotropic liquid crystalline cubic phases upon heating, that are characterized by the appearance of a large yield stress. Importantly, in this particular example, the transition temperature is found to strongly depend on polymer concentration in solution.[14]

As a second example we employ a water-based microgel colloidal dispersion. Generally speaking, microgel particles are spherical, cross-linked polymer particles in the colloidal-size range that swell or de-swell in response to external stimuli, such as temperature, pH, osmotic pressure, ionic strength, and solvent composition.[15,16] Here we are particularly interested in temperature-responsive microgels. Among all of them, P-NIPA crosslinked with bisacrylamide (BA) is one of the best studied model colloidal microgel that is temperature-sensitive. The LCST of P-NIPA in water is approximately 32 ºC and this makes these microgels attractive, for biomedical and sensing applications.[17,18] Below the LCST, the microgel particles swell (the polymer is

hydrophylic) and above this temperature the microgel particles shrink (the polymer becomes hydrophobic and collapses). When the microgel concentration is large enough, dispersions may exhibit transitions between glassy, liquid-like, and gel-like behavior as the temperature is varied through the LCST. In this note we are not interested in dispersions operating well above the LCST (in the gel-like regime) where interparticle attractive interactions may promote the formation of a volume-spanning colloidal gel.[13] On the contrary, we will mostly focus on temperatures below the LCST. Importantly, size, degree of softness and swelling ratio of these microgel particles can be easily tailored depending on the synthesis conditions.[19]

Triblock copolymers, commonly known as Pluronics F127 was a product of BASF Corp. purchased from Sigma-Aldrich. The copolymers were used as received without further fractionation or other purification. P-NIPA microgels were fabricated from a single-step emulsion polymerization reaction.[20] Initially, 2.5 g of N-isopropylacrylamide (NIPAM) and 0.25 g of N,N'-methylenebisacrylamide crosslinker (BA) were mixed in 500 g of water at room temperature. The reaction mixture was thoroughly stirred while purged with nitrogen to displace the dissolved oxygen. Then, the water bath temperature was raised to 70 ºC, and 0.25 g of potassium persulfate initiator (KSP) was added. The polymerization was allowed to continue for 24 hours under an atmosphere of nitrogen. Finally, the microgel dispersion was allowed to cool and then exhaustively dialyzed against distilled water to remove any unreacted monomer and other impurities. Carbonyl iron microparticles employed in the formulation of the MR fluids where a gift from BASF SE (grade HQ).

The hydrodynamic diameter of water-based P-NIPA microgels was determined by Photon Correlation Spectroscopy (PCS, Malvern Nano Z). For this purpose, microgel dispersions were prepared at a concentration of 0.05 wt% in distilled water. Measurements were carried out from 10 ºC to 50 ºC taking measurements every 2.5 ºC. The stabilizing time between measurements was 20 min.

The kinetic stability of MR composites was ascertained under gravity using a Turbiscan Classic 2000 (Formulaction, France). MR composites were poured into cylindrical polyethylene tubes placed vertically inside the device. The height of the supernatant (i.e. clear layer formed at the top of the fluid due to the sedimentation of the dispersed magnetic particles in the corresponding MR composites) was measured by scanning the sample using an optical sensor that detected the intensity of light transmitted through the sample (180º from the incident laser light). The reading head acquired transmission data every 40 μm while moving along the entire height of the tube (60 mm). The light source was an electro-luminescent diode. The height of the formed supernatant at different times was subtracted from the initial height of the corresponding MR composites (H_0), and the result (H) was divided by H_0 in order to obtain the sedimentation ratios.

Rheological tests were carried out in an Anton Paar MCR302 torsional rheometer under the presence of, steady and unsteady, simple shearing flows. A plate-plate geometry

(diameter 40 mm) was used operating at a commanded gap of 300 μm. A solvent trap was employed to avoid sample evaporation. Accurate and fast temperature control was achieved by Peltier elements placed at the lower plate. The rate of increase/decrease of the temperature had to remain at a low value to get reproducible results. In this work the heating/cooling rate was always fixed at 1 ºC min^{-1}. A strict experimental protocol was followed in order that dispersion loading and memory effects are eliminated. The sample was first liquefied to correctly fill the gap and for easy handling (10 ºC for PEO-PPO-PEO and 40 ºC for P-NIPA dispersions). Then, the temperature was brought to the desired value and stabilized for a total of 200 s at rest before starting the measurement. The uniform magnetic field was generated using a custom-built solenoid coil surrounding the parallel-plate geometry. The magnetic field was oriented perpendicular to the shear-flow direction.

The linear viscoelastic behavior of the MR composites was ascertained using dynamic rheology tests. Small-amplitude dynamic oscillatory shear temperature-sweeps were carried out at a strain amplitude of 0.05 % and an excitation frequency of 1 Hz. Also, the non-linear rheological behavior was interrogated in an attempt to evaluate the MR effect. In this sense, steady shear flow rheology tests were carried out at two different temperatures without and with magnetic field applied. Temperature values were chosen in order to guarantee the solidification of liquefaction of the carriers. The shear rate was logarithmically increased from 0.01 to 1000 s^{-1}. A total of 25 data points were acquired with a time interval length of 10 s.

Figure 1 demonstrates the thermoresponsive character of the polymeric carriers used as suspending media in the formulation of MR composites. On the one hand, Figure 1a depicts the mechanical loss factor within the viscoelastic linear region, tan δ (i.e. the ratio between the loss modulus to the storage modulus) of PEO-PPO-PEO triblock copolymer solutions as obtained from small-amplitude shear rheometry. The temperature dependence of the loss factor suggests the existence of a "liquid-to-solid" transition in PEO-PPO-PEO solutions at approximately 15 ºC for a copolymer concentration of 20 wt% (this is the temperature where tan δ =1 for this particular copolymer concentration). These results were further checked using multiwave rheology (results not shown here for brevity). The "liquid-to-solid" transition observed in PEO-PPO-PEO solutions is due to the formation of a lyotropic liquid crystal cubic phase upon heating. Interestingly, the associated critical temperature can be tuned by changing the polymer concentration. On the other hand, Figure 1b depicts the hydrodynamic diameter of the P-NIPA microgels, as obtained from dynamic light scattering, as a function of temperature. According to Figure 1b, the particle diameter (and therefore the effective volume fraction of the dispersion) can be rapidly increased by a factor of two (eight) upon cooling in a narrow temperature range around 30-40 ºC. Therefore, for a large enough microgel loading, this may result in an eventual temperature-driven "liquid-to-solid" transition due to the formation of a repulsive colloidal glass. Figures 1c and 1d demonstrate that the sedimentation of carbonyl iron is prevented when the carrier medium is in the "solid" phase.

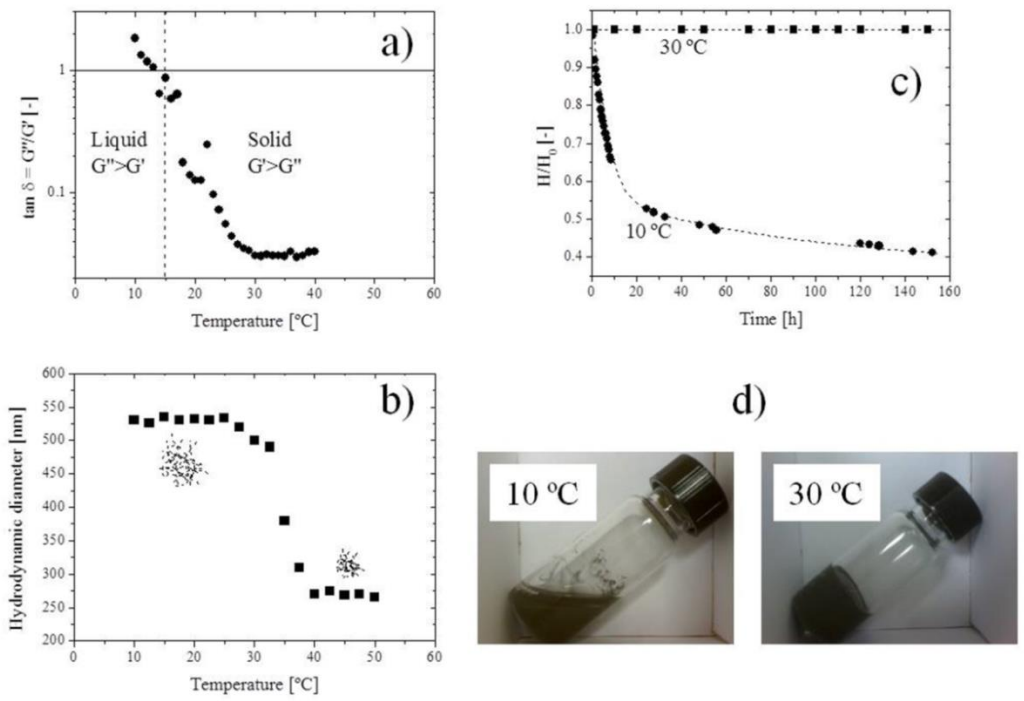

Figure 1. a) Loss factor as a function of the temperature for a 20 wt% copolymer solution. b) hydrodynamic diameter of P-NIPA microgel particles. c) Sedimentation ratio of the copolymer-based MR composites (20 wt% copolymer + 20 vol% carbonyl iron) at two different temperatures. d) Snapshots of the copolymer-based MR composites tubes after 1 h at rest

On the contrary, the viscous resistance of the carrier fluid to the particle movement is negligible when the carrier medium operates in the "liquid" phase. In this case, particles rapidly sediment under gravity in the absence of field as demonstrated in Figure 1c and, accordingly, a large MR effect is expected under field, in the on-state (see below).

The temperature-driven transition still occurs when iron microparticles are dispersed in the polymeric matrix (both in the absence and presence of magnetic fields). The transition from MR fluid to MR elastomer of the composite is demonstrated in Figure 2. As a way of example, we plot the (linear viscoelastic) storage moduli as a function of temperature for the two polymeric systems investigated. As observed, a very abrupt transition is found in the case of copolymer solutions. However, a smoother transition is observed in the case of P-NIPA microgel dispersions. The reason for this stems from the different physical mechanism behind the kinetic arrest of micronsized magnetizable particles. Of course, a much more noticeable effect of the magnetic field is found when the carrier media is in the "liquid" state.

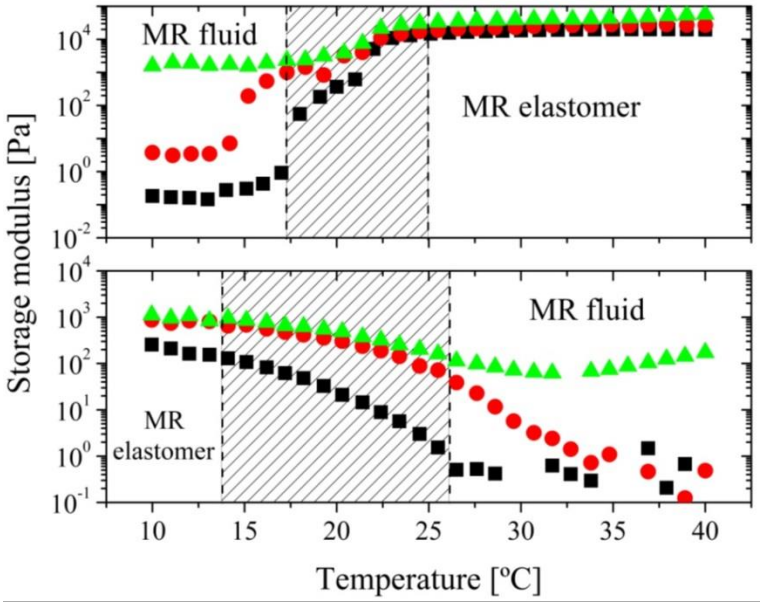

Figure 2. Storage modulus as a function of temperature for MR composites. Upper panel corresponds to MR composites in 20 wt% copolymer solutions. Lower panel corresponds to MR composites in 8.66 wt% P-NIPA microgel dispersions. ■: polymer-based carrier fluid without particles, ●: polymer-based carrier fluid + 5 vol% carbonyl iron particles (no field), ▲: polymer-based carrier fluid + 5 vol% carbonyl iron particles in the presence of a DC magnetic field strength of 15 kA/m. Shear strain amplitude 0.05 %. Excitation frequency 1 Hz. Shaded region corresponds to a viscoelastic MR composite that behaves in between conventional MR fluids and MR elastomers.

Steady shear rheology was used to investigate the non-linear flow behavior of MR composites. Figure 3 depicts the flow curves, i.e. the steady-state shear stress as a function of shear rate. For the carrier media (without particles) we observe that the shear stress for copolymer solutions at 10 ºC and microgel dispersions at 40 ºC is essentially proportional to the shear rate over the entire range of shear rates, which is indicative of Newtonian behavior (cf. Figures 3a and 3d). The shear viscosity is found to be larger in the case of copolymer solutions (32.7 mPa.s) if compared to microgel dispersions (1.6 mPa.s). On the contrary, a Bingham plastic-like behavior is observed for copolymer solutions at 30 ºC and microgel dispersions at 10 ºC manifested by an apparent yield stress (cf. Figures 3b and 3c).

Filling the carrier with particles and superimposing an external magnetic field has a very clear effect in the non-linear rheological behavior of the MR composite when the suspending medium operates in the “liquid” phase (copolymer solutions at 10 ºC and microgel dispersions at 40 ºC).

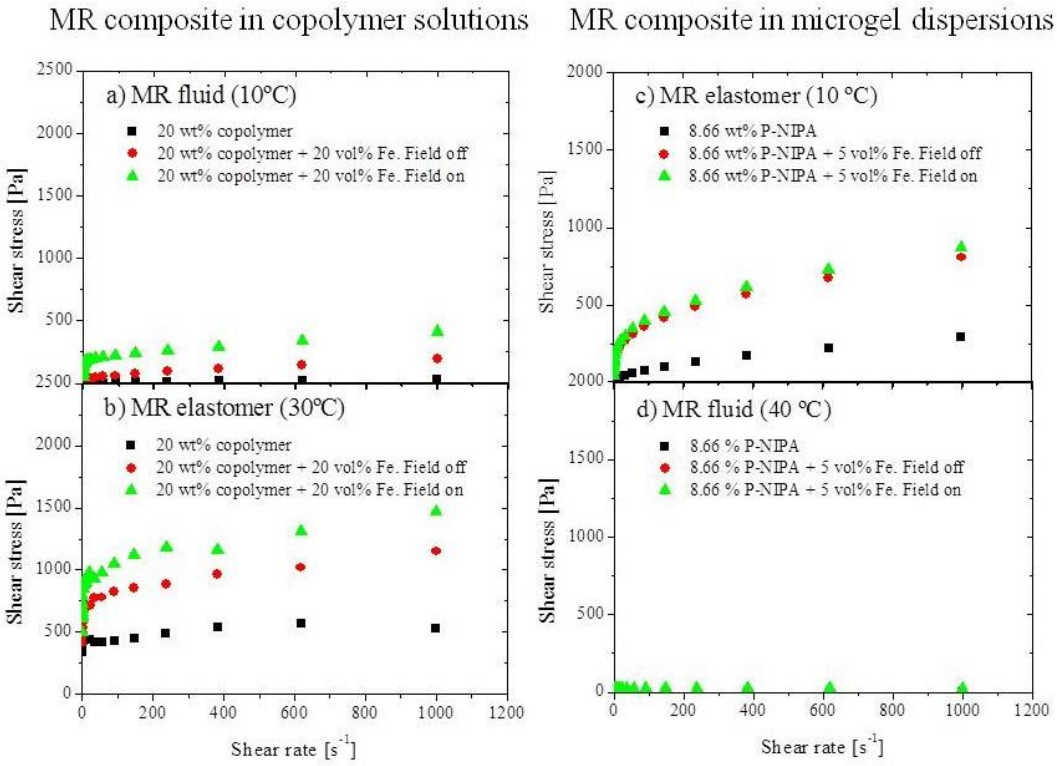

Figure 3. Shear stress as a function of shear rate (rheograms) for MR composites prepared by dispersion of carbonyl iron microparticles in polymer-based carrier media. Left column: 20 vol% carbonyl iron suspensions in 20 wt% copolymer solutions at two different temperatures: a) 10 ºC and b) 30 ºC. Right column: 5 vol% carbonyl iron suspensions in 8.66 wt% P-NIPA microgel dispersions at two different temperatures: c) 10 ºC and d) 40 ºC. ●: without field, ▲: with field (15 kA/m). As a reference we also include rheograms for the polymeric carrier fluids without particles (■).

As expected, adding particles increases viscous dissipation while superimposing a magnetic field promotes the formation of particle aggregates in the field direction eventually enhancing the MR response. Contrarily, when the carrier medium is in the "solid" phase the effect of particles and field is remarkably less important. This statement is better observed in terms of the MR effect (see below). The MR effect is defined here as the ratio between the shear viscosity increment under field (15 kA/m) and the shear viscosity value in the absence of the field [see for example reference 21]. Figure 4 shows the MR effect for different MR composites at three different shear rates. In general, the larger the shear rate, the smaller the MR effect because hydrodynamic interactions dominate magnetostatic ones.

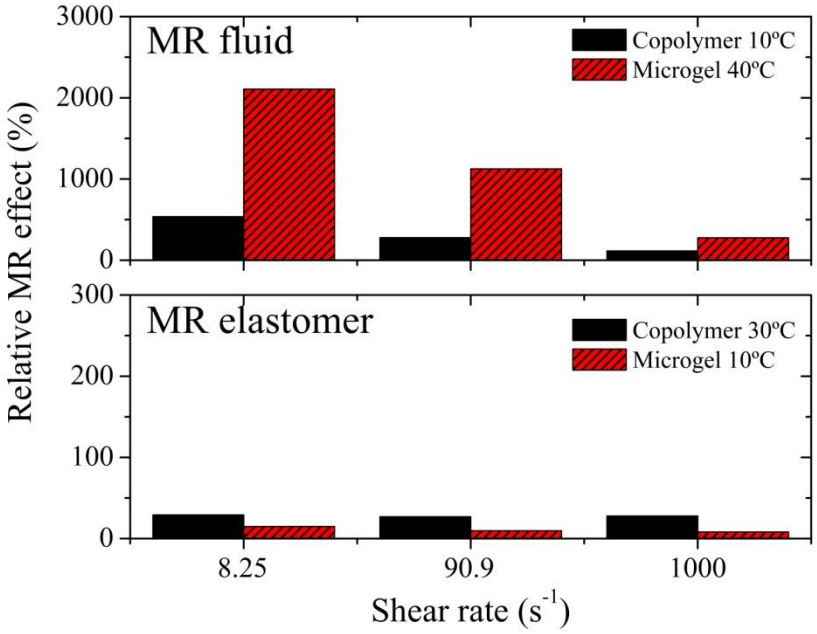

Figure 4. Relative MR effect as a function of the shear rate for iron suspensions in thermoresponsive solutions in the "liquid" (a) and "solid" (b) phase. The relative MR effect is defined here as the ratio between the shear viscosity increment under field (15 kA/m) and the shear viscosity value in the absence of the field. Copolymer: 20 vol% carbonyl iron suspensions in 20 wt% copolymer solutions. Microgel: 5 vol% carbonyl iron suspensions in 8.66 wt% P-NIPA microgel dispersions.

As observed, the MR effect is negligible when the suspending medium operates in the “solid” phase (see lower panel in Figure 4). Contrarily, a relative storage moduli enhancement is measured: 0.7 % for 5 vol% iron suspensions in 20 wt% copolymer solutions and 28 % for 5 vol% iron suspensions in 8.66 wt% P-NIPA microgel dispersions. On the other hand, a MR effect increase of at least one order of magnitude is measured when the carrier medium operates in the “liquid” phase (see upper panel in Figure 4).

In conclusion, we have shown a feasible way to prevent particle sedimentation in magnetorheological fluids but at the same time, retaining a very large MR effect in the excited state (on-field). The key point is to introduce another control parameter in order to tune the rheological characteristics of the carrier medium. Two different examples are provided that demonstrate a "liquid-to-solid" transition in the carrier, either heating (triblock copolymers) or cooling (microgel dispersions). When the carrier operates in

the "liquid" phase, the MR composite behaves as a conventional MR fluid. On the contrary, in the "solid" phase, the MR composite behaves as a conventional MR elastomer. We hope that our work will promote further experimental and theoretical works on the use of non-Newtonian carrier media in the formulation of multi-responsive magnetorheological fluids in the frontier between conventional MR fluids and MR elastomers.

REFERENCES

1 J. de Vicente, D. J. Klingenberg and R. Hidalgo-Álvarez, *Soft Matter,* 2011, **7**, 3701.

2 B. J. Park, F. F. Fang and H. J. Choi, *Soft Matter,* 2010, **6**, 5246.

3 J. P. Segovia-Gutiérrez, C. L. A. Berli and J. de Vicente, *J. Rheol.,* 2012, **56(6)**, 1429.

4 J. de Vicente and C. L. A. Berli, *Rheol. Acta,* 2013, **52**, 467.

5 F. D. Goncalves, J-. H. Koo and M. Ahmadian, *The Shock and Vibration Digest,* 2006, **38**, 203.

6 A. G. Olabi and A. Grunwald, *Mater. Des.,* 2007, **28**, 2658.

7 J. Rabinow, *AIEE Trans,* 1948, **67**, 1308.

8 J. D. Carlson and M. R. Jolly, *Mechatronics,* 2000, **10**, 555.

9 E. Coquelle and G. Bossis, *Int. J. Solids and Structures,* 2006, **43**, 7659.

10 W. M. Stewart, J. M. Ginder, L. D. Elie and M. E. Nichols, M. E. US Patent 5,816,587, 1998

11 L. Yang and H. Liu, *Powder Technology,* 2013, **240**, 54.

12 G. Wanka, H. Hoffmann and W. Ulbricht, *Macromolecules,* 1994, **27**, 4145.

13 G. Romeo, A. Fernández-Nieves, H. M. Wyss, D. Acierno and D. A. Weitz, *Advanced Materials,* 2010, **22**, 3441.

14 G. Wanka, H. Hoffmann and W. Ulbricht, *Colloid Polym. Sci.,* 1990, **268**, 101.

15 M. H. Murray and M. Snowden, *Adv. Colloid Interface Sci.,* 1995, **54**, 73.

16 B. R. Saunders and B. Vincent, *Adv. Colloid Interface Sci.,* 1999, **80**, 1.

17 S. Xu, J. Zhang, C. Paquet, Y. Lin and E. Kumacheva, *Adv. Matter,* 2003, **13**, 468.

18 Z. Guo, H. Sauterau and D. E. Kranbuehl, *Macromolecules,* 2005, **38**, 7992.

19 V. Städele, U. Gasser and H. Dietsch, *Soft Matter,* 2012, **8**, 4427.

20 M. Bradley, J. Ramos and B. Vincent, *Langmuir,* 2005, **21**, 1209.

21 A. Boczkowska and S. Awietjan Microstructure and Properties of Magnetorheological Elastomers *Advanced Elastomers - Technology, Properties and Applications* (D.Sc. Anna Boczkowska Ed., ISBN: 978-953-51-0739-2, InTech, DOI: 10.5772/50430).

CHAPTER 2

Thermogelling magnetorheological fluids

Keshvad Shahrivar and Juan de Vicente

This article is published in: Smart Material and Structure. 23 (2014) 025012.

Abstract

A novel approach is proposed for the formulation of kinetically stable magnetorheological (MR) fluids exhibiting MR effect. Thermoresponsive carrier fluids are used that develop a sol-gel transition when increasing the temperature. Turbidity measurements, multiwave rheology and steady shear flow tests are carried out on model conventional MR fluids prepared by dispersion of carbonyl iron microparticles in triblock copolymer solutions of type PEO_x-PPO_y-PEO_x with x = 100 and y = 65. Experiments demonstrate that MR fluids remain stable against sedimentation in the gel phase and exhibit a very large (relative) MR effect (up to 1000 %) in the sol phase.

INTRODUCTION

Conventional magnetorheological (MR) fluids are colloidal suspensions of magnetizable (micronsized) particles dispersed in a non-magnetic medium. In the absence of magnetic fields, these suspensions behave as usual colloidal systems. However, in the presence of an external magnetic field of the order of a few tens of kA/m, particles aggregate to form elongated structures in the direction of the field. The resulting field-induced structures promote the appearance of a yield stress and field-dependent viscoelasticity (so-called MR effect) [1-3]. In practice, for a given rheological material function, the (relative) -MR effect is defined as the ratio between the material function increment under field and the material function value in the absence of the field [e.g. 4]. The relative MR effect has been documented in the literature for a range of material functions that include the elastic/storage modulus [5, 6] and the shear viscosity, both in MR fluids [7] and electrorheological fluids [8].

One long-standing challenge in MR fluid technology is the quest for a kinetically stable colloid. When considering MR fluid stability, two forms of stability must be addressed; sedimental and agglomerative stability [3, 9]. In this manuscript we focus on the sedimental stability. In general, particles sediment quickly under gravity due to the large density mismatch between particles (≈ 7.5 g/cm^3) and dispersing medium (≈ 1 g/cm^3). The mechanisms for controlling long-term stability are often dictated by the particular fluid application. Traditionally, different routes have been followed to minimize the settling of particles over time either impacting on the carrier fluid (mainly by introducing additives) or the dispersed magnetic particles (by surface chemical functionalization or tuning their size and/or shape among others). A number of MR fluid formulations involve the use of thixotropic agents (eg. fumed silica or clay particles) that form weakly bonded structures in the carrier fluid [10, 11]. If the concentration of the additive is large enough, the low-shear viscosity increases, eventually preventing particle settling during long times. Importantly, the additive concentration cannot increase too much as otherwise the MR effect would become negligible. Other works involve the use of ferromagnetic, Co-γ-Fe_2O_3 and CrO_2, nanoparticles that result in improved stability against sedimentation and furthermore, an increase in the yield stresses especially for large magnetic field strengths (of the order of 0.60 KOe) [12]. Plastic-like carrier fluids, such as greases, have also been successfully employed [13]. In this case, a gravity yield parameter Y_G has been defined as the ratio of viscous to gravitational forces. Large values of Y_G are associated to a better ability of the plastic carrier fluid to suspend the particles. Values reported in the literature for the critical (minimum) Y_G vary, but all values are of the order $Y_G^{min} = 0.1$ [13, 14].

MR fluids also exhibit improved gravitational stability when dispersed magnetic particles are of the order of 100 nm diameter. Unfortunately, these so-called nano MR fluids tend to have an order of magnitude less yield stress than the usual carbonyl iron based MR fluids [15]. Also, elongated magnetic particles have been reported in the past

to enhance sedimentation stability as well as to promote a larger MR effect [16-18]. Moreover, mixtures of magnetizable particles of two different diameters (bidisperse suspensions) have also been widely exploited to enhance MR behavior and improve sedimentation stability [19-22]. Finally, another approach involves low-density core/shell-structured and functionalized magnetic particles that may improve the dispersibility, also avoiding the oxidation and corrosion of the surface [23].

Importantly, all of the approaches followed in the past to minimize sedimentation suffer from an important drawback; in all cases the zero-field (off-state) viscosity increases and this is not desirable. A way to overcome this problem could be the use of thermoresponsive (smart) carrier fluids whose viscosity could be externally controlled by changing the temperature. Bearing this idea in mind it would be possible to keep the carrier fluid at a high viscosity level in the absence of magnetic fields and reduce its viscosity to a minimum value when the field is applied. This would prevent the particles from sedimenting in the absence of magnetic fields but at the same time it would provide the suspensions of a low off-viscosity value to enhance MR effect during operation [24]. In order to achieve this goal, in this contribution we use a triblock copolymer that experiences a sol-gel transition resulting in the formation of lyotropic liquid crystalline cubic phases upon heating.

BACKGROUND

It is well known that amphiphilic triblock copolymers of type PEO_x-PPO_y-PEO_x, where PEO stands for poly(ethylene oxide) and PPO stands for poly(propylene oxide), are surface active compounds and form micelles and lyotropic liquid crystalline phases (i.e. self-assembled structures) in selective solvents. The mechanism behind self-assembly comes from the temperature-dependent solubility of the PPO block, and in particular, the dehydration of PPO with increasing temperature [25, 26].

Low concentration copolymer solutions behave as conventional surfactant solutions with the peculiarity that their critical micelle concentration (cmc) depends strongly on temperature (within the range 20-50 ºC); the cmc decreases with increasing temperature. Typically, a 1 wt% copolymer solution is present in the monomer state (i.e. isotropic solution) below room temperature and transforms into micelles via hydrophobic interaction at higher temperatures as the PPO blocks form a water-free central core surrounded by a hydrated PEO corona [25]. This micellar structure is used in pharmaceutical applications to help in the solubilization of both water-soluble and oil-soluble solutes/drugs [27-30]. At higher copolymer concentrations, isotropic micellar solutions form lyotropic liquid crystalline phases upon heating. Interestingly, the transition temperature can be adjusted by varying the concentration of copolymer and/or introducing surfactants and nanoparticles [26]. SANS and DSC measurements demonstrate that the associated gelation process is actually due to the formation of structured mesophases and results from the packing of micelles [25, 31, 32].

In this work we exploit the micellar to lyotropic liquid crystalline phase transition that occurs in triblock copolymers of type PEO_x-PPO_y-PEO_x with x = 100 and y = 65 (namely Pluronics F127) mainly because the temperature-driven gelation process that occurs when increasing the temperature, of this particular concentrated polymer solution, is actually due to the formation of a *cubic phase* [25, 31], as confirmed by SAXS and SANS experiments [32], and interestingly, contrarily to other mesophases (such as *hexagonal* and *lamellar phases*), the rheology of this *cubic phase* is characterized by the presence of a large enough yield stress (and storage modulus) to keep iron microparticles, used in typical MR fluid formulations, in suspension ($Y_G^{min} > 0.1$). These immobile gels are frequently called "hard gels" in the polymer specialized literature in contrast to "soft gels" that lie between the extremes of sols and hard gels where a finite although very small yield stress exists [32]. The yield stress observed in soft gels is generally too small to confer immobility in the tube inversion test and therefore to keep the carbonyl iron microparticles in suspension.

The phase diagram for Pluronics F127 has been extensively investigated in the literature using tube inversion, rheometry, SAXS, DSC and polarized light microscopy among others [25, 26, 33]. In figure 1 we show the phase diagram for this copolymer where the typical C-shaped hard gel boundary curve is clearly observed. It is probably the simplest phase diagram among other triblock copolymers of type PEO_x-PPO_y-PEO_x -as for example P123 [32]- and may serve as a basis for future work involving other more complex surfactants and mixtures. As observed, gelation can occur on increasing temperature from a low temperature fluid (so called "cold gelation") or on reducing temperature from a high temperature fluid ("hot gelation"). In this work we will only focus on the first route (cold gelation) as the maximum temperature used in this work will be 40ºC.

In this manuscript we aim to evaluate the feasibility of using water dispersions of thermoresponsive Pluronics F127 triblock copolymers in the MR properties of carbonyl iron based MR fluids.

EXPERIMENTAL

Materials

Triblock copolymer, commonly known as Pluronics F127 was a product of BASF Corp. purchased from Sigma-Aldrich. The copolymer was used as received without further fractionation or other purification. According to the manufacturer, the copolymer has a total molecular weight of 13388 [25]. Other relevant molecular characteristics have been well documented in the previous literature (e.g. see table 1 in [33]). In this work we are interested in high copolymer concentrations for the lyotropic liquid crystalline phases to form upon heating (cf. Figure 1). As the cmc of this copolymer at 15 ºC is reported to be

of only 0.7 wt% (e.g. see Table 2 in [25]), the copolymer concentrations employed in this contribution will always be around 10 wt% or larger.

Carbonyl iron microparticles employed in the formulation of the MR fluids where a gift from BASF SE (grade HQ). They are quasispherical in shape and polydisperse. Their average particle diameter has been reported in the literature to be around 900 ± 300 nm [34]. Other relevant properties such as particle size histograms, magnetization curves, electrokinetics and chemical composition have been reported elsewhere [34-36]. The particle concentration range studied spans from dilute systems (0.5 vol%) up to much higher concentrations closer to commercial applications (30 vol%).

The preparation of the MR fluids consisted of the following steps: i) the copolymer was first dissolved in Milli-Q distilled water at 10 ºC, ii) the magnetic powder and copolymer solution were mixed in a polyethylene container, iii) the mixture was stirred first by hand and then in an ultrasonic bath; iv) step iii) was repeated several times to ensure the required final homogeneity. The gradual homogenization of the samples was confirmed by the disappearance of the aggregates initially observed in the container bottom.

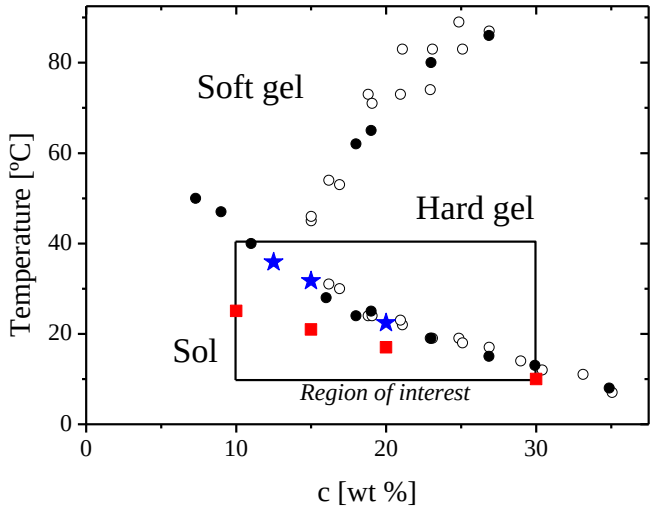

Figure 1. Gel diagram of Pluronics F127 obtained by tube inversion and rheometry. Open circles: gel boundary by tube inversion; solid circles: gel boundary by rheometry. Adapted from Figure 7 in [33]. Red squares correspond to the temperature at which the storage modulus first begins to dramatically increase in figure 2. Blue stars correspond to the gelling temperature as obtained from multiwave tests (cf. figure 3).

Colloidal stability

A Turbiscan Classic 2000 (Formulaction, France) was used to investigate the kinetic stability of the MR fluids. In this device the sample was scanned by using two synchronous optical sensors that detected the intensity of light transmitted through and backscattered by the sample (180º and 45º from the incident laser light, respectively). The reading head acquired backscattering and transmission data every 40 μm while moving along the entire height of the cell (60 mm). The light source was an electro-luminescent diode. For the MR fluids investigated in this work, only the transmission measurements provided useful data.

Scans were repeated over time (during 150 hours), each one providing a new curve, and all curves were overlaid on one graph to show stability over time. Reference mode was also used by simply subtracting the first curve from the subsequent ones, in order to see variations of profiles relative to the initial state. The sediment height was eventually calculated from the raw sedimentation curves for a direct comparative study of the MR fluids at two different temperatures (10 ºC and 30 ºC).

Rheometry

The rheological properties of the suspensions were determined in an Anton Paar MCR302 torsional rheometer under the presence of simple shearing flows. Copolymer solutions were measured using a cone-plate geometry (diameter 50 mm; angle 1º) while MR fluids were investigated using a plate-plate geometry (diameter 40 mm, 300 μm gap). A solvent trap was used to avoid sample evaporation. Typically, prior to the test, both the sample and rheometer tools were cooled down to circa 10 ºC. Then the (fluid-like) sample was loaded onto the lower plate of the rheometer and further equilibrated at 10 ºC for a total of 200 s at rest. This preconditioning was necessary to avoid filling errors and eventually resulted in very reproducible results. The magnetic field, perpendicular to the shear field, was generated with a custom-built solenoid coil surrounding the parallel-plate geometry.

Small-amplitude dynamic oscillatory shear temperature-sweeps were carried out in the copolymer solutions at a strain amplitude of 0.05 % and an excitation frequency of 1 Hz. Multiwave rheology experiments were also carried out to precisely determine the gel point. This allows the application of multiple frequencies simultaneously in oscillatory experiments. Here, an oscillatory small strain $\gamma(t)$ is imposed on the sample: $\gamma(t) = \sum_{i=1}^{m} \gamma_i \sin(\omega_i t)$ where m is the number of the superimposed harmonics, and γ_i and ω_i denote the amplitude and the frequency of the ith harmonic, respectively. The frequencies of the harmonics were $\omega_n = n\omega_f$ with the fundamental frequency ω_f. In our studies, ω_f = 2π rad s^{-1} (n = 2, 4, 7, 10, 20, 40, 70 and 100) and γ_i = 0.05 %. In all cases the samples were heated at 1 ºC min^{-1} from 10 to 40 ºC. It is important to remark

that the rate of increase of the temperature had to remain at a low value to get reproducible results.

Steady shear flow rheology tests were carried out at two different temperatures (10 ºC and 30 ºC), without and with magnetic field applied, using a parallel-plate geometry (40 mm diameter, 300 μm gap). In all cases the shear rate was logarithmically increased from 0.01 to 1000 s^{-1}. A total of 25 data points were acquired with a time interval length of 10 s. To get the rheogram at 10 ºC we did first load the sample at 10 ºC and equilibrate it during 200 s at 10 ºC. To get a rheogram at 30 ºC, we did first load the sample at 10 ºC and equilibrate it at 10 ºC during 200 s at rest. Then, the temperature was increased to 30 ºC at a rate of 1 ºC per minute at rest. Finally the steady shear flow test started.

RESULTS AND DISCUSSION

Gelling point of triblock copolymer solutions

The gelation behavior of water-based solutions of Pluronics F127 copolymers has been interrogated in the previous literature using a vast number of experimental techniques. For instance, rheological investigations by Wanka and coworkers [31] demonstrated that solutions exhibited a Newtonian character with constant viscosity (as a function of shear rate) and negligible elasticity for concentrations below 10 wt%. On the contrary, solutions with larger concentrations became a gel when the temperature was raised above a characteristic value (gelation temperature) that is slightly above room temperature in agreement with figure 1. Traditionally, the gelation point was either ascertained by a rapid increase of the zero-shear viscosity (approaching to infinity) or manifested by a large increase in the storage modulus when plotted as a function of the temperature at a commanded excitation frequency.

As a way of example, in figure 2 we show the temperature dependence of the storage modulus G' (measured at a strain amplitude of 0.05 % and a frequency of 1 Hz) for copolymer concentrations ranging from 10 wt% to 30 wt%. These curves clearly envisage the appearance of a sol-gel transition upon increasing the temperature, from 10 ºC to 40 ºC, as demonstrated by the fact that the storage modulus rapidly increases more than three orders of magnitude in only a few degrees. Eventually, the storage modulus approaches to a saturation value on further increase of temperature. This saturation value increases with increasing the concentration of the copolymer in agreement with previous communications [31, 33]. Also, with increasing the copolymer concentration, the characteristic temperature for gelation moves towards lower values in agreement with similar copolymers investigated in the literature [31].

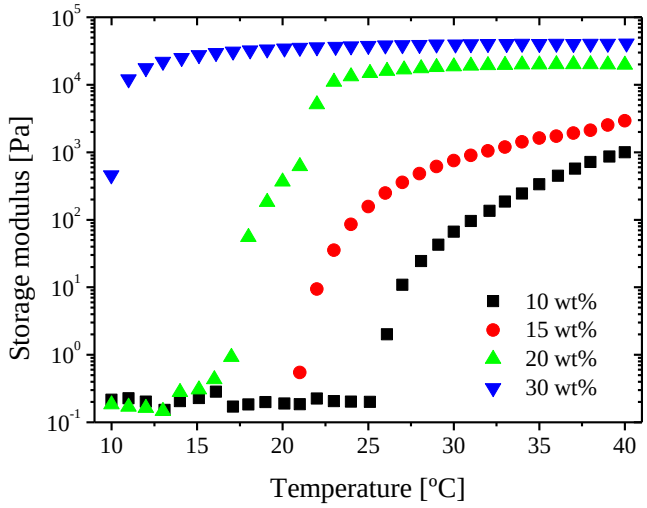

Figure 2. Storage modulus as a function of temperature for copolymer solutions. Strain amplitude 0.05 %. Frequency 1 Hz. The geometry used was a cone-plate of 50 mm diameter and 1º angle. Prior to the temperature sweep (1ºC per minute) the sample was equilibrated at 10 ºC for 200 s.

The temperature associated to the rapid rise of storage modulus is included in figure 1 for completeness. As observed in figure 1, these values are found to be lower than other reported in the literature.

As stated above, the gelling process of copolymer solutions has been traditionally interrogated by small-amplitude oscillatory shear techniques, in which the viscoelastic moduli are monitored in the viscoelastic linear region at constant frequency (see [31] and references therein). However, it is well known that performing dynamic oscillatory tests at a constant frequency is not sufficient for the accurate determination of the true gelation temperature because it can lead to frequency-dependent gelation temperatures [37]. The true gelation temperature is associated to an excitation frequency-independent loss tangent, tan δ = G''/G', and therefore, the gelation must be obtained from the intersection of loss tangent versus temperature curves at various frequencies, e.g., by using multiple waveform rheology.

In figure 3 we show the results obtained from multiple waveform rheology tests in an attempt to precisely determine the gelation temperature for the copolymer solutions. Results shown in figure 3 correspond to a 20 wt% polymer concentration. At low temperature (in the sol phase) the copolymer solutions essentially behaved as liquids of negligible elasticity (close to the sensitivity of the rheometer). The loss modulus exhibited a typical $G'' \approx \omega$ power law dependence. On the other hand, the storage

modulus was very low and approached the $G' \approx \omega^2$ in the terminal zone. When the temperature increased (in the gel phase), both G' and G" grew in magnitude, with G' dominating G", and the terminal zone shifted to lower frequencies. In fact, for the highest temperatures investigated, the terminal zone could not be appreciated within the frequency range investigated and the viscoelastic moduli became frequency-independent. Therefore, the gelation point can also be seen as the temperature when G' and G" exhibit the same power law index with the frequency.

Similar multiwave tests were carried out for other copolymer concentrations in order to determine the gelation temperature. The resulting curves show very similar trends and therefore, these data are not shown in this manuscript for brevity. Nevertheless, the gelation temperatures obtained are included in figure 1 (star symbols) for a direct comparison with previous data reported in the literature. As observed, a very good agreement is found. It is worth to remark that for a 10 wt% concentration, the gel point, as obtained from multiwave rheology, is found to be larger than 40 ºC. Actually, the multiwave curves obtained for the lowest frequencies investigated do not collapse even at 40 ºC. This is the reason why the point corresponding to 10 wt% is missing in figure 1.

To sum up, figures 2 and 3 suggest that Pluronics F127 triblock copolymer solutions may serve as carrier fluids in the formulation of novel MR fluids with improved kinetic stability, thermoresponsive character and enhanced MR effect. In the next sections we aim to further check these statements by incorporating the carbonyl iron microparticles in the MR fluid formulation.

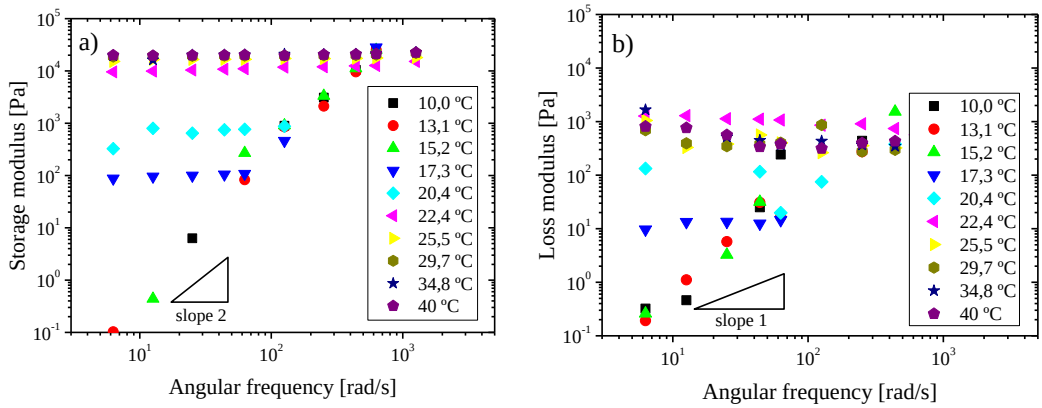

Figure 3. Frequency dependence of the linear viscoelastic properties of 20 wt% copolymer solutions as obtained from multiwave oscillatory tests. a) storage modulus, b) loss modulus. The strain amplitude was 0.05 %.

Kinetic stability of MR fluids

The stability against sedimentation was ascertained by turbidity measurements. Figure 4 includes results for a 20 vol% carbonyl iron suspensions in 20 wt% copolymer solutions at two different temperatures (10 ºC and 30 ºC). The column on the left contains raw transmission data for the two samples at two different temperatures. When operating at 10 ºC, the transmission signal clearly increases immediately after introducing the tube in the device. This reflects the clarification of the suspension in the upper region of the tube. Then, as time passes the transmission peak becomes wider indicative of particle sedimentation. On the contrary, the MR fluid at 30 ºC does exhibit a constant transmission value independently of time in good agreement with a suspension were particles are not sedimenting under gravity. These experimental data are further reinforced by visual inspection of the samples. Snapshots of the MR suspensions after three hours are also included in Figure 4. The column on the right contains sediment height data (H/H_0) for the MR suspensions at two temperatures. It is again very clearly observed that sedimentation is inhibited in MR fluids at 30 ºC. However, MR fluids at 10 ºC do clearly sediment under gravity and the sediment reaches a final plateau height after a couple of days.

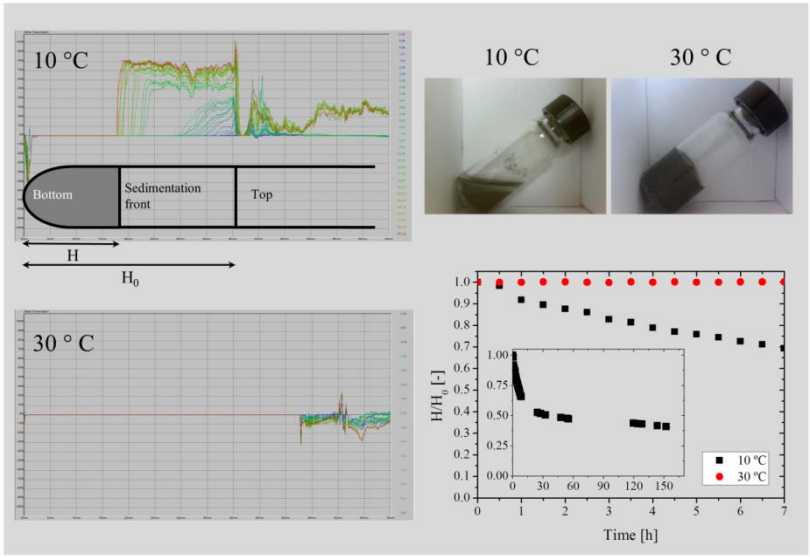

Figure 4. Sedimentation stability of 20 vol% carbonyl iron suspensions in 20 wt% copolymer solutions at two different temperatures (10 ºC and 30 ºC). Left column; raw transmission data in reference mode: upper panel 10 ºC, lower panel 30 ºC. Right column; up: Snapshots of the MR fluids at 10 and 30 ºC after 3 hours, down: Sediment height as a function of time: squares 10 ºC, circles 30 ºC. H0 represents the initial sample height.

Thermoresponsive MR fluids

MR fluids used in commercial applications typically involve carbonyl iron particle loadings of the order of 20-30 vol%. Therefore, the goal now is to investigate whether the temperature-driven transition reported in section 4.1 still occurs in the presence of iron microparticles at these high concentrations.

Multiwave rheology experiments revealed that the transition still happens when particles are present, as demonstrated in figure 5 for a 30 vol% carbonyl iron in 20 wt% copolymer solutions. As observed, the magnitude of the storage modulus severely increases when adding the particles in comparison to copolymer solutions without particles. Interestingly, in contrast to what happened with copolymer solutions, when iron microparticles are dispersed in the polymer matrix the overall shape of the curve does not depend on the excitation frequency and therefore, the determination of the gelation temperature using the method by Winter and coworkers [37] is not applicable. This point can be more clearly seen by comparing figure 5a and figure 3a.

Figure 5b demonstrates that the transition can still be tuned by changing the copolymer concentration in solution. Actually, for a given particle concentration, increasing the copolymer content lowers the transition temperature. Finally, it is also important to remark that there appears a normal force acting on the upper plate when the suspensions gel. This normal force did not appear when heating copolymer solutions without particles and is found to be very sensitive to the gelling process.

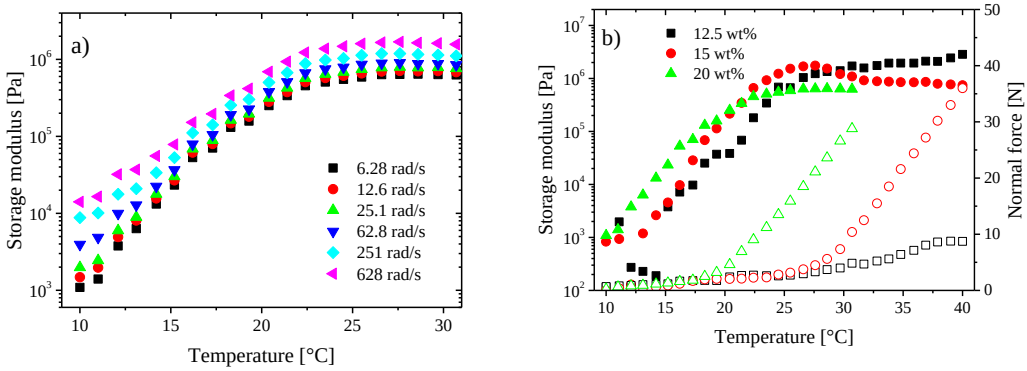

Figure 5. Multiwave rheology for 30 vol% iron suspensions in copolymer solutions in the absence of magnetic fields. a) effect of excitation frequency (from 6.28 rad/s to 628 rad/s) in 20 wt% copolymer solutions. b) effect of copolymer concentration (12.5 wt%, 15 wt% and 20 wt%) at the fundamental frequency (1 Hz). Solid symbols: storage modulus. Open symbols: normal force acting on the upper plate of the geometry.

In a next step, magnetic fields were superimposed to the suspensions during the tests (see figure 6). Preliminary experiments were carried out for 30 vol% iron suspensions in copolymer solutions at different concentrations ranging between 10 wt% and 30 wt%. In all cases investigated, the effect of magnetic field was negligible at large temperature. This was expected because the carrier fluid experiences a micellar to lyotropic liquid crystalline phase transition upon heating and therefore particles remain entrapped in the polymer matrix. In contrast, at low temperatures, below the gelation temperature, the effect of magnetic field was noticeable. Importantly, contrary to the initial expectation, the presence of the magnetic field reduced the elastic modulus. A reason for this may come from the fact that field-induced particle rearrangement breaks the initial polymeric structure giving a smaller elastic modulus. In order to validate the hypothesis, we decided to investigate lower particle concentrations in the MR fluid formulation.

In figure 7 we show the effect of magnetic field on the gelling process of 20 wt% copolymer solutions including iron particles for a wide concentration range from 0.5 vol% to 30 vol%. As expected, at very low particle content (below 5 vol%) the effect of magnetic field was negligible, even at low temperature. The reason for this is the formation of field-induced structures with only one or zero end attached to the shearing plates.

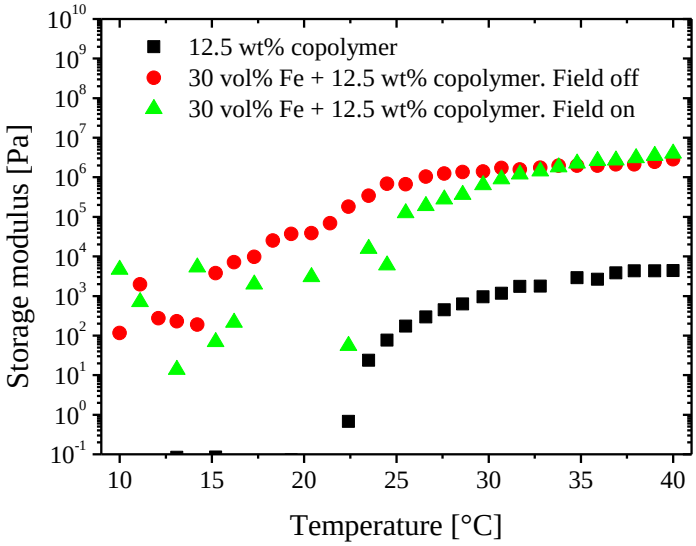

Figure 6. Storage modulus as a function of temperature for copolymer solutions (black squares), MR fluids in the absence of magnetic field (red circles) and MR fluids in the presence of a magnetic field of 15 kA/m (green triangles). Copolymer concentration 12.5 wt%. Iron concentration 30 vol%. Strain amplitude 0.05 %. Frequency 1 Hz.

Contrarily, for intermediate particle concentrations, the effect of field was remarkable (please note that we are using logarithmic scales). At these concentrations, the presence of magnetic particles in suspension contributes to a rise in the storage modulus in agreement with the Particle Magnetization Model. Finally, if the particle concentration was too large (larger than 20 vol%) a negative MR effect was observed as reported above (cf. Figure 6).

The effect of magnetic field in the rheological performance of MR fluids at different particle concentrations can be better visualized by plotting the normalized storage modulus as a function of temperature. In this manuscript the normalized storage modulus is calculated by the ratio between the storage modulus increment under field and the zero-field storage modulus. Results obtained are shown in figure 8 and serve as a first attempt to interrogate the MR effect.

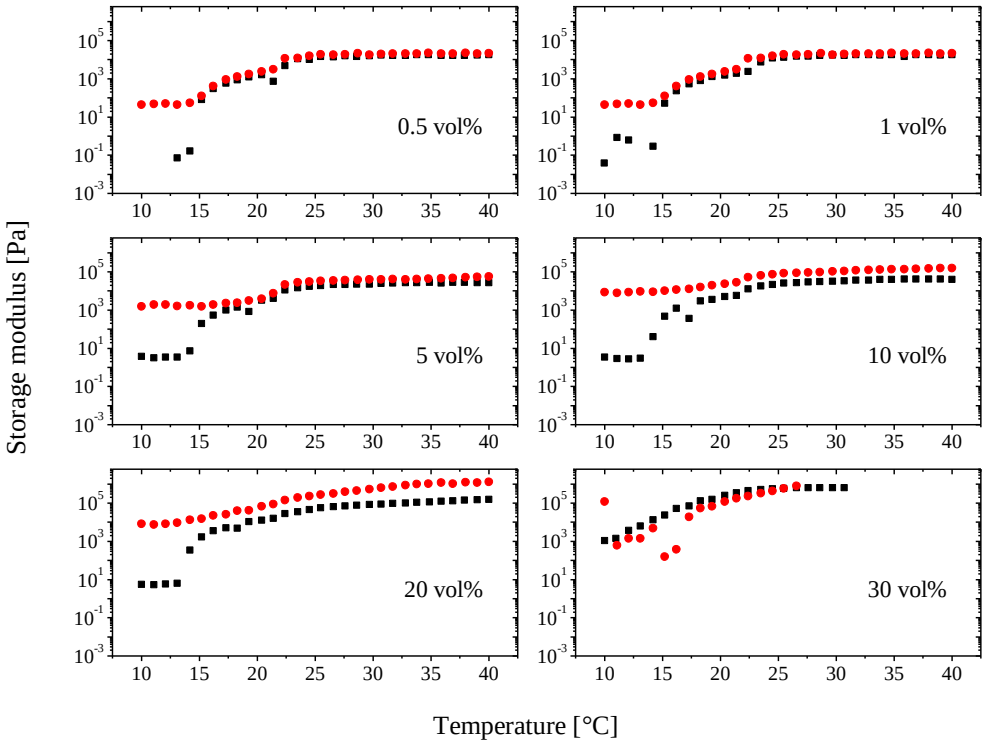

Figure 7. Storage modulus as a function of temperature for MR fluids in 20 wt% copolymer solutions at different iron concentrations. Strain amplitude 0.05 %. Excitation frequency 1 Hz. Black squares: field off. Red circles: field on.

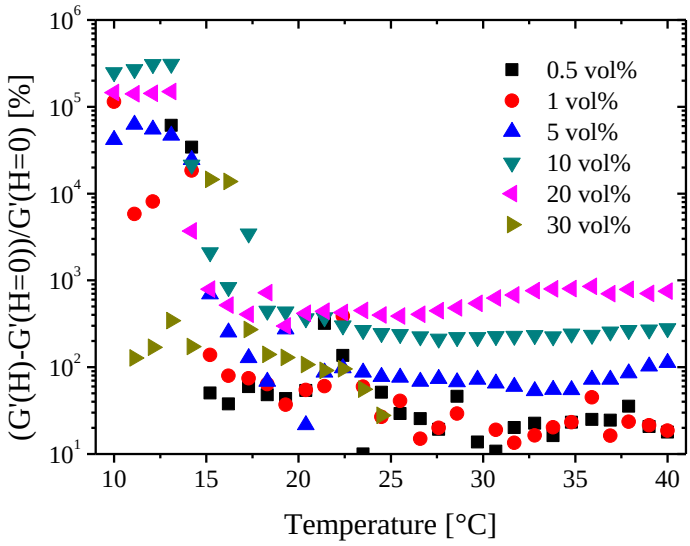

Figure 8. Dimensionless representation of the storage modulus as a function of temperature for MR fluids in 20 wt% copolymer solutions at different iron concentrations.

On the one hand, for temperatures larger than 20 ºC, well in the gel phase, the normalized storage modulus remains essentially constant. Slightly larger values for the storage modulus are obtained for 10 vol% and 20 vol% iron suspensions. For lower (< 10 vol%) and higher (≈ 30 vol%) concentrations, the MR effect is negligible as commented in the paragraph above. On the other hand, decreasing the temperature below 15 - 20 ºC results in a very sharp increase of the storage modulus.

This increase is again associated to the liquid crystal to micellar transition in the carrier fluid. The large scatter in the data is due to the fact that the measured torque values are very close to the sensitivity of the rheometer because of the very viscous behavior of the suspension. Next, steady shear flow experiments were carried out to avoid this problem and further increase the torque value at low temperature.

MR effect in steady shear flow

The MR performance of a MR fluid is typically examined using steady shear flow tests. In this section the MR effect is evaluated in the suspensions by comparing steady shear flow curves below and above the sol/gel transition and both in the absence and presence of magnetic fields. In figure 9, the shear stress is plotted as a function of shear rate for 20 vol% suspensions of carbonyl iron in 20 wt% copolymer solutions at 10 ºC (figure 9a) and 30 ºC (figure 9b). As observed in figure 9a, at low temperature (10 ºC), below

the sol-gel transition, copolymer water solutions do essentially behave as Newtonian fluids. This is manifested by a linear relationship between the shear stress and the shear rate. When adding iron particles to this copolymer solution, the suspension exhibits an apparent yield stress possible coming from interparticle (remant) magnetic interactions. Finally when a magnetic field is applied (15 kA/m) the apparent yield stress significantly increases up to 100 Pa. In contrast, at high temperature (30 ºC), above the sol-gel transition, the polymeric matrix dominates the rheological response (see figure 9b). Both in the absence and presence of particles the material exhibits a yield stress. When applying an external magnetic field the yield stress very slightly increases.

The relative MR effect is better observed in figure 10. Here we plot the ratio between the shear viscosity increment under field and the viscosity value in the absence of the field as a function of the shear rate for the two temperatures under investigation. At high temperature, the MR effect is significantly low and remains constant for the range of shear rates studied. In contrast, a very large MR effect is observed at low temperature especially at low shear rates. When the shear rate increases, hydrodynamics interactions compete against magnetostatic forces and the MR effect decreases.

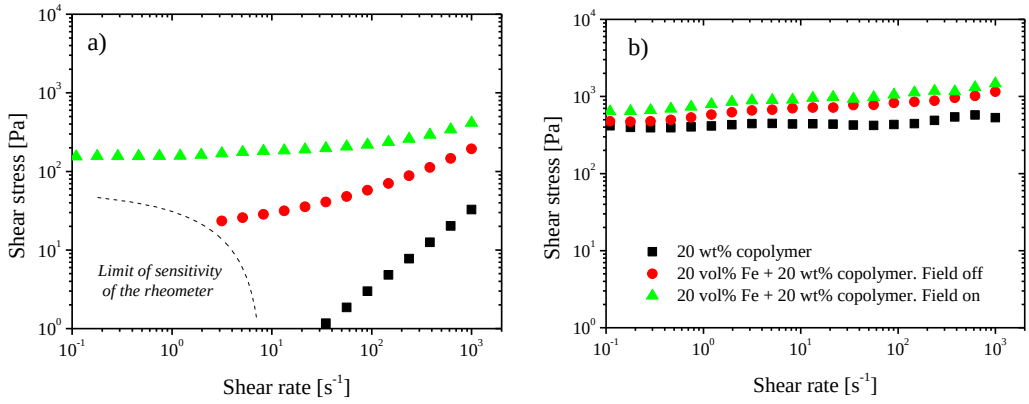

Figure 9. Shear stress as a function of shear rate for 20 vol% carbonyl iron suspensions in 20 wt% copolymer solutions at two different temperatures. a) 10 ºC. b) 30 ºC.

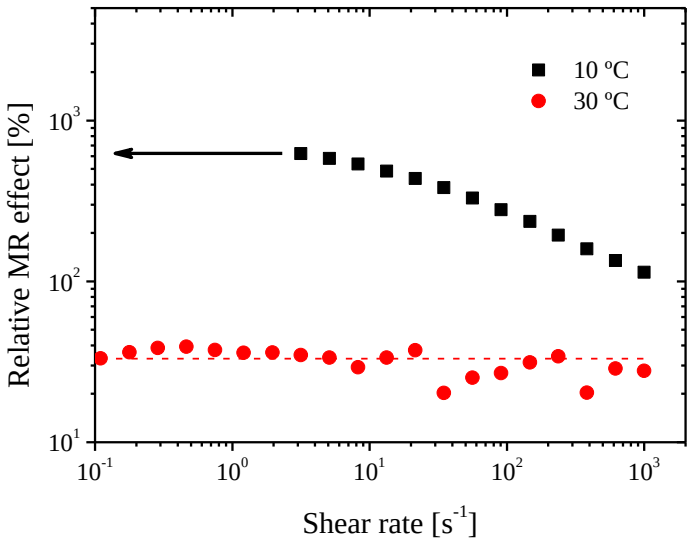

Figure 10. Relative MR effect as a function of the shear rate for a 20 vol% iron suspension in 20 wt% copolymer solution for temperatures below (10 ºC) and above (30 ºC) the sol/gel transition. The relative MR effect is defined as the ratio between the shear viscosity increment under field (15 kA/m) and the shear viscosity value in the absence of the field.

CONCLUSIONS

Thermoresponsive carrier fluids are promising candidates that can be used in highly concentrated MR fluids formulations (20 vol%) to prevent the sedimentation of magnetizable particles still exhibiting a very large (relative) MR effect (1000 %). For the first time, in this manuscript we evaluate the MR performance of carbonyl iron dispersions in triblock copolymer solutions -of type PEO_x-PPO_y-PEO_x with x = 100 and y = 65-. For polymer concentrations larger than 10 wt%, copolymer micellar solutions do (rapidly) transform into gel-like cubic liquid crystals, exhibiting a large yield stress, upon heating. At low temperature, below the sol/gel transition temperature of the polymer matrix, the MR fluid exhibits a large MR effect as a result of a very low viscosity carrier fluid (of the order of 30 mPa·s). In contrast, at high temperature, above the sol/gel transition, the dynamics of the iron particles is arrested and sedimentation is inhibited. The sol/gel transition temperature as well as the yield stress (in the gel phase) in this thermoresponsive carrier fluid can be easily tuned by changing the polymer concentration in the MR fluid formulation.

REFERENCES

[1] Vekas L 2008 Ferrofluids and magnetorheological fluids Advances in Science and Technology 54 127-136

[2] Park B J, Fang F F and Choi H J 2010 Magnetorheology: materials and application Soft Matter 6 5246-5253

[3] de Vicente J, Klingenberg D J and Hidalgo-Álvarez R 2011 Magnetorheological fluids: a review Soft Matter 7 3701-3710

[4] Boczkowska A and Awietjan S Microstructure and Properties of Magnetorheological Elastomers Advanced Elastomers - Technology, Properties and Applications (D.Sc. Anna Boczkowska Ed., ISBN: 978-953-51-0739-2, InTech, DOI: 10.5772/50430)

[5] Lokander M and Stenberg B 2003 Performance of isotropic magnetorheological rubber materials Polymer Testing 22 245–251

[6] Jiang W, Yao J –J, Gong X and Chen L 2008 Enhancement in Magnetorheological Effect of Magnetorheological Elastomers by Surface Modification of Iron Particles Chinese Journal of Chemical Physics 21 87-92

[7] Bombard A J F, Alcantara M R, Knobel M and Volpe P L O 2005 Experimental study of MR suspensions of carbonyl iron powders with different particle sizes Int. J. Mod. Phys. B 19 1332-1338

[8] Jordan T C and Shaw M T 1989 Electrorheology IEEE Transactions on Electrical Insulation 24 849-878

[9] Goncalves F D, Koo J- H and Ahmadian M 2006 A review of the state of the art in magnetorheological fluid technologies – Part I: MR fluid and MR fluid models The Shock and Vibration Digest 38 203-219

[10] de Vicente J, López-López M T, González-Caballero F and Durán J D G 2003 A Rheological Study of the Stabilization of Magnetizable Colloidal Suspensions by Addition of Silica Nanoparticles J. Rheol. 47(5) 1093-1109

[11] Lim ST, Cho M S, Jang I B and Choi H J 2004 Magnetorheological characterization of carbonyl iron based suspensions stabilized by fumed silica J. Magn. Magn. Mater 282 170-173

[12] Chin B D, Park J H, Kwon M H and Park O O 2001 Rheological properties and dispersion stability of magnetorheological (MR) suspensions Rheol. Acta 40 211-219

[13] Rankin P J, Horvath A T and Klingenberg D J 1999 Magnetorheology in viscoplastic media Rheol. Acta 38 471-477

[14] Chhabra R P 1993 Bubbles, drops and particles in non-Newtonian fluids (CRC Press, Boca Raton)

[15] Kormann C, Laun H M and Richter H J 1996 MR fluids with nanosized magnetic particles Int. J. Mod. Phys. B 10 3167-3172

[16] Bell R C, Karli J O, Vavreck A N, Zimmerman D T, Ngatu G T and Wereley N M 2008 Magnetorheology of submicron diameter iron microwires dispersed in silicone oil Smart Mater. Struct. 17 015028

[17] de Vicente J, Segovia-Gutiérrez J P, Andablo-Reyes E, Vereda F and Hidalgo-Álvarez R 2009 Dynamic Rheology of Sphere- and Rod-based Magnetorheological Fluids J. Chem. Phys. 131 194902-01-10

[18] Kor Y K and See H 2010 The electrorheological response of elongated particles Rheol. Acta 49 741-756

[19] Foister R T 1997 US patent 5,667,715

[20] Trendler A M and Bose H 2005 Influence of particle size on the rheological properties of magnetorheological suspensions Int. J. Mod. Phys. B 19 1416-1422

[21] Song K H, Park B J and Choi H J 2009 Effect of magnetic nanoparticle additive on characteristics of magnetorheological fluid IEEE Trans. Mag. 45(10) 4045-4048

[22] Jonsdottir F, Gudmundsson K H, Dijkman T B, Thorsteinsson F and Gutfleisch O 2010 Rheology of perfluorinated polyether-based MR fluids with nanoparticles J. Intel. Mat. Syst. Str. 21(11) 1051-1060

[23] Choi J S, Park B J, Cho M S and Choi H J 2006 Preparation and magnetorheological characteristics of polymer coated carbonyl iron suspensions J. Magn. Magn. Mater 304 374-376

[24] Shahrivar K and de Vicente J 2013 Thermoresponsive polymer-based magneto-rheological (MR) composites as a bridge between MR fluids and MR elastomers Soft matter 9 11451

[25] Wanka G, Hoffmann H and Ulbricht W 1994 Phase diagrams and aggregation behavior of poly(oxyethylene)-poly(oxypropylene)-Poly(oxyethylene) triblock copolymers in aqueous solutions Macromolecules 27 4145-4159

[26] Nambam J S and Philip J 2012 Thermogelling properties of triblock copolymers in the presence of hydrophilic Fe3O4 nanoparticles and surfactants Langmuir 28 12044-12053

[27] Gilbert J C, Hadgraft J, Bye A and Brooks L G 1986 Drug release from Pluronics F-127 gels Int. J. Pharm. 32 223-228

[28] Miyazaki S, Yokouchi C, Nakamura T, Hashiguchi N, Hou W and Takada M 1986 Pharmaucetical application of biomedica polymers. 20. Pluronic F127 gels as a novel vehicle for rectal administration of indomethacin Chem. Pharm. Bull. 34 1801-1808

[29] Linse P and Malmsten M 1992 Temperature-dependent micellization in aqueous block copolymer solutions Macromolecules 25 5434-5439

[30] Qin J, Asempah I, Laurent S, Fornara A, Muller R N and Muhammed M 2009 Injectable superparamagnetic ferrogels for controlled release of hydrophobic drugs Advanced Materials 21 1354-1357

[31] Wanka G, Hoffmann H and Ulbricht W 1990 The aggregation behavior of poly(oxyethylene)-poly(oxypropylene)-Poly(oxyethylene)-block-copolymers in aqueous solution Colloid Polym. Sci. 268 101-117

[32] Hamley I W, Mai S -M, Ryan A J, Patrick J, Fairclough A and Booth C 2001 Aqueous mesophases of block copolymers of ethylene oxide and 1,2-butylene oxide Phys. Chem. Chem. Phys. 3 2972-2980

[33] Chaibundit C, Ricardo N M P S, Costa F M L L, Yeates S G and Booth C 2007 Micellization and gelation of mixed copolymers P123 and F127 in aqueous solution Langmuir 23 9229-9236

[34] de Vicente J, López-López M T, Durán J D G and Bossis G 2005 A Slender-body Micromechanical Model for Viscoelasticity of Magnetic Colloids. Comparison with Preliminary Experimental Data J. Colloid Interface Sci. 282 193-201

[35] de Vicente J, Bossis G, Lacis S and Guyot M 2002 Permeability Measurements in Cobalt Ferrite and Carbonyl Iron Powders and Suspensions Journal of Magnetism and Magnetic Materials 251(1) 100-108

[36] de Vicente J, Durán J D G, Delgado A V, González-Caballero F and Bossis G 2002 Effect of Magnetic Hysteresis of the Solid Phase on the Rheological Properties of Magnetorheological Fluids Int. J. Mod. Phys. B 16(17-18) 2576-2582

[37] Winter H H and Chambon F 1986 Analysis of linear viscoelasticity of a crosslinking polymer at the gel point J. Rheol. 30 367-82.

CHAPTER 3

Creep and recovery of magnetorheological fluids: experiments and simulations

Zuowei Wang, Keshvad Shahrivar, Juan de Vicente

This article is published in: Journal of Rheology, 58, 6, 1725-1750, 2014.

Synopsis

A direct comparative study on the creep-recovery behavior of conventional MR fluids is carried out using magnetorheometry and particle-level simulations. Two particle concentrations are investigated ($\phi = 0.05$ and 0.30) at two different magnetic field strengths (53 kA·m^{-1} and 173 kA·m^{-1}) in order to match the yield stresses developed in both systems for easier comparison. Simulations are mostly started with random initial structures with some additional tests of using preassembled single chains in the low concentration case. Experimental and simulation data are in good qualitative agreement. The results demonstrate three regions in the creep curves: i) In the initial viscoelastic region, the chain-like (at $\phi = 0.05$) or percolated three-dimensional network (at $\phi = 0.30$) structures fill up the gap and the average cluster size remains constant; ii) Above a critical strain of 0.1 (10 %), in the retardation region, these structures begin to break and rearrange under shear. At large enough imposed stress values, they transform into thin sheet-like or thick lamellar structures, depending on the particle concentration; iii) Finally in the case of larger strain values either the viscosity diverges (at low stress values) or reaches a constant low value (at high stress values), showing a clear bifurcation behavior. For stresses below the bifurcation point the MR fluid is capable to recover the strain by a certain fraction. However, no recovery is observed for large stress values.

INTRODUCTION

Magnetorheological (MR) fluids are field-responsive colloidal suspensions that exhibit dramatic changes in their rheological response when magnetized. From a fundamental point of view, they can be used as model systems to explore non-equilibrium transitions from the liquid-state to the solid-state by externally tuning the magnetic field strength. From a practical point of view, there exist currently many commercial applications that involve the use of MR fluids [Ginder (1998); Carlson (2003); de Vicente et al. (2011); Wereley (2013)].

There is nowadays great interest in getting a better understanding of the yielding behavior of MR fluids. In most cases, the yield stress is determined by measuring steady shear properties of MR fluids subjected to a finite range of shear stresses. In principle, by simply extrapolating the steady data at low shear, it is possible to obtain the yield stress. In practice, the situation is more complex as the result may depend on the amount of time we spend measuring every point in the rheogram (if we are not in steady state), and also on whether we are increasing or decreasing the stress (thixotropy and other time-related effects such as sedimentation).

Similar to what occurs for other complex fluids, the study of the creep flow of MR fluids is of valuable help in understanding the yielding behavior of these materials. A total of four regimes have been distinguished when performing creep-recovery tests on MR fluids depending on the stress level applied [Otsubo and Edamura (1994); Li *et al.* (2002); See *et al.* (2004); de Vicente and Berli (2013)]. These regimes can be viewed under the frame of the creep-recovery behavior of non-linear viscoelastic materials (see Figure 1). Initially, at very low stresses, MR fluids exhibit a linear viscoelastic response that is characterized by an instantaneous elastic strain γ_e, a retarded elastic strain γ_r and a viscous strain γ_v. Here, the creep compliance $J = \gamma/\tau_0$ remains constant independently of the stress value τ_0. Also, both the instantaneous creep strain γ_{ic} ($= \gamma_e + \gamma_p$, with γ_p the plastic contribution) and the instantaneous recovery strain γ_{ir} are equal to the elastic contribution γ_e, i. e., $\gamma_{ic} = \gamma_{ir} = \gamma_e$ and $\gamma_p = 0$ (Figure 2a). Upon increasing the stress, the MR fluid behaves as a non-linear viscoelastic material and the retarded elastic and viscous strain decrease (see Figure 2b). At this stage, the plastic contribution to the instantaneous strain grows ($\gamma_{ic} > \gamma_{ir}$ as $\gamma_p > 0$). For even larger stresses the MR fluid behaves as a viscoelastic solid (Figure 2c). Here, the strain is instantaneous and fully plastic, and both retarded and viscous strains are negligible. In this regime, $\gamma_e = \gamma_{ir} = 0$ and $\gamma_{ic} = \gamma_p$. Finally, for stresses larger than the so-called "yield stress", the MR fluid behaves as a plastic fluid with a negligible instantaneous creep compliance ($J_0 = 0$) and a low viscosity level (small η_0) (see Figure 2d). This stage is characterized by the fact that the recovery is negligible and $\gamma_{ic} = \gamma_{ir} = 0$.

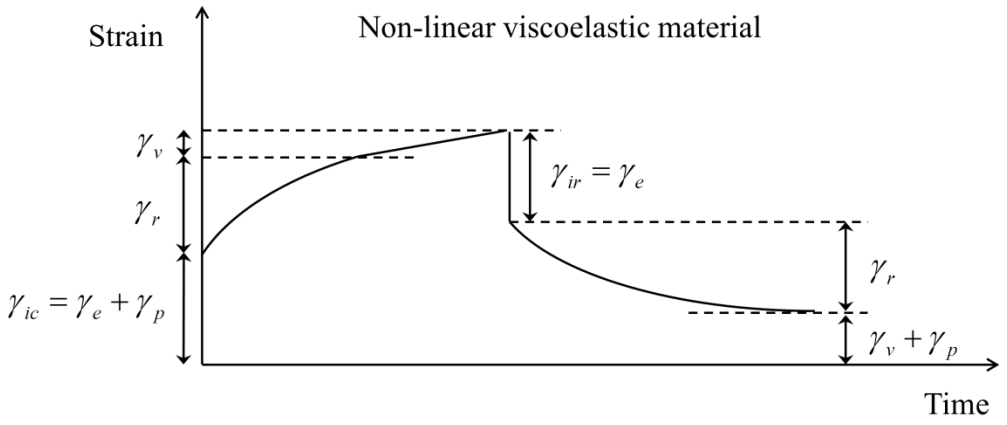

Figure 1. Schematics of the creep-recovery behavior of a non-linear viscoplastic material. γ_{ic} is the instantaneous (creep) strain, γ_e is the elastic contribution to the instantaneous strain, γ_p is the plastic contribution to the instantaneous strain, γ_r is the retardation strain, γ_v is the viscous (unrecoverable) strain and γ_{ir} is the instantaneous recovery strain.

In this work we aim to investigate the creep-recovery behavior of MR fluids using rheometry and particle level dynamic simulations. Previous experimental work by de Vicente and Berli (2013) focused on dilute MR fluids and suggested a complex yielding mechanism where field-induced aggregates are formed and broken dynamically under shearing. In this manuscript we will present results for highly concentrated MR fluids as well, in an attempt to compare the yielding behavior between dilute and more concentrated suspensions that are closer to commercial applications. Also, the effect of carrier fluid viscosity and waiting times will be investigated.

Finally, it is important to remark that chain-like micromechanical models that are typically and successfully employed under steady shearing flows, fail when trying to explain the creep-recovery behavior of MR fluids [de Vicente and Berli (2013)]. Because of this, in this manuscript we aim to apply dynamic simulations. It is worth to note that in spite of the fact that particle level dynamic simulations have been extensively used in the literature to predict steady shear properties such as viscosity and unsteady small-amplitude oscillatory shear properties such as viscoelastic moduli, the use of particle level simulations in creep flows has not been done yet in the literature. In this manuscript we will show particle level simulation results on creep-recovery tests to better understand the yielding behavior of MR fluids.

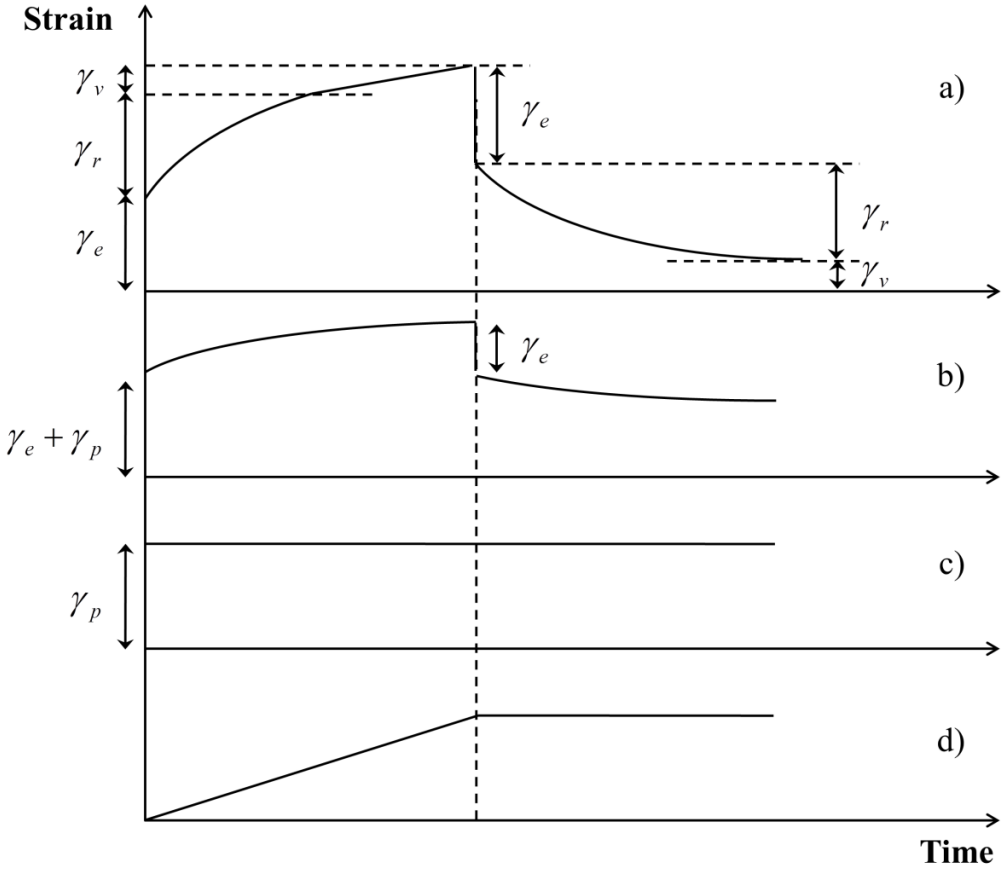

Figure 2. Schematics of the creep-recovery behavior of a MR fluid. The stress increases from top to bottom. a) Linear viscoelastic response; b) Non-linear viscoelastic response; c) Viscoplastic solid; d) Plastic fluid.

MATERIALS AND EXPERIMENTAL MEASUREMENT METHODS

MR fluids were formulated by dispersing carbonyl iron microparticles in a silicone oil without additives. Carbonyl iron particles were a gift from BASF SE (grade HQ) and silicone oils were purchased from Sigma-Aldrich (20 ± 3 mPa·s, 98 ± 3 mPa·s, 340 ± 5

mPa·s and 487 ± 2 mPa·s). MR fluids were prepared at two different particle concentrations: 5 vol% ($\phi = 0.05$) and 30 vol% ($\phi = 0.30$).

Rheology experiments were conducted in a stress-controlled MCR 501 magnetorheometer (Anton Paar) to explore the yielding behavior of MR fluids in the presence of magnetic fields. A plate-plate geometry (diameter 20 mm) was used unless otherwise stated. The gap thickness was 300 microns and the magnetic field was perpendicular to the plates. The temperature of the sample was stabilized at 25 ºC using a circulating fluid bath.

Steady shear flow tests were carried out as described in Segovia-Gutiérrez *et al.* (2012). Briefly, the experimental procedure is summarized as follows: (a) initially the sample was preconditioned at a constant shear rate 200 s^{-1} for 30 s, (b) next the suspension was left to equilibrate for 1 min in the presence of a magnetic field, (c) finally the shear stress was logarithmically increased from 0.1 Pa at a rate of 10 points per decade. Experiments were repeated at least three times with fresh new samples.

Step stress and recovery tests were also performed under shear. The experimental protocol used is summarized as follows: (a) a preshear was first applied to eliminate shear history effects during 30 s (shear rate 100 s^{-1}); (b) an equilibration step followed at rest in a quiescent state (stress equal to zero), again during 30 s; (c) the magnetic field was suddenly applied for a "waiting time" of 120 s –unless otherwise stated– to promote the field-induced structuration; (d) finally, step stress and recovery tests followed still in the presence of the magnetic field. In a typical assay, a constant shear stress τ_0 was applied for a time of 300 s while the resulting strain was measured. The stress was then removed and the recovered strain was measured for another 300 s. In all cases investigated, the strain was reset to zero at the beginning of the creep test. Again, experiments were repeated at least three times with fresh new samples.

BROWNIAN DYNAMICS (BD) SIMULATION METHODS

General algorithm

Upon application of a magnetic field, the particles (diameter σ) dispersed in a MR fluid become magnetized. The field-induced magnetic dipole moment on particle i is given as:

$$\vec{m}_i = \pi \mu_0 \mu_s \beta \sigma^3 \vec{H}_{loc}/2 \quad (1)$$

where H_{loc} is the local magnetic field acting on the particle and the value of the contrast factor $\beta = \frac{\mu_p - \mu_s}{\mu_p + 2\mu_s}$ depends on the relative permeabilities of the particles, μ_p, and the suspension, μ_s. For the carbonyl iron particles employed in this work, we can find several expressions in the literature for their relative magnetic susceptibility. For example, experiments by Gorodkin *et al.* (2009) suggested that the specific magnetic susceptibility of iron particles χ_s is a linear function of the median particle size D_{50} (measured in micrometers) with the empirical form of $\chi_s = 0.668 D_{50} + 0.961$. Hence, for a typical particle size of 1μm, using Maxwell-Garnett equation, $\chi_s = 3\chi_p/(3 + \chi_p)$, we get that $\chi_p = 3.56 \approx 4$ and $\beta \approx 4/7$. Another popular expression that properly fits the experimental magnetic properties of carbonyl iron particles is the Frölich-Kennely equation [Bozorth (1993)], which gives.

$$\mu_p = 1 + \frac{\chi_i}{1 + \frac{\chi_i}{M_s} H} \tag{2}$$

with $\chi_i = 131$ and $M_s = 1990$ kA·m^{-1} [de Vicente *et al.* (2005)]. Using this equation the iron particles are expected to possess a much larger permeability and therefore form stronger microstructures than that predicted by Gorodkin *et al.* (2009). For instance, when simulating MR fluids at $\phi = 0.05$ under a magnetic field strength of 173 kA·m^{-1}, the use of the Gorodkin equation in estimating the particle permeability resulted in a yield stress in between 100 Pa and 250 Pa, while a much larger stress in between 400 Pa and 1000 Pa was obtained by using the Frölich-Kennely equation. In this work we will stay with the Frölich-Kennely approach [eq.(2)] because it seems to be more widely used in the literature and also generates yield stress values closer to experimental data as will be seen in the following sections.

The dimensionless equation of motion of particle i can be written in the overdamped situation as [Wang (2000)]

$$\frac{d\vec{r}_i^*}{dt^*} = \sum_{j \neq i} (\vec{F}_{ij}^{mag*} + \vec{F}_{ij}^{rep*}) + \vec{v}_S^*(\vec{r}_i^*) + B\overrightarrow{W}_i^*(t^*) \tag{3}$$

where $F^* = F/\tilde{F}^{mag}$, $r^* = r/\sigma$ and $t^* = t/\tilde{t}$ with the time scaling factor $\tilde{t} = \frac{3\pi\eta_s\sigma^2}{\tilde{F}^{mag}} = 16\eta_s/\mu_0\mu_s\beta^2 H_0^2$. The magnetic interaction force $\vec{F}_{ij}^{mag}$ between two particles is scaled by $\tilde{F}^{mag} = \frac{3}{16}\pi\mu_0\mu_s\beta^2\sigma^2 H_0^2$. Accordingly the shear stress scales as $\tilde{\tau} = \frac{\tilde{F}^{mag}}{\sigma^2} = \frac{3}{16}\pi\mu_0\mu_s\beta^2 H_0^2$. $\overrightarrow{v_S}(\vec{r_i})$ is the flow velocity at the particle position $\vec{r_i}$. The stochastic

force $\overrightarrow{W_i}(t)$ follows a standard Gaussian noise distribution and the coefficient B ($=\sqrt{\frac{2k_BT}{\bar{F}^{mag}\sigma dt^*}}$) measures the ratio between the Brownian and magnetic interaction forces. dt^* is the dimensionless time step. In the current work, we took a variable step size scheme in which the value of dt^* at each BD step was determined to be the time that took the particle under the largest force in the system to move a distance of 0.05σ. In addition, dt^* was subject to an upper bound that was either $dt_u^* = 5 \times 10^{-4}$ or 1×10^{-3}, depending on the volume fraction of particles and the external field strength. When dt^*=1×10^{-3}, the coefficient B takes a value of about 0.241 at $H_0 = 53$ kA·m^{-1} and 0.086 at $H_0 = 173$ kA·m^{-1}.

BD simulations were performed in a confined geometry as sketched in Figure 3 where the MR fluids were confined in between two parallel planar hard walls. The bottom wall was fixed, while the upper one was allowed to move in the x-direction, either under constant stress or constant shear rate. The simulation box took a cubic shape with periodic boundary conditions in the two unconfined directions. Since for the sample formulation and magnetic field strengths studied in the current work wall slip was not observed in experiments by running measurements at different gaps in plate-plate geometries [de Vicente and Berli (2013)], the non-slipping boundary conditions were applied in simulations. If the center of a particle was at a distance less than 0.55σ from the surface of a wall, it was assumed to be stuck on the wall laterally, but allowed to move back to the cell in the normal direction. A detailed study on the impact of different boundary conditions will be left for future work.

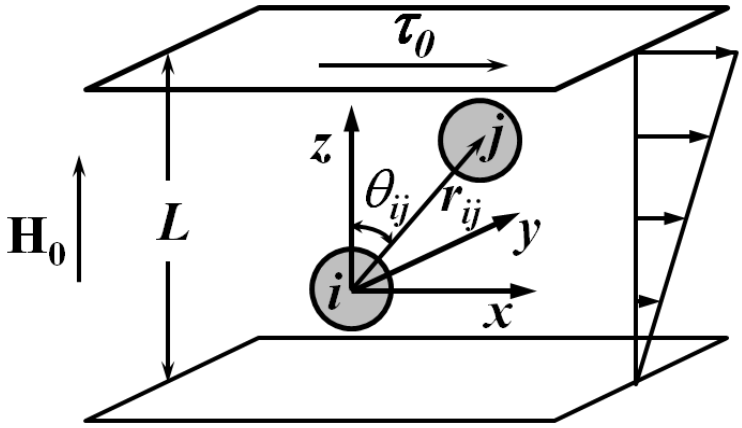

Figure 3. Sketch of the dynamics simulation system.

The short-range interactions between the particles have been argued to play an important role in determining the rheological behavior of MR fluids [Segovia-Gutierrez *et al.* (2012); Fernández-Toledano *et al.* (2014)]. Simulation results in the current work were obtained by using an exponential form of the short-range repulsive forces both in between the particles and between the particles and the walls:

$$\vec{F}_{ij}^{rep*}(\vec{r}_{ij}^{*}) = \begin{cases} exp\left[-\dfrac{(r_{ij}^{*}-1)}{R_0^{*}}\right](-\vec{e}_r), & j = particle \\ exp\left[-\dfrac{(h_i^{*}-0.5)}{R_0^{*}}\right]\vec{n}, & j = wall\,, \end{cases} \tag{4}$$

where h_i^* is the distance from the center of particle i to the wall surface and $\vec{n}$ is the unit vector in the normal direction of the wall. The cut-off distance of the particle-particle repulsion was $r_{cut} = 1.5\sigma$, while that with the wall was 0.55σ. The steepness of the repulsive forces in eq. (4) is controlled by the dimensionless length scale R_0^* whose value was taken to be $R_0^* = 0.01$. The resulted sharp repulsive potential closely mimics that of hard spheres and so favors the formation of thick column structures. [Klingenberg (1991); Wang *et al.* (1997)]. The influence of different types of short-range interaction forces on the simulation results will be left for a further study.

The magnetic interaction forces between the particles were calculated using the dipole-dipole approximation. We employed the coupled-dipole-moment model to take into account the many-body magnetization effect [Wang *et al.* (1996)]. In this model the instantaneous dipole moment on each particle is evaluated using the local magnetic field at its center:

$$\vec{H}_{loc}=\vec{H}_0 + \textstyle\sum_{j\neq i}\vec{H}_j \tag{5}$$

where $\vec{H}_j$ is the dipolar magnetic field generated by particle j at the center position of i. The magnitude of the mutual magnetization effect can be quantified by the mean-square strength of the dipole moments:

$$\lambda(t^*) = \frac{1}{N}\sum_{1}^{N} m_i^{*2}(t^*) \tag{6}$$

where N is the total number of magnetic particles in the simulation box and $m^* = m/(\pi\mu_0\mu_s\beta\sigma^3 H_0/2)$. $\lambda(t^*)$ is a time-dependent function that can be used to

characterize the change of microscopic structures in the system. Its value also tells to what extent that the coupled-dipole-moment model can improve the quantitative description of the magnetic interaction forces over the generally used fixed dipole moment approach where $\lambda = 1$ due to the approximation of $H_{loc} = H_0$.

In addition to the mean-square dipole moment strength λ [eq. (6)], we introduce two more sets of physical quantities to characterize the structural changes in the system. One is the weight-average size of the field-induced clusters of particles,

$$S_{avg} = \frac{\sum n_i S_i^2}{\sum n_i S_i} \tag{7}$$

where n_i is the number of clusters consisting of S_i particles and $\sum n_i S_i = N$ is the total number of particles in the system. Two particles are considered to be in the same cluster if their center-to-center distance is not larger than 1.05σ. In another measurement, we classify the N particles in the system into three groups. The fraction of the particles that belong to clusters which are in contact with both confining walls is termed as f_{2-ends}. Similarly the fractions of those in clusters contacting with only one wall or no wall are termed as f_{1-end} and f_{0-end}, respectively. These fraction values sum up to unity at each time step. In this work, a cluster is considered to be in contact with a confining wall if the center of any particle in this cluster is at a distance $r \leq 0.55\sigma$ from the surface of the wall. This criterion is consistent with that used for the non-slipping boundary conditions.

Creep-recovery simulation.

In creep experiments a constant step stress τ_0 is applied to the upper wall of the confined system at time zero. The creep strain of the system is determined by the balance between the applied stress and the internal stress resulted from the viscous friction of the carrier liquid and the interactions among the magnetic particles. The viscous contribution to the internal stress can be estimated by

$$\tau_{vis}(t) = \eta_s \dot{\gamma}(t) \tag{8}$$

where η_s is the dynamic viscosity of the carrier liquid. Here we have neglected the contributions from the viscous dissipation produced by the flow around the particles and the hydrodynamic interactions among particles, which are predicted to give rise to the Newtonian viscosity of a hard sphere suspension $\eta = \eta_s \left[1 + \frac{5}{2}\phi + (6 \pm 0.2)\phi^2\right]$ at low particle concentrations. [Larson (1999); Verberg and de Schepper (1997)] For

$\phi = 0.05, \eta/\eta_s \approx 1.67$, while this ratio is estimated to be around 2.5~3.5 at ϕ=0.30 by using high-concentration expressions for $\eta(\phi)$ [Verberg and de Schepper (1997)]. In the MR systems we studied, the value of η can also be affected by other experimental conditions such as the particle shape and the residual interparticle aggregations. As will be described in Sec. 4.2, we take an effective value of the carrier liquid viscosity, $\eta_s^{eff} = c_s\eta_s$ with c_s a constant larger than unity, for mapping the experimental and simulation shear stresses at high shear rates. This approach will to a certain extent compensate the approximation made in Eq. (8). The non-hydrodynamic contribution from the interacting particles can be evaluated by a simple approach

$$\tau_H(t) = -\frac{1}{V}\sum_{i,j(all\ pairs)} \langle F_{ij}^x(t)(z_i(t) - z_j(t))\rangle \tag{9}$$

where F_{ij}^x refers to the projection of the magnetic and short-range interaction forces between particles i and j along the shear direction and $z_{i(j)}$ are their position coordinates in the magnetic field direction.Using the stress balance in the system [Doi and Edwards (1986); See and Doi (1992)]

$$\tau_0 = \tau_{vis}(t) + \tau_H(t), \tag{10}$$

the instantaneous strain rate is estimated to be

$$\dot{\gamma}(t) = [\tau_0 - \tau_H(t)]/\eta_s, \tag{11}$$

which in dimensionless units takes the form of

$$\dot{\gamma}^*(t^*) = 3\pi[\tau_0^* - \tau_H^*(t)], \tag{12}$$

The instantaneous viscosity of the MR fluid can then be estimated as

$$\eta(t) = \tau_0/\dot{\gamma}(t) \tag{13}$$

and the creep strain is

$$\gamma(t) = \int_0^t \dot{\gamma}(t)\, dt \tag{14}$$

The shear creep compliance $J(t)$ can also be obtained from $J(t) = \gamma(t)/\tau_0$. In BD simulations the strain increment is updated by

$$d\gamma = \dot{\gamma}^*(t^*)dt^* \tag{15}$$

using the instantaneous strain rate $\dot{\gamma}^*(t^*)$ calculated in eq. (12) at every time step.

The creep-recovery simulation of an MR system was performed in three steps with a constant magnetic field H_0 applied throughout: a) quiescent state: starting from a configuration with randomly distributed particles, the system was equilibrated for a dimensionless time of $5 \times 10^5 dt_u^*$ to allow the formation of field-induced structures; b) creep process: a constant step stress τ_0 was applied to the upper wall of the system at time $t^* = 0$ and held for a time duration of $10^7 dt_u^*$; c) recovery process: the external stress was suddenly removed and the system was relaxed for another time period of $2 \times 10^6 dt_u^*$.

In this work, the total number of magnetic particles was fixed to $N = 1000$ and a cubic simulation box was used. The side length of the box and also the gap between the two walls were $L = 21.88\sigma$ for the system with particle volume fraction $\phi = 0.05$ and $L = 12.04\sigma$ for $\phi = 0.30$, respectively. For convenience of comparing with experiments, the dimensionless simulation time has been mapped to real time by multiplying the time scaling factor $\tilde{t}$ calculated from experimental parameters with the only exception of using the effective carrier liquid viscosity η_s^{eff} obtained in Sec.4.2 rather than the experimental value of η_s. For a MR system with $\eta_s^{eff} = 2.0$ Pa·s and $H_0 = 173$ kA·m^{-1}, $\tilde{t}$ is approximately 1.4×10^{-3} s. It means that a typical BD run time of $t^* = 10^7 dt_u^*$ with $dt_u^* = 10^{-3}$ is mapped to a real time of $t \approx 14$s. This is apparently much shorter than that studied in experiments. We will thus keep the comparison between simulation and experimental results at the qualitative level. Nevertheless, as will be seen below, the simulation time window is large enough to capture all the interesting creep-recovery behavior of MR fluids. More importantly analyses of simulation results are able to provide microscopic understanding of such behavior that is not directly accessible in experiments, particularly at small time scales (e.g., $t \leq 10^{-2}$ s).

Since the single-particle-width chain model has been widely used as the simplest approach to interpret the rheological behavior of MR fluids, we have performed an extra set of creep-recovery simulations using preassembled single-width chains. The system setup is the same as that sketched in Figure 3. In the initial configurations linear chains each consisting of 22 particles were aligned straightly along the magnetic field (z-) direction so as to bridge the two walls with a gap width of $L = 22\sigma$. In the x-y plane, these chains were arranged into a triangular lattice with the lattice vector lengths determined by the particle volume fraction $\phi = 0.05$. Periodic boundary conditions were applied in the x- and y-directions. A number of step stress values were chosen for comparison with simulations using same set of system parameters but random initial configurations.

One remark to be made is that the viscosity η_s, or more precisely η_s^{eff}, of the carrier liquid does not enter the dimensionless equation of motion [eq.(3)] or particle interaction forces. It only affects the time scaling factor $\tilde{t}$. If a different carrier liquid viscosity is used in experiment, the simulation time can be simply rescaled by the ratio between the two η_s values.

RESULTS AND DISCUSSION

First, creep-recovery experiments were performed using carrier fluids of different viscosities (98 mPa·s, 340 mPa·s and 487 mPa·s) at a given particle concentration ($\phi = 0.30$) under an external magnetic field strength of $H_0 = 53$ kA·m^{-1}. Results demonstrated that the viscosity does only affect the time scale for structuration as demonstrated by the fact that creep curves do actually collapse when plotted as a function of the ratio between time and shear viscosity. This finding is important in order to later compare experimental results and simulation data essentially because the time scale used in simulations does also predict that viscosity does not affect the final structure under shear. We note that the shear stress of the MR system will be affected by the viscosity of the carrier liquid. In our simplified theoretical treatment, this effect is taken into account by including the viscous contribution [eq. (8)] in the calculation of the total stress [eq. (10)]. However, the neglect of the hydrodynamic contributions, which also rely on η_s, may lead to an underestimation of the shear stress, together with other approximations made in the theoretical framework. Such effects have been partly taken into account by using an effective carrier liquid viscosity for mapping the simulation results to experimental data. Next we carried out experiments in parallel-plate (20 mm diameter, 300 μm gap) and cone-plate (20 mm diameter, 2º) geometries in order to check the impact of a non-homogeneous shear rate acting on the sheared MR fluids. Experiments were done in a concentrated MR fluid ($\phi = 0.30$) formulated in a silicone oil of 487 mPa·s at 53 kA·m^{-1}. Experimental results demonstrate that both geometries provide very similar results except in the vicinity of the yielding point. This

finding also allows a comparison with simulation data where homogeneous shearing flow is assumed (see Figure 3).

Finally, we also explored the effect of waiting time. The waiting time is defined here as the time elapsed in interval c) (see Sec. 2) when the magnetic field is applied, just after the equilibration step. This is an important point because depending on the material under study, some samples significantly age during the rest period. Three different waiting times were investigated (10 s, 60 s and 120 s). Experiments were done again in a $\phi = 0.30$ MR fluid formulated in a silicone oil of 487 mPa·s at 53 kA·m^{-1}. Experimental results demonstrate that structuration occurs very quickly, in less than 10 s, and therefore the effect of the waiting times investigated is negligible except at the yielding point where reproducibility is worse. Again, this permits a comparison with simulation data where structures are annealed prior to the creep test.

Following these tests (summarized in Supplementary Information), we performed experimental and simulation studies on the rheological behavior of two MR systems. In one system the volume fraction of particles and the external field strength are taken to be $\phi = 0.05$ and $H_0 = 173$ kA·m^{-1}, respectively. In the other case, the particle loading and magnetic field strength were $\phi = 0.30$ and $H_0 = 53$ kA·m^{-1}, respectively. Field strengths were changed in order for the MR fluids to exhibit a similar "yield stress" value of the order of 400 Pa and for more easy comparison [Segovia-Gutiérrez *et al.* (2012)]. All simulation data have been mapped to real time and length scales by using the experimental parameters. But as mentioned above the comparison should still be considered as qualitative rather than quantitative due to many assumptions made in the simulation model, including the simplified theoretical treatment of the magnetic and short-range interactions between particles, the neglect of hydrodynamic interactions, the assumption of non-slipping boundary conditions, as well as the limited time window and simulation box sizes. From now on we denote the simulation time as t_{sim} to distinguish from the true experimental time scales.

Creep-recovery process

Low particle volume fraction (ϕ = 0.05)

Figures 4(a, b) present the experimental and simulation results on the creep-recovery curves of the low concentration MR system for a wide range of step stresses. The yield stress of such a system was estimated to be $\tau_y \approx 400$ Pa in a previous publication by de Vicente and Berli (2013). The classical Bingham plastic model predicts a purely elastic solid behavior for step stresses below the yield stress τ_y.

However, curves depicted in Figures 4(a, b) clearly demonstrate three distinctive regimes. At short times (below 10^{-2} s in experiments and 10^{-3} s in simulations) there is an instantaneous increase in the strain γ_{ic}.

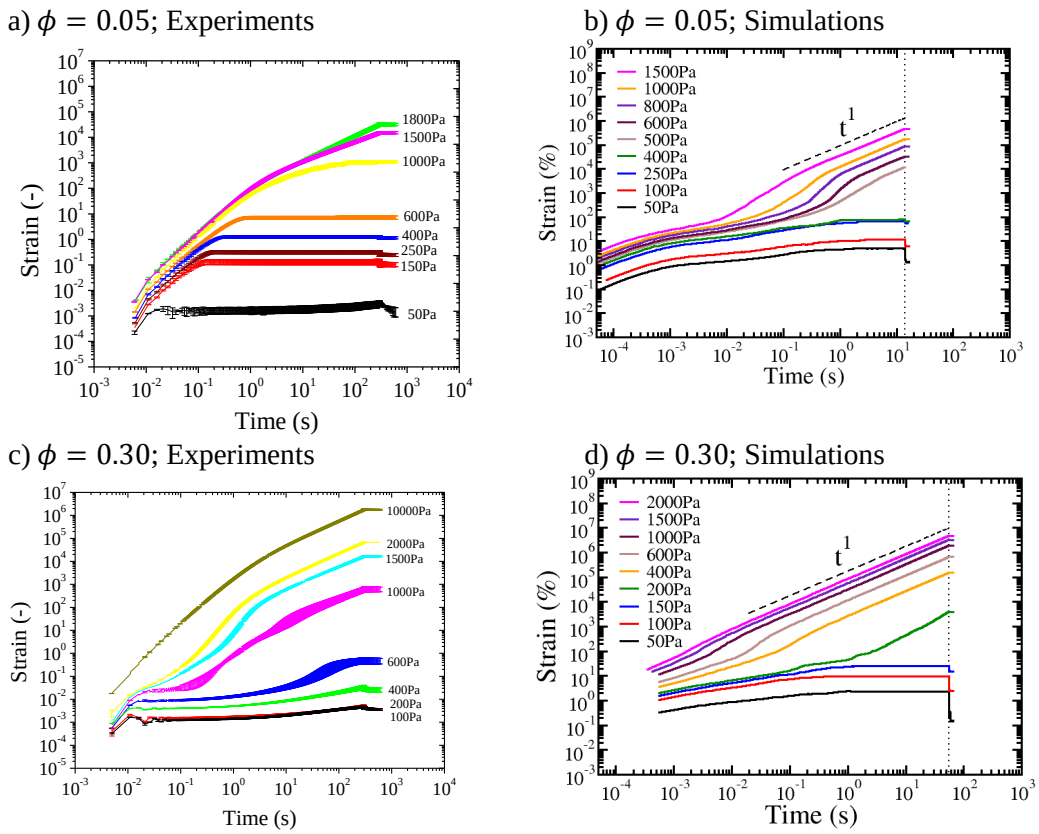

Figure 4. Creep-recovery curvesobtained at various step stresses as indicated in the graphs for the MR systemswith a) $\phi = 0.05$; $H_0 = 173$ kA·m^{-1}; $\eta_s = 20$ mPa·s; b) $\phi = 0.30$; $H_0 = 53$ kA·m^{-1}; $\eta_s = 487$ mPa·s. The simulation time scales are calculated using an effective carrier liquid viscosity η_s^{eff}=2.0Pa.s.

For longer times the retarded strain γ_r increases and finally at long times a state of constant strain rate is achieved. Also important to remark is that the recovered strain is only a small fraction of the instantaneous creep strain in contrast to the behavior of linear viscoelastic materials whose behavior is schematized in Figure 2(a). The incomplete recovery of the strain indicates that the MR fluid behaves as a plastic material [de Vicente and Berli (2013)]. For large stresses the MR fluid is not capable to recover the initial strain. The creep curves obtained in BD simulations also demonstrate three regimes in response to the applied stress, namely an initial response regime, an intermediate retardation regime and a long-time steady state whose feature is determined by the step stress value. The creep curves obtained at stresses below a critical value around 400 Pa gradually level off at large times, while those achieved at much higher stresses show a typical viscous flow behavior with a constant strain rate. A noticeable difference between the simulation and experimental creep curves is that the former ones

possess an inflection point at intermediate time, especially at high stress values. These creep-recovery behavior are analyzed in detail below in relation to the structural changes in the system.

Initial response regime. Upon the application of the step stress, both experimental and simulation creep curves show a nearly instantaneous jump in strain which is beyond the resolution of the measurement. After that, all these curves grow in parallel with time, regardless of stress values. We have calculated the instantaneous shear strain rate, $\dot{\gamma}(t)$, by taking the time derivatives of each creep curve contained in Figures 4(a, b). This in turn gives the instantaneous viscosity, $\eta(t) = \tau_0/\dot{\gamma}(t)$, and the rate of the creep compliance, $\dot{J}(t) = \dot{\gamma}(t)/\tau_0 = 1/\eta(t)$. The simulation data on $\eta(t)$ are presented in Figure 5(b). In consistence with the parallel feature of the creep curves, all the $\eta(t)$ data collapse onto a universal curve up to a time scale $t_{sim} \approx 3{\times}10^{-3}s$. The same universal behavior was found for the creep compliances $J(t)$, which means that the MR fluid behaves as a viscoelastic material at early time. The response is in the linear viscoelastic region if $\eta(t)$ and so $\dot{J}(t)$ are constant. This region however lasts only for a very short period of time ($t_{sim} \leq 10^{-4}s$). Beyond that, the viscoelastic behavior is nonlinear with time-variant $\eta(t)$ and $\dot{J}(t)$ values. Experiments reported in Figure 5(a) also demonstrate a linear viscoelastic region for real times lower than 10^{-2} s.

Figure 6(a) presents the simulation data on the instantaneous stress $\tau_H(t)$ calculated using eq. (9) for four stress values, namely $\tau_0 =$ 100, 250, 1000 and 1500 Pa, respectively. Note that the total internal stress in the system is given by $\tau_{tot}(t) = \tau_H(t) + \eta_s^{eff}\dot{\gamma}(t)$. The results show that the time taken for $\tau_H(t)$ to reach its plateau value and so for $\tau_{tot}(t)$ to match τ_0 is roughly the same for all the applied stress values. The good agreement between the simulation data obtained from random and preassembled initial configurations also indicates that the stress building-up time is independent of the detailed structures of the system at the beginning of the creep process. It is in this period of time ($t_{sim} < 3{\times}10^{-3}s$) that the MR fluid behaves as a viscoelastic material.

The stress component τ_H is determined by the microstructures formed by magnetic particles. We plot in Figures 7(a) and (b) the average cluster size, S_{avg}, and the three wall-contact fraction values, f_{2-ends}, f_{1-end} and f_{0-end}, as a function of time for the MR systems under a step stress of $\tau_0 =$ 250 Pa. The vertical dashed line located in between $t_{sim} = 10^{-3}$ s and 10^{-2} s is introduced as a rough guideline marking the end of the initial response regime. Inside the initial regime, the average cluster size remains constant, indicating that the increase of the stress τ_H is solely due to the deformation of the chains or columns formed in the quiescent state.

It is interesting to look at the changes of the quantities f_{2-ends} and f_{0-end} in Figure 7(b) where all the preassembled single chains were initially in touch with both walls, giving $f_{2-ends} = 1$ at time $t =$ 0 s (not shown in the plot due to the use of logarithmic time

scale). This fraction value drops to zero almost instantaneously upon the application of the stress. In the meantime, the value of f_{0-end} jumps from 0 to 1 and remains at 1 for the entire initial regime as well as part of the following retardation regime.

a) $\phi = 0.05$; Experiments

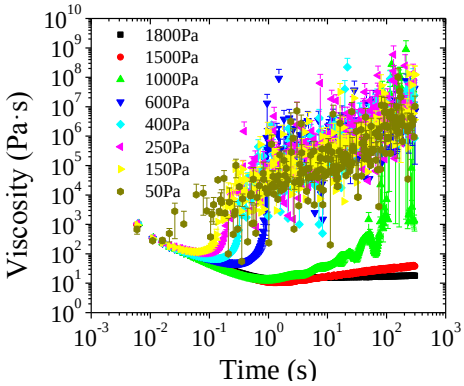

b) $\phi = 0.05$; Simulations

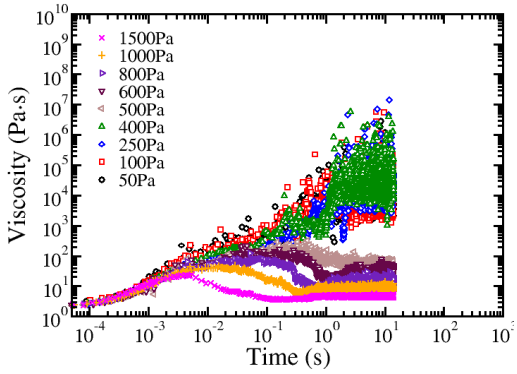

c) $\phi = 0.30$; Experiments

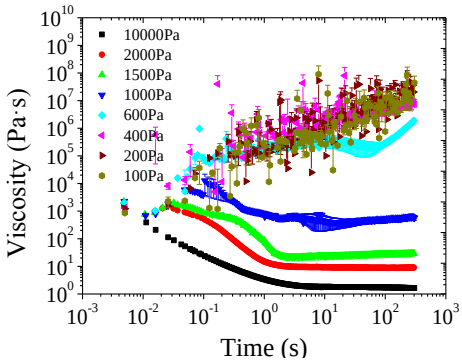

d) $\phi = 0.30$; Simulation

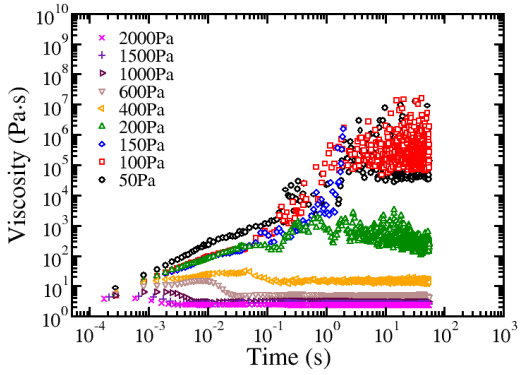

Figure 5. Instantaneous viscosity as a function of time for the MR systems with a) $\phi = 0.05$; $H_0 = 173$ kA·m^{-1}; $\eta_s = 20$ mPa·s; b) $\phi = 0.30$; $H_0 = 53$ kA·m^{-1}; $\eta_s = 487$ mPa·s. The results were obtained by taking the time derivatives of the creep strain curves shown in Figure 4. The simulation time scales and instantaneous viscosities are calculated using an effective carrier liquid viscosity η_s^{eff}=2.0Pa.s.

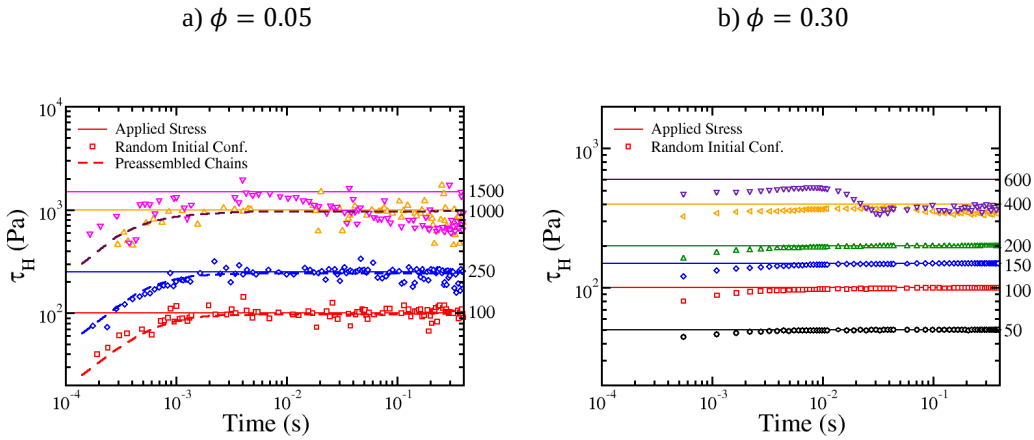

Figure 6. Building-up of the internal stress τ_H [eq.(9)] in response to the applied external stress τ_0 (horizontal lines). The system parameters are: a) $\phi = 0.05$; $H_0 = 173$ kA·m^{-1}; $\eta_s = 20$ mPa·s; b) $\phi = 0.30$; $H_0 = 53$ kA·m^{-1}; $\eta_s = 487$ mPa·s. Simulation results obtained from random initial configurations are given by symbols, while those from preassembled single-width chains are presented as dashed curves [only in a)]. The simulation time scales are calculated using an effective carrier liquid viscosity η_s^{eff}=2.0 Pa·s.

The breaking of chain end connection with the walls, rather than in the middle of the chain, is qualitatively different from that observed in electrorheological (ER) fluids. In the latter case, the image dipole moments provide strong bonding energy between the polarized particles and the electrodes, and so the chain breakage tends to occur in the middle part of the chain.

The weak linking between the particle clusters and the walls can also be found in Figure 7(a) from the systems with random initial configurations. There the average cluster size at time zero is $S_{avg} \approx 33.6$ much larger than the single-width chain length of 22. The polydispersity in the cluster sizes can be visualized in the snapshot on the left panel of Figure 9(a). In this case the initial values of $f_{2-ends}$and f_{1-end} are about 0.4 and 0.6, respectively. Compared with single-width chains, the thicker columns can tolerate larger strain deformation by adjusting the relative positions of the particles without losing the internal connectivity or the contact with the walls. The values of f_{2-ends} and f_{1-end} thus stay constant for a short period of time, but further shear leads to the drop in f_{2-ends} and increase in f_{1-end} and f_{0-end}. There is however no chain breakage, as reflected in the constant value of S_{avg} in this regime.

In Figure 6(a) the $\tau_H(t)$ data of the systems with random initial configurations show relative large fluctuations in comparison with that from the systems with preassembled

single chains. At longer times the sensitivity of this stress component to the detailed microstructure can result in a quantitative, but not qualitative, diversity in the creep curves obtained from the MR fluids with the same set of system parameters but different initial configurations.

a) $\tau_0 = 250$ Pa; Random initial configurations.

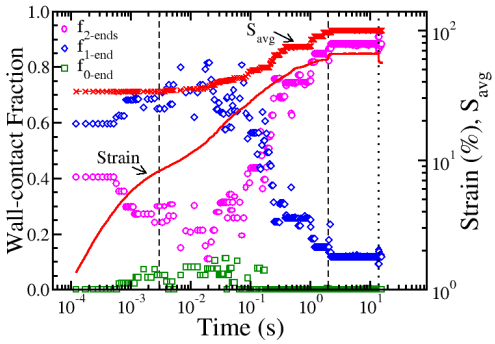

b) $\tau_0 = 250$ Pa; Preassembled chain-like structures.

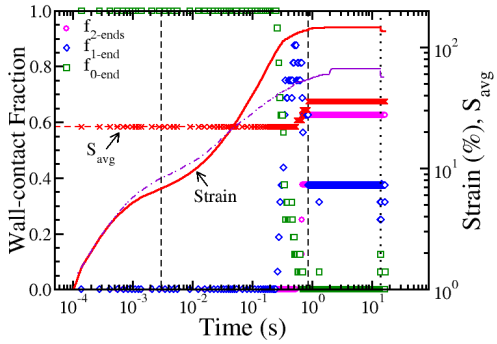

c) $\tau_0 = 1000$ Pa; Random initial configurations.

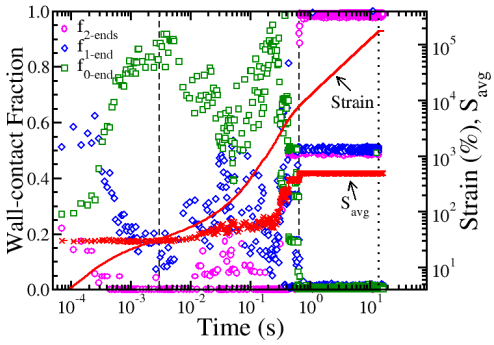

Figure. 7. Shear strain γ, average cluster size S_{avg}, and wall-contact fractions parameters$f_{2-ends,1-end,0-end}$ (see definitions in main text) as a function of time obtained from simulations starting with random initial configurations (a and c) and preassembled array of single-width linear chains (b). In all plots $\phi = 0.05$ and H_0 =173 kA·m^{-1}. The applied stress is $\tau_0 = 250$ Pa for (a) and (b), and 1000 Pa for (c). The strain curve obtained in (a) is also plotted in (b) as the dotted-dashed line for comparison. The vertical dashed lines in the plots are qualitative guidelines for dividing the creep process into three dynamic regimes. The simulation time scales are calculated using an effective carrier liquid viscosity η_s^{eff}=2.0Pa·s.

Figure 7(b) shows such an example by comparing the creep curves obtained using random and preassembled initial configurations at a stress value of $\tau_0 = 250$ Pa. Similar results have been observed in other stress values studied in our simulations. Therefore larger scale ensemble average and bigger simulation box are always desired to get more quantitative results comparable to experiments.

The creep curves in Figure 7 imply that the initial viscoelastic regime ends at a strain value around 0.1 (10%). To check the generality of this observation, we present in Figure 8(a) the simulation results on S_{avg}, λ and f_{2-ends} as a function of the shear strain for various stress values. The mean-square dipole moment λ characterizes the overall structure changes in the system by combining the contributions from the cluster size distribution, partly measured by S_{avg}, and the deformation of these clusters under shear, partly reflected in f_{2-ends}. Apart from the smallest stresses ($\tau_0 \leq 100$ Pa) where the maximum strain is only of a few percentages over the entire creep process, the simulation data on λ at all other stress values initially collapse onto the same constant value, which is determined by the structures formed in the quiescent state, up to a critical shear strain of γ_c = 0.1. Below γ_c, S_{avg} remains stable except for the cases with smallest stress values. On the other hand, the value of f_{2-ends} starts to decrease at smaller γ values under larger step stresses. This is reasonable because the chain or column structures need to tilt or deform more strongly under larger stress in order to generate internal stress comparable to the applied one. These observations reveal that independent of the system parameters, the shear-induced structure changes in MR fluids before a critical strain value of 0.1 only involve the deformation or reorientation of the chains or columns formed in the quiescent state, in absence of structural coarsening. We note that the critical strain value revealed in the creep simulations is in good agreement with the crossover yield strain reported by Segovia-Gutierrez *et al.* (2012), which is defined as the strain corresponding to the equality of the storage and loss moduli G'=G". BD simulations [Wang *et al.* (1997)] and theoretical calculations [Gulley and Tao (1993)] of ER fluids in confined geometry also found a chain breaking behavior at the shear strain of 0.1.

It is interesting to look at the changes of the quantities f_{2-ends} and f_{0-end} in Figure 7(b) where all the preassembled single chains were initially in touch with both walls, giving $f_{2-ends} = 1$ at time $t = 0$ s (not shown in the plot due to the use of logarithmic time scale). This fraction value drops to zero almost instantaneously upon the application of the stress. In the meantime, the value of f_{0-end} jumps from 0 to 1 and remains at 1 for the entire initial regime as well as part of the following retardation regime.

The λ data obtained under different step stresses deviate from each other right after γ_c. For small stress values such as τ_0 = 250 and 400 Pa, both the S_{avg} and f_{2-ends} values begin to increase with the creep strain, which consequently results in the increase of λ. When referring to schematics in Figure 1, it is reasonable to take the instantaneous

strains in these cases as $\gamma_{ic} = 0.1$. At larger stresses the clusters in the system keep roughly the same average size, but experience larger scale tilting or deforming, as implied by the continuous decrease of f_{2-ends}, up to the ending time ($t_{sim} \approx 3\times10^{-3} s$) of the initial response regime. The nonlinear viscoelastic behavior of the system thus lasts beyond the creep strain of 0.1, even though the value of λ starts to decrease after γ_{ic}. In this work, we will determine the initial response regime using the universal ending time as estimated in Figures 5(a) and 6(a), rather than the critical strain value, because the former gives a better specification of the region of viscoelastic behavior.

The creep data in Figure 4(a) seem to suggest that the initial response regime found in simulations ($t_{sim} < 3\times10^{-3}$ s, as a qualitative measurement) corresponds to the region of time $t < 10^{-2}$ s in the experimental curves. In this region the experimental data on the instantaneous viscosity collapse onto a universal curve, which shows a decaying trend at early times [see Figure 5(a)]. But in simulations the $\eta(t)$ data increase with time in the initial response regime. The latter is understood as the result of the decreasing strain rate when the field-induced stress τ_H is approaching to the applied stress value τ_0. In experiments, inertial effects are clearly affecting such a short time measurements as the initial strain response is quadratic in time [Ewoltd and McKinley (2007)].

a) $\phi = 0.05$ b) $\phi = 0.30$

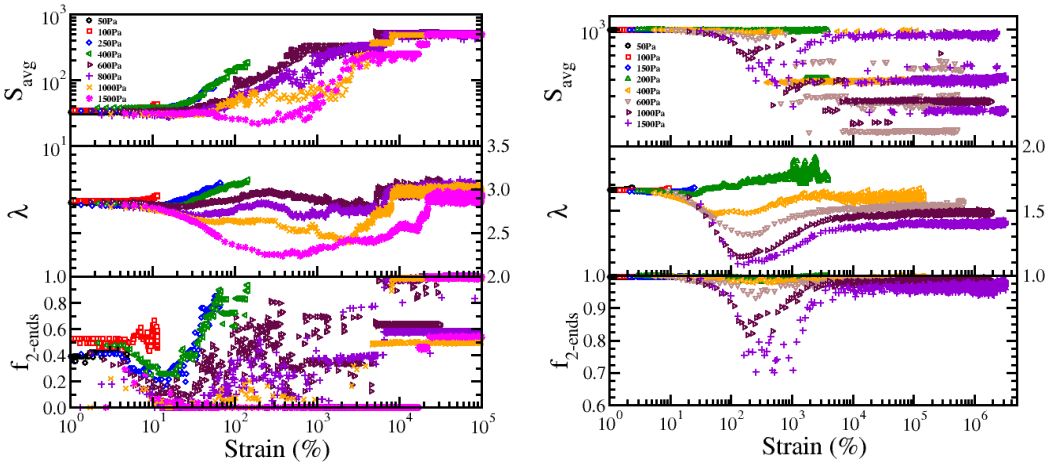

Figure 8. Average cluster size S_{avg}, mean-square strength of the dipole moments λ, and fraction of particles that belong to the clusters attaching to both walls f_{2-ends}, as a function of the shear strain. The system parameters are: a) $\phi = 0.05$; $H_0 = 173$ kA·m^{-1}; $\eta_s = 20$ mPa·s; b) $\phi = 0.30$; $H_0 = 53$ kA·m^{-1}; $\eta_s = 487$ mPa·s.

Retardation regime. After the initial viscoelastic regime, the dynamics of the MR system is controlled by the balance between the applied step stress and the stress contributions from the particle interactions and viscous flow. When the step stress value is very low, e. g. $\tau_0 \leq 400$Pa, the stress contribution τ_H generated by the deformed chain or column structures is comparable to or slightly lower than τ_0. The strain rate $\dot{\gamma}(t)$ as determined by eq. (12) becomes small, which corresponds to a fast growth in the instantaneous viscosity $\eta(t)$ in these cases. The structural changes of the system in this regime can be seen in Figure 7(a) for the case of $\tau_0 = 250$ Pa with random initial configuration. The increase of the average cluster size, S_{avg}, in this regime indicates the slow aggregation of the smaller clusters into larger ones under shear. This increase shows a stepwise manner owing to the discrete merging events in the simulation box. The system with preassembled single chains behaves somewhat differently. Figure 7(b) shows that the chain size remains constant for most of the retardation regime before a quick rise at the very end. This is because these chains are well separated in the initial state. It takes them much longer migration time than the smaller clusters to aggregate with others, because the friction coefficients of the clusters are proportional to their hydrodynamic sizes. The larger creep strain observed in the preassembled chain system can be directly attributed to the thinner chains in comparison with the system starting from random initial configurations.

The mechanical strengths of the column structures get enhanced with the increase in their thickness. As a consequence they become less tilted to sustain the same magnitude of applied stress. This is reflected in the variation of the value of f_{2-ends} which shows an upturn at an intermediate time in this regime, while the values of f_{1-end} and f_{0-end} show inversed trend. When the stress τ_H produced by the thickened structures is large enough to balance τ_0, the creep curve levels off and all the structural parameters reach their plateau values, as can be seen in Figures 4, 7 and 8. The system enters the next relaxation regime. During the period of retardation, the average cluster size in the system with random initial configuration at $\tau_0 = 250$ Pa has increased by a factor of 3 from $S_{avg} = 33.6$ to 99.7. The growth in the cluster thickness can be visualized in the snapshots in Figure 9(a). For the system with preassembled single chains, there is no chain breaking observed. A fraction of the single chains have merged to form double-strand chains. All the chains in the system have at least one of their ends in contact with the walls again, as indicated by the value of $f_{0-end} \sim 0$ at the end of this regime.

Under the action of higher step stresses ($\tau_0 \geq 500$ Pa), the chain or column structures are highly deformed and become very unstable under shear. In the cases of $\tau_0 \geq 1500$ Pa, some of the clusters are found to be broken by shear flow, which is quantified by the decrease in the S_{avg} value in Figure 8(a). More generally, the shear flow forces the columns to change their shapes into thin sheet-like structures oriented in the planes defined by the shear and magnetic field directions. These structures bear less mechanical strength and lower flow resistance in comparison with the thick columns. There is consequently a reduction in the instantaneous stress $\tau_H(t)$, which is most evident in Figure 6(a) for the case of $\tau_0 = 1500$ Pa.

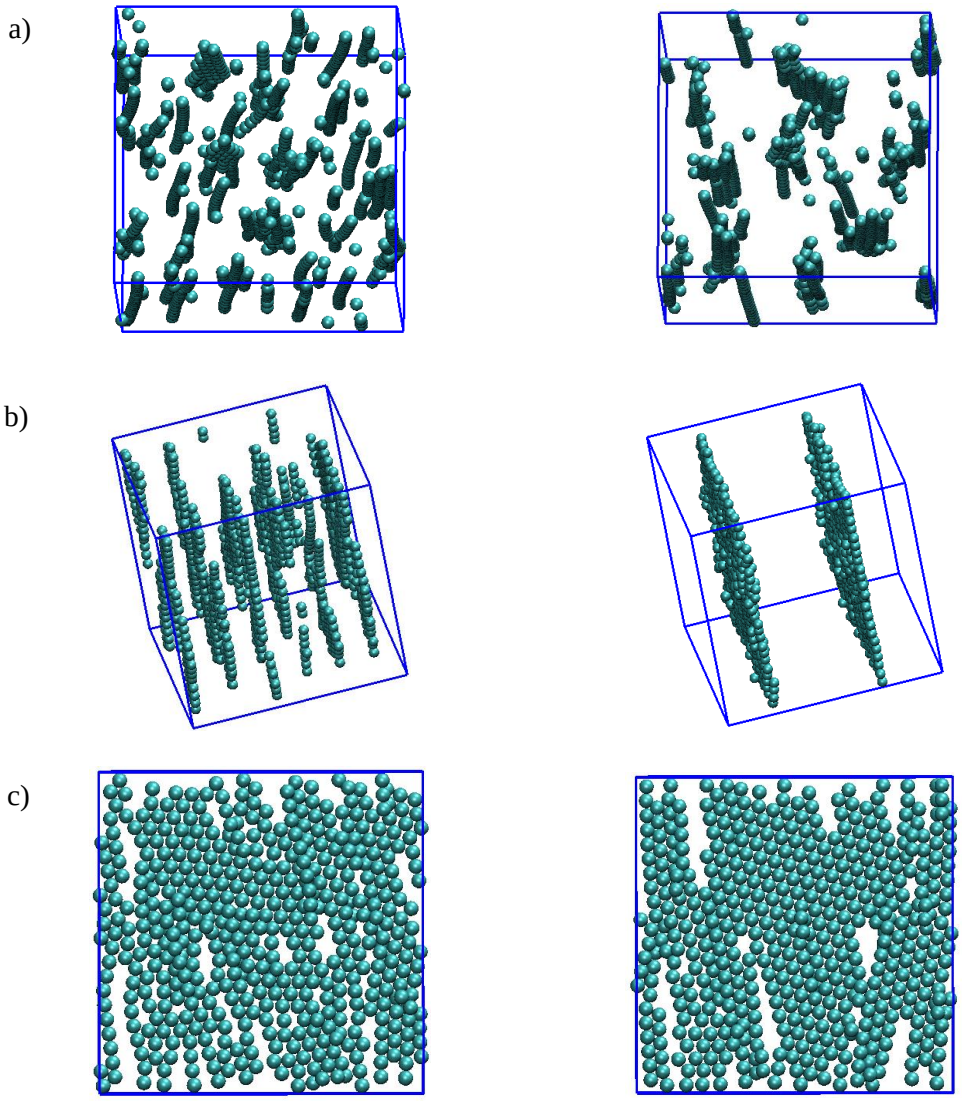

Figure 9. Snapshots of the MR system with $\phi = 0.05$ and $H_0 = 173$ kA·m^{-1} under applied stresses $\tau_0 = 250$ Pa (a) and 1000 Pa (b and c), respectively. In a) the frames are taken at the beginning ($t_{sim} = 0$, left) and end ($t_{sim} = 14$ s, right) of the creep process, while in b) the frames are at $t_{sim} = 124.6$ ms (left) and t_{sim} = 14 s (right), respectively. The configuration at $t_{sim} = 0$ for the case of $\tau_0 = 1000$ Pa (not shown) is very similar to that in the left panel of a). The snapshots in c) are the side views of one of the layers formed at $\tau_0 = 1000$ Pa, taken at time $t_{sim} = 14$ s (left) that is just before the removal of the stress and 16 s (right) that is in the recovery process. The simulation time scales are calculated using an effective carrier liquid viscosity η_s^{eff} = 2.0Pa.s.

The enlarged difference between τ_0 and τ_H leads to the increase in the strain rate $\dot{\gamma}(t)$, as implied by eq. (12). The inflection points in the creep curves and so the peaks in the $\eta(t)$ [$\sim\dot{\gamma}(t)^{-1}$] data at these high stress values thus correspond to the sign change of the derivatives of $\dot{\gamma}(t)$ at the crossover of the initial and retardation regimes. Such inflection points are not clearly visible in the experimental creep curves in Figure 4. The reason may lie in that in the low concentration system these points are located at very short time scales (below 10^{-2}s) which are not accessible by experimental measurements. Figure 5(b) shows that after the peak value $\eta(t)$ obtained at high τ_0 decreases with time until reaching a constant value. This is in contrast to the continuous growth of the $\eta(t)$ data at lower stress values, and so results in a viscosity bifurcation behavior. This observation is in good agreement with experimental results in Figure 5(a). The viscosity bifurcation phenomena have been reported traditionally in pasty materials [see de Vicente and Berli (2012) and references therein].

Figure 7(c) presents the time dependence of the creep strain and various structural parameters for the case of $\tau_0 = 1000$ Pa. The increase in the average cluster size implies that the small pieces of sheet structures gradually merge into large layer structures. This process can be partly visualized in the snapshots in Figure 9(b). The number and thickness of the layers will depend on the volume fraction of the particles. At $\phi = 0.05$ only two single layers are formed at the end of the retardation regime, giving the value of $S_{avg} = 500$. But considering the periodic boundary conditions applied, these layers actually extend infinitely in the shear (x-) direction. The formation of layer or lamellar structures have also been reported in ER and MR fluids under oscillatory shear [Wang *et al.* (1997); von Pfeil *et al.* (2002); Carletto and Bossis (2003)] and in ER and MR fluids under steady shear [Cao *et al.* (2006); Fernández-Toledano *et al.* (2014)]. One driving force for the formation of such structures is to lower the flow resistance.

It is clear from our experimental and simulation results that the MR system behaves qualitatively differently below and above a critical step stress value. The viscosity bifurcation shown in Figures 5(a) and (b) provides a potential pathway to identify the location of this value, or at least narrow down its possible range. In this dilute MR system, the critical stress, which we will notate as τ_{bifur}, is apparently sitting in between 600 and 1000 Pa in experiments and between 400 and 500 Pa in simulations. It is believed that this stress value is closely related to the yield stress estimated from steady shear experiments. We will discuss this relationship in more detail below.

Long-time steady state. In simulations the onset of the steady state is marked by the time scale at which the structural parameters, such as S_{avg} and λ, reach their plateau values. At step stresses below the critical bifurcation value ($\tau_0 \leq 400$ Pa), the increment of the shear strains is basically invisible in the creep curves. The instantaneous viscosity grows continuously by several orders of magnitude. This means that the motion of the upper wall is still not fully stopped, although the strain rate is getting extremely small. There is thus an aging effect in the system under low step stress.

At large stress values ($\tau_0 \geq 500$ Pa), the system enters a constant strain rate regime. The value of the constant rate increases with the increase of the applied stress. From the simulation data in Figures 5(b), 6(a) and 8(a), we see that this regime begins at earlier time, but larger creep strain, for higher τ_0 values. The reason is that under higher stress the particles on average have to travel a longer distance before joining the final stable layer structures. The left panel in Figure 9(c) provides a typical side view of the layer structure. Domains that consist of single chains closely packed into triangular lattices are formed, but there is lack of long-range order in the shear direction. In this regime the upper and lower edges of the two single layers take turns to touch the confining walls. Thus the parameters f_{0-end}, f_{1-end} and f_{2-ends} can only take three discrete values 0, 0.5 and 1.0, see Figure 7(c). For example, when $f_{0-end} = 0$, $f_{1-end} = 0.5$ and $f_{2-ends} = 0.5$, one of the layers is only in contact with one wall, while the other is bridging the two walls.

Recovery process. The recovery behavior of the MR system has strong dependence on the step stress values. As shown in Figure 4(b), there is no strain recovery at stresses above the critical value τ_{bifur}. After the removal of the stress, the shear-induced deformation of the layer structures can be released locally by re-orientation of the individual domains and adjustment of the positions of surrounding particles. So no global elastic force is generated to restore some of the strain. The snapshot on the right panel in Figure 9(c) shows that the domain structures can further develop into larger areas in the absence of the external stress.

The situation is qualitatively different at small stress values. The restoration of the deformed chain or column structures causes an instantaneous recovery of the strain, γ_{ir}. It is followed by a further recovery of magnitude γ_r before reaching the final stable state. The second recovery process is associated with the slow rearrangement of the column structures. In Figure 10 we present experimental and simulation results on the instantaneously recovered strain, γ_{ir}, and the total recovered strain, $\gamma_{ir} + \gamma_r$, as a function of the stress value τ_0. Together with them are the relative fractions of the recovered strains that are calculated as the ratios between the recovered strains and the creep strains achieved right before the removal of the stress. Experiments and simulations are in good agreement. The absolute values of the recovered strains first increase with increasing step stress values, and gradually saturate as τ_0 getting close to the critical value τ_{bifur}. The saturation value of γ_{ir} is about 5 ± 1%, while that of $\gamma_{ir} + \gamma_r$ is around 12 ± 1%. It is interesting to note that the total recovered strain is close to the instantaneous creep strain of $\gamma_c \approx 0.1$ as observed in the initial response regime for these low stress values ($\tau_0 \leq$ 400Pa). The recovered strains can thus be directly attributed to the viscoelastic property of the system consisting of field-induced chain or column structures. On the other hand, the fractions of the recovered strains decay with the increase of the applied stress. In the case of $\tau_0 = 50$ Pa, 31 % of the creep strain is recovered instantaneously and a total of 72 % has been recovered. At $\tau_0 = 400$ Pa, these fractions are only 1.1 % and 8.7 %, respectively.

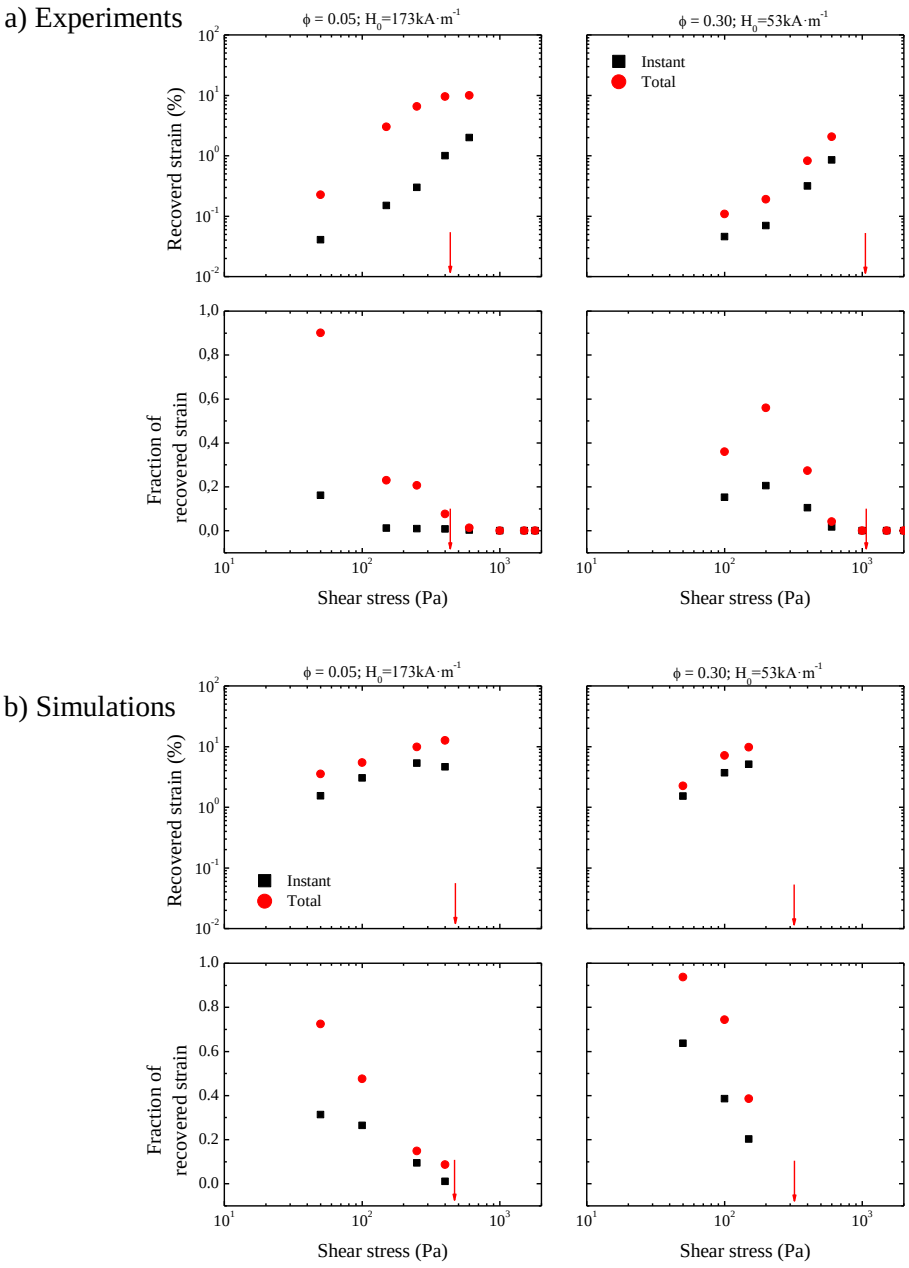

Figure 10. Instantaneous (γ_{ir}) and total ($\gamma_{ir} + \gamma_r$) recovery strains and their ratios to the strain at the onset of the recovery process as a function of applied stress. Vertical arrows correspond to the static yield stress obtained from the extrapolation to zero shear rate of the flow curves in log-log representation, see Figure 12.

The relative magnitude of recovered strain becomes negligible as the stress value approaches τ_{bifur}. These results are again in good agreement with experiments.

High particle volume fraction (ϕ = 0.30)

The experimental and simulation results on the creep-recovery behavior of the system with $\phi = 0.30$ and $H_0 = 53$ kA·m^{-1} are presented in Figures 4-6, 8 and 10-11 for various step stress values. The creep curves in Figure 4 imply that the creep process of the system can still be divided into three regimes, analogous to that observed in the low concentration system. This is further supported by the instantaneous viscosity data in Figure 5 and the structural parameters in Figure 8(b). In the high particle concentration case, both experimental and simulation creep curves obtained at high stress values show the existence of inflection points, which in experiments locate at time scales above 10^{-2}s.

Figure 8(b) shows that the average cluster size at the onset of creep process is $S_{avg} = 1000$, which is equal to the total number of particles in the simulation box. Taking into account the periodic boundary conditions, this means that all the chains or columns in the system are interlinked to form a three-dimensional (3D) percolated gel-like structure. At low stress values ($\tau_0 \leq 150$ Pa), the percolated network survives the entire creep-recovery simulation time. The snapshot of such a gel-like structure taken at the end of the creep process at $\tau_0 = 150$ Pa is given in Figure 11(a). In our simulation model the short-range interactions between particles are purely repulsive. Thus the network formation is solely due to the magnetic interaction forces.

In studying the yielding behavior of MR fluids under steady shear, de Vicente and co-workers (2012) proposed a weak-link mechanism for the systems with particle volume fractions above 10%, in which the interlinks between different clusters are weaker and so broken earlier under shear than the bonds inside the clusters. The particle concentration of $\phi = 0.30$ clearly falls into that regime. To understand the microscopic picture of the weak-link mechanism, a key issue is to find the correct short-range interaction potential between particles in the experimental systems. This will be left for later study.

Similar to the system with $\phi = 0.05$, the general structural properties of the high concentration system remain unchanged up to a creep strain around 0.1 (10 %), see Figure 8(b). The process of stress building-up in this system is demonstrated in Figure 6(b), where the instantaneous stress curves are much smoother than that in the dilute system in Figure 6(a). The reason is that in the initial response regime there are less structural fluctuations in the gel-like network than in the polydispersed chain or column structures. In the retardation regime, the network structure is relatively stable and the average cluster size stays at the constant value of $S_{avg} = 1000$ at step stresses $\tau_0 \leq 150$ Pa.

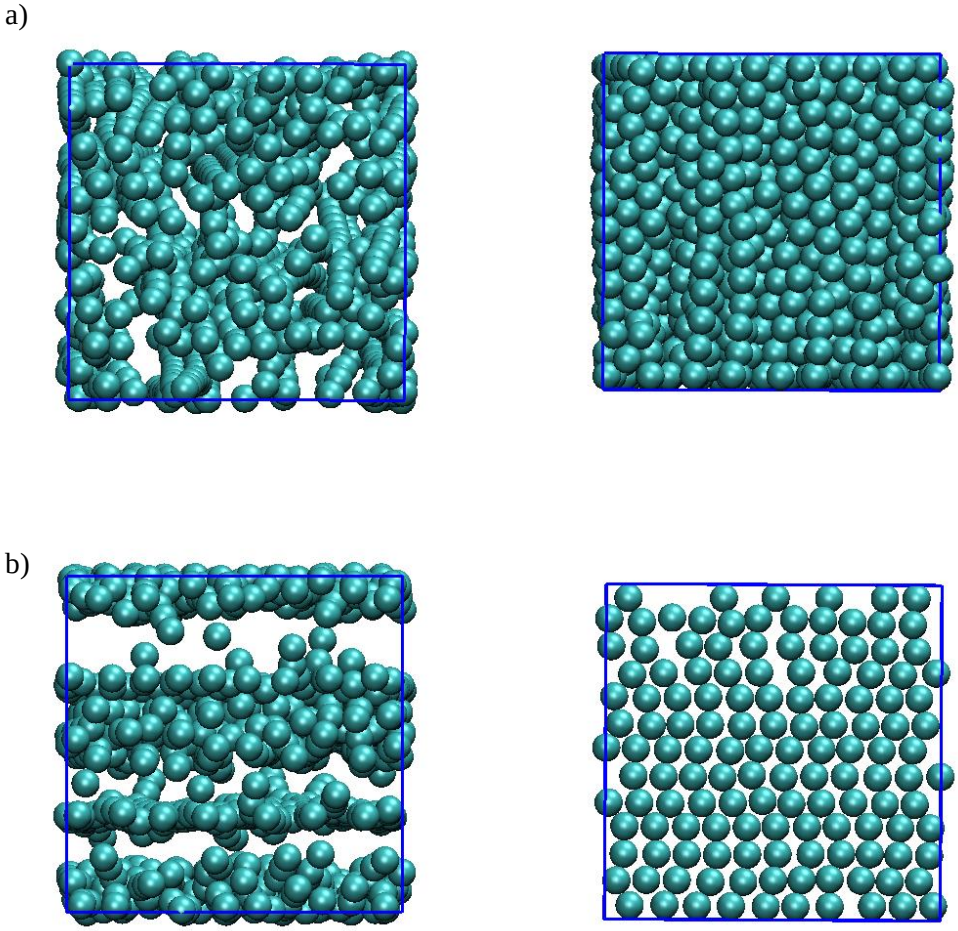

Figure 11. Snapshots of the MR system with $\phi = 0.30$ and $H_0 = 53\text{kA}\cdot\text{m}^{-1}$ under applied stresses $\tau_0 = 150$ Pa (a) and 1000 Pa (b), all taken at the end of the creep process. The snapshots in the left panels are the top views along the magnetic field direction, while those on the right are the side views in the x-z (shear–field) plane. In (b) only one layer is shown where the particles form arrays aligning along the shear (horizontal) direction.

But at higher stresses the value of S_{avg} starts to decrease due to the splitting of the 3D network into lamellar structures with various thicknesses, see Figure 11(b) for an example. This structure transition leads to a reduction in the overall mechanical strength of the system, as reflected in the decrease of the instantaneous stress τ_H in the top set of data points in Figure 6(b) where $\tau_0 = 600$ Pa. As a result, a constant rate flow is

eventually developed in the system. In this constant rate regime, the lamellar structures still undergo splitting and recombining by exchanging layers over time. The value of S_{avg} thus jumps in between several discrete values, especially at the highest stresses studied. The right panel of Figure 11(b) presents the side view of a single layer taken from a thicker lamellar structure formed at $\tau_0 = 1000$ Pa. Different from the domain formation found in Figure 9(c), the particles here arrange into linear arrays aligning along the shear direction. This difference can be understood from the relatively low magnetic field strength ($H_0 = 53$ kA·m^{-1}) in this case. The destruction of the chain or column-like structures along the field direction also weakens the mutual magnetization effect among the particles. The plateau values of λ in this regime are lower than their initial values at the onset of the creep process.

The experimental and simulation data on the instantaneous viscosity in Figures 5(c) and (d) also demonstrate a bifurcation behavior at a critical stress. Experiments locate this value in between 400 Pa and 1000 Pa. On the other hand, simulations suggest that the value is located in between $\tau_0 = 150$ Pa and 400 Pa. Only when the step stress is below this critical value, there is a partial recovery of the strain. The absolute values of the instantaneous and total recovered strains are close to that obtained in the low density system with $\phi = 0.05$, see Figure 10. The saturation value of the total recovered strain is again around 10 %. The fractions of the recovered strains are relatively high in this case, but still decays towards zero as the stress approaches to the critical value. Experiments and simulation data are again in good agreement.

Steady shear

The critical stress value at which the viscosity bifurcation is observed in creep experiments is considered to be related to the yield stress estimated from steady shear measurements. Therefore we have performed two sets of steady shear experiments and simulations using the same system parameters as studied in the creep-recovery simulations. The time-averaged simulation results on the field-induced stress, τ_H [Eq.(9)], and the total shear stress, $\tau_H + \eta_s^{eff}\dot{\gamma}$ as used in Eq.(10), are plotted in Figure 12 as a function of the shear rate $\dot{\gamma}$. For comparison, we have also included the creep simulation data at high step stresses where the strain rates were obtained by linear fitting to the constant rate regime of the creep curves. The creep data are related to the total shear stresses measured in steady shear. As expected, the results obtained from these two different types of simulations collapse onto a universal curve and so can be used together for data analysis.

The shear stress data of MR fluids are generally fitted to the Bingham plastic model, $\tau(\dot{\gamma}) = \tau_y + \eta_p\dot{\gamma}$, to give the yield stress τ_y. But as discussed in the Introduction, the results heavily rely on how the experimental measures are carried out. This is one of the main reasons for studying the creep-recovery behavior. Instead of trying to find the exact value of τ_y from the steady shear experiments, we use the concept of Bingham

model for estimating the time scaling factor to map the simulation data to real time units. According to this model, the shear stress grows linearly with the shear rate, at least in the high $\dot{\gamma}$ region. The slope of the $\tau(\dot{\gamma})$ line is the so-called plastic viscosity η_p which is determined by the viscosity of the carrier liquid and the particle loading. As shown in Figures 12(a) and (b) by the dashed lines, we fit the experimental data points at high shear rates to the Bingham formula to get the values of η_p, which are found to be 2.0 ± 0.2Pa·s in both systems. Since the plastic viscosity can also be affected by the residual interparticle aggregation, the similar η_p values found at different particle concentrations may indicate that the particle clusters are not completely disaggregated even at high shear rates. Experimental evidences on this effect are presented in Figure 12(c) and discussed below. For the purpose of making convenient but not fully quantitative comparison between simulation and experimental data, we consider that all the hydrodynamic and particle aggregation effects have been implicitly included in the η_p values and so set the effective carrier liquid viscosity $\eta_s^{eff} = \eta_p$ (2.0Pa·s) in both systems. By replacing η_s with η_s^{eff} in Eq.(8) and mapping the dimensionless simulation time to real time units by multiplying $\tilde{t} = 16\eta_s^{eff}/\mu_0\mu_s\beta^2H_0^2$, a reasonably good match between the experimental and simulation shear stresses is achieved in the high $\dot{\gamma}$ region, see Figure 12. The corresponding time scaling factors are $\tilde{t} \approx 1.4$ms at $\phi = 0.05$ and $H_0 = 173$ kA·m^{-1} and 11ms at $\phi = 0.30$ and $H_0 = 53$ kA·m^{-1}. These $\tilde{t}$ values have been used to scale all simulation times presented in the current work. We note that this time mapping approach involves some crude approximations. First of all the viscous friction experienced by the particles, as used in the particle equation of motion [eq.(3)], is mainly determined by the carrier liquid viscosity η_s, rather than the effective value η_s^{eff}. Secondly the exact value of η_p depends on the shear rate range used for the fitting. Therefore the horizontal shift of the simulation time scales could not be taken as quantitatively well defined. All comparisons between experimental and simulation results should remain at the qualitative level.

We have performed the Bingham model fitting to the simulation results in Figures 12(a) and (b), which include both the steady-shear and creep simulation data points. The yield stress values are found to be $\tau_y = 475 \pm 20$ Pa for the system with $\phi = 0.05$ and $H_0 = 173$ kA·m^{-1} and 317 ± 15 Pa for the system with $\phi = 0.30$ and $H_0 = 53$ kA·m^{-1}. These values are marked by vertical arrows on the abscissa axis in Figure 10.

They fall well into the range of the critical stress as estimated from the viscosity bifurcation data in Figure 5. This observation thus supports the intrinsic correlation between the yield stress and the critical stress in creep experiments.

It is evident in Figure 12 that although the $\tau(\dot{\gamma})$ curves obtained in simulations and experiments show qualitatively consistent behavior, the simulation data are significantly lower than the experimental values, particularly in the high concentration case. As mentioned before, this discrepancy can be partially attributed to the simplified simulation model. For the system with $\phi = 0.05$ and $H_0 = 173$ kA·m^{-1}, the mean-

square dipole moment of the particles is found to be $\lambda = 3.0 \pm 0.2$. It means that the consideration of the local field correction in eq. (5) has already improved the simulation data by at least a factor of 3 in comparison with the point dipole approximation with fixed field strength H_0. The mutual magnetization effect is relatively weak in the dense system with $\phi = 0.30$ and $H_0 = 53$ kA·m^{-1}. The value of λ calculated from the gel-like networks in the quiescent state is 1.7 ± 0.1, which is apparently smaller than that found in the dilute system consisting of separated chain or column structures.

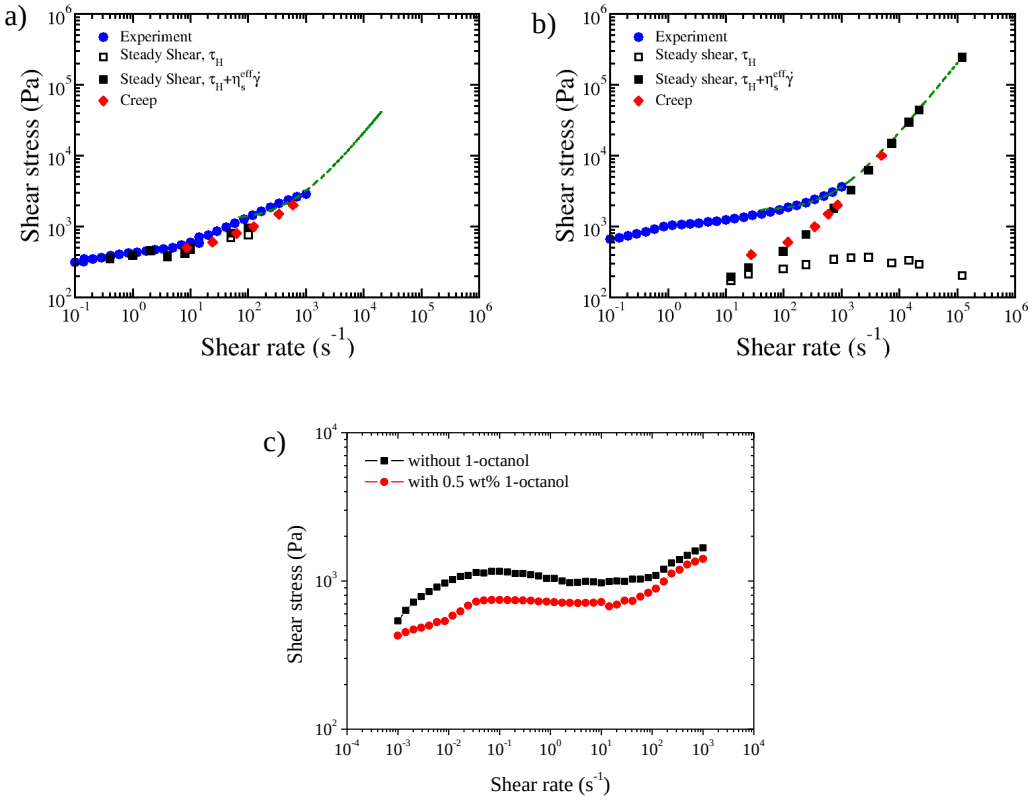

Figure 12. Shear stress as a function of shear rate obtained from the steady-shear and creep simulations. In the steady-shear case, the contributions from the particle interactions alone, τ_H, are also given for reference. The steady-shear experimental data are also included for comparison. The system parameters are a) $\phi = 0.05$, $H_0 = 173$ kA·m^{-1} and silicon oil with $\eta_s = 20$ mPa·s; b) $\phi = 0.30$, $H_0 = 53$ kA·m^{-1} and silicone oil with $\eta_s = 487$ mPa·s; c) $\phi = 0.30$, $H_0 = 53$ kA·m^{-1} and polyalphaolefin oil with $\eta_s = 6$ mPa·s without and with (5 wt%) 1-octanol additive. The simulation shear rates are calculated using an effective carrier liquid viscosity $\eta_s^{eff} = 2.0$Pa·s. The dashed lines are Bingham model fittings to the experimental data points at high shear rates.

As shown in Figure 11(b), the particles in the shear-induced lamellar structures are arranged into arrays aligning along the shear direction, rather than along the magnetic field direction. As a consequence, the data in Figure 12(b) show that the stress τ_H generated by the magnetic interactions between particles reaches a plateau value around 370 Pa, and then slowly increases at higher shear rates. The total shear stresses in these cases are thus dominated by the viscous contribution $\eta_s^{eff}\dot{\gamma}$. This explains why the Newtonian viscosity obtained from the linear fitting to the Bingham model in this case is basically equal to the effective viscosity of the carrier liquid.

The relatively large difference between the experimental and simulation steady shear data in Figure 12(b) can also be correlated to the facts that particles at this concentration are very close to each other and the field strength is very small. These two circumstances make the short-range interparticle interactions, such as remnant magnetization and/or colloidal forces, to play a key role here. One consequence is that some residual interparticle aggregation may exist even at rest (before shearing the sample), which would necessarily result in an extra-contribution to the shear stress as actually observed. The residual interparticle aggregation is present in most of MR fluid formulations and manifests more clearly at large particle loadings or smaller interparticle distances. Figure 12(c) shows the experimental steady shear stress data obtained from MR fluid with a different formulation where a fraction of $\phi = 0.30$ magnetic particles are dispersed in polyalphaolefin oil (PAO) with and without 1-octanol additive. The additive is introduced to help reducing the short-range attractions and consequently the residual aggregations among the particles. The shear stresses obtained from the MR system with additives are clearly lower than that of its counterpart without additives, which can in part explain the discrepancy between the experimental and simulation data in Figure 12(b). Creep experiments on these systems (not presented) have also shown that at a given applied stress the MR fluid with additives achieves larger steady-state strain values or smaller viscosities due to the suppression of residual interparticle aggregation.

CONCLUSIONS

Independently of the particle loading, three regimes are observed in the creep curves: i) Initial response regime where the systems behave in the viscoelastic region and the average cluster size remains constant. In this region field-induced structures deform and reorientate under shear and the material functions collapse onto a universal curve whatever the stress value; ii) Retardation regime where the system behavior results from the balance between the applied stress and the stress contributions from the particle interactions and viscous flow. In this regime, small clusters begin to aggregate forming larger ones but less tilted with respect to the magnetic field direction. For large enough stresses, structures become unstable under shear and eventually assemble into sheet-like or lamellar structures oriented in the planes defined by shear and magnetic field

directions; iii) Long time steady state where structural parameters reach plateau values. In the case of large enough stress values the system enters a constant strain rate regime and viscosity bifurcation occurs.

The recovery behavior strongly depends on the stress level. For low stress levels below the bifurcation value, the MR fluid is capable to recover part of the strain. In this case strain increases with increasing stress and gradually saturate. Instantaneous and total recovered strains are in good agreement between experiments and simulations. For stresses larger than the bifurcation value, the recovery is negligible as a result of irreversible structure rearrangements.

As expected, long time creep simulation data are consistent with steady shear flow. In the case of $\phi = 0.05$ MR fluids, the comparison between experiments and simulations is good. However, for $\phi = 0.30$ MR fluids the agreement is not so good because this system is more sensitive to interparticle (remnant and colloidal) forces as the concentration is large and the field strength is low. In general, a good qualitative agreement is found between experiments and simulations.

REFERENCES

Bozorth, R. M., "Ferromagnetism, " Wiley - IEEE Press, 1993.

Cao, J. G., J. P. Huang, and L. W. Zhou, "Structure of electrorheological fluids under an electric field and a shear flow: experiment and computer simulation, " J. Phys. Chem. B 110, 11635 (2006).

Carletto, P., and G. Bossis, "Field-induced structures and rheology of a magnetorheological suspension confined between two walls," J. Phys.: Condens. Matter 15, 1437-1449 (2003).

Carlson, D. J., "Critical factors for MR fluids in vehicle systems," Int. J. Vehicle Des. 33, 207-217 (2003).

de Vicente J., and C. L. A. Berli, "Aging, rejuvenation, and thixotropy in yielding magnetorheological fluids," Rheol. Acta 52, 467 (2013).

de Vicente, J., D. J. Klingenberg, and R. Hidalgo-Álvarez, "Magnetorheological fluids: a review," Soft Matter 7, 3701-3710 (2011).

Doi, M., and S. F. Edwards, “The theory of polymer dynamics”, Oxford Science Publications (1986).

Ewoldt, R., and G. H. McKinley, "Creep ringing in rheometry or how to deal with oft-discarded data in step stress tests," Rheology Bulletin 76(1), 4-24 (2007).

Fernández-Toledano, J. C., J. Rodríguez-López, K. Shahrivar, R. Hidalgo-Álvarez, L. Elvira, F. Montero, and J. de Vicente, "Elucidating the origin of the two-step yielding in magnetorheology," Submitted.

Ginder, J. M., "Behavior of magnetorheological fluids," MRS Bulletin, August, 26-29 (1998).

Gorodkin, S. R., R. O. James, and W. I. Kordonski, "Magnetic properties of carbonyl iron particles in magnetorheological fluids," J. Phys.: Conference Series 149, 012051 (2009).

Gulley, G. L., and R. Tao, "Static shear stress of electrorheological fluids, " Phys. Rev. E 48, 2744 (1993).

Klingenberg D. J., "Effects of body forces on electro- and magnetorheological fluids," Appl. Phys. Lett. 86, 104101 (2005).

Klingenberg, D. J., "Simulation of the dynamic oscillatory response of electrorheological suspensions: Demonstration of a relaxation mechanism," J. Rheol. 37, 199 (1993).

Klingenberg, D. J., F. van Swol, and C. F. Zukoski, "The small shear rate response of electrorheological suspensions. I. Simulation in the point–dipole limit," J. Chem. Phys. 94, 6160 (1991).

Larson, R. G., "The structure and rheology of complex fluids", Oxford University Press, Oxford (1999).

Li, W. H., H. Du, G. Chen, and S. H. Yeo, "Experimental investigation of creep and recovery behaviors of magnetorheological fluids," Materials Science and Engineering A333, 368-376 (2002).

Otsubo, Y., and K. Edamura, "Creep behavior of electrorheological fluids," J. Rheol. 38, 1721-1733 (1994).

See, H., and M. Doi, "Shear resistance of electrorheological fluids under time-varying electric fields," J. Rheol. 36, 1143 (1992).

See, H., R. Chen, and M. Keentok, "The creep behaviour of field-responsive fluids," Colloid Polym. Sci. 282, 423-428 (2004).

Segovia-Gutierrez, J. P., C. L. A. Berli, and J. de Vicente, "Nonlinear viscoelasticity and two-step yielding in magnetorheology: A colloidal gel approach to understand the effect of particle concentration," J. Rheol. 56, 1429-1448 (2012).

Verberg, R. and I. M. de Schepper, " Viscosity of colloidal suspensions," Phys. Rev. E 55, 3143 (1997).

von Pfeil, K., M. D. Graham, D. J. Klingenberg, and J. F. Morris, "Pattern Formation in Flowing Electrorheological Fluids," Phys. Rev. Lett. 88(18), 188301 (2002).

Wang, Z. W., "Simulation of field-induced structural formation and transition in electromagnetorheological suspensions," Phys. Rev. E 61, 6837 (2000).

Wang, Z. W., Z. F. Lin and R. B Tao, "Many-body effect in electrorheological responses," Int. J. Modern Phys. B. 10, 1153 (1996).

Wang, Z. W., Z. F. Lin, and R. B Tao, "Structure and viscoelasticity of an electrorheological fluid in oscillatory shear: computer simulation investigation," J. Phys. D: Appl. Phys. 30, 1265 (1997).

Wereley, N. M., "Magnetorheology: Advances and Applications," Royal Society of Chemistry (2013).

CHAPTER 4

Ferrofluid lubrication of compliant polymeric contacts: effect of non-homogeneous magnetic fields

K. Shahrivar and J. de Vicente

This article is published in: Tribology Letters, 56.2 , 281-292, 2014.

Abstract

This paper demonstrates a new route to control friction in the isoviscous elastic lubrication regime between compliant point contacts. For this aim it is proposed the superposition of non-homogeneous magnetic fields in ferrofluid lubricated contacts. Under appropriate conditions a friction reduction is observed by simply displacing the magnetic field distribution in the flow direction towards the inlet of the contact. This friction reduction is associated to a lower Couette friction contribution as a result of the fact that surfaces become more separated under field. Experiments and simulations are in good qualitative agreement.

INTRODUCTION

Ferrofluids are stable (Brownian) colloidal dispersions of (dipolar) magnetic nanoparticles [1]. In the absence of magnetic fields they behave as conventional Newtonian fluids. However, a magnetic body force appears under the presence of magnetic field gradients. This field-induced body force locally increases the magnetic pressure within the ferrofluid and promotes its migration towards the regions of positive field gradient. Interestingly, the viscosity of well-formulated ferrofluids does not change significantly with the superposition of a magnetic field in contrast to the behavior exhibited by magnetorheological fluids [2,3]. Recent studies suggest that, under the appropriate conditions, magnetic fluids improve the contact load capacity and help preventing leakage at high operating speed or under the action of gravity [reference 4 and references therein].

Currently, there is growing interest in the isoviscous-elastic or 'soft-elastohydrodynamic' lubrication (soft-EHL) regime [5-11]. This occurs in the lubricated contact of non-conforming bodies when the contact pressure is high enough to cause considerable elastic deformation of one or both of the surfaces but not so high as to produce a significant increase of lubricant viscosity in the contact inlet and thereby influence fluid entrainment. In this work we are interested in the lubrication of surfaces having low elastic modulus. Traditionally, the modeling of isoviscous-elastic lubrication regime has focused almost entirely on the prediction of film thickness separating the lubricating surfaces. Only recently, interest has risen with regards to friction [5, 12-14].

Most of the past efforts have been devoted to understand the bulk rheological behavior of ferrofluids in the presence of viscometric flows under external magnetic fields. However, from a practical point of view, it is also interesting to study their thin-film rheological and tribological properties as most of the applications concern strongly confined geometries under exceedingly large shear rates 10^4–10^6 s^{-1} [3]. Hence, the goal of this manuscript is to study the tribological performance of ferrofluids in fully lubricated compliant point contacts. Especial emphasis is paid to the effect of non-homogeneous magnetic fields along the flow direction in the full film lubricating properties. Experimental Stribeck's curve is presented in the absence and presence of magnetic fields. Also, the full numerical solution of the ferrohydrodynamic Reynolds equation together with elasticity equation and Finite Element Method (FEM) calculations are carried out and compared to experimental data.

BACKGROUND

Friction coefficient μ in compliant contacts is governed by the $U\eta/W$ ratio, where U is the entrainment speed, η is the Newtonian viscosity of the lubricant in the contact, and

W is the load applied to the contact [7]. In the present work (pure sliding contacts), the entrainment speed is simply given by $U = V/2$, where V is the sliding speed. Generally speaking, the friction has two contributions. On the one hand, a so-called "sliding friction" which arises from relative motion of the contacting surfaces. This "sliding friction" originates from adhesion of the contacting asperities at low $U\eta$ and from Couette flow of lubricant film in the contact at large $U\eta$. On the other hand, a so-called "rolling friction" which results from the movement of the surfaces relative to the contact. This "rolling friction" has two main components, one contribution arising from deformation/elastic hysteresis independent of $U\eta$, and the other coming from Poiseuille flow of the lubricant in the contact at large $U\eta$. In a pure-sliding unidirectional compliant contact (slide-to-roll ratio, $SRR = 2$) both contributions to the friction (i.e. "sliding" and "rolling") are present and need to be addressed. Therefore, Couette, Poiseuille and elastic hysteresis terms need to be calculated to determine the total friction in these lubricated contacts.

From the Reynolds and elastic deformation equations, the Couette contribution to the friction coefficient in compliant contacts operating in the isoviscous elastic lubrication regime can be computed by integrating the Couette shear stress over the lubricant-filled region of the contact:

$$\tau_C = -\frac{SRR \cdot U\eta}{h} \tag{1}$$

Here, h is the film thickness between the compliant surfaces. The Couette contribution from the shear stress generated in the fluid film is due to surfaces moving relative to each other. Couette forces have different sign for each surface depending upon the sign of the sliding speed.

The Poiseuille contribution to the friction coefficient is calculated by integrating the Poiseuille shear stress over the lubricant-filled region of the contact:

$$\tau_P = -\frac{h}{2}\frac{\partial p}{\partial x} \tag{2}$$

The Poiseuille contribution arises from the fluid film pressure gradient in the entrainment direction $\partial p/\partial x$. It contributes always with a negative sign and hinders the surface moving relative to the contact. It acts in the same direction on the two surfaces trying to stop them moving through the contact [6]. Regression equations (for Newtonian fluids) were developed in reference [6] to predict the separate Couette and Poiseuille flow contributions to the friction coefficient μ_C and μ_P, respectively. In particular, regression equations were obtained to within 4% confidence over the range of

$\overline{U} = 1.5 \times 10^{-7}$ to $\overline{U} = 4 \times 10^{-5}$ and $\overline{W} = 7.5 \times 10^{-4}$ to $\overline{W} = 2.5 \times 10^{-2}$. According to these authors:

$$\mu_C = SRR(3.8\overline{U}^{0.71}\overline{W}^{-0.76} + 0.96\overline{U}^{0.36}\overline{W}^{-0.11}) \quad (3a)$$

$$\mu_P = 1.46\overline{U}^{0.65}\overline{W}^{-0.70} \quad (3b)$$

Here $\overline{U} = \frac{U\eta}{E'R'}$, $\overline{W} = \frac{W}{E'R'^2}$, E' is the reduced elastic modulus ($\frac{2}{E'} = \frac{1-\nu_1^2}{E_1} + \frac{1-\nu_2^2}{E_2}$) and R' is the reduced radius in the entrainment direction ($\frac{1}{R'} = \frac{1}{R_{x1}} + \frac{1}{R_{x2}}$). From these equations it is clearly seen that the Poiseuille contribution does not depend on SRR (c.f. Equation 3b).

For a sphere on flat the friction coefficient contribution coming from elastic hysteresis (i.e. deformation energy losses) can be estimated as follows:

$$\mu_D = \alpha \frac{3}{16} \frac{a}{R} \quad (4)$$

where a is the Hertzian contact radius, R is the sphere radius, and α is the loss factor. The loss factor, $\alpha = k\pi tan\delta$, where $k \in [1,3]$ is a constant and $tan\delta$ the loss tangent, is the ratio of energy dissipated to the average energy stored per cycle in a deformation process. Previous works have demonstrated that as a first approximation the loss factor can be assumed to be constant [7]. However, α is not strictly constant and a slightly better agreement between experiments and simulations can be achieved if the frequency dependence of the elastic properties of the compliant surfaces is considered in the analysis [11].

With this in mind, the total friction coefficient in a Newtonian fluid-lubricated compliant contact working in the isoviscous elastohydrodynamic regime can be estimated as $\mu = \mu_C + \mu_P + \mu_D$. At this point is worth to note that the contribution from interfacial adhesion is negligible if a full film lubricating layer exists and therefore, this contribution is not considered in the lubricating behavior at large $U\eta$ values which is the case of interest in this work.

EXPERIMENTAL

Materials

Silicone oils of different viscosities, in the range from 0.1 Pa·s to 10 Pa·s, were bought from Sigma-Aldrich. These oils were used in this work as reference model fluids. They behave as Newtonian fluids up to shear rates of the order of 10^4 s^{-1}. The ferrofluid used in this work was purchased from Ferrotec (APG series). This particular APG series is typically used in audio speaker applications. The ferrofluid is a magnetite nanoparticle dispersion based on a synthetic hydrocarbon carrier. It has a saturation magnetization of 24.3 ± 0.7 $kA \cdot m^{-1}$ and Newtonian shear viscosity 560 mPa·s. Considering a particle size lognormal distribution and using the Langevin function, a value of 9 nm was obtained for the average nanoparticle diameter with a polidispersity of 20 %. Particle volume fraction is around 5.5 vol% assuming a saturation magnetization for bulk magnetite of 447 $kA \cdot m^{-1}$ [15].

We studied three different compliant contacts always operating in the isoviscous elastic regime. The polymeric materials used were: Polyoxymethylene (acetal resin; POM), Polytetrafluoroethylene (PTFE) and a silicon elastomer (PDMS). POM possesses high tensile strength, creep resistance and toughness. It also exhibits low moisture absorption. It is chemically resistant to hydrocarbons, solvents and neutral chemicals. These properties along with its fatigue endurance make POM ideal for many industrial applications such as in the automotive, appliance, construction, hardware and electronics. PTFE is used here as compliant material because it exhibits appreciably lower friction coefficients than most other polymers and have important applications as solid lubricant and bearing material. The more compliant surfaces employed in this manuscript were made of PDMS. This elastomer material has been recently used as model system to understand the lubrication behavior in compliant contacts [5-11,16]. The tribopairs investigated in this work comprise POM-POM, PTFE-PTFE and PDMS-PDMS contacts.

POM and PTFE specimens where obtained from Goodfellow. On the contrary, PDMS tribopairs where prepared in-situ using conventional techniques. Briefly, PDMS specimens were fabricated from a two-component silicone elastomer kit (Sylgard^{TM} 184, Dow Corning); the base and curing agent in a mass ratio of 10:1. The plates were made by casting a 3 mm thick sheet in a prefabricated mould. After allowing any air bubbles to escape using a vacuum chamber, the PDMS was cured for 8 h in the vacuum chamber at 70 ºC. After cooling overnight, the PDMS sheet was removed from the mould and plates of size 3 mm × 6 mm × 16 mm were peeled off. In a similar way, PDMS spheres were cast with a radius of 6.35 mm. Table 1 contains elastic modulus, Poisson ratio and surface characteristics of all the surfaces employed in this work.

Table 1. Physical characteristics of the tribopairs studied in this work. a from reference [28], b from reference [29], and c from reference [30]. Also included in the table is the Lambda parameter corresponding to the minimum friction in the Stribeck curves.

	POM	PTFE	PDMS
Youngs modulus (Pa)	3.1×10^9	0.5×10^9	1.84×10^6
Poisson ratio (-)	0.350	0.460	0.500
Loss tangent, $\tan(\delta)$ (-)	0.0111[a]	0.07[b]	0.0716[c]
Hertzian radius, a (μm)	2.33×10^{-4}	4.13×10^{-4}	1.22×10^{-3} (F_N = 1 N)
			1.94×10^{-3} (F_N = 4 N)
Maximum pressure, p_{max} (Pa)	4.13×10^7	1.31×10^7	1.50×10^5 (F_N = 1 N)
			2.38×10^5 (F_N = 4 N)
R_q Plate (μm)	0.263	0.700	0.190
R_q Ball (μm)	0.713	0.510	0.216
R_q Average (μm)	0.759	0.866	0.287
Lambda parameter, Λ (-)	10.6	9.3	6.3

Apparatus

Friction measurements were carried out in a non-conforming ball-on-three-plates contact using a modified form of the MCR 302 Rheometer (Anton Paar). The schematic diagram of the test set-up is shown in Figure 1a. In this set-up, a ball (radius R = 0.25 inch = 6.35×10^{-3} m) is pressed at a given normal force F_N against three plates that are mounted on a movable stage [17-19]. As a result, the same load is acting evenly on all three frictional pairs. Next, the ball is commanded to rotate at an increasing sliding speed V while the plates are held stationary, at rest. This generates three sliding point contacts. In this device, the sliding speed V is related to the angular velocity (ω, rad/s) through $= R\omega/\sqrt{2}$.

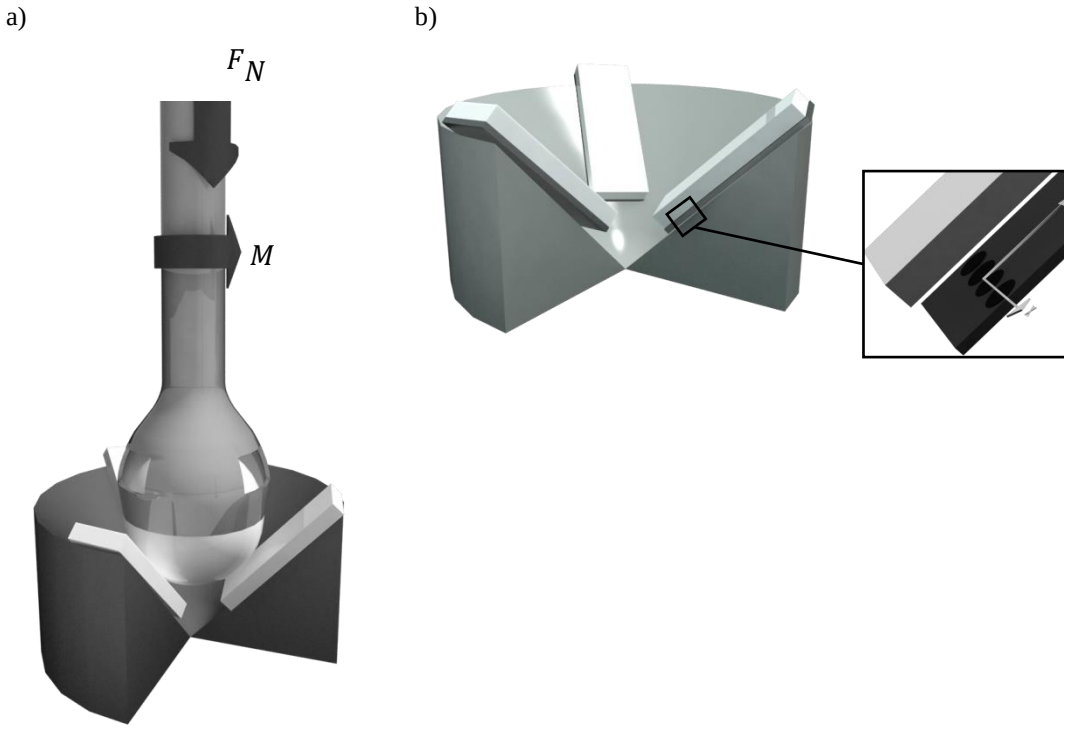

Figure 1. Schematics of the ball-on-three-plates contact for tribology tests under the absence and presence of magnetic fields. a) Schematics of the ball-on-three plates contacts without magnetic fields applied. b) Detail of the holder adaptation employed to superimpose non-homogeneous magnetic fields.

Geometrical arguments reveal that the normal force is related to the total normal load, F_L, acting on the plates as:

$$F_L = \sqrt{2}F_N \tag{5}$$

On the other hand, the torque sensed by the ball, T, is related to the total frictional force, F_F, using the following expression:

$$F_F = \frac{\sqrt{2}T}{R} \tag{6}$$

Finally, the friction coefficient μ can be simply obtained from Equations 5 and 6 as follows:

$$\mu = \frac{F_F}{F_L} = \frac{T}{F_N R} \tag{7}$$

In this study, the applied loads ranged from $F_N = 1N$ to $F_N = 10N$. All tests were carried out at a temperature of 25 °C and at a constant slide-to-roll ratio of $SRR = 2$ (i.e., pure sliding conditions). In order to generate magnetic fields, the set-up was modified by introducing 1 mm thickness spacers underneath 2 mm thickness polymeric plates (see Figure 1b). These spacers were used to hold cylindrical Neodymium-Iron-Boron (NdFeB) permanent magnets (one for each spacer) in contact with the polymer (PDMS) plates at the required position.

CALCULATION OF FRICTION IN FERRO-ISOVISCOUS-ELASTIC LUBRICATION REGIME

Simulation of magnetic field distribution by FEM

The magnetic field generated by the cylindrical NdFeB magnets (2 mm diameter and 1 mm height) placed underneath the point contacts was simulated using finite element methods. For this aim, the finite element method magnetics (FEMM) software [20] was employed to calculate the magnetic field distribution, at the contact region, i.e. at a distance of 1.75 mm over the upper surface of the magnet. This distance is slightly smaller than the 2 mm thickness of the polymer specimen because of the indentation correction. The problem solved using FEMM is graphically depicted in Figure 2a. Axisymmetric mode was used together with *Asymptotic Boundary Conditions* (ABC) in the circular outer edge of the computational domain, that approximates the impedance of an unbounded, open space. This makes the simulation act as if the analysis were made on a truly unbounded domain. The mesh size was optimized to get accurate results. Data reported here correspond to a mesh size of 0.05 and a computational box size that was at least one order of magnitude larger than the magnet size to further minimize finite size effects. The magnetic character of the NdFeB magnet was simulated taking the particular N value for the magnet (N = 48). The coercitivity of the magnets was calculated as $\mathrm{H_C} = 155319 \cdot \frac{\mathrm{A}}{\mathrm{m}} \cdot \sqrt{\mathrm{N}}$ and the relative magnetic permeability was fixed at 1.05. Figure 2 also shows the vertical magnetic field strength (Figure 2b) and magnetic field gradient (Figure 2c) along the horizontal segment represented in Figure 2a.

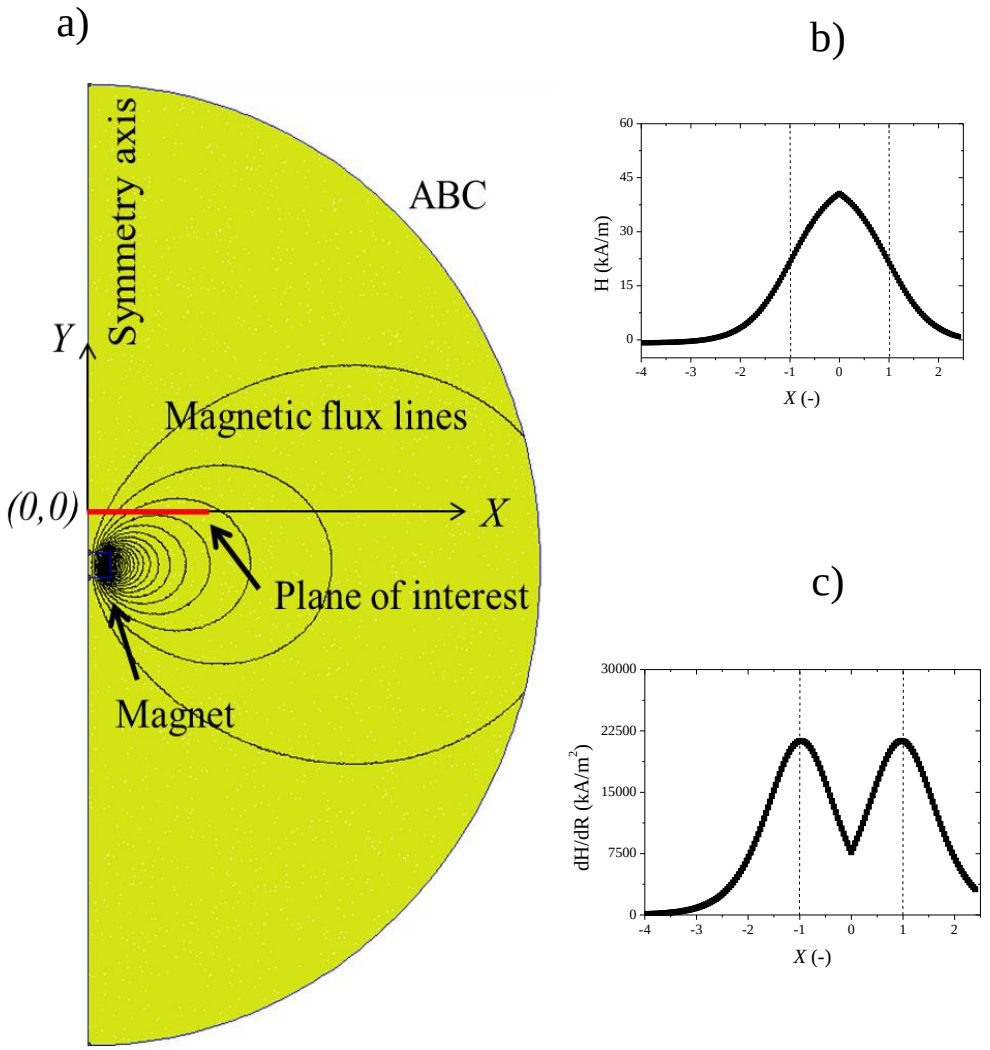

Figure 2. Axisymmetric 2D geometry and Finite Element mesh model of the magnetic field distribution generated by the NdFeB magnets (1mm height and 2 mm diameter). a) Schematics of the simulation domain with mesh size 0.05. Red horizontal line corresponds to the region of interest within the contact. It is exactly placed at a distance of 1.75 mm from the upper surface of the magnet. In the calculation of this distance we considered the indentation in PDMS tribopairs loaded at F_N = 1 N. b) Vertical component of the magnetic field strength, along the red line shown in panel a, as a function of the dimensionless distance $X = x/a$. The dimensionless distance X is measured from the center of the point contact. Here a is the radius of the Hertzian contact. c) magnetic field gradient along the red line.

Ferrohydrodynamic Reynolds equation

The ferrohydrodynamic 2-D Reynolds equation was solved in this manuscript simultaneously to the elasticity equation:

$$\frac{\partial}{\partial x}\left(h^3\left(\frac{\partial p}{\partial x}-\mu_0 M\frac{\partial H}{\partial x}\right)\right)+\frac{\partial}{\partial y}\left(h^3\left(\frac{\partial p}{\partial y}-\mu_0 M\frac{\partial H}{\partial y}\right)\right)=12U\eta\frac{dh}{dx} \tag{8a}$$

$$\delta(x,y)=\frac{2}{\pi E'}\iint_A\frac{p(x',y')}{r}dx'dy' \tag{8b}$$

Here μ_0 is the magnetic permeability of vacuum, M is the magnetization of the ferrofluid, H is the external magnetic field and δ is the total elastic deflection. The Reynolds equation is a non-linear partial differential equation for which a finite difference approximation can be employed. Here, we employed a Gauss Seidel relaxation process to solve the equations together with multilevel techniques to accelerate the convergence as described by references [21 and 22]. At the boundaries of the computational domain, the gauge pressure was assumed to be zero. In the outlet region, when cavitation occurs, the Reynolds boundary condition was adopted. All equations were made dimensionless using the simulation box length and Hertzian dry contact parameters. How partial filling of the inlet to an elastohydrodynamic conjunction influences pressure and film thickness can readily be explored numerically by adopting different inlet distances for pressure boundary [6]. In the current manuscript, the effect of several different starting points, $X=x/a$, between 2.4 to 5.1 were modeled. Here a stands for the Hertzian radius of the contact. Data reported in this manuscript were obtained under the assumption that the inlet was filled at X = 4.8.

The magnetic field distribution, $H=H(x,y)$, used in the solution of the ferrohydrodynamic Reynolds equation was taken from direct FEM simulations of the external magnetic field at the lubricant position taking into account the Hertzian indentation depth for the particular load applied (see Section 4.1.). Simulation data were well fitted to a Boltzmann distribution function:

$$H(R)=A_2+\frac{A_1-A_2}{1+e^{\frac{R-R_0}{dR}}} \tag{9}$$

with A_1 = 45242.68, A_2 = -888.532, R_0 = 1.19 × 10^{-3} , dR = 5.42 × 10^{-4}. The magnetization M versus external magnetic field dependence of the ferrofluid was directly measured using a vibrating sample magnetometer at room temperature [15].

By numerically solving the ferrohydrodynamic 2-D Reynolds equation together with elasticity equation (Equations 8a and 8b) we did calculate the film thickness h and pressure distribution p within the gap. With them, the Couette and Poiseuille contributions to the shear stress, τ_C and τ_P, were calculated using Equations 1 and 2 and finally, by numerical integration of the shear stress we determined the Couette and Poiseuille contributions to the friction coefficient μ_C and μ_P, respectively.

Calculation of the elastic hysteresis term

Apart from μ_C and μ_P, another important contribution to the rolling friction is the hysteresis's effect of deformation. As stated in the Introduction Section, the deformation term arises from the incomplete recovery of the energy dissipated by subsurface viscoelastic deformation. The friction coefficient due to deformation energy losses is given by Equation 4. $\tan(\delta)$ values used in the friction calculations are reported in Table 1.

RESULTS AND DISCUSSION

Operating regime of the tribopairs

Lubrication subregimes can be visualized in terms of the following dimensionless parameters $g_E = \overline{W}^{8/3}\overline{U}^{-2}$ and $g_V = \bar{\alpha}E'\overline{W}^{3}\overline{U}^{-2}$ [14]. Here $\bar{\alpha}$ is the lubricant pressure viscosity coefficient. A value of $\bar{\alpha} = 0.5 \times 10^{9}\, Pa^{-1}$ was assumed in this work. Depending on the value of the dimensionless parameters for a particular operating contact, the 2D space can be divided in four regions each one corresponding to a different subregime [23]: isoviscous-rigid (I-R), piezoviscous-rigid (P-R), isoviscous-elastic (I-E) and piezoviscous-elastic (P-E). Tribopairs employed in this work operate in the isoviscous-elastic subregime as demonstrated in Figure 3 where we show the lubrication map over the range of test conditions. In all tests contained in Figure 3 the normal force F_N was fixed at 10 N with the exception of PDMS-PDMS contacts. In the case of PDMS-PDMS contacts the normal force applied was of only 4 N. On the other hand, the angular speed was increased from 0 to 2000 rpm. Therefore the maximum sliding speed achieved was $V = 1$ m·s^{-1}.

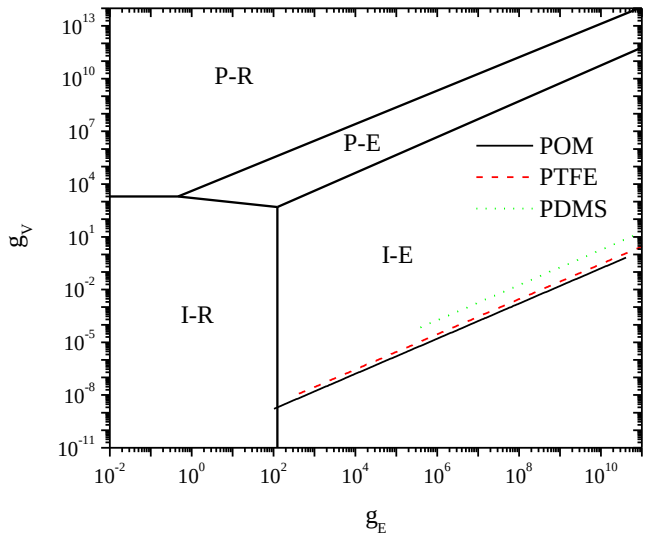

Figure 3. Fluid lubrication regimes map for all polymeric tribopairs. The three lines show the range covered in the experimental measurements. The map confirms that, so long as a fluid film is present, the measurements lie in the isoviscous elastic regime.

Newtonian fluids

First, we aimed to ascertain the tribological behavior of the simplest fluid possible under isoviscous-elastic lubrication conditions. To attain this goal we used Newtonian silicone oils with shear viscosities within the range from 0.487 Pa·s to 10 Pa·s. As a way of example, Figure 4a depicts the Stribeck curves for the silicone oils in a PDMS-PDMS tribopair. Every Stribeck curve was obtained by logarithmically increasing the rotation speed of the ball at a constant load. The figure demonstrates that the contact operated in the mixed-to-full film regime. As expected, the friction curves reasonably collapse into a single master curve when plotted as a function of $U\eta$ for the three oils investigated. Figure 4a also contains the friction data for the ferrofluid. As expected the tribological behavior of the ferrofluid in the absence of magnetic fields is very similar to other Newtonian fluids having a similar viscosity.

The good scaling with $U\eta$ observed for the case of the PDMS-PDMS tribopair was also observed in the case of other polymeric tribopairs investigated (POM-POM and PTFE-PTFE). Some representative results are included in Figure 4b where we compare the tribological behavior of a high viscosity silicone oil (10 Pa·s) in POM-POM, PTFE-PTFE and PDMS-PDMS contacts.

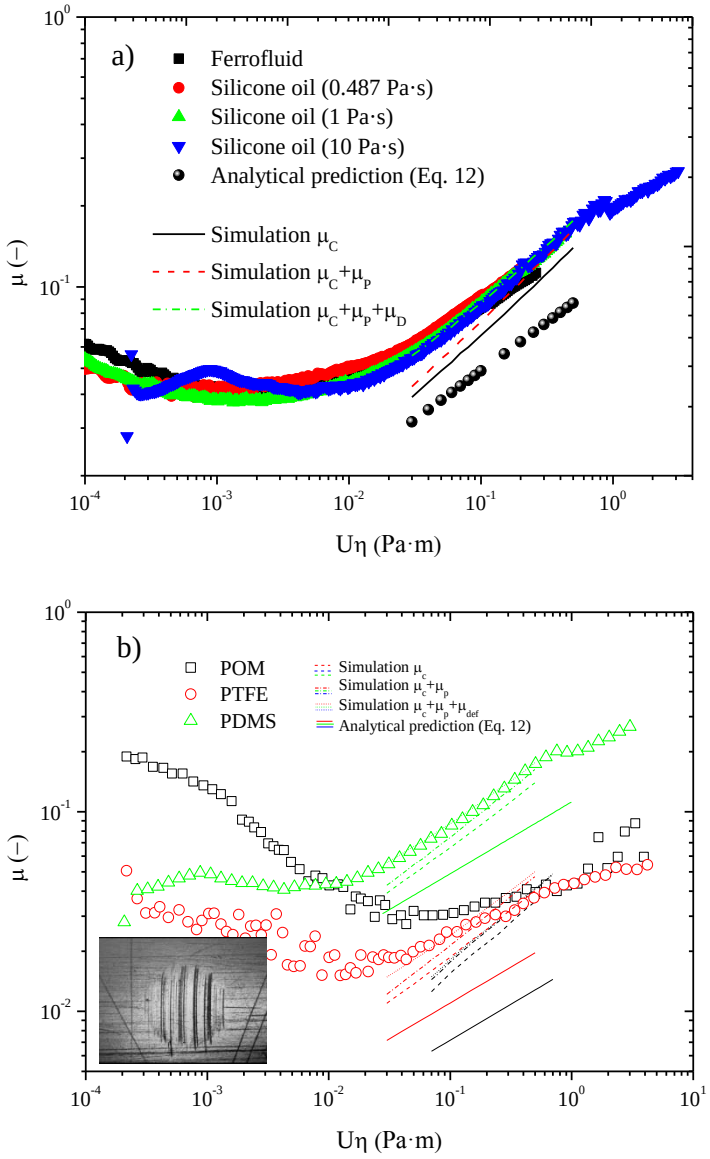

Figure 4. Experimental and simulation data corresponding to the friction coefficient versus entrainment speed × viscosity for the lubricants in the absence of magnetic fields. a) Effect of $U\eta$ in the lubrication of PDMS-PDMS tribopairs at a load of F_N = 4 N. b) Effect of the tribopair in the lubrication of a high-viscosity silicone oil (η = 10 Pa·s). POM and PTFE tribopairs: load 10 N. PDMS tribopairs: load 4 N. Inset in Figure b shows a typical wear scar on the polymer flats after the test, concretely in POM tribopairs.

As observed, all tribopairs start from mixed lubrication at low $U\eta$. Then, increasing the sliding speed promotes the formation of a full film that is capable to separate the surfaces entering in the isoviscous elastohydrodynamic regime. At very high $U\eta$ some deviations from a linear behaviour are observed as a result of flow instabilities and/or starvation.

Historically a common way to judge which lubrication regime a system is running in is by using the film thickness parameter. This dimensionless parameter (also called Lambda parameter Λ) is the ratio of the theoretical film thickness to the measured (averaged) surface roughness. Calculated Lambda parameters, at the friction minimum, for POM-POM, PTFE-PTFE and PDMS-PDMS contacts are Λ = 10.6, 9.33 and 6.33, respectively. These values are in good agreement with a Lambda parameter of $\Lambda = 10$ suggested by [23] for the transition from mixed lubrication to elastohydrodynamic lubrication regime. The minimum in the Stribeck curve slightly shifts to the left for the smoother surfaces (PDMS in this case) in good agreement with previous literature in this field [6,10]. As expected from EHL theory, within the isoviscous-elastic regime, the three tribopairs investigated should overlap at a given normal load. This is actually what happens to POM and PTFE contacts. The fact that PDMS friction data become significantly higher comes from the fact that the load is significantly smaller. A load of 4 N is employed when measuring with PDMS-PDMS tribopairs. Larger loads could not be applied in these highly compliant surfaces. These results are in qualitatively good agreement with load dependences investigated by [11].

Figures 4a and 4b also contain friction coefficient calculations. The simplest approach to predicting friction in isoviscous elastic lubrication is to assume that elastic deformation produces a thin film, circular Hertzian contact region of constant film thickness, h_c , and that effectively all of the friction originates from Couette flow within this region [5,6]. Then the friction force, F_F, can be calculated by integrating the "Couette" shear stress over the circular Hertz contact radius, and finally, the friction coefficient, μ, is thus given by:

$$\mu_{C,approx} = \frac{F_F}{F_L} = \eta\pi a^2 \frac{V}{h_c F_L} \tag{10}$$

As demonstrated in Equation 10, the friction coefficient strongly depends on the film thickness h_c.

Classical full film work has led to regression equations for predicting film thickness in the isoviscous-elastic lubrication regime for both line [24] and elliptical contacts [12,14,24-27].

Probably the most widely used are those from Hamrock and Dowson [25], which, for the circular contact of interest here reduces to:

$$h_c = 3.3 \cdot R' \cdot \overline{U}^{0.64} \cdot \overline{W}^{-0.22} \tag{11}$$

Other regression equations produce very similar results (not shown here for brevity). By simply substituting the regression equation of h_c in Equation 10, the friction coefficient is thus given by:

$$\mu_{C,approx} = 0.4 \cdot SRR \cdot \overline{U}^{0.36} \overline{W}^{-0.11} \tag{12}$$

Similar to other works reported in the literature [6], this simplified theoretical approach results in a lower friction value if compared with experimental results (see Figure 4). This deviation demonstrates that Poiseuille and elastic hysteresis contributions need to be incorporated in the friction calculation as anticipated in the Introduction Section.

Clearly, a more accurate calculation of the friction coefficient involves the numerical solution of the ferrohydrodynamic isoviscous Reynolds equations (Equations 8a and 8b). This requires simultaneously solving the isoviscous 2-D Reynolds equation and the elasticity equation, using the Gauss-Seidel line relaxation method as described in Section above. As demonstrated in Figure 4, the total simulated friction coefficient is in good agreement with experimental data in the tribopairs investigated for the particular $\overline{U}$ and $\overline{W}$ parameters explored in this work. The best consistency was achieved for the PDMS-PDMS contact obviously because these experimental conditions are closer to the assumptions made in the numerical simulation approach; in particular, these contacts are perfectly elastic solids.

The numerical data reported in this manuscript are in very good agreement with regression equations provided by de Vicente *et al.* [6] to within 5 %. In the case of POM and PTFE tribopairs, the simulation predictions give a larger slope if compared to experimental data. These results are possibly due to the formation of a wear track on both POM and PTFE that eventually affects the friction characteristics (see inset in Figure 4b). A similar behavior was described by [11] in the lubrication of Polycarbonate and LDPE tribopairs.

Effect of magnetic field in the tribological performance of ferrofluids

Next we aimed to explore the effect of superimposing an external magnetic field on the tribological performance of ferrofluid lubricated PDMS-PDMS contacts. The PDMS-PDMS contact was chosen here because it more closely resembles the simulated conditions as it experiences a purely elastic deformation (c.f. Figure 4b). As reported in Section 3.2, the magnetic field was generated by placing cylindrical NdFeB magnets below the three contact points within the sample holder (see Figure 1b). As expected, the application of a magnetic field promotes a friction decrease with respect to the no-field condition that, *a priori*, may be associated to an extra contribution to the pressure within the contact (see the curve corresponding to $X_M = 0$ in Figure 5).

As the film thickness and pressure distributions, in isoviscous elastohydrodynamic contacts, are not symmetric along the inlet-outlet center line [6], we decided to explore the effect of displacing the field strength distribution along the contact towards the inlet. Displacing the magnetic field distribution can be easily done experimentally, by simply moving the magnet behind the contact (see Figure 1b) and also in simulations. Hence, in Figure 5 we demonstrate the effect of displacing the magnets, along the inlet, a given normalized distance $X_M = x_M/a$. Here a stands for the Hertzian radius of the contact. Negative X_M values correspond to displacements towards the inlet. On the other hand, positive X_M values would correspond to displacements towards the outlet. Error bars in this figure correspond to the standard deviation of the friction coefficient from three independent runs. For small enough displacements, small $|X_M|$, friction coefficient data clearly decrease when the field gradient is displaced towards the inlet. Importantly, this effect is manifested along the full range of $U\eta$ values explored within the full-film lubrication regime. In Figure 5b we show the effect of displacing the magnet for a constant $U\eta$ = 0.1 Pa·m. This figure clearly reveals a minimum in the friction coefficient for a particular displacement of $X_M = -0.61$.

Next we intended to give an explanation for the minimum in friction observed in Figure 5b. A detailed analysis of the effect of magnetic fields in the ferrofluid lubrication of the contacts definitely requires the numerical solution of the ferrohydrodynamics Reynolds equation as described in Section 4.2. Figure 6 includes film thickness h, pressure p, and Couette τ_C and Poiseuille τ_P shear stress calculations in the absence and presence of magnetic fields (for different displacements X_M). The inspection of the film thickness and pressure profiles along the contact demonstrates that the pressure in the inlet rises to a maximum and just passing the center of the contact ($X = 0$) it decreases rapidly strongly affecting Couette and Poiseuille contributions to the friction. Accordingly, the film thickness profiles exhibit a minimum while moving from the inlet ($X < 0$) to the outlet ($X > 0$) of the contact. These results are in very good agreement with previous numerical solutions of the Reynolds equation in isoviscous lubrication [6].

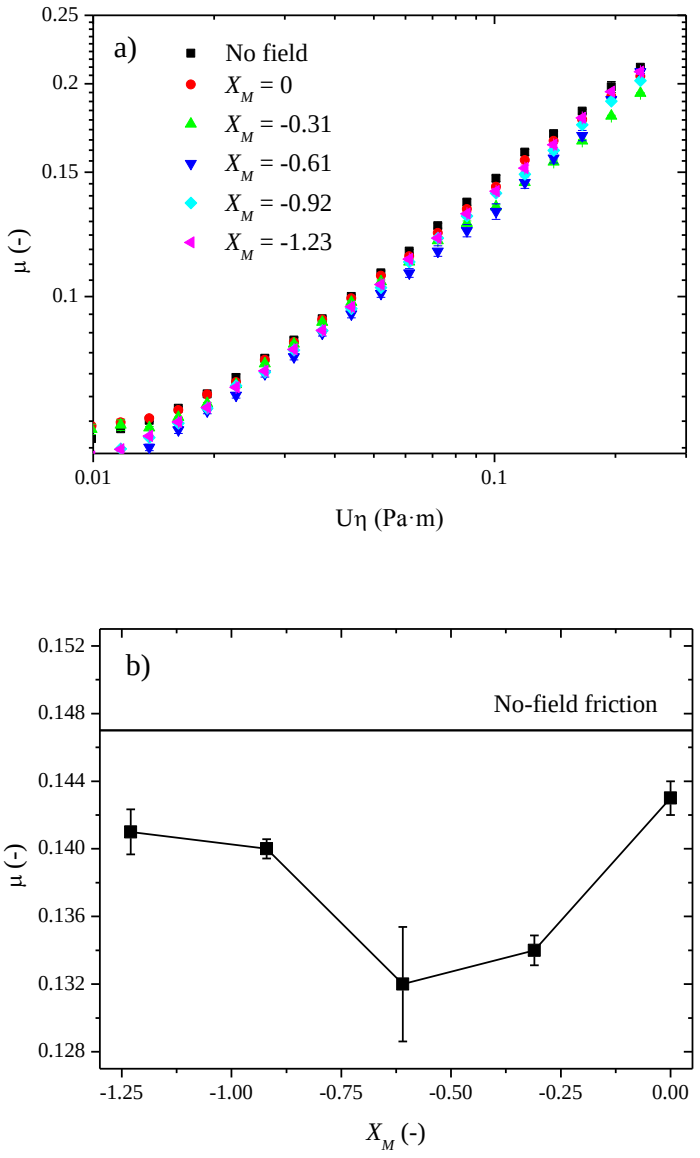

Figure 5. Effect of the presence of a non-homogeneous magnetic field distribution shifted towards the inlet at a given distance $X_M = x_M/a$. All curves correspond to ferrofluid lubricated PDMS-PDMS tribopairs loaded at F_N = 1 N. a) Full Stribeck curve for different X_M values. b) Friction data as obtained from Figure 5a for $U\eta = 0.1$ Pa·m.

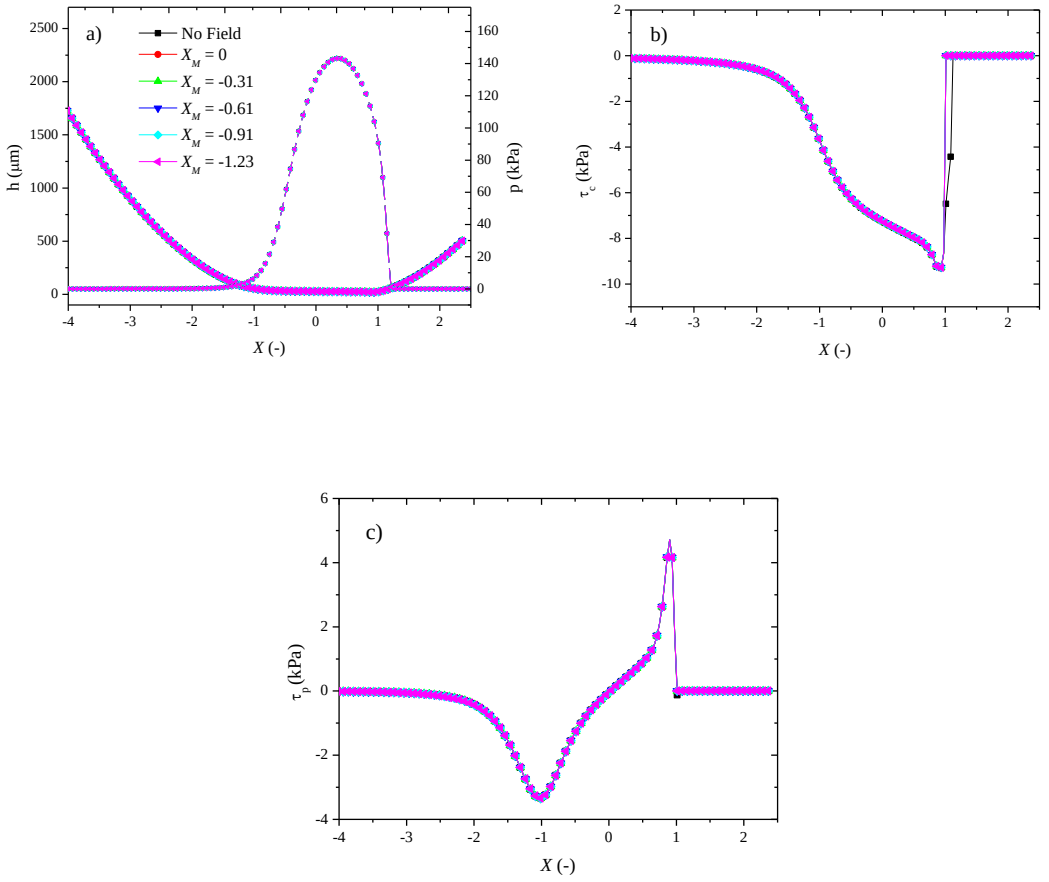

Figure 6. Simulation of the film thickness h, pressure p and shear stress contributions (Couette τ_C and Poiseuille τ_P) for different X_M values. All simulations correspond to ferrofluid lubricated PDMS-PDMS tribopairs loaded at F_N = 1 N.

Interestingly, the effect of magnetic field is not appreciated in the representations contained in Figure 6 because hydrodynamic pressure is always larger than the magnetostatic one for the magnetic field strengths investigated (< 45 kA·m^{-1}). As a consequence, in order to better see the effect of magnetic field on the lubrication behavior, in Figure 7 we show relative measurements by subtracting the calculations at $X_M = 0$. Hence, for instance, Δh is defined as the difference between the film thickness for $X_M \neq 0$ and the film thickness when $X_M = 0$: $\Delta h = h(X_M \neq 0) - h(X_M = 0)$.

The observation of Figure 7 demonstrates the effect of magnetic field in the simulation region. The effect of magnetic field is clearly less important in the Hertzian region

($-1 < X < 1$; $-1 < Y < 1$) as expected because of the large hydrodynamic pressure values within this region. Displacing the magnetic field distribution towards the inlet results in a Δp increase in the inlet of the contact ($X < 0$), that is associated to the appearance of a Δp decrease within the Hertzian contact in order to balance the external load (see Figure 7a).

The fact that the magnetic field does not significantly affect the outlet region ($X > 0$) was expected in view of Figure 6a. On the other hand, Δh contour plots contained in Figure 7b clearly demonstrate a concomitant increase of Δh in the inlet when displacing the magnet towards the inlet.

Next we also calculate Couette and Poiseuille shear stresses in the contact region. $\Delta\tau_C$ contour plots demonstrate that the superposition of a magnetic field mostly affects the inlet and Hertzian region (see Figure 7c). Generally speaking $\Delta\tau_C$ increases (i.e. becomes more positive) when the field is applied as a result of the fact that the film thickness also increases (see Figure 7b). Bearing in mind that the Couette shear stress is negative (c.f. Equation 1 and Figure 6b), this means that the application of a magnetic field results in a lower shear stress in absolute value if compared to the no-field condition, and therefore to a lower friction value as otherwise expected (see discussion above). Couette shear stress contour plots give the clue for the minimum in friction that was experimentally observed in Figure 5b. As observed in Figure 7c, for $X_M = -0.31$ and $X_M = -0.61$, $\Delta\tau_C$ increases because the film thickness Δh increases and therefore the friction coefficient decreases. However, a clear reduction in $\Delta\tau_C$ is found for $X_M = -0.92$ and $X_M = -1.23$. In fact, for the later, we clearly observe the appearance of side lobes where $\Delta\tau_C < 0$ (bluish regions), within the Hertzian contact, that are associated to a sharp increase in friction giving place to the appearance of the minimum in the friction curve.

Finally, we will discuss the $\Delta\tau_P$ contour plots generated (see Figure 7d). These plots clearly demonstrate that $\Delta\tau_P < 0$ in the inlet when moving the magnet towards the inlet. This eventually results in a larger friction as discussed in the paragraph above. In any case, $\Delta\tau_P$ is clearly one order on magnitude smaller than $\Delta\tau_C$ and therefore its effect on the overall friction is expected to be negligible.

Figure 8 includes typical simulated friction data for different X_M values. Simulation data correspond to ferrofluid lubricated PDMS-PDMS tribopairs loaded at F_N = 1 N and $U\eta = 0.1$ Pa·m. As expected from the previous discussion, the Couette contribution dominates. In this particular case, Couette contribution is one order of magnitude larger than the Poiseuille contribution. On the one hand, when the field distribution moves to the inlet ($X_M < 0$), as the film thickness becomes larger, the Couette friction decreases because it scales as $\propto U\eta/h$ (c.f. Equation 1).

Then, a minimum is observed for $X_M = -0.61$ as a result of the appearance of regions within the contact where $\Delta\tau_C < 0$. However, when the field distribution moves to the

inlet, the Poiseuille friction increases because the pressure gradient becomes larger as a result of the fact that the pressure in the inlet increases. This results in a monotonic increase in the Poiseuille friction contribution. On the other hand, when the field distribution moves to the outlet ($X_M > 0$), the Couette friction further increases but the Poiseuille friction remains constant because of the fact that the pressure at the exit is negligible (c.f. Figure 6a).

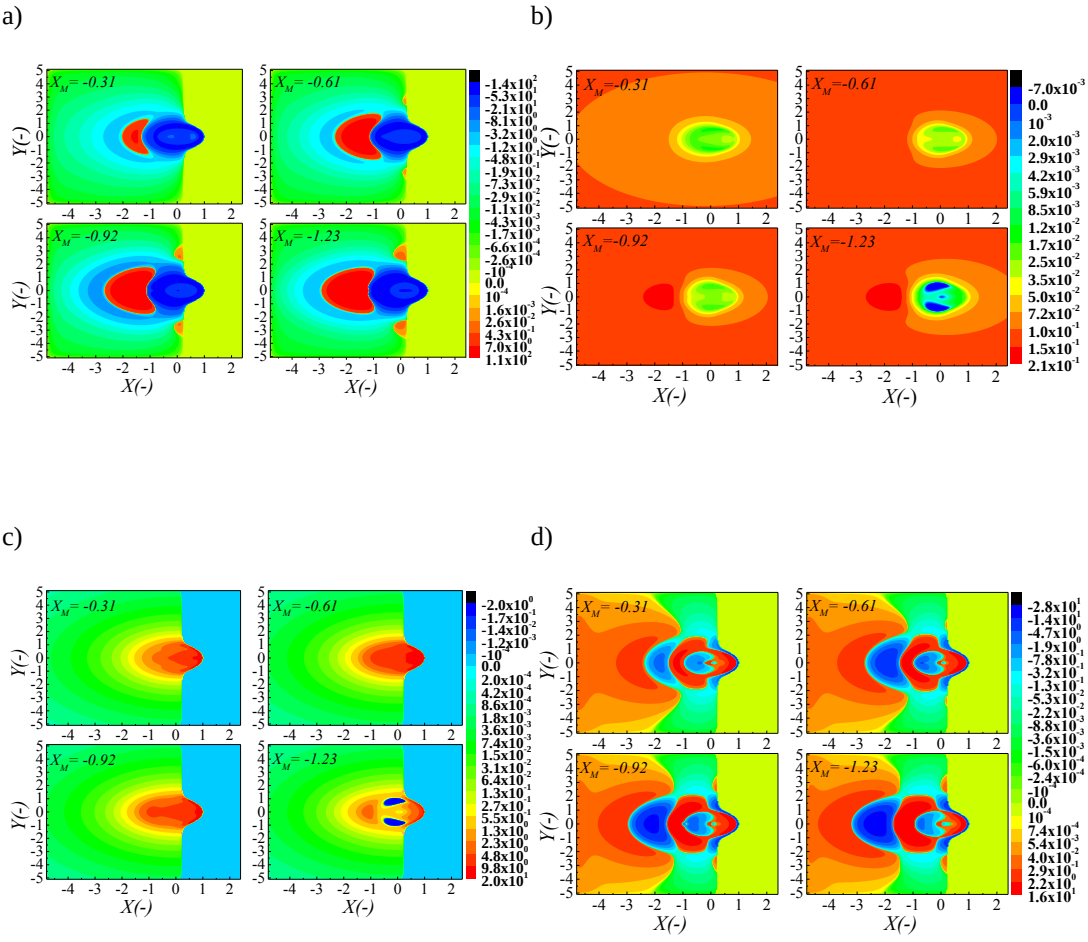

Figure 7. Relative effect of the presence of a non-homogeneous magnetic field distribution. Curves are constructed by subtracting the $X_M = 0$ simulation curves. All simulations correspond to ferrofluid lubricated PDMS-PDMS tribopairs loaded at F_N = 1 N. Field distributions are displaced towards the inlet a given dimensionless distance X_M. a) Δp (Pa), b) Δh (μm), c) $\Delta \tau_C$ (Pa), and d) $\Delta \tau_P$ (Pa).

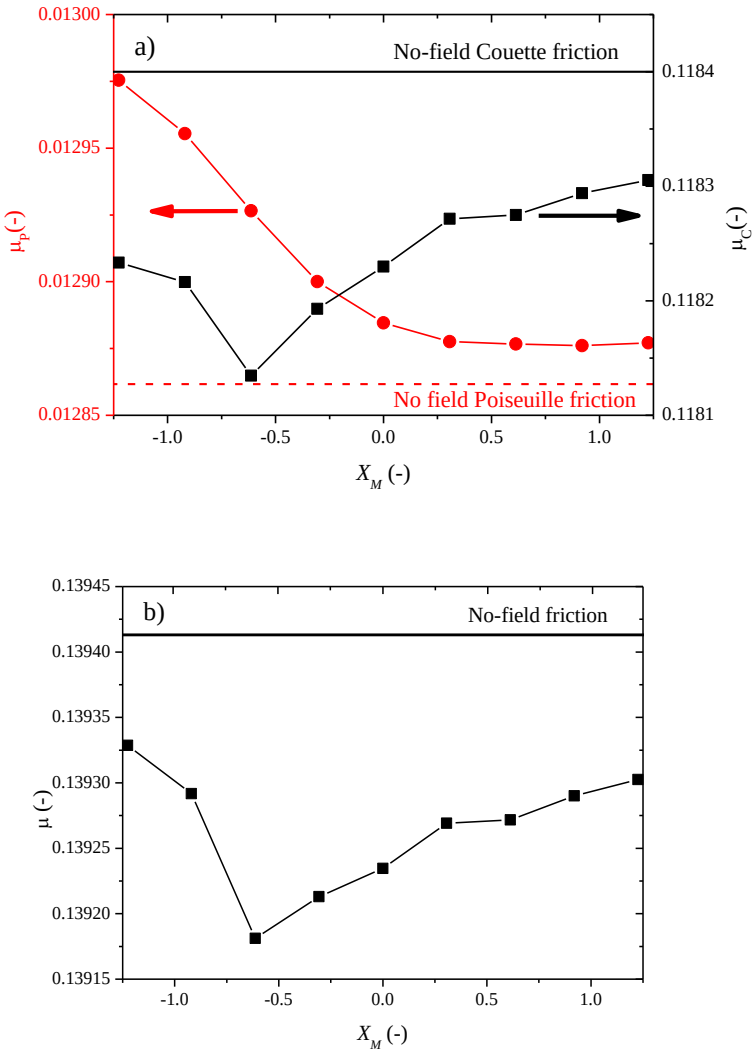

Figure 8. a) Simulated Couette and Poiseuille friction contributions for shifted non-homogeneous magnetic fields ($X_M \neq 0$). b) Calculated total friction (simulated Couette + simulated Poiseuille + Deformation) as a function of the displacement distance X_M. All simulations correspond to ferrofluid lubricated PDMS-PDMS tribopairs loaded at F_N = 1 N and $U\eta = 0.1$ Pa·m. Only those regions where the total pressure is positive, $p > 0$, have been considered for the calculation of the Couette friction.

Bearing in mind that the total friction within the contact can be essentially estimated by the addition of the Couette and Poiseuille contribution, it is anticipated that the friction

coefficient will exhibit a minimum value when the field distribution is placed somewhere around the inlet and not exactly in the center point of the contact. Figure 8b shows the calculated total friction (simulated Couette + simulated Poiseuille + Deformation) as a function of the displacement distance X_M. It clearly demonstrates that the minimum in friction is obtained at $X_M = -0.61$ which is in very good qualitative agreement with experimental data, reported in Figure 5b, that exhibit a minimum in friction at the same X_M value for the same experimental conditions, F_N = 1 N and $U\eta$ = 0.1 Pa·m, well within the full-film lubrication regime. It is worth to remark at this point that in the calculation of the friction coefficient, by integrating the shear stress over the surfaces, we only computed those regions where the total pressure is positive. Further simulations revealed that the X_M position of the minimum slightly depends on the external load applied (results not shown here for brevity).

Generally speaking, the agreement between experiments (Figure 5b) and simulations (Figure 8b) is qualitatively good bearing in mind the many approximations employed in the simulation model. The fact that experimental friction data span over a wider range than simulations can be partly due to the fact that in the on-field simulations we are assuming that the contacts are fully flooded whereas in practice recirculation may occur as the ferrofluid is positioned as a "stagnant" drop within the contact because of the non-uniform magnetic field generated by the permanent magnets. Also, in the simulations we are using the external magnetic field, instead of the *internal* magnetic field. Computing the *internal* magnetic field is difficult because the demagnetization factor of the ferrofluid drop within the contact is unknown and changes when X_M varies.

CONCLUSIONS

The frictional properties of Newtonian fluids and ferrofluids have been investigated in compliant point contacts. Special emphasis is given to the full-film isoviscous elastic lubrication regime where neither surface roughness nor surface tension play a role. In the absence of magnetic fields the tribological behaviour of the ferrofluids can be described in terms of a Stribeck curve that closely matches the one obtained for Newtonian fluids. However, in the presence of magnetic fields, and for sufficiently small loads, friction decreases with respect to the no-field friction coefficient. These observations are consistent with an extra (magnetic) contribution to the fluid pressure and numerical simulations of the ferrohydrodynamics Reynolds equation. Importantly, the friction coefficient can be further decreased when the field distribution is displaced towards the inlet of the contact, at a reduced distance of $X_M = -0.61$ for a load of F_N = 1 N. Experiments and simulations are in qualitative good agreement. Even though the minimum in the friction coefficient reported in this work is relatively small, it is expected that the latter could be enhanced with stronger field strengths and distributions.

REFERENCES

1. Rosensweig, R. E.: Ferrohydrodynamics, Dover Publications Inc, New York, (1997)

2. Odenbach, S., Thurm, S.: Magnetoviscous effects in ferrofluids, Ferrofluids, 185-201 (2002)

3. de Vicente, J., Klingenberg, D. J., Hidalgo-Alvarez, R.: Magnetorheological fluids: a review.Soft Matter 7.8, 3701-3710 (2011)

4. Andablo-Reyes, E., de Vicente, J., Hidalgo-Álvarez, R., Myant, C., Reddyhoff, T., Spikes, H. A.: Soft-Elasto-Hydrodynamic Lubrication. Tribology Letters 39, 109-114 (2010)

5. de Vicente, J., Stokes, J. R., Spikes, H. A.: Lubrication properties of non-adsorbing polymer solutions in soft elastohydrodynamic (EHD) contacts. Tribology International 38.5, 515-526 (2005a)

6. de Vicente, J., Stokes, J. R., Spikes, H. A.: The frictional properties of Newtonian fluids in rolling-sliding soft-EHL contact. Tribology Letters 20.3-4, 273-286 (2005b)

7. de Vicente, J., Stokes, J. R., Spikes, H. A.: Rolling and sliding friction in compliant, lubricated contact. Proceedings of the Institution of Mechanical Engineers, Part J: Journal of Engineering Tribology 220.2, 55-63 (2006a)

8. de Vicente, J., Stokes, J. R., Spikes, H. A.: Soft lubrication of model hydrocolloids. Food Hydrocolloids 20.4, 483-491 (2006b)

9. de Vicente, J., Spikes, H. A., Stokes, J. R.: Viscosity ratio effect in the emulsion lubrication of soft EHL contact. Journal of Tribology 128.4, 795-800 (2006c)

10. Bongaerts, J. H. H., Fourtouni, K., Stokes, J. R.: Soft-tribology: lubrication in a compliant PDMS-PDMS contact. Tribology International 40.10, 1531-1542 (2007)

11. Myant, C., Spikes, H. A., Stokes, J. R.: Influence of load and elastic properties on the rolling and sliding friction of lubricated compliant contacts. Tribology International 43.1, 55-63 (2010)

12. Biswas, S., Snidle, R. W.: Elastohydrodynamic lubrication of spherical surfaces of low elastic modulus. Journal of Tribology 98.4, 524-529 (1976)

13. Dowson, D., Yao, J. Q.: Elastohydrodynamic Lubrication of Soft-Layered Solids at Elliptical Contacts: Part 2: Film Thickness Analysis. Proceedings of the Institution of Mechanical Engineers, Part J: Journal of Engineering Tribology 208.1, 43-52 (1994)

14. Esfahanian, M., Hamrock, B. J.: Fluid-film lubrication regimes revisited. Tribology Transactions 34.4, 628-632 (1991)

15. Andablo-Reyes, E., Hidalgo-Álvarez, R., de Vicente, J.: Controlling Friction using Magnetic Nanofluids. Soft Matter 7, 880-883 (2011)

16. Lee S., Spencer, N. D.: Aqueous lubrication of polymers: influence of surface modification. Tribology International 38.11, 922-930 (2006)

17. Heyer, P., Läuger, J.: Correlation between friction and flow of lubricating greases in a new tribometer device. Lubrication Science 21.7, 253-268 (2009)

18. Bombard, A. J. F., de Vicente, J.: Boundary lubrication of magnetorheological fluids in PTFE/Steel point contacts. Wear 296.1, 484-490 (2012a)

19. Bombard, A. J. F., de Vicente, J.: Thin-film rheology and tribology of magnetorheological fluids in isoviscous-EHL contacts. Tribology Letters 47.1, 149-162 (2012b)

20. Meeker, D. C.: Finite element method magnetics, Version 4.2, 2009, http://www.femm.info.

21. Brandt, A., Lubrecht, A. A.: Multilevel matrix multiplication and fast solution of integral equations. Journal of Computational Physics 90.2, 348-370 (1990)

22. Venner, C. H., Lubrecht, A. A.: Multilevel Methods in Lubrication, Elsevier (2000)

23. Hamrock, B. J., Schmid, S. R., Jacobson, B. O.: Fundamental of Fluid Film Lubrication, Marcel Dekker Inc. (2004)

24. Dowson, D., Higginson, G. R.: Elastohydrodynamic lubrication, Pergamon Press, Oxford (1977)

25. Hamrock, B. J., Dowson, D.: Elastohydrodynamic Lubrication of Elliptical Contacts for Materials of Low Elastic Modulus I—Fully Flooded Conjunction. Journal of Tribology 100.2, 236-245 (1978)

26. Jamison, W. E., Lee, C. C., Kauzlarich, J. J.: Elasticity effects on the lubrication of point contacts. ASLE TRANSACTIONS 21.4, 299-306 (1978)

27. Roberts, A. D., Tabor, D.: The extrusion of liquids between highly elastic solids. Proceedings of the Royal Society of London. A. Mathematical and Physical Sciences 325.1562, 323-345 (1971)

28. Henry, D.: Materials and Coatings for Medical Devices-Cardiovascular, ASM International, Ohio, USA, 151-186 (2009)

29. Blumm, J., Lindemann, A., Meyer, M., Strasser, C.: Characterization of PTFE Using Advanced Thermal Analysis Techniques. International Journal of Thermophysics 31.10, 1919-1927 (2010)

30. Moore, D. F.: The friction and lubrication of elastomers, Pergamon Press Oxford, (1972)

CHAPTER 5

A comparative study of the tribological performance of ferrofluids and magnetorheological fluids within steel-steel point contacts

K. Shahrivar, A. L. Ortiz, J. de Vicente

This article is published in: Tribology International 78, 125-133, (2014).

Abstract

The lubricating properties of two different magnetic colloids were evaluated both in the absence and presence of external magnetic fields under sliding friction using the ball-on-three-plates geometry and stainless steel-steel point contacts. Specifically, the magnetic colloids studied were commercially-available ferrofluids (i.e., low concentration dispersions of nanosized magnetic particles) and magnetorheological fluids (i.e., high concentration dispersions of microsized magnetic particles). To evaluate the wear damage, the wear scar on the steel plates was examined by optical microscopy and scanning electron microscopy. Experimental results demonstrate a clearly lower friction coefficient and wear damage under lubrication with the ferrofluid, indicating that the effect of particle concentration in the magnetic dispersions dominate over that of particle size.

INTRODUCTION

Generally speaking, magnetic colloids are dispersions of fine magnetic particles in non-magnetic liquid carriers. Depending on the size of the magnetic constituents one can distinguish between ferrofluids and magnetorheological (MR) fluids. The former are constituted by monodomain magnetic particles (approx. 10 nm diameter) while the later are constituted by multidomain magnetic particles (approx. 1 μm diameter). This difference in size results in remarkable differences in their mechanical properties; while ferrofluids remain liquid both in the absence and presence of magnetic fields, MR fluids exhibit a "liquid-to-solid" transition when magnetized [1-7].

The rheological properties of ferrofluids and MR fluids have been studied over the last 50 years and currently a vast knowledge and literature exists, and even there are books published in this topic [5,7]. In contrast to the rheological behavior, the tribological properties of these fluids have been scarcely investigated despite they are used in applications requiring strong confinement where friction and wear come into play [8-13]. Thus, it is fundamental to understand the interactions between these fluids and the devices in which they are used (for an example see the paper by Iyengar et al. [14]). On the one hand, pioneering papers in the field of ferrofluid lubrication were devoted to the study of plain cylindrical journal bearings [15-17], and later extended to other journal bearing configurations (e.g. porous inclined bearings [18,19], four-pockets bearings [20], three pads bearings [21], and short bearings [22]). In most of these studies, the ferrofluid is indeed treated as a continuum media and therefore a film of lubricant is considered in the theoretical analyses. According to the literature, the performance of ferrofluid-lubricated tribopairs in load capacity, anti-vibration, and service life is greater than that of their conventionally-lubricated counterparts. Interestingly, these contacts operate without leakage and fed systems under magnetic fields. Recently, Li-Jun et al. [23] demonstrated a slight reduction in friction and wear-scar diameter for 6 wt% mixed MnZn ferrite ferrofluids using a four-ball tester adapted for the application of magnetic fields. Scanning-electron microscopy (SEM) observations of the worn surfaces suggested the formation of a ferrite protection tribofilm in the contact.

On the other hand, the tribological properties of MR fluids are even less understood. A pioneering paper by Lingard *et al.* [24] demonstrated very high wear rates in steel lubricated with ER fluids (the electric counterparts of MR fluids) compared to typical lubricants. They quantified a ten-thousand-fold greater level with respect to conventional lubricants when using ER fluids that suggested an unsatisfactory performance under boundary lubrication conditions. In fact, this finding was later exploited using MR fluids for *finishing* applications by Kordonski and co-workers [25-27], Jain and co-workers [28,29], and other groups [30,31]. The first paper addressing the tribological performance of MR fluids in the boundary lubrication regime was that of Wong *et al.* [32]. They compared the tribological behavior of a commercial MR fluid (i.e., MRF-132 from Lord Corporation) and of an in-house prepared zeolite-based ER

fluid under the block-on-ring geometry. They observed that both the friction coefficient and wear were lower for the MR fluid even though the iron particles are harder than the zeolites in the ER fluid. Their work was later completed by Bullough *et al.* [33]. A subsequent paper by Leung *et al.* [34] addressed the effect of particle concentration (up to 32 vol%) in the boundary-lubricated wear mechanisms of MR fluids in smooth ring-on-block bearing surfaces, one relatively hard (i.e., the ring) and the other soft (i.e., the block). The block wear was found to increase slightly as the particle concentration increased, but the trend was not monotonic most likely due to the formation of a thin iron tribolayer that protects the block surface.

The wear performance of MRF-132 was also investigated by Sohn *et al.* [35] under boundary lubrication conditions under the pin-on-disk geometry. Three different specimens were tested: aluminum, cooper, and steel. The results revealed that the friction coefficient slightly decreased from 0.8 to 0.6 for sliding distances up to 2400 m, loads of 20 N and sliding speeds in the range 0.44-0.95 $m \cdot s^{-1}$. Under these conditions, the wear rates remained at a value of about 0.0005 $mg \cdot m^{-1}$. A follow-up paper by the same group [9], in this case superimposing a magnetic field generated by a solenoid, demonstrated that the wear loss increased linearly with sliding distance, and that the friction coefficient remained essentially constant during the tests. Both wear rates and friction were lower in the presence of magnetic fields, but surprisingly increased when increasing the sliding speed. The dominant wear mechanism involved was identified as being abrasive wear by asperities and carbonyl iron particles. In fact, SEM observations demonstrated that iron particles were trapped in the contact surfaces during the tests. Lee *et al.* [8] carried out an experimental investigation on the tribological performance of commercial MR fluids (i.e., MRF-132) and a modified MR fluid using both the Schwingungs-, Reibungs- und Verschleisstest (SRV) and four-ball wear testers. Antifriction (zinc-dithiophosphate), wear (molybdenum-dithiocarbamate), and amine anti-oxidant additives were incorporated in the formulation of the MR fluid to reduce friction and wear under operation. The modified MR fluid exhibited better lubrication properties, at high loads and slow sliding speeds, than the commercial MR fluid. However, the worn surfaces after the tests were rougher for the case with modified MR fluid. More recently, Hu *et al.* [10] modified a four-ball tester in order to apply magnetic fields. Custom made MR fluids were formulated and tested. It was found that the larger the magnetic field strength, the higher the friction but the lower the wear rate. These phenomena were rationalized using viscosity-dependent arguments. Under field, the main wear mode was speculated to change from three body abrasion to two body abrasion.

In spite of the fact that the tribological behavior of both ferrofluids and MR fluids has been interrogated in independent studies, little or no work has been devoted to compare ferrofluids and MR fluids using the same tribological conditions and tribopairs. Indeed, the use of very different tribopairs, experimental conditions (loads, sliding speeds, etc.), and configurations (pin-on-disk, four-ball, etc.) in the previous studies precludes to extract sound conclusions, as demonstrated by notorious conflicting results. For

instance, Song *et al.* [9] reported a friction and wear rate reduction with the exposure to magnetic fields, while Hu *et al.* [10] reported an increase in friction under the presence of magnetic fields. These results also suggest that the particular application of the magnetic fields seems to play a key role, evidencing that particle migration may occur in some cases.

Although highly desirable for successful commercial applications, studies to improve the tribological characteristics of MR fluids have been very rarely conducted in the literature [8]. Thus, a comparative study of the behavior of ferrofluids and MR fluids together under the same experimental/tribological conditions would pave the way to enhance the tribological properties of MR fluids. In the current manuscript we continue our previous work on the tribological properties of magnetic suspensions, in this case within steel-steel contacts [11,12].

EXPERIMENTAL

Materials

Commercial ferrofluids and magnetorheological (MR) fluids were acquired from Ferrotec (APG, US) and Lord Corporation (MRF-132, US), respectively. The tribopairs used in this work were commercial plates and balls of AISI 316 stainless steel obtained from Goodfellow (UK) and STL (UK), respectively. Both the plates and the balls were used in their as-received condition without any further polishing or finishing treatment. Wear and friction tests were carried out under the laboratory environmental conditions of <10 % relative humidity and 21 ºC.

Rheology of test fluids

The rheological characterization of the two lubricants was performed at 25 ºC using an Anton Paar MCR302 torsional rheometer configured either in the plate-plate geometry (20 mm diameter) or in the cone-plate geometry (20 mm diameter, 2º), and operated in the controlled strain mode. The measurements were carried out both in the absence of magnetic field and under the application of a magnetic field (generated using the MRD70/1T magnetocell from Anton Paar), and involved a logarithmic increase of the shear rate from 0.001 to 1000 s^{-1} during a total of 400 s.

Friction measurement method

Friction measurements were carried out in the contact geometry of non-conforming ball-on-three-plates using a modified form of the MCR302 rheometer [11,12,36]. A schematic diagram of the test set-up is shown in Figure 1. In this experimental set-up, a

ball of radius R is loaded at a given normal force F_N against three plates mounted on a movable holder with their surface normals in tetrahedral coordination relative to the ball rotation axis, which ensures an equal distribution of the applied load on the three frictional pairs. Subsequently, the ball is rotated at a commanded sliding speed V while the plates are held in place, thus generating three stationary sliding point contacts. Clearly, the sliding speed V is related to the angular velocity (ω, in rad·s^{-1}) through the expression $V = R\omega/\sqrt{2}$. Simple geometrical arguments also lead to that the normal force correlates to the normal load acting on the ith plate (F_{Li}) by the following expression:

$$F_N = \sum_{i=1}^{3} F_{Li} \cos\alpha \tag{1}$$

where $\alpha = 45^o$ is the tilt angle of the plate(s) in this particular experimental set-up. Therefore, the total normal load ($F_L = \sum_{i=1}^{3} F_{Li}$) can be calculated as follows:

$$F_L = \sqrt{2} F_N \tag{2}$$

Also, the torque underwent by the ball (M) is related to the total frictional force ($F_F = \sum_{i=1}^{3} F_{Fi}$) via the following expression:

$$M = F_F R \sin\alpha \tag{3}$$

and hence,

$$F_F = \frac{\sqrt{2} M}{R} \tag{4}$$

Lastly, the friction coefficient μ can be simply obtained from Eqs. (2) and (4) as follows:

$$\mu = \frac{F_F}{F_L} = \frac{M}{F_N R} \tag{5}$$

In the present tribological tests, the ball is made of stainless steel (AISI 316; radius R = $6.35 \cdot 10^{-3}$ m), and the plates are identical parallelepipeds (of dimensions 3 mm × 6 mm × 16 mm) also made of same stainless steel (AISI 316). The Young's modulus of this stainless steel is 193 GPa, and its Poisson's ratio is 0.3. This gives a reduced elastic modulus (E') of 212 GPa. The applied load F_N was 10 N, which according to the Hertz theory without friction should cause a contact radius a of $5.96 \cdot 10^{-5}$ m, an indentation depth δ of $5.6 \cdot 10^{-7}$ m, and maximum contact pressure p_{max} of $6.34 \cdot 10^{8}$ Pa. The magnetic field was generated using three permanent magnets located below the steel plates, as is shown in Figure 1.

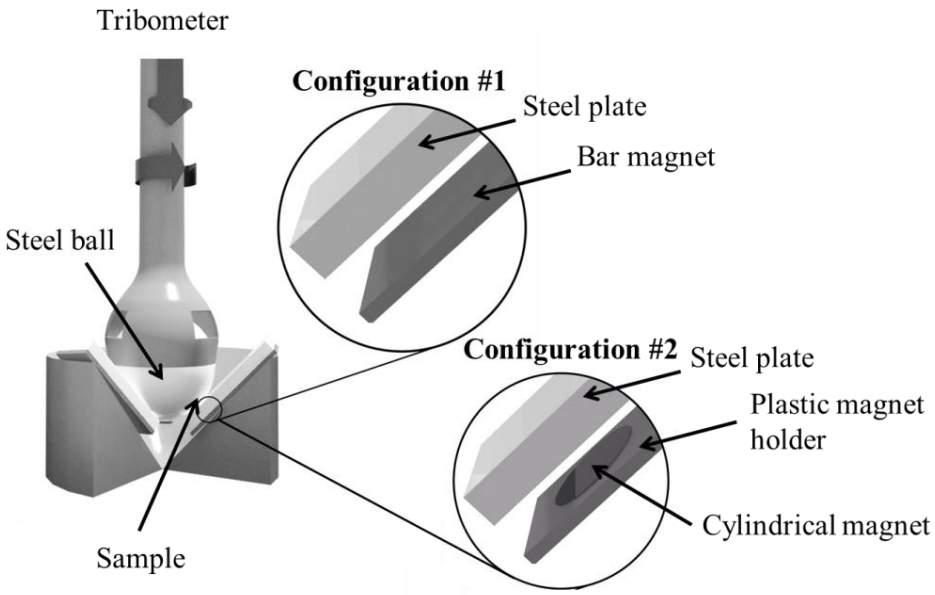

Figure 1. Schematic diagram of the ball-on-three plates contact.

Two approaches were employed to generate the field. On the one hand the magnetic field was generated using a bar-shaped neodymium magnet of exactly the same size as the steel plates placed below them. In the other case, the magnetic field was generated using a cylindrical neodymium magnet placed at the center of the Hertzian contact immediately below the steel plates. The external field generated within the contact is to 35 mT in the case of bar magnets. For the case of cylindrical magnets the field within the contact was calculated to be 14 mT.

Tribology tests

All tests were carried out at a temperature of 25 ºC under a constant slide-to-roll ratio (SRR) of 2 (i.e., under pure sliding conditions). In general, the parameter SRR is defined as the ratio of the absolute value of the sliding speed $|V| = |u_B - u_P|$ to the entrainment speed $U = (u_B + u_P)/2$, where u_B and u_P are the surface speeds of the ball and plate, respectively. Clearly, for pure sliding conditions it is fulfilled that $V = 2U$ because $u_P = 0$. Essentially, the tests were devoted to interrogate the Stribeck curve. In order to construct the entire Stribeck friction curve, friction measurements were carried out over a broad sliding-speed range while progressively increasing the speed from V = $5 \cdot 10^{-5}$ to 1 $m \cdot s^{-1}$; the tests correspond to approximately 30 m of total sliding distance.

The experimental protocol was as follows. First of all, the AISI 316 tribopairs (plates and balls) were ultrasonically cleaned with ethanol, next rinsed with acetone, and then dried. Subsequently, the test rig was assembled and 400 μL of lubricant were added to fully immerse the three point contacts by ~1 mm. The temperature was then stabilized at 25 ºC, after which the ball was loaded against the three plates. Next, the ball was rotated over the plates at increasing speed V, while the resulting torque underwent by the ball M is registered and the friction coefficient calculated using Eq. (5). Fresh balls and plates were used for each test. Furthermore, the friction curves were measured several times to ensure their repeatability. All curves reported in the present study are thus the average of at least three different measurements.

Wear damage characterization

After running each test, the surfaces of the steel plates were carefully cleaned employing acetone-wetted paper and dried in air, after which the wear scar was examined. The radius of the circular wear scars on each plate were measured (two orthogonal measurements per plate, 3 plates per sample) under the optical microscope (Epiphot 300, Nikon, Japan) operated in bright-field mode, and used as quantification of the extent of wear damage. Finally, the wear damage at the microstructural level was observed under the scanning electron microscope (S-3600N, Hitachi, Japan) using

secondary electrons and 30 kV accelerating potential. No surface metallization was used.

RESULTS AND DISCUSSION

Materials

The exact composition of the commercial ferrofluid and MR fluid employed in this work is proprietary, and therefore unknown. Nonetheless, the magnetic hysteresis curves measured experimentally by us (not shown here) indicate at least that the ferrofluid contains a concentration of about 5.5 vol% magnetite particles, which according to transmission electron microscopy (TEM) images (not shown) have equiaxed shape and nanometric sizes. On the other hand, the carbonyl iron particle concentration of the MR fluid is however as high as 32 vol% according to the manufacturer. These iron particles are equiaxed microparticles as revealed by the TEM images (not shown); fused silica and clay nanoparticles are expected to be present too, but only in trace amounts. Images for the carbonyl iron powder in the same MRF-132 fluid are reported by Wong *et al.* [32] (see figure 1 in their paper). The stainless steel tribopairs used in this work were analyzed with a surface profilometer, and the results indicate that the plates and balls employed have a similar surface roughness of about $R_a = 0.313 \pm 0.015$ and $R_q = 0.527 \pm 0.023$ μm, respectively.

Rheology of test fluids

Figures 2a and 2b show the shear viscosity (η) curves of the ferrofluid and MR fluid, respectively, measured experimentally; shear stress versus shear rate curves for the systems investigated are also presented as inset in Figure 2b. There are various interesting features in these figures. Firstly, within the experimental error the ferrofluid viscosity remains nearly constant at $5–6 \cdot 10^{-1}$ Pa·s for the whole range of shear rates investigated, both in the absence and presence of a 35 mT magnetic field. Moreover, the magnetic field has a negligible effect on the ferrofluid viscosity, which is not a surprise considering that the ratio between magnetostatic to thermal energies in a ferrofluid is small. As a result, the only contribution of the magnetic field to the shear viscosity is the so-called rotational viscosity effect (coming from the fact that dipoles within magnetite particles tend to remain oriented with the field) and hence contributing to a very slight viscosity increase that is within the error bar of the measurement [5]. Secondly, the MR fluid exhibits, on the contrary, a marked shear-thinning behaviour, with its viscosity decreasing notably with increasing shear rate to eventually reach a plateau at shear rates greater than $10^2–10^3$ s^{-1}.

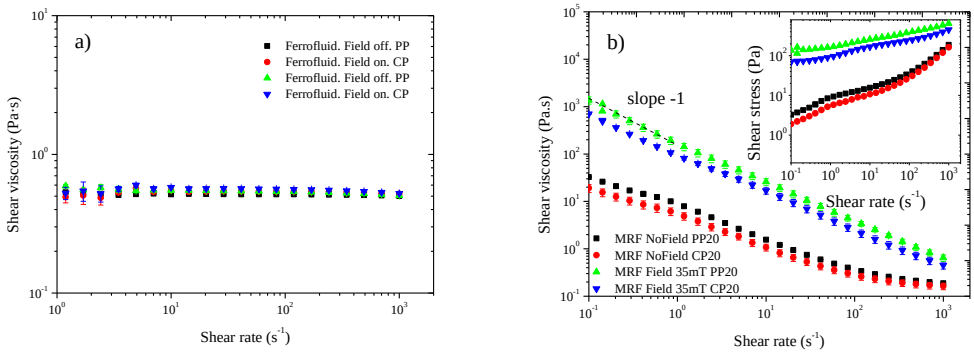

Figure 2. Viscosity curves of the ferrofluid (a) and the MR fluid (b) in the absence and presence of a 35 mT external magnetic field (generated with the MRD70/1T Anton Paar magnetocell). Measurements are shown for both plate-plate (PP) and cone-plate (CP) geometries in order to illustrate the effect of a non-constant shear rate within the sample. Dashed line in Figure 2b represents a -1 power law behaviour associated to a plastic behaviour at low shear rates. Inset in Figure b represents the rheograms (shear stress versus shear rate curves) for the MR fluids investigated in PP and CP geometries.

Also, the application of a magnetic field increases notably the viscosity of the MR fluid, an effect that becomes however less pronounced with increasing shear rate because in this case hydrodynamic forces overcome magnetostatic ones. Thirdly, during the tribocontact at very narrow gap separations the viscosity of the ferrofluid and MR fluid is expected to be 520 and 160 mPa·s, respectively. These values correspond to the lowest viscosities attainable at the higher shear rates. Fourthly, to check the geometry effect of the fixture in the viscosity measurements we did carry out experimental mesurements using both the plate-plate (PP) and cone-plate (CP) geometries. While in the case of the ferrofluid no differences are observed between the viscosity data registered using PP and CP geometries, the viscosity of the MR fluid is, although little, always apparently greater if measured under the PP geometry. This may result from the fact that the shear rate is constant in the CP configuration, but is not constant in the PP configuration. And fifthly, the ferrofluid has lower viscosity than the MR fluid when the shear rate is low, a trend however that eventually reverses at high shear rates (the exact value of which depends on the measurement geometry, and the absence or presence of applied magnetic field). Bearing in mind that it is the high shear viscosity the one involved in the tribological behavior, it is expected that ferrofluids may form a thin-film of lubricant while MR fluids are on the contrary less capable for the formation of this film.

Friction measurements: friction as a function of sliding speed

The lubrication regime was identified using the hydrodynamic lubrication regime map for circular contacts. For the range of conditions used this study, $U\eta$ spans from $4{\cdot}10^{-6}$ to 0.26 Pa·m; in particular, the ferrofluid operates in the range $U\eta$ from $1.3{\cdot}10^{-5}$ to 0.26 Pa·m, while the MR fluid does it from $4{\cdot}10^{-6}$ to 0.08 Pa·m. Consequently, tribological experiments with the ferrofluid are all contained in a straight line between (g_E, g_V) = ($5.48{\cdot}10^{2}$, $4.77{\cdot}10^{2}$) and (g_E, g_V) = ($2.19{\cdot}10^{11}$, $1.91{\cdot}10^{11}$). The corresponding values for the MR fluid are (g_E, g_V) = ($5.79{\cdot}10^{3}$, $5.03{\cdot}10^{3}$) and (g_E, g_V) = ($2.32{\cdot}10^{12}$, $2.01{\cdot}10^{12}$). Note that $g_V = (W/E'R^2)^{8/3}(E'R/U\eta)^2$ and $g_V = \alpha E'(W/E'R^2)^3(E'R/U\eta)^2$, where W is the load at the contact point, α is taken to be $5{\cdot}10^{-10}$ Pa^{-1}, and the rest of magnitudes have been defined before. Accordingly, as long as a full fluid film is present, the contact should be operating in the isoviscous-elastic lubrication regime. Nevertheless, in the tribological experiments reported here, the contacts mainly operate either in the boundary or mixed lubrication regimes (see below).

Figure 3a shows the dependence of the friction coefficient on the sliding speed for the AISI 316 tribopairs lubricated with the ferrofluid and MR fluid in the absence of a magnetic field. It can be seen that the ferrofluid operates in the boundary lubrication regime at low sliding speeds (approximately below 10^{-3} $m{\cdot}s^{-1}$). Then, at higher sliding speeds the friction decreases most likely due to the inclusion of a ferrofluid layer within the contact that effectively separates and lubricates the sliding steel surfaces. On the contrary, the MR fluid essentially operates in the boundary lubrication regime during the whole range of sliding speeds investigated here, as inferred from the nearly constant or slightly increasing friction coefficient. In the boundary regime, the effect of the lubricant viscosity is not expected to play a role in the wear behaviour since there is asperity contact between the two steel surfaces. The friction coefficient of this commercial MR fluid has also been measured in Bullough *et al.* [33], but at a different load (i.e., 292 N), rpm (i.e., 500 rpm) and steel tribopairs (but not the AISI 316 employed here) using the ring-on-block wear geometry. Under these experimental conditions, a constant friction coefficient was obtained in the range from 0.06 and 0.08 up to a wear distance of 1200 m.

The effect of magnetic field in the tribological performance of the ferrofluid and MR fluid is demonstrated in Figure 3b for the two configurations used. Interestingly, the magnetic field has little influence on the frictional behavior of both lubricants, which is an expected result considering that the viscosity of the lubricants at high shear rates does not significantly depend on the magnetic field strength (cf. Figure 2). Also, the two configurations used in the generation of the magnetic field provide very similar results. In the case of MR fluids, bar magnets result in a slightly larger friction coefficient at the lowest speeds investigated if compared to the cylindrical magnets.

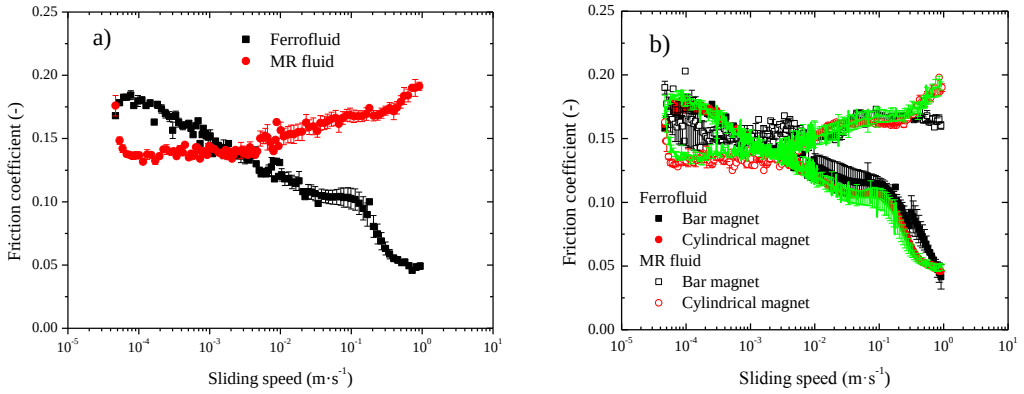

Figure 3. Friction coefficient as a function of sliding speed for the steel-steel sliding point contacts lubricated with the ferrofluid and MR fluid. Results are shown both in the absence and presence of magnetic fields at a constant normal force FN = 10 N. a) Stribeck curves in the absence of magnetic fields. b) Stribeck curve in the presence of magnetic fields generated by bar and cylindrical magnets. Solid (green) lines in B) correspond to no field measurements.

For the later, the friction curves are remarkably similar to those obtained in the absence of the magnetic field whatever the lubricant used (either ferrofluid or MR fluid).

As observed from Figure 3 the friction curves measured for the ferrofluid and MR fluid are markedly different, with the ferrofluid clearly exhibiting much lesser friction at higher sliding speeds (i.e., > 10^{-2} m/s). This reflects the differences in the particle sizes and solid concentrations in both lubricants because their carrier oil is expected to have a similar viscosity. Note that the particle morphology in the fluids is not expected to affect the friction because both the nanoparticles in the ferrofluid and the microparticles in the MR fluid are equiaxed without sharp faces. In principle, the larger particles present in the MR fluid should lead to lower friction because of the lower local pressure contact under the same applied load. However, the particle concentration in the MR fluid is much greater than in the ferrofluid, which should lead to higher friction due to the greater number of frictional contacts. Clearly, the lower friction coefficients measured under lubrication with the ferrofluid, both without and with the magnetic field, indicate that the effect of the particle concentration dominates over that of the particle size.

In order to get a further insight on the effect of particle concentration in the tribological performance of MR fluids we have also formulated a range of MR fluids having different particle volume fractions from 0.5 up to 30 vol%. Note that the highest concentration is indeed very close the particle loading of the MR fluid studied above.

Custom fabricated MR fluids were prepared by dispersing carbonyl iron microparticles (HQ grade from BASF SE, Germany) in a 487 mPa·s viscosity silicone oil (Sigma-Aldrich). The results shown in Figure 4 demonstrate that friction remains at a high value (larger than that measured with the commercial MR fluid) suggesting that the contact operates in the boundary regime for all concentrations investigated.

This reflects that the effect of particle concentration is negligible here, thus indicating that the reason for the high friction level may come from the oil starvation within the contact as a result of particles blocking the oil entrance. The fact that friction is so large for the custom made MR fluid is understandable as the commercial MR fluid contains undisclosed additives (presumably clay nanoparticles and fumed silica) that surely promote better lubricating properties.

The better lubrication imposed by the ferrofluid in relation to the MR fluid should result in a lower extent of the wear damage. With this in mind, the worn surfaces of the plates were observed after running the tribological tests. Certainly, as shown in the optical micrographs of Figure 5, the wear scars are notably smaller and contains a much lower density of scratches and pits when the tribopair was lubricated with the ferrofluid. The quantitative measurement by image analysis software confirms these visual observations, indicating that the wear-scar radii are 177 ± 1 and 428 ± 8 μm for the ferrofluid and MR fluid lubrications without magnetic field, respectively, and 166 ± 2 and 322 ± 18 μm the ferrofluid and MR fluid lubrications under the field generated by the bar magnets, respectively.

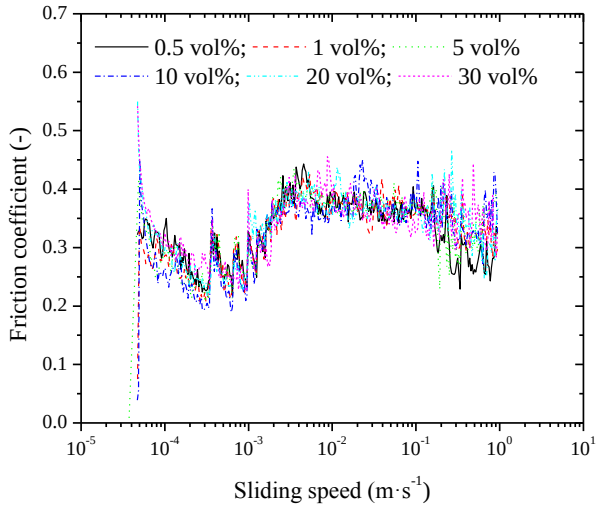

Figure 4. Stribeck curve for homemade MR fluids prepared by dispersing carbonyl iron particles (HQ grade from BASF) in a 487 mPa·s viscosity silicone oil at different particle concentrations from 0.5 to 30 vol%. F_N = 10 N.

The fact that the wear-scar dimensions for the MR fluid lubrication in the absence of magnetic fields are larger than in the presence of the magnetic field is understandable considering that the magnetic field lines promote the particle concentration in a given region. This confines the abrasion region to a small zone and therefore the wear-scar dimension becomes smaller. These results are in agreement with previous data [9, 10]. However, contrary to the present results, Hu *et al.* [10] also observed a remarkable change in the steady friction values, in disagreement with what has been observed here. In particular, they reported a four-fold increase in friction under the field. Note here the fact that according to the present results the friction without field at the highest speeds investigated increases rapidly prior to the end of the test. On the other hand, the wear-scar radii for the ferrofluid lubrication are very similar without and with magnetic fields applied, in agreement with the similarity observed in the friction data. Using cylindrical magnets instead of bar magnets has a similar effect: wear-scar radii of 175 ± 9 and 421 ± 5 μm for the ferrofluid and MR fluid lubrications, respectively.

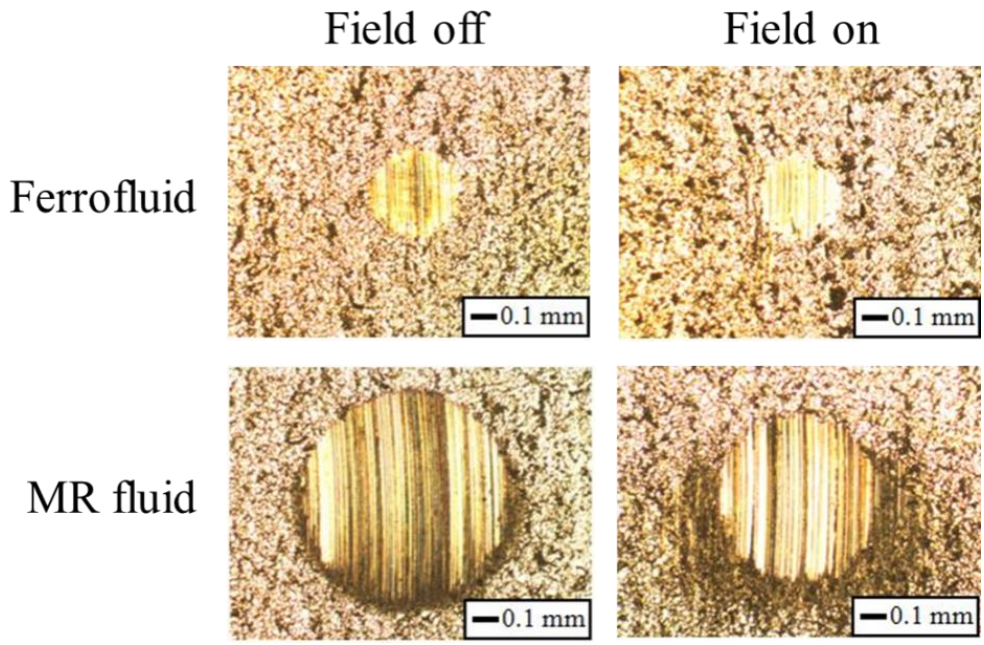

Figure 5. Bright-field optical micrographs of the wear scars obtained in the cases of lubrication with the ferrofluid and MR fluid without and with magnetic fields applied. "Field on" corresponds to the results obtained using bar magnets.

Again, the wear-scar diameter is smaller in the presence than in the absence of the magnetic field. Also, a larger wear-scar diameter is obtained for cylindrical magnets if

compared to bar magnets because the magnetic field generated is smaller in the case of cylindrical magnets. On the one hand, the magnetic field strength generated within the point contact using bar magnets is 35 mT. On the other hand, the magnetic field generated by the cylindrical magnets within the contact is of only 14 mT.

The observation of the wear damage at higher magnifications by scanning electron microscopy (SEM) can shed light on the wear mechanisms. The SEM micrographs of the worn plates lubricated with the ferrofluid, as the ones presented in Figure 6, show very few grooves, which in addition are smoother and less deep, apart from evidence of abundant formation of ridges. This reflects that, both in the absence and presence of the magnetic field, the sliding wear occurred mainly by two-body abrasion with no or little three-body abrasion, and however noticeable ploughing (which does not involve direct material removal). In the case of the lubrication with the commercial MR fluid the SEM micrographs taken on the worn plates, as the ones shown in Figure 7, show many well-defined, deep grooves with particles from the MR fluid embedded in their interior, as well as microchip formation. These observations indicate that the sliding wear occurred, both in the absence and presence of the magnetic field, by two-body and three-body abrasion, with appreciable material removal induced by microcutting.

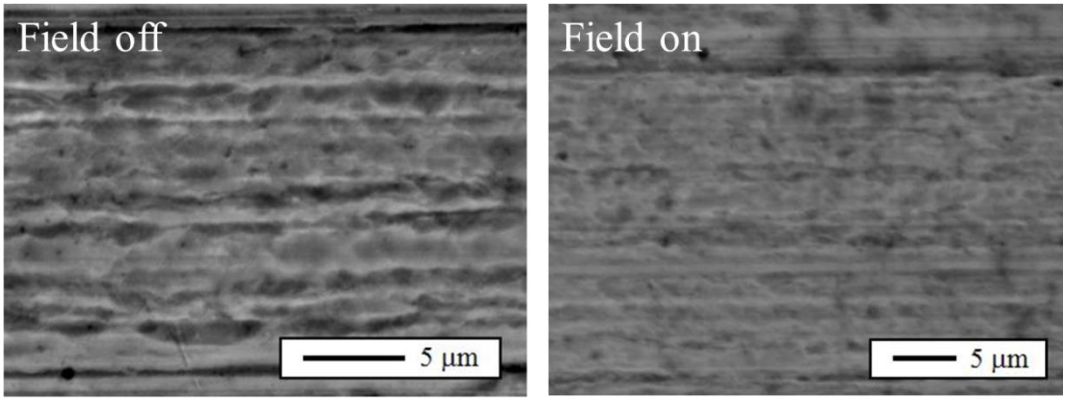

Figure 6. SEM micrographs taken within the wear scars of the steel-steel contacts lubricated with the ferrofluid. “Field on” corresponds to the results obtained using bar magnets.

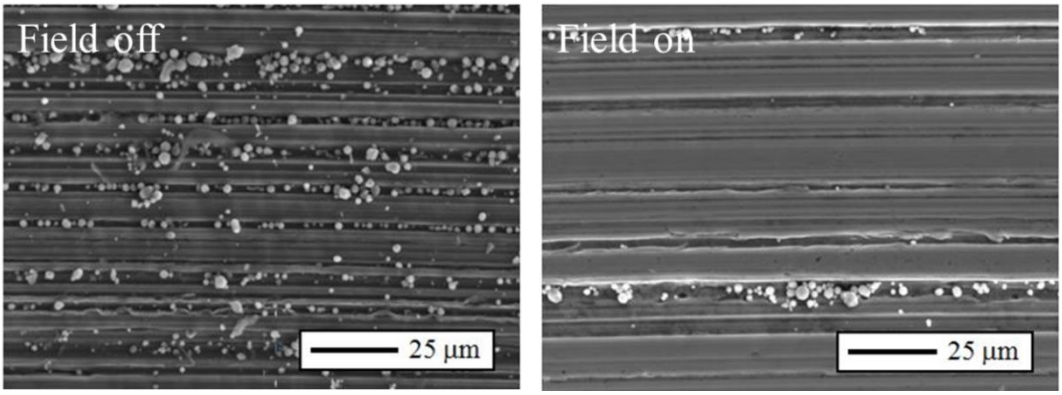

Figure 7. SEM micrographs taken within the wear scars of the steel-steel contacts lubricated with the MR fluid. "Field on" corresponds to the results obtained using bar magnets.

Friction measurements: friction as a function of sliding distance

Further information on the tribological mechanisms involved can be obtained by running friction tests at constant load and speed, as a function of time. Figure 8 shows the friction coefficient as a function of sliding distance for low sliding speeds (i.e., 0.0003 $m \cdot s^{-1}$) over a sliding distance of 5 m. The load was fixed at F_N = 10 N. The results demonstrate that in the case of the ferrofluid lubrication the friction coefficient starts at a high value (i.e., ~0.17) and rapidly levels off to reach a steady friction value (i.e., ~0.14) in less than 0.2 m. The effect of the magnetic field is negligible in the frictional properties, and also on the wear properties. In fact, the wear-scar radii of the surfaces lubricated with the ferrofluid are 220 ± 4 and 236 ± 3 μm in the absence and presence of the magnetic field, respectively. On the other hand, for the MR fluid lubrication the friction is larger in the presence of the magnetic field, especially for sliding distances smaller than 2 m. For larger distances the friction coefficient reaches a steady value (i.e., ~0.16). In the case of the MR fluid lubrication the wear-scar radius in the absence of the magnetic field is slightly larger (i.e., 242 ± 4 μm) than in the presence of the magnetic field (i.e., 217 ± 13 μm).

As a result of the fact that the frictional behaviour of the MR fluid seems to be dependent on the time rubbed (cf. Figure 8), we decided to pursue next an experimental investigation on the effect of the sliding distance, at larger sliding speeds (i.e., 0.3 $m \cdot s^{-1}$).

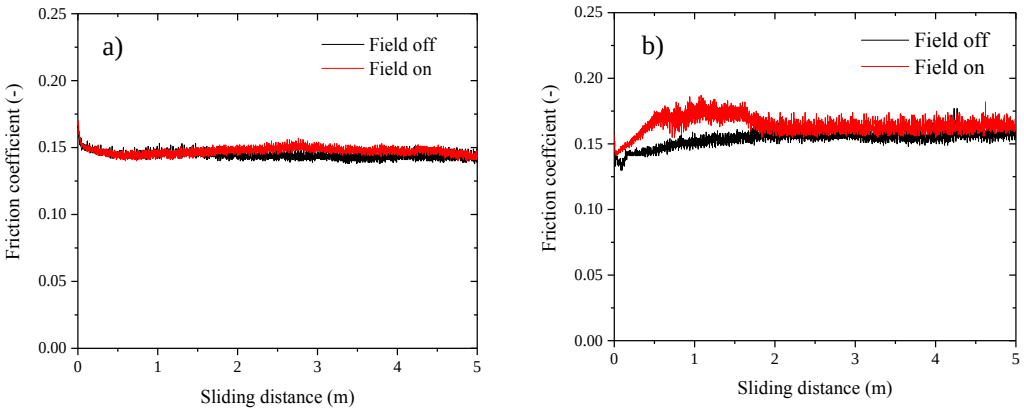

Figure 8. Continuously recorded friction coefficient as a function of sliding distance for low sliding speeds (V = 0.0003 m·s^{-1}) over a total of 5 m sliding distance. F_N = 10 N. a) Ferrofluid. b) MR fluid. "Field on" corresponds to the results obtained using bar magnets.

The results obtained are presented in Figure 9. As observed in this figure, the ferrofluid induces a low friction value both in the absence and presence of the magnetic field. This is due to that the contact operates in the mixed regime and that the pressure is partially supported by both contacting asperities and a fluid thin film. On the contrary, the MR fluid induces a different behaviour at low and large sliding distances. For short distances, the friction remains higher in the presence of the magnetic field than in its absence. However, for longer distances (i.e., > 40 m) the friction becomes smaller in the presence of the magnetic field. Quantitative results of the wear-scar dimensions are shown in Figure 10. It can be seen that the wear-scar radius clearly increases with increasing the sliding distance, as was expected. Also, the presence of a magnetic field results in a wear-scar radius reduction that is more clearly observed for the larger sliding distances. This wear-scar radius reduction can be explained by the fact that the magnetic field lines promote the particle concentration in a given region.

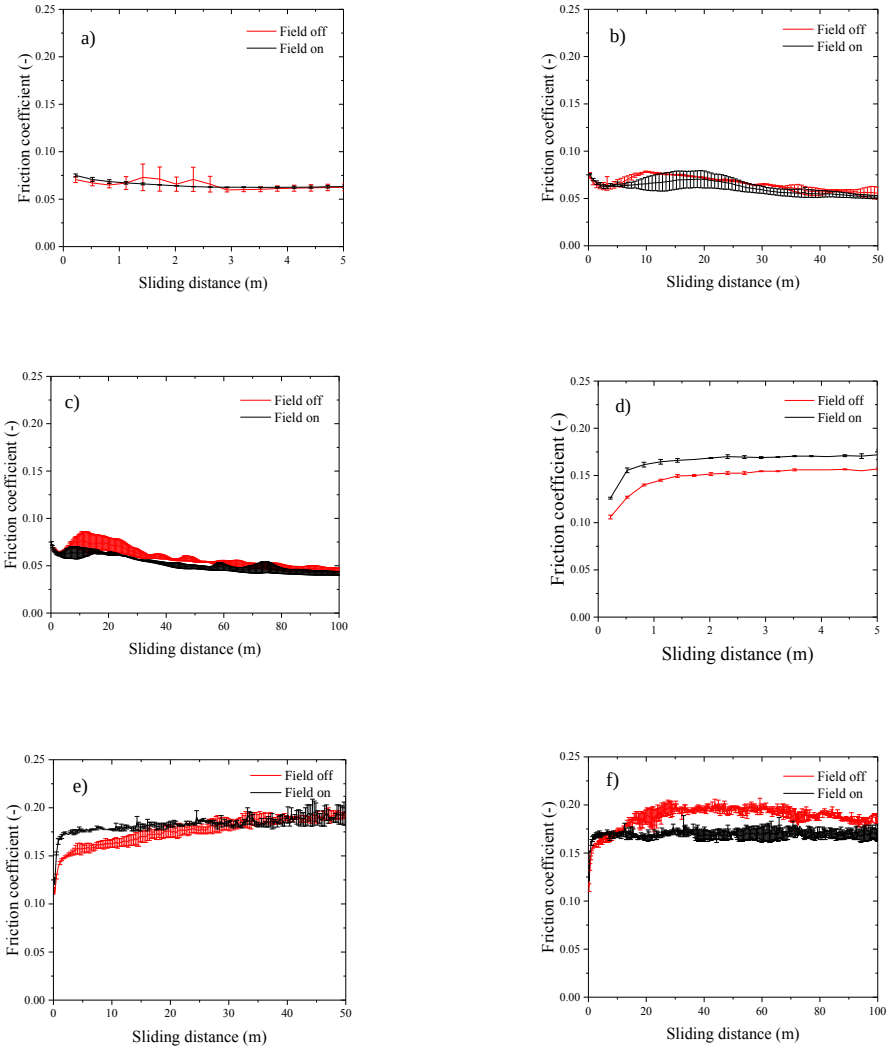

Figure 9. Friction coefficient as a function of sliding distance for a constant sliding speed of 0.3 $m \cdot s^{-1}$. FN = 10 N. a-c) Ferrofluid. d-f) MR fluid. “Field on” corresponds to the results obtained using bar magnets.

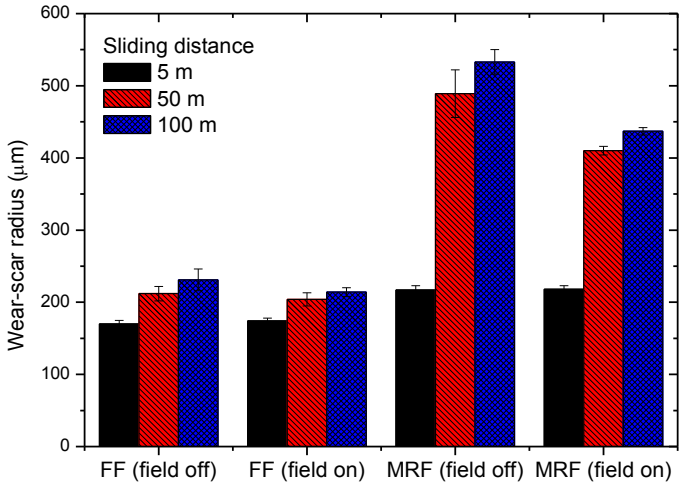

Figure 10. Wear-scar radii in steel plates lubricated with the ferrofluid (FF) and MR fluid (MRF) for three different sliding distances (i.e., 5, 50, and 100 m) at a sliding speed of 0.3 $m \cdot s^{-1}$. FN = 10 N. "Field on" corresponds to the results obtained using bar magnets.

CONCLUSIONS

The tribological behavior of ferrofluid and MR fluid lubricated steel-steel point contacts has been compared in a custom-built experimental set-up both in the absence and presence of magnetic fields. Stribeck curves reveal that the ferrofluid is capable to form a lubricating thin-film at large enough sliding speeds. In contrast, the MR fluid operates well within the boundary lubrication regime whatever the sliding speeds. The lower friction coefficients measured under lubrication with the ferrofluid indicate that the effect of particle concentration in the magnetic suspension dominates over that of particle size. These lower friction values correlate well with a lower extent of the wear damage. The superposition of a magnetic field during the rubbing tests does not have any significant frictional effect for the ferrofluid lubricated contacts. However, in the case of the lubrication with the MR fluid a slight friction reduction is observed as a result of the concentration of the iron particles within a confined region. The effect of magnetic field in the frictional properties of the MR fluid lubricated contacts is more noticeable with increasing the sliding distance.

In the case of the ferrofluid lubrication the sliding wear occurs mainly by two-body abrasion with no or little three-body abrasion and noticeable ploughing. On the other

hand, in the case of MR fluid lubrication the sliding wear occurs by two-body and three-body abrasion with appreciable material removal induced by microcutting.

REFERENCES

[1] J. M. Ginder, Behavior of magnetorheological fluids, MRS Bulletin, August (1998) 26-29.

[2] G. Bossis, O. Volkova, S. Lacis, A. Meunier, Magnetorheology: fluids, structures and rheology. In: S. Odenbach (Ed) Ferrofluids. Magnetically controllable fluids and their applications (Lecture notes in Physics, 594, Springer-Verlag 2002) pp 202-230.

[3] D. J. Carlson, Critical factors for MR fluids in vehicle systems, Int. J. Vehicle Des. 33 (2003) 207-217.

[4] B. J. Park, F. F. Fang, H. J. Choi, Magnetorheology: materials and application, Soft Matter 6 (2010) 5246-5253.

[5] S. Odenbach, Magnetoviscous Effects in Ferrofluids, Springer (2010).

[6] J. de Vicente, D. J. Klingenberg, R. Hidalgo-Álvarez, Magnetorheological fluids: a review, Soft Matter 7 (2011) 3701-3710.

[7] N. M. Wereley, Magnetorheology: Advances and Applications, Royal Society of Chemistry (2013).

[8] C. H. Lee, D. W. Lee, J. Y. Choi, S. B. Choi, W. O. Cho, H. C. Yu, Tribological characteristics modification of magnetorheological fluids, Journal of Tribology 133 (2011) 031801.

[9] W. -L. Song, S. -B. Choi, J. -Y. Choi, C. -H. Lee, Wear and friction characteristics of magnetorheological fluid under magnetic field activation, Tribology Transactions 54 (2011) 616-624.

[10] Z. D. Hu, H. Yan, H. Z. Qiu, P. Zhang, Q. Liu, Friction and wear of magnetorheological fluid under magnetic field, Wear 278-279 (2012) 48-52.

[11] A. J. F. Bombard, J. de Vicente, Thin-film rheology and tribology of magnetorheological fliuds in isoviscous-EHL contacts, Trib. Lett. 47 (2012) 149-162.

[12] A. J. F. Bombard, J. de Vicente, Boundary lubrication of magnetorheological fluids in PTFE/steel point contacts, Wear 296 (2012) 484-490.

[13] J. de Vicente, A. J. F. Bombard, "Thin-film Rheology and Tribology of Magnetorheological Fluids" in Magnetorheology: Advances and Applications, Royal Society of Chemistry, 2013.

[14] V. R. Iyengard, A. A. Alexandridis, S. C. Tung, D. S. Rule, Wear testing of seals in magneto-rheological fluids, Tribol. Trans. 47 (2004) 23-28.

[15] R. E. Rosensweig, G. Miskolczy, F. D. Ezekiel, Magnetic fluid seals, Machine Design 28 (1968) 145.

[16] I. Tarapov, Movement of a magnetizable fluid in lubricating layer of a cylindrical bearing, Magnetohydrodynamics 8 (1972) 444-448.

[17] R. E. Rosensweig, Thermomechanics of magnetic fluids (1978) p. 231.

[18] V. K. Agrawal, Magnetic fluid based porous inclined slider bearing, Wear 107 (1986) 133-139.

[19] R. C. Shah, M. V. Bhat, Anisotropic permeable porous facing and slip velocity on squeeze film in an axially undefined journal bearing with ferrofluid lubricant, J. Magn. Magn. Mat. 279 (2004) 224-230.

[20] H. S. Chang, C. Q. Shi, P. Z. Zhao, A theoretical and experimental study of ferrofluid lubricated four-pocket journal bearings, Journal of Magnetism and Magnetic Materials 65 (1987) 372-374.

[21] C. Q. Chi, Z. S. Wang, P. Z. Zhao, Research on a new type of ferrofluid-lubricated journal bearing, J. Magn. Magn. Mater 85 (1990) 257.

[22] T. A. Osman, G. S. Nada, Z. S. Safar, Static and dynamic characteristics of magnetized journal bearings lubricated with ferrofluid, Trib. International 34 (2001) 369-380.

[23] W. Li-jun, G. Chu-wen, Y. Ryuichiro, W. Yue, Tribological properties of Mn-Zn-Fe magnetic fluids under magnetic field, Tribology International 42 (2009) 792-797.

[24] S. W. Lingard, A. Bullough, W. M. Shek, Tribological performance of an electrorheological fluid, J. Phys. D: Appl. Phys. 22 (1989) 1639-1645.

[25] W. I. Kordonski, S. D. Jacobs, Magnetorheological finishing. Int. J. Mod. Phys. B 10 (1996) 2837-2848.

[26] W. I. Kordonski, A. Shorey, Magnetorheological (MR) jet finishing technology, Journal of Intelligent Material Systems and Structures 18 (2007) 1127-1130.

[27] W. I. Kordonski, S. Gorodkin, Material removal in magnetorheological finishing of optics, Applied Optics 50 (2011) 1984-1994.

[28] D. K. Singh, V. K. Jain, V. Raghuram, R. Komanduri, Analysis of surface texture generated by a flexible magnetic abrasive brush, Wear 259 (2005) 1254-1261.

[29] S. Jha, V. K. Jain, Modeling and simulation of surface roughness in magnetorheological abrasive flow finishing (MRAFF) process, Wear 261 (2006) 856-866.

[30] J. Seok, S. O. Lee, K. -I. Jang, B. -K. Min, S. J. Lee, Tribological properties of a magnetorheological (MR) fluid in a finishing process, Tribology Transactions 52 (2009) 460-469.

[31] A. Saqid, M. S. Shunmugam, A novel method to improve finish on non-magnetic surfaces in magnetorheological abrasive honing process, Tribology International 43 (2010) 1122-1126.

[32] P. L. Wong, W. A. Bullough, C. Feng, S. Lingard, Tribological performance of a magneto-rheological suspension, Wear 247 (2001) 33-40.

[33] W. A. Bullough, P. L. Wong, C. Feng, W. C. Leung, Fundamental boundary tribology: ESF, Journal of Intelligent Materials and Structures 14 (2003) 71-78.

[34] W. C. Leung, W. A. Bullough, P. L. Wong, C. Feng, The effect of particle concentration in a magneto rheological suspension on the performance of a boundary lubricated contact. Proc. I. Mech. E. J. 218 (2004) 251-263.

[35] J. W. Sohn, S.-B. Choi, C. -H. Lee, M. -W. Cho, Wear characteristics of magnetorheological fluid under boundary lubrication, Advanced Materials Research 79-82 (2009) 83-86.

[36] P. Heyer, J. Läuger, Correlation between friction and flow of lubricating greases in a new tribometer device. Lubr. Sci. 21 (2009) 253-268.

CHAPTER 6

On the Importance of Carrier Fluid Viscosity and Particle-wall Interactions in Magnetic Guided Assembly of Quasi-2D systems

Keshvad Shahrivar, Elizabeth Carreón-González and Juan de Vicente

Submitted for publication

Abstract

We demonstrate the influence of experimental conditions (carrier fluid viscosity and particle-wall interactions -friction-) on the quasi-2D deterministic aggregation kinetics of carbonyl-iron magnetic suspensions in rectangular microchannels. On the one hand, the carrier fluid viscosity determines the time scale for aggregation. On the other hand, friction strongly determines the aggregation rate and therefore the kinetic exponent (mean cluster size versus time dependence). When particle-wall interactions are weak the mean cluster size increases with a power of 0.65 ± 0.06, for open cavities (≥ 500 microns channel width), in very good agreement with theories and particle level simulations. However, when the particle-wall interactions are strong the kinetic exponent decreases and the aggregation is eventually arrested. This work suggests that particle-wall interactions may be one of the reasons for the discrepancies found in the experimental determination of the aggregation kinetic exponents in the literature.

INTRODUCTION

The aggregation kinetics of magnetic suspensions has been thoroughly studied in plenty of experimental works reported in the literature.[1-8] Most of these works concentrate on quasi-2D aggregation processes. Despite the fact that the values of the kinetic exponents are a finger print of the aggregation process,[3,6,9-11] a surprisingly large discrepancy is typically found between reported scaling exponents (especially in the case of magnetic latexes).[10] In this context, the quality of the experiments reported in the literature has been recently questioned.

Experimentalists are aware that aggregation tests are delicate and require many precautions. For instance, Cernak *et al.*[12] reported remarkable difficulties in reproducing experimental data. Also, Erb *et al.*[13] took special precautions to clean the confining surfaces in order to avoid the particles being stuck onto them. More recently, Domínguez-García *et al.*[10] observed that the kinetic exponents were strongly dependent on the surfactant concentration used to stabilize the suspensions.

Undoubtedly, one point of outstanding interest concerns particle-wall interactions especially because 2D aggregation typically occurs onto a flat planar surface holding a monolayer of sedimented particles. It is well known that in the particular case of inverse ferrofluids, particle-wall interactions are negligible because of *image dipoles* created on the walls that repel the non-magnetic particles to the center of the ferrofluid layer.[12,13] However, this is not the case in conventional magnetic particle suspensions that are of more practical interest. Pioneering works devoted to the aggregation of magnetic latexes did not employ surfactants.[2,14] Under these circumstances it is not surprising that adhesion of the particles to the walls was observed.[14] In an attempt to improve the kinetic stability of the suspensions and to avoid particle-wall adhesion, other authors added a range of surfactants to the formulations. Among them, sodium dodecyl sulfate seems to be a preferred choice and has been added to aqueous suspensions of magnetic latex by many authors (e.g. refs. 3 , 4). In other cases, glycerol:water mixtures are used to slow-down particle diffusion.[5,15,16] Other researchers deliberately introduced electrostatic repulsion between particles and walls (e.g. COOH functionalized polystyrene particles and glass surfaces in ref. 17). In this manuscript we aim to systematically study the influence of relevant experimental conditions (i.e. carrier fluid viscosity and surfactant concentration) in the particle-wall interactions and aggregation kinetics of carbonyl iron suspensions. Carbonyl iron particles are chosen because they are extensively used in the formulation of magnetorheological fluids.[18-22]

Surprisingly, particle-wall interactions are neglected in most of the theoretical analyses and simulations despite the fact that there are some evidences that particle-wall interactions could play a crucial role in the aggregation dynamics observed in the experiments. For instance, abnormally small kinetic exponents could be ascribed to possible particle-wall adhesion (e.g. Fig 3 in ref. 6). In their paper, Černák *et al.*[6]

showed that for the largest sizes investigated (14 microns diameter), the mean cluster size increased very slowly, possibly because of sticking between the particles and the walls. More recently, Reynolds *et al.*[8] observed that a fraction of particles was pinned to the confining wall and this hindered the growth of the clusters, particularly at long times as they are incorporated into chains. Another anomalous behaviour concerns the characteristic aggregation time. Domínguez-García *et al.*[9] determined it using theory, experiments and simulations. They demonstrated that the experimental aggregation time was three orders of magnitude larger than both theoretical results and simulations. A possible explanation for this could be the existence of particle-wall interactions.[9] In this manuscript, experimental results are compared to particle-level simulations incorporating particle-wall friction.

THEORY AND SIMULATIONS

The aggregation behaviour of magnetic suspensions has been extensively reported in the literature with special emphasis in the aggregation performance on 2D planar surfaces. There are two governing parameters: the packing fraction ϕ_{2D} (i.e. particle area fraction) and the Lambda ratio λ (i.e. the ratio between the magnetic inter-particle interaction to thermal energy). In fact, the field-driven aggregation phenomena can be described using two length scales involving these dimensionless numbers: i) $R_\phi = \sqrt{\pi} a \phi_{2D}^{-1/2}$ i.e. the initial average interparticle distance, ii) $R_m = 2a\lambda^{1/3}$ i.e. the distance at which the magnetostatic interparticle interaction energy is equal to the energy of thermal fluctuations.[9,23] In the case where $R_\phi > R_m$, the aggregation process is slow and limited by diffusion. On the other hand, when $R_m > R_\phi$, the aggregation process is fast and ballistic. In the present work we are interested in the deterministic aggregation process in carbonyl iron suspensions where $\lambda \gg 1$ and therefore $R_m > R_\phi$.[24]

The kinetics of irreversible aggregation is usually described in terms of the temporal evolution of the clusters size distribution, $n_s(t)$. Experimental and computer simulation methods show that the asymptotic behaviour at large times of the mean cluster size$S(t) = \sum_s s^2 n_s(t) / \sum_s s n_s(t)$ follows a power law behaviour: $S(t) \sim t^z$. Other statistical variables and dynamic exponents are sometimes used in the literature such as the average cluster length $l(t)$.[5,6,9]

The theory behind the deterministic aggregation process in the particular case of electric field-responsive colloids was first proposed by See and Doi.[25] According to their work, particles are treated as non-Brownian Hard Spheres and their motion is only dictated by a interparticle magnetic dipole-dipole interaction and a free-draining approximation to mimic particle-solvent interaction (i.e. Stokes drag). Clusters move isotropically and at a given time, all clusters have same size (e.g. N). Then after Δt they form clusters of size $2N$ and so forth. Obviously, it is a crude approximation but has recently been

successfully applied to capture the dynamics of non-Brownian magnetic suspensions as well [see for instance ref. 8].

In a deterministic aggregation process, the mean cluster size increases with time according to $S(t) = S(0)[1 + (t/t_s)^z]$ where the scaling time is $t_s \propto \frac{a^2}{D\lambda\phi_{2D}^{5/2}}$. With this, bearing in mind that the particle diffusion coefficient for an isolated particle is given by $D = \kappa_B T/6\pi\eta a$ we get that $t_s \propto \eta$. Therefore, the carrier fluid viscosity is expected to shift the $S(t)$ curves along the time axis without affecting the overall shape of the curves.

Particle level simulations were carried out using a well-established methodology that is successful in the description of magnetorheological suspensions in dilute conditions.[18-21,24] We assumed pair-wise point-dipole magnetostatic interparticle interactions, Hard Sphere repulsions (exponential like) and hydrodynamic drag (Stokes' law). Molecular dynamic simulations were performed in a rectangular simulation cell mimicking a 2D microchannel (Figure 1a). Upper and lower walls were stationary Hard walls separated by a fixed distance $L_z^* = 100$ (i.e. a microchannel width of 377 μm). No-slip boundary conditions were assumed on these walls. On the other hand, periodic boundary conditions were applied in the left and right walls. These walls were separated a distance L_x^*. The number of particles used in the simulations was always $N = 1000$. Hence, the particle surface fraction was tuned using the following expression: $\phi_{2D} = \frac{N\pi}{4L_z^* L_x^*}$. We neglected inertia to numerically solve the equation of motion for every particle within the ensemble. The equations of motion were integrated numerically using an explicit Euler method, with time step $\Delta t^* = 10^{-3}$ to ensure a stable convergence of integration.

In some simulations, friction between particles and walls was included in the code in a very simplified way. In each time step, if the total horizontal force acting on a particle nearby a wall is smaller than $\mu_s F_N$ then the particle is considered to be at rest. Here, μ_s and F_N are the static friction coefficient and the normal force acting on the particle, respectively. However, if the total force acting on the particle is larger than $\mu_s F_N$ then a frictional force equal to $\mu_D F_N$ and opposite to the direction of the total force is applied. Here, μ_D is the dynamic friction coefficient and for convenience it was chosen to be $\mu_D = 0.7\mu_s$. Using a different dynamic friction coefficient does not qualitatively affect the results reported in this manuscript.

EXPERIMENTAL

Carbonyl iron particles used in this work were from BASF SE (EW grade). These particles are mostly pure iron (> 96.8 %) but have a very thin silica coating that promotes their redispersibility in suspension. They are quasi-spherical in shape with

diameter $d_{50} \approx 3.0$ μm and density of $\rho = 7.86$ kg/m^3. The carrier fluids were formulated by mixing glycerol (Scharlau, Spain) and distilled water (Millipore). Additionally, a certain amount of sodium dodecyl sulfate (SDS) was added. SDS was purchased from Sigma-Aldrich and used as received. Suspensions were prepared by thoroughly mixing the carbonyl iron particles in the carrier fluid according to the following protocol: i) first, the required amount of SDS was mixed within the glycerol:water mixture, ii) then, magnetic particles were added and the suspension was manually stirred for 5 minutes and iii) finally, the suspension was ultrasonicated for 5 more minutes.

The viscosity of the glycerol:water mixtures was ascertained in a stress-controlled torsional rheometer (Anton Paar) MCR 302 using a cone-plate (1º, 50 mm diameter) geometry. The tests were performed using the following protocol: (i) First, the sample was preconditioned at a constant shear rate of 100 s^{-1} for 1 minute; (ii) second, the shear rate was linearly increased from 0.001 s^{-1} to 1000 s^{-1}. The acquisition time was 10 seconds per data point.

Figure 1b depicts the experimental set-up used in this work to study the aggregation kinetics of carbonyl iron particles. The aggregation tests were carried out in rectangular polydimethylsiloxane (PDMS) microchannels (25 μm depth, 500 μm width), fabricated using conventional Soft Lithography techniques. After carefully pumping the suspension inside the microchannels, we waited for about 15 more minutes before starting the experiment in order to make sure that the particles settled. All experiments were repeated at least three times. In this work, the particle volume fraction was fixed at $\phi \approx 1 \times 10^{-4}$. This corresponds to a particle surface fraction of $\phi_{2D} = 0.024 \pm 0.001$. Aggregation was induced under external uniaxial DC fields in the 2D plane perpendicular to the channel walls (see Figure 1b). For the particular suspension formulation at typical field strengths (28.65 kA/m), the λ ratio was $\lambda \approx 10^6 \gg 1$. Therefore $R_m/R_\phi \approx 20$ and as a result, the aggregation was expected to the deterministic.

The image analysis was carried out using a pixel based cluster detection algorithm to detect clusters of particles following Ref. 24. Briefly, the image was converted to a grayscale image by removing the hue and saturation values while keeping only the luminescence information. Thresholding of images in order to obtain a binary image and remove errors due to background noise and out-of-focus particles was carried out using Otsu method.[26,27] The algorithm locates particles in neighbouring positions of every particle by finding dark pixels around every pixel (maximum of 8 neighbouring pixels). Clusters are then detected by tracing out neighbours of each pixel and organizing them into individual groups until the boundary, with no dark pixels surrounding it, is demarcated.

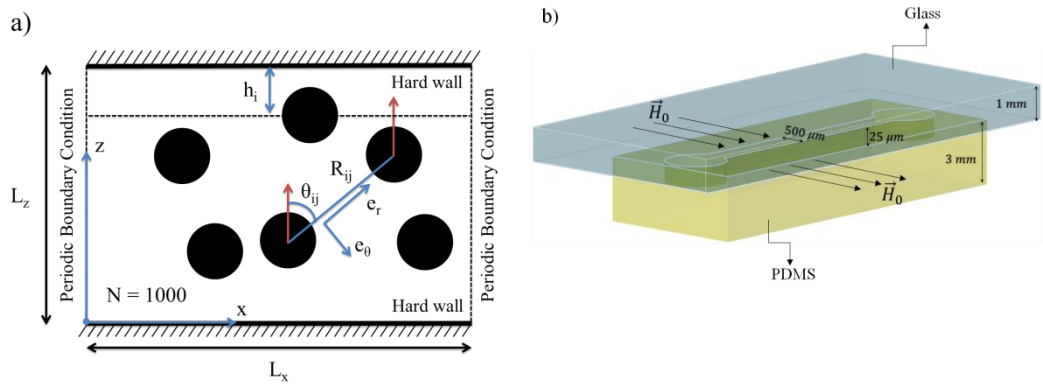

Figure 1. Panel a) Simulation cell. b) Schematic depiction of the experimental set-up (not to scale).

RESULTS AND DISCUSSION

Experiments were conducted in carbonyl iron suspensions for different carrier fluid viscosities and SDS concentrations. On the one hand, particle diffusivity was reduced by increasing the glycerol content in glycerol:water mixtures. On the other hand, particle-wall interactions were reduced by the addition of SDS.

The viscosities of the different glycerol:water mixtures studied in this work are shown in Table 1. As expected, the shear viscosity increases upon increasing the amount of glycerol in the mixture. The addition of only 1 wt% SDS as a surfactant had a negligible effect in the viscosity values of the mixtures (results not shown for brevity).

Figure 2a shows the mean cluster size as a function of time $S(t)$ for carbonyl iron suspensions in glycerol:water mixtures. As observed, the initial aggregation state is strongly affected by the viscosity of the carrier fluid; $S(t \to 0)$ decreases when increasing the viscosity. This is clearly appreciated in Figure 3 where we show snapshots of the suspensions exactly at the beginning of the aggregation test ($t \to 0$). This effect was expected because particle diffusion is enhanced the lower the glycerol content in the mixture and therefore, the presence of a residual magnetic field in the electromagnetic circuit is capable to form aggregates in suspension before complete settling.

Interestingly, as observed in Figure 2b, the time dependence is reasonably well described with the scaling time obtained from our particle level simulations $t_s =$

$\frac{a^2}{69.8D\lambda\phi_{2D}^{2.614}}$. In accordance, the experimental power law behavior follows a slope of $z_{exp} = 0.65 \pm 0.06$ while the simulations predict a slope of $z_{sim} = 0.55 \pm 0.02$.

Table 1. Shear viscosity of glycerol:water mixtures at 25 ºC.

Glycerol:water	Shear viscosity (Pa·s)	Standard deviation
0:100	0.0009	1.2×10^{-6}
10:90	0.0012	6.9×10^{-7}
30:70	0.0020	2.2×10^{-6}
50:50	0.0041	6.6×10^{-5}
70:30	0.0102	1.9×10^{-5}
75:25	0.0146	7.5×10^{-5}
80:20	0.0200	7.5×10^{-5}
85:15	0.0304	1.4×10^{-4}
90:10	0.0450	1.4×10^{-4}
92:8	0.0530	1.3×10^{-4}
94:6	0.0650	1.6×10^{-4}
96:4	0.0778	9.0×10^{-5}
98:2	0.0943	3.5×10^{-5}
100:0	0.1250	7.4×10^{-5}

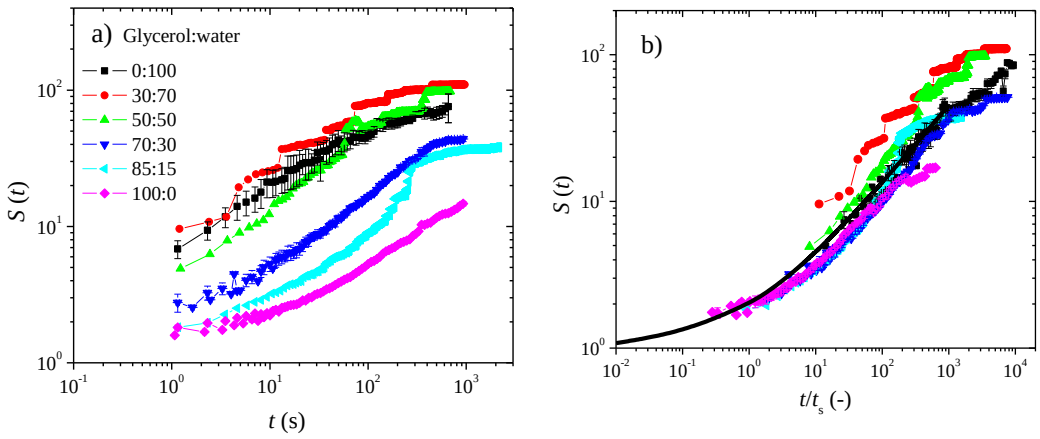

Figure 2. Aggregation kinetics of carbonyl iron suspensions in glycerol:water mixtures. a) Mean cluster size $S(t)$ as a function of time t. b) Mean cluster size $S(t)$ as a function of the reduced time t/t_s. Black solid line corresponds to particle-level simulations: $S(t) = 1 + (t/t_s)^z$ with $t_s = \frac{a^2}{69.8D\lambda\phi_{2D}^{2.614}}$ and $z = 0.55$. Particle surface fraction: $\phi_{2D} = 0.024 \pm 0.001$. Magnetic field strength: 6.22 kA/m. SDS concentration: 1 wt%.

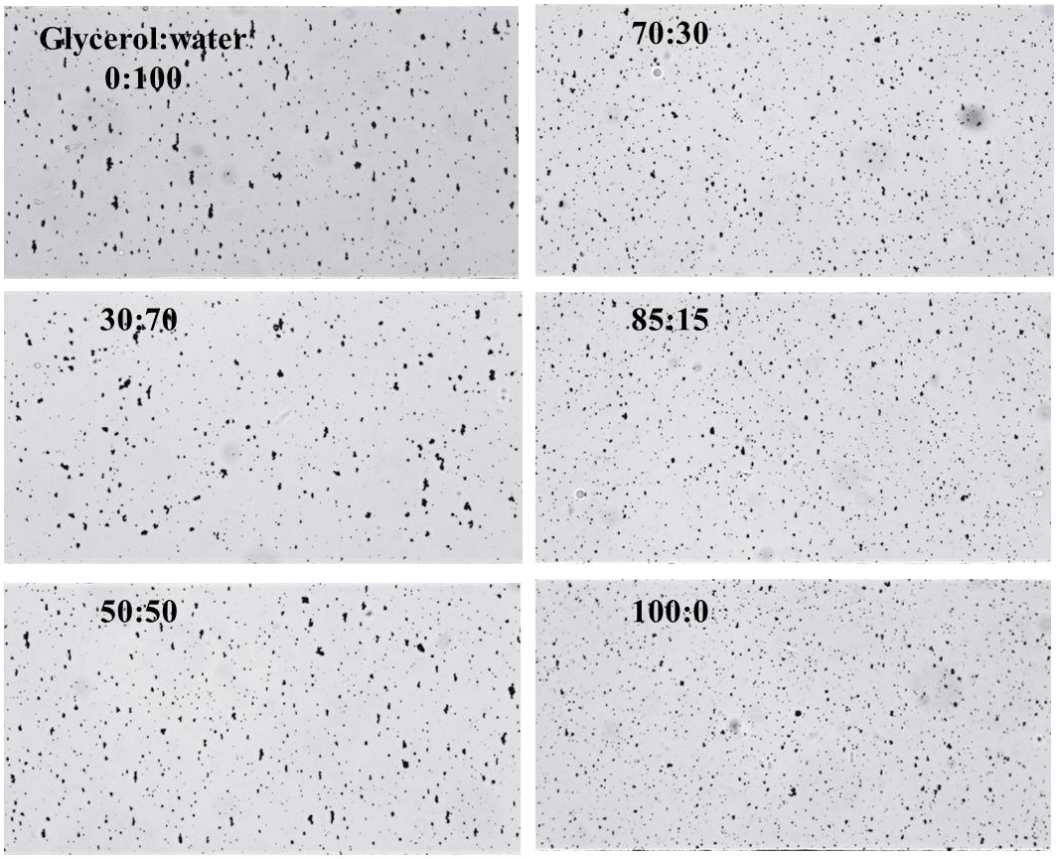

Figure 3. Initial aggregation state (prior to the application of the magnetic field) of the carbonyl iron suspensions in glycerol:water mixtures in the presence of 1 wt% SDS surfactant.

Bearing in mind that there are not free fitting parameters, the good collapse between experiments and simulations suggests that the aggregation regime is dominated by a deterministic aggregation process.

As expected, the addition of SDS to glycerol-based iron suspensions did not have a pronounced effect in the electrokinetic properties (results not shown here for brevity). This suggests that particle surface charge remains unchanged when adding SDS. This was corroborated from the visual observation of the suspensions for a given glycerol:water content at the initial stage prior to the aggregation process. For a constant $\phi = 10^{-4}$, image analyses revealed minor changes in ϕ_{2D} for the range of SDS concentrations explored in this manuscript; the standard deviation for ϕ_{2D} remained below 0.003. Despite the fact that the addition of SDS did not influence the surface charge of the particles, the addition of SDS was expected to enhance the lubrication

properties of the carrier with respect to the particle-wall tribopair. To test this hypothesis, we prepared a range of glycerol-based suspensions containing SDS in different proportions.

As anticipated above, the addition of SDS had a very important role on the particle-wall interactions. In Figure 4a we show the time evolution of the mean cluster size for carbonyl iron suspensions in glycerol at different SDS concentrations. As observed, aggregation is hampered in the absence of SDS. On the other hand, the curves overlap for SDS concentrations larger than 0.7 wt%. This suggests that particle-wall interactions are negligible for SDS concentrations above 0.7 wt%. Particle level simulations (neglecting friction) are plotted together with experimental data in Figure 4b. The collapse reinforces our hypothesis that frictional forces between particles and the wall are negligible for large SDS concentrations.

In order to elucidate the influence of friction in the aggregation process we also carried out particle level simulations explicitly incorporating friction between the particles and the wall. Results are shown in Figure 5. They clearly demonstrate that friction promotes the appearance of a plateau in the mean cluster size $S(t)$ for long times but does not affect t_s (see Figure 5b). As observed, simulation results including friction are in good qualitative agreement with experiments reported in Figure 4 for the lowest SDS concentrations.

The SDS concentration dependence of the dynamic exponent z and the maximum in the mean cluster size $S_{max} \equiv S(t \to \infty)$ are shown in Figure 6 together with particle level simulation results. Figures 6a and 6b show that both z and S_{max} increase when increasing the SDS concentration. Similarly, both z and S_{max} increase when decreasing the friction coefficient in particle level simulations (see Figures 6c and 6d). This suggests that the experimental observations for different SDS concentrations are correlated to a change in the effective friction coefficient between the particles and the walls (i.e. $[SDS] \propto 1/\mu_s$). The deterministic kinetic exponent ($z \approx 0.6$) is only observed when the SDS concentration is sufficiently large and therefore the particle/wall friction is sufficiently small. Concomitantly, the maximum in the mean cluster size sharply increases.

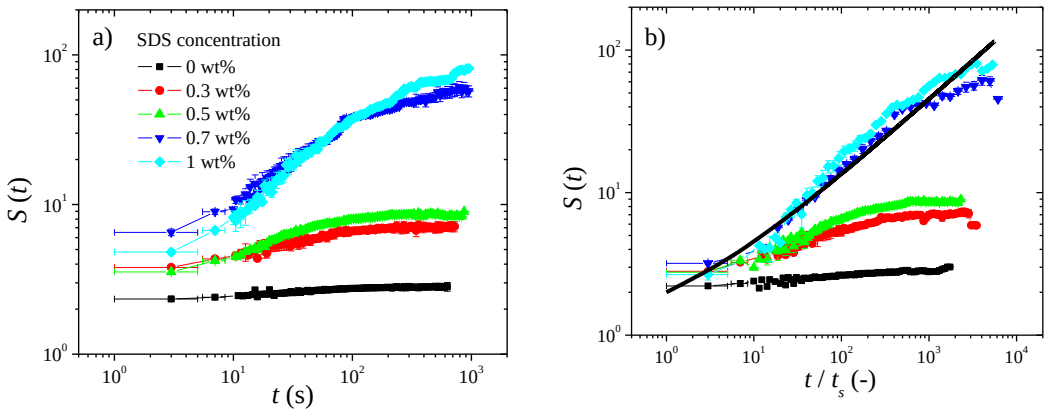

Figure 4. Aggregation kinetics of carbonyl iron suspensions for different SDS concentrations in glycerol-based suspensions. a) Mean cluster size $S(t)$ as a function of time t. b) Mean cluster size $S(t)$ as a function of the reduced time t/t_s. Black solid line corresponds to simulations: $S(t) = 1 + (t/t_s)^z$ with $t_s = \frac{a^2}{69.8D\lambda\phi_{2D}^{2.614}}$ and $z = 0.55$. Particle surface fraction: $\phi_{2D} = 0.024 \pm 0.001$. Magnetic field strength: 28.65 kA/m.

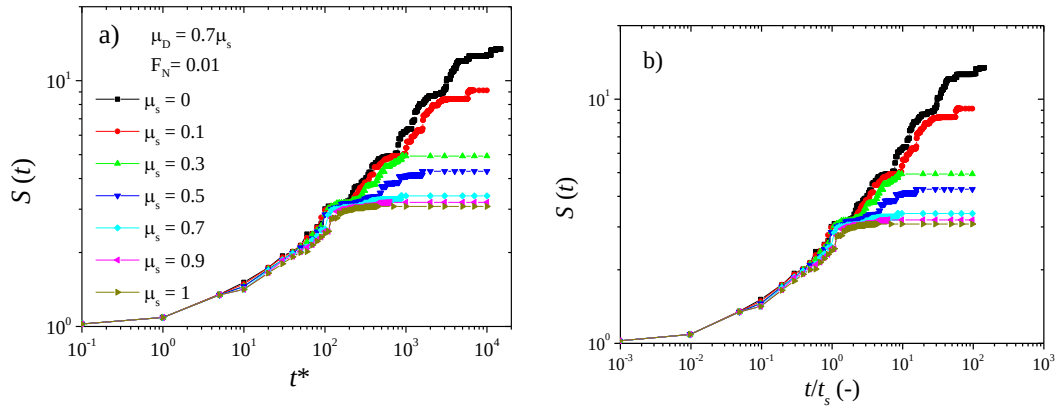

Figure 5. Particle level simulations of the aggregation process under different friction levels between particles and wall. $\mu_D = 0.7\mu_s$. $F_N = 0.01$. a) Mean cluster size S as a function of dimensionless simulation time t^*. b) Mean cluster size S as a function of reduced time t/t_s.

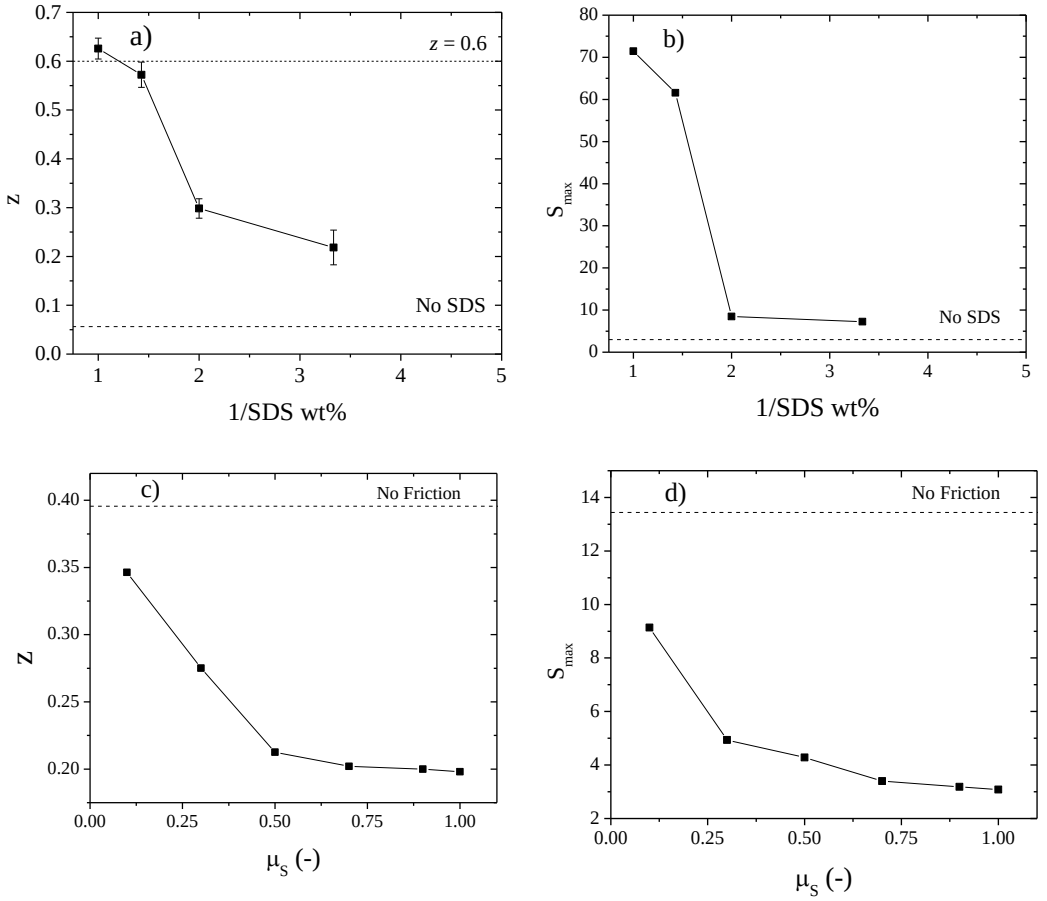

Figure 6. Dependence of the dynamic exponent z and the maximum in the mean cluster size $S_{max} \equiv S(t \to \infty)$ on the reciprocal of SDS concentration (from experiments: a and b) and friction coefficient (from simulations: c and d).

CONCLUSIONS

Even though there are plenty of experimental works dealing with the aggregation of magnetic particle suspensions, the variability in the reported kinetic exponents is still an open question. In this manuscript we demonstrate that they strongly depend on experimental conditions during the aggregation process.

In particular, we demonstrate that the time scale for the aggregation process changes with the carrier fluid viscosity. A stronger aggregation is observed at the initial times for

the less viscous carriers as a result of the enhanced diffusion of the particles. Experimental curves are in very good agreement with simulations under the frame of a deterministic aggregation process.

The surfactant (SDS) concentration drives the friction level between particles and the confining wall. Friction is reduced the larger the amount of SDS in the formulation. When particles interact strongly with the wall, aggregation is hindered and the mean cluster size remains essentially constant at a low value or slightly increases to reach a plateau. However, when friction is reduced (e.g. lubricating the particle-wall contacts with SDS) the mean cluster size increases following a deterministic aggregation process. Particle level simulations including friction are in good qualitative agreement with the experimental observations.

REFERENCES

(1) Jordan, P. C. Association phenomena in a ferromagnetic colloid. *Mol. Phys* **1973**, 25, 961.

(2) Helgesen, G.; Skjeltorp, A. T.; Mors, P. M.; Botet, R.; Jullien, R. Aggregation of magnetic microspheres: experiments and simulations. *Phys. Rev. Lett* **1988**, 61, 1736.

(3) Fermigier, M.; Gast, A. P. Structure evolution in a paramagnetic latex suspension. *J. Colloid Interface Sci* **1992**, 154, 522.

(4) Promislow, J. H. E.; Gast, A. P.; Fermigier, M. Aggregation kinetics of paramagnetic colloidal particles. *J. Chem. Phys* **1995**, 102, 5492.

(5) Melle, S.; Calderón, O. G.; Rubio, M. A; Fuller, G. G. Microstructure evolution in magnetorheological suspensions governed by Mason number. *Phys. Rev. E.* **2003**, 68(4), 41503.

(6) Černák, J.; Helgesen, G.; Skjeltorp, A. T. Aggregation dynamics of nonmagnetic particles in a ferrofluid. *Phys. Rev. E* **2004**, 70, 031504.

(7) Erb, R. M.; Krebs, M. D.; Alsberg, E.; Samanta, B.; Rotello, V. M.; Yellen, B. B. Beyond diffusion-limited aggregation kinetics in microparticle suspensions. *Phys. Rev. E* **2009**, 80, 051402.

(8) Reynolds, C. P.; Klop, K. E.; Lavergne, F. A.; Morrow, S. M.; Aarts, D. G. A. L.; Dullens, R. P. A. Deterministic aggregation kinetics of superparamagnetic colloidal particles. *J. Chem. Phys* **2015**, 143, 214903.

(9) Domínguez-García, P.; Melle, S.; Pastor, J. M.; Rubio, M. A. Scaling in the aggregation dynamics of a magnetorheological fluid. *Phys. Rev. E* **2007**, 76, 051403.

(10) Domínguez-García, P.; Pastor, J. M.; Rubio, M. A. Aggregation and disaggregation dynamics of sedimented and charged superparamagnetic micro-particles in water suspension. *Eur. Phys. J. E* **2011**, 34, 36.

(11) Vicsek, T.; Family, F. Dynamic scaling for aggregation of clusters. *Phys. Rev. Lett* **1984**, 52(19), 1669.

(12) Černák, J.; Helgesen, G. Aggregation of magnetic holes in a rotating magnetic field. *Phys. Rev. E* **2008**,78, 061401.

(13) Erb, R. M.; Son, H. S.; Samanta, B.; Rotello, V. M.; Yellen, B. B. Magnetic assembly of colloidal superstructures with multipole symmetry. *Nature* **2009**, 457, 999.

(14) Fraden, S.; Hurd, A. J.; Meyer, R. B. Electric-field-induced association of colloidal particles. *Phys. Rev. Lett* **1989**, 63, 2373.

(15) Silva, A.; Wirtz, D. Dominant diffusing mode in the self-similar phase separation of a magnetic suspension in a magnetic field. *Langmuir* 1998, 14(3), 578.

(16) Sohn, D. Kinetic studies of magnetic latex particles' self-assembly under applied magnetic field. *J. Magn. Magn. Mater* 1997, **173**, 305.

(17) Koser, A. E.; Keim, N. C.; Arratia, P. E. Structure and dynamics of self-assembling colloidal monolayers in oscillating magnetic fields. *Phys. Rev. E* **2013**, 88, 062304.

(18) Fernandez-Toledano, J. C.; Rodríguez-López, J.; Shahrivar, K., Hidalgo-Alvarez, R.; Elvira, L.; Montero de Espinosa, F.; de Vicente, J. Two-step yielding in magnetorheology. *J. Rheol* **2014**, 58, 1507.

(19) Wang, Z; Shahrivar, K; de Vicente ,J. Creep and recovery of magnetorheological fluids: Experiments and simulations. *J. Rheol* **2014**, 58(6), 1725.

(20) Klingenberg, D. J.; Ulicny, J. C.; Golden, M. A. Mason numbers for magnetorheology. *J. Rheol* **2007**, 51(5), 883.

(21) Kittipoomwong, D.; Klingenberg, D. J. Simulation of bidisperse magnetorheological fluids. *Int. J. Mod. Phys. B* **2002**, 16, 2732.

(22) de Vicente, J.; Klingenberg, D. J.; Hidalgo-Alvarez, R. Magnetorheological fluids: a review. *Soft Matter* **2011**,7, 3701.

(23) Melle, S.; Rubio, M. A.; Fuller, G. G. Time scaling regimes in aggregation of magnetic dipolar particles: scattering dichroism results. *Phys. Rev. Lett* 2001, **87**, 115501.

(24) Shahrivar, K.; Carreón-González, E.; Morillas, J. R.; de Vicente, J. Aggregation kinetics of carbonyl iron based magnetic suspensions in 2D. *Submited* **2017**.

(25) See, H.; Doi, M. Aggregation kinetics in electro-rheological fluids. *J. Phys. Soc. Jpn.*, **1991**, 60(8)**,** 2778.

(26) Otsu, N. A threshold selection method from gray-level histograms. *Automatica* **1975**, 11(285-296), 23.

(27) Zhang, J.; Hu, mage segmentation based on 2D Otsu method with histogram analysis. *Proc. 2008 Int. IEEE Conf. on Computer Science and Software Engineering* **2008**, 6, 105.

CHAPTER 7

Aggregation Kinetics of Carbonyl Iron based Magnetic Suspensions in 2D

Keshvad Shahrivar, Elizabeth Carreón-González, Jose R. Morillas and Juan de Vicente

Submitted for publication

Abstract

We investigate the (irreversible) two-dimensional aggregation kinetics of dilute non-Brownian magnetic suspensions in rectangular microchannels using video-microscopy, image analysis and particle-level dynamic simulations. Especial emphasis is given to carbonyl iron suspensions that are of interest in the formulation of magnetorheological fluids. The results are compared to non-Brownian suspensions of magnetic latexes. We demonstrate that both suspensions follow a deterministic aggregation process. Furthermore, experimental and simulation aggregation curves can be collapsed in a master curve when using the appropriate scaling time ($\propto \lambda^{-1}\phi_{2D}^{-2.5}$) as a function of only two dimensionless numbers: Lambda ratio (λ) and particle surface fraction (ϕ_{2D}).

INTRODUCTION

Magnetic suspensions are two-phase systems where at least one of the phases is magnetic field responsive. Of interest in this work are those magnetic suspensions where the particulate material is non-Brownian and has a typical size of above a micron. Two kinds of suspensions fulfil this condition: conventional magnetorheological (MR) fluids and inverse ferrofluids.[1,2] In the case of conventional MR fluids it is the particulate phase that is magnetic (either carbonyl iron or magnetic latex particles). In the case of inverse ferrofluids (also called magnetic holes) it is the carrier fluid that is magnetic (i.e. a ferrofluid). In this work, we are interested in conventional MR fluids and more specifically in carbonyl iron suspensions because they serve as a basis for MR fluids formulations.[3]

The aggregation kinetics of Brownian magnetic suspensions under uniaxial DC fields in quasi-2D confinement has been thoroughly investigated in the literature.[4-8] Most previous works showed that their aggregation kinetics can be explained in the frame of Diffusion Limited Cluster Aggregation (DLCA) theories.[9] Clearly, less works exists on non-Brownian suspensions. For instance, Černák and Helgesen[10] investigated the cluster formation in inverse ferrofluids and reported a discrepancy with Dynamic Scaling Theory for large particle sizes (14 μm diameter) for which Brownian motion was small. A similar finding was reported by Erb *et al.*[11]; they found that the scaling exponents were not compatible with the DLCA theory. More recently, Reynolds *et al.*[12] showed that chain formation of non-Brownian superparamagnetic latex particles is in agreement with a deterministic aggregation theory.

Under an external magnetic field, in the linear magnetization regime (low fields), an isolated magnetizable sphere of radius a acquires a magnetic moment $m = 4\pi\mu_0\mu_{cr}\beta a^3 H_0$, where μ_0 is the permeability of vacuum, μ_{cr} is the relative permeability of the continuous phase, $\beta = (\mu_{pr} - \mu_{cr})/(\mu_{pr} + 2\mu_{cr})$ is the contrast factor or coupling parameter, μ_{pr} is the relative permeability of the particles, a is the particle radius and H_0 is the external magnetic field strength. The magnitude of the magnetic interaction energy between two magnetic moments relative to the thermal energy is the so-called λ ratio:[2,13]

$$\lambda = \frac{\pi\mu_0\mu_{cr}\beta^2 a^3 H_0^2}{2\kappa_B T} \tag{1}$$

where $0 < \beta < 1$ for conventional MR fluids. For very small λ values Brownian motion dominates and field-induced aggregates are absent. However, for sufficiently large values of λ, magnetostatic particle interactions overcome thermal motion, resulting in

chain-like particle aggregates under uniaxial DC fields. In this work we are interested in the aggregation behaviour of conventional MR fluids for $\lambda \gg 1$ because this is the case of practical interest.

The structure evolution of dilute magnetic suspensions has been extensively studied in the literature using very different approaches depending on the size scale of the particles: video microscopy,[14,15] optical tweezers,[16] light scattering techniques,[17-20] and birefringence.[21] Interestingly, previous work demonstrates that the equilibrium structure is determined by only the particle concentration (ϕ) and the ratio between magnetostatic to thermal energy (λ).[22] This is illustrated in Figure 1 where the dominant mechanisms of lateral chain aggregation are mapped as a function of ϕ and λ.

It seems widely accepted that the aggregation kinetics in magnetic 2D systems involves two lengths scales (containing ϕ and λ): i) the distance at which the magnetostatic dipole-dipole interaction energy is equal to the energy of thermal fluctuations $R_m = 2a\lambda^{1/3}$, and i) the initial average interparticle distance: $R_\phi = \sqrt{\pi}a\phi_{2D}^{-1/2}$.[8,21,22] Here, ϕ_{2D} is the surface fraction of the particles. As a result, the ratio $R_m/R_\phi \propto \lambda^{1/3}\phi_{2D}^{1/2}$ determines whether the aggregation process is limited by diffusion ($R_m/R_\phi < 1$), or on the contrary, the aggregation process is deterministic (i.e. ballistic) ($R_m/R_\phi > 1$).

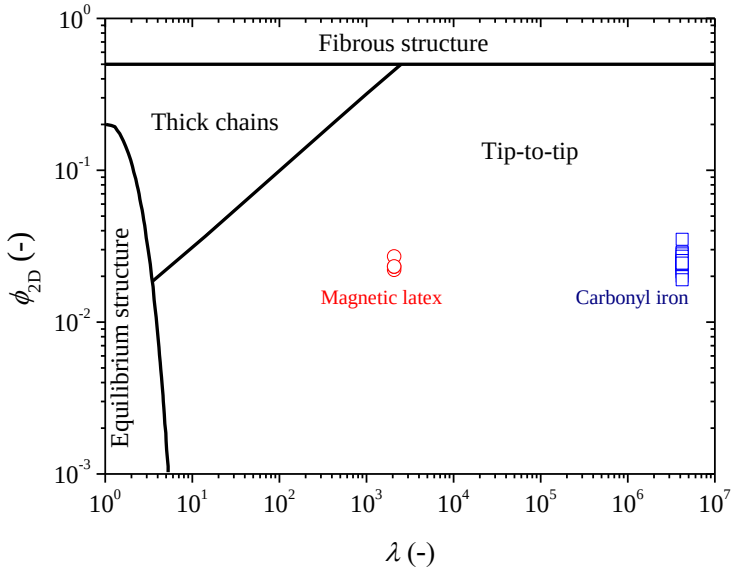

Figure 1. Aggregation regimes as a function of the dipolar interaction strength (λ) and the area fraction (ϕ_{2D}). Adapted from Figure 12 in Fermigier and Gast[5]. Represented in the regime map we also include experiments corresponding to this work.

In the particular case of carbonyl iron suspensions $\lambda \sim 10^6$ due to the large particle size (typically above a micron; $2a \geq 1\ \mu m$) even for small magnetic field strengths. On the other hand, the particle surface fraction is typically $\phi_{2D} \sim 10^{-2}$ to permit the optical visualization of the aggregation process and the comparison to particle-level simulations. As a result, under these conditions $R_m/R_\phi \sim 10 > 1$ and therefore, the aggregation is expected to be deterministic following a tip-to-tip mechanism[12,23] (c.f. Figure 1). However, in spite of the interest of these particles in the formulation of magnetorheological fluids, their aggregation kinetics has not been reported yet even in quasi-2D systems and in dilute conditions. A goal of this work is to ascertain whether the aggregation kinetics of carbonyl iron suspensions is truly deterministic. Another goal of this work is to compare their aggregation kinetics with traditional non-Brownian magnetic latex suspensions that are better understood.

EXPERIMENTAL

Magnetic particles

Carbonyl iron microparticles were a gift from BASF SE (Germany) (grade EW). In these particles, the iron content is greater than 96.8 %. According to the manufacturer, their average diameter is approx. ~ 3.0 μm and their density is $\rho = 7.86$ g/cm^3. A very thin surface layer of silica covers the iron core. This facilitates the re-dispersibility of the particles in suspension.[24]

Micronsized magnetic latexes were purchased from Nanogetic (Spain) and used for comparative purposes. These particles were prepared by first coating a layer of magnetic iron oxide onto a polystyrene core. Then an additional second polymer coating was applied to fully encapsulate the iron oxide shell. These latexes were functionalized with amino groups on their surface to minimize interparticle aggregation and particle/wall adhesion. The particles have a diameter of approx. ~ 5 μm, a density of ~ 1.1 g/cm^3 and a magnetic content of 5.72 wt% (determined from thermogravimetric analysis). Their polydispersity index is well below 0.027 which indicates a very high monodispersity. The major physical properties of the particles used in this work are summarized in Table 1.

Preparation of the magnetic suspensions

Magnetic suspensions were carefully prepared by mechanical dispersion of the carbonyl iron powder in glycerol (Sigma Aldrich) and magnetic latex in glycerol/water mixtures (1:1 in weight). A small amount of sodium dodecyl sulfate (SDS) was also added to the suspensions (1 wt%) to prevent particle aggregation and minimize particle surface interactions.

Table 1. Physical properties of the microparticles used in this work. (a) From image analysis of the deposited suspensions. (b) From magnetic hysteresis curves of the powders. (c) From thermogravimetric analysis. (d) From supplier datasheet.

Particle properties	Carbonyl iron particles	Magnetic latex
Mean diameter (μm) [(a)]	3.77	6.0
Density (g/cm^3)	7.86 [(d)]	1.1 [(c)]
Magnetic content (wt %)	96.8 [(d)]	5.72 [(c)]
Saturation magnetization (kA/m) [(b)]	796	4.8
Initial susceptibility (χ_i) [(b)]	0.12	0.08
Contrast factor (β) [(b)]	0.65	0.018

We followed a strict protocol as follows: i) the required amount of SDS was first mixed with the glycerol/water mixture, ii) the particles were added and the suspension was stirred -by hand for several minutes- and vortex mixed, and iii) the suspension was ultrasonicated for 5 minutes. We worked at a low particle concentration (volume fraction $\phi \approx 5 \times 10^{-4}$, surface fraction $\phi_{2D} \approx 0.02$). The relationship between the volume to surface fraction was empirically measured: $\phi_{2D} = 193.44\phi^{1.18}$for carbonyl iron powder and $\phi_{2D} = 11.55\phi^{0.96}$ for magnetic latex. All experiments reported in this work were performed on freshly prepared suspensions.

Fabrication of the confinement geometry

The magnetic suspensions were confined in a rectangular polydimethylsiloxane (PDMS) cell. For a precise control of the confinement geometry we used Soft Lithography techniques (i.e. *rapid prototyping* and *replica molding*).[25] With this, the cell depth is carefully controlled in contrast to previous works that typically use spacers. The master for each rectangular cell was created on a silicon wafer using an epoxy-based photoresist (SU 8). Then, PDMS was cast against a patterned master producing the moulded cell and openings for the connections. In more detail, PDMS specimens were fabricated from a two-component silicone elastomer kit (Sylgard^{TM} 184, Dow Corning); the base and curing agent in a mass ratio of 10:1. After manually mixing the two components, the mixture was introduced in a desiccator for degassing. Then, the mixture was poured over the master, and cured at room temperature for 24 hours. The final step was to release the elastomer from the master. In this way we obtained a PDMS replica with three of the four walls necessary to form a rectangular microchannel. In order to provide the fourth wall, the PDMS replica was sealed onto a plasma treated microscope

glass slide by heating at 175 ºC during 4 hours. PDMS cells used in this work were fabricated having microchannel widths of 500 µm and 1000 µm and a constant depth of 25 µm (see Figure 2a).

Opto-magnetic assembly and aggregation tests

The confinement geometry (i.e. rectangular microchannel) was placed on top of an inverted microscope (Leica DMI3000) provided with a home-made external electromagnetic circuit that was capable to generate uniaxial DC fields (up to approx. 50 kA/m) perpendicular to the flow direction.[26] A schematics of the assembly is shown in Figure 2a. We worked at low magnification and very thin depths (25 microns) to remain in a quasi-2D regime and to prevent the motion of the particles away from the microscope focal plane. The relatively large depth of field available at low magnification (approx. 8 microns) helped to keep the particles in focus. The external magnetic field applied (typically 30 kA/m) guaranteed a very large Lambda ratio: $\lambda = 10^6$ for carbonyl iron particles and $\lambda = 10^3$ for magnetic latexes (c.f. Figure 1). In all experiments reported in this work we waited for about 15 minutes before starting the experiment in order to make sure that the suspension settled. Therefore, our experimental system consisted of a monolayer of microparticles in a thin layer near the PDMS surface. We performed at least three aggregation trials and the distributions were averaged together.

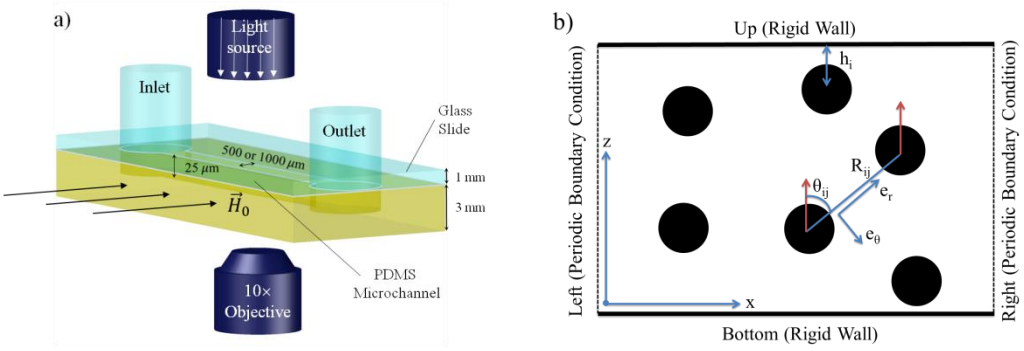

Figure 2. a) Schematic depiction of the experimental set-up (not to scale). b) Simulation box.

Image analysis

The image analysis was carried out using a pixel based cluster detection algorithm to identify clusters of particles. The raw image was converted to a grayscale image by removing the hue and saturation values while keeping only the luminescence

information. Then, thresholding was carried out to obtain a binary image and also to remove errors due to background noise and out-of-focus particles. Two image processing methods were used to analyse the images. i) Leica Software, ii) a Matlab subroutine by implementing Otsu method.[27,28] Both imaging processing methods gave approximately the same results as demonstrated in Annex I. The cluster detecting algorithm finds particles in neighbouring positions of every particle by detecting dark pixels around every pixel. Clusters are then detected by tracing out neighbours of each pixel and organizing them into individual groups until the boundary, with no dark pixels surrounding it, is delimited. We discarded regions that have an area below a critical value. This critical value was considered to eliminate small regions (smaller than the particle size) that still were detected due to background noise and out-of-focus shadow of the particles.

In order to calculate the statistical parameters describing the aggregation process, it was needed to relate the number of particles within a cluster to its corresponding surface area. From the raw data obtained via video microscopy analysis we get distinct clusters and their area in pixels. Suspensions reported in this manuscript are polydisperse in size so that it was necessary to assign a mean number of pixels to the surface area associated to an individual particle. Also, it was needed to calculate the number of particles in each cluster. Two possibilities were explored, either providing the number of clusters a fractional number or an integer number, both giving similar results. Results presented in this manuscript correspond to the second option.

PARTICLE-LEVEL SIMULATIONS

We followed a robust and well-tested methodology for the simulation of the aggregation process.[29-31] The magnetostatic force between the spheres was treated in the point-dipole limit. According to this, under the presence of a magnetic field $\vec{H} = H_0\hat{e}_z$, the force on a sphere i, at the origin of spherical coordinate system, due to sphere j, located at (R_{ij}, θ_{ij}), is given by (see Figure 2b):

$$\vec{F}_{ij}^{mag} = F_0\left(\frac{2a}{R_{ij}}\right)^4\left[\left(3\cos^2\left(\theta_{ij}\right) - 1\right)\hat{e}_r + \sin(2\theta_{ij})\hat{e}_\theta\right] \quad (2)$$

Here $F_0 = \frac{3}{4}\pi\mu_{cr}\mu_0 a^2\beta^2 H_0^2$ is the magnetic force scale. This approximation neglects multi-pole and multi-body interactions.

We assumed Hard Sphere repulsive interactions between particles (pp) and between particles and walls (pw). The short-range repulsive force on sphere i due to sphere j was mimicked as follows:

$$\vec{F}_{ij}^{pp} = -F_0 \exp\left(-\kappa \frac{R_{ij} - 2a}{2a}\right) \hat{e}_r \tag{3}$$

Short-range repulsive forces due to bounding surfaces were given by:

$$\vec{F}_i^{pw} = F_0 \exp\left(-\kappa \frac{h_i - a}{2a}\right) \hat{e}_w \tag{4}$$

Here, $\kappa = 100$ and h_i is the distance between the particles centre and the wall. $\hat{e}_w$ is the unit normal vector of the wall surface directed into the fluid. Hydrodynamic forces between spheres were neglected. For simplicity, the drag force acting on them was approximated using Stokes' law:

$$\vec{F}_i^{drag} = -6\pi\eta a \frac{d\vec{x}_i}{dt} \tag{5}$$

Neglecting particle inertia, the equation of motion for any sphere is given by:

$$\sum_{j \neq i} \vec{F}_{ij}^{mag} + \sum_{j \neq i} \vec{F}_{ij}^{pp} + \vec{F}_i^{pw} + \vec{F}_i^{drag} = 0 \tag{6}$$

Using characteristic length, force and time scales: $l_c = 2a$, $f_c = F_0$ and $t_c = 12\pi\eta a^2/F_0$, the equation of motion is transformed into dimensionless form:

$$\sum_{j \neq i} \vec{F}_{ij}^{mag*} + \sum_{j \neq i} \vec{F}_{ij}^{pp*} + \vec{F}_i^{pw*} = \frac{d\vec{x}_i^*}{dt^*} \tag{7}$$

According to the sketch shown in Figure 2b, $N = 1000$ particles were initially distributed randomly in a 2D rectangular simulation box. Up and Bottom walls were Stationary hard walls while Periodic Boundary Conditions were applied in the Left and Right walls. The distance between Up and Bottom walls, $L_z^* = 100$, determined the microchannel width, while the distance between the Left and Right walls, L_x^*, was given by the surface fraction according to: $L_x^* = \frac{N\pi}{4L_z^*\phi_{2D}}$. The equations of motion for each

sphere were integrated numerically using an explicit Euler method, with time step $\Delta t^* = 1 \times 10^{-3}$ up to $t^* = 10^5$. Inter-particle exponential repulsive interactions were evaluated for a surface-to-surface separation below a cut-off radius of $4a$. Also, particle-wall repulsive interactions were evaluated only for particles within a distance $h_i^* \leq 1.5$ from the walls.

RESULTS AND DISCUSSION

Representative experimental results for carbonyl iron suspensions are shown in Figure 3. This figure contains data for typical statistical variables in colloidal aggregation studies $S(t)$, $l(t)$, $N_c(t)$, $N_1(t)$ and $N_a(t)$ (see Table 2 for their definitions). As observed from Figure 3, at the initial time, $N_c > N_1$ and $N_a \neq 0$ meaning that there appears to exist initial aggregates in suspension because of poor redispersion and/or limited resolution of the microscope in the recognition of isolated particles. As the time increases, $S(t)$ rapidly goes up following a power law during at least one decade in time. Similar to Domínguez-García *et al.*[8] a power law region is shared between $S(t)$, $l(t)$, $N_c(t)$ and $N_1(t)$. Therefore, in this work, the dynamic exponents were calculated within the common region of power law behavior. The calculated power-law exponent z is included in Table 3 for the experiments reported in this work in comparison with other works in the literature. As observed, the values obtained for z in carbonyl iron suspensions are compatible with most results yet published on other Brownian magnetic suspensions, which report values of $z \approx 0.6$.

In the case of interest in this work, in the dilute regime, magnetized particles interact forming chain-like structures in the field direction. Due to the fact that the magnetic field strength is very large ($\lambda \gg 1$) aggregation is irreversible and structures grow infinitely with time following a power law unless the structures eventually connect the confining walls, which is not the case for the microchannel widths employed in this study. Similar to other experiments and simulations reported in the literature,[32] our aggregation experiments demonstrate the existence of two regions in time.

1) Quasi-static random structure: At short times $S(t)$ remains constant because of the large inter-particle distance and the existence of a large number of isolated particles in dispersion; $\lim_{t\to 0} S(t) = 1$. Typically, this region is hardly observed in experiments because of limited time resolution or initial inter-particle aggregation (c.f. Figure 3). To partially overcome this issue, in the current work we used glycerol/water mixtures as a dispersing carriers.

2) Tip-to-tip aggregation: For long times a power law dependence is found, $S(t) \propto t^z$, basically as a result of the formation of linear chains aggregating tip-to-tip parallel to the field. This is a transport-limited process that essentially produces a square root of time growth.[5] In practice, the kinetic exponent z is somewhat greater than $z = 0.5$.[8,10,11,32,33]

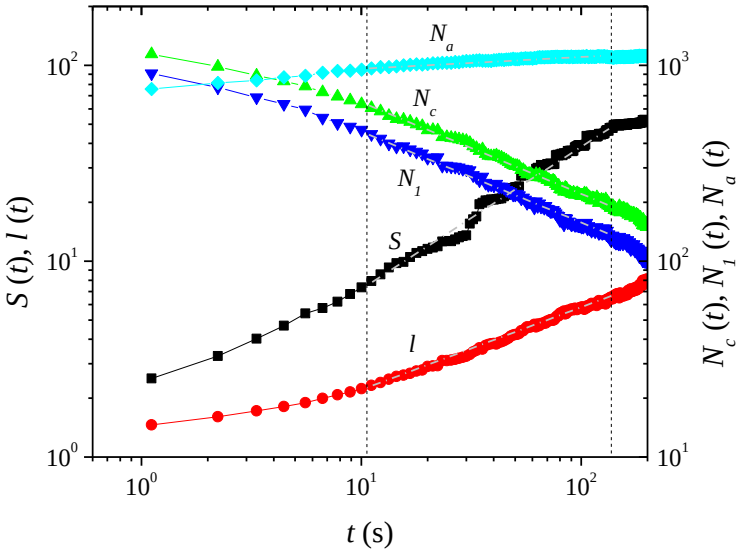

Figure 3. Evolution of the kinetic variables in a typical experiment involving a carbonyl iron suspension confined in a rectangular microchannel of width 500 μm ($L_z^* = 132.63$), $\phi_{2D} = 0.0239$, $H_0 = 28.65$ kA/m, $R_m/R_\phi \approx 20$ and $\lambda \approx 10^6$. The vertical lines indicate the region of power law behavior.

Table 2. Typical statistical variables and dynamic exponents used in the description of the aggregation kinetics. $n_s(t)$ stands for the clusters size distribution.

Symbol	Definition	Expression	Dynamic exponent
$S(t)$	Weight average cluster size at time t (*mean cluster size*) expressed in unit of $2a$	$S(t) = \sum_s s^2 n_s(t) \Big/ \sum_s s n_s(t)$	$\sim t^z$
$l(t)$	Number average cluster size at time t (*average length of the cluster*) expressed in unit of $2a$	$l(t) = \sum_s s n_s(t) \Big/ \sum_s n_s(t)$	$\sim t^{z'}$
$N_c(t)$	Total number of clusters at time t	$N_c(t) = \sum_s n_s(t)$	$\sim t^{-z'}$
$N_1(t)$	Number of non-aggregated (isolated) particles*	$N_1(t) = [n_s(t)]_{s=1}$	$\sim t^{-w}$
$N_a(t)$	Number of aggregated particles (i.e. the number of particles forming clusters)	$N_a(t) = \sum_{s\geq 2} s n_s(t)$	$\sim t^{\beta}$

Table 3. Comparison with literature results for dimensionless quantities and dynamic exponents. Experiments in this work correspond to a microchannel width of 500 μm ($L_z^* = 132.6$ for carbonyl iron and $L_z^* = 83.3$ for magnetic latex), ϕ_{2D} = 0.0239 and H_0 = 28.65 kA/m. Simulations in this work correspond to $L_z^* = 100$.

Reference	Suspension	$2a$ (μm)	λ	ϕ	z	z'
Experiments (this work)	Carbonyl iron	3.77	1.12×10^6 $R_m/R_\phi = 22$	0.024 ± 0.001	0.66 ± 0.03	0.42 ± 0.04
Experiments (this work)	Magnetic latex	6.16	3.7×10^3 $R_m/R_\phi = 3.4$	0.027± 0.003	0.32 ± 0.03	0.24+0.01
Simulations (this work)	-	-	-	0.020	0.55 ± 0.01	0.57 ± 0.01
Erb *el al.* [11] (a)	Inverse ferrofluid	10	4420	0.032	0.54	0.44
Domínguez-García *et al.*[8]	Magnetic latex	0.97	1422 $R_m/R_\phi = 3.3$	0.043	0.61	0.45
Domínguez-García *et al.*[8]	Simulation	-	1500 $R_m/R_\phi = 2.8$	0.03	0.42	0.44
Climent *et al.* [36 (a)]	Simulation	-	50	0.009	0.77	-
Promislow *et al.*[32 (a)]	Magnetic latex	0.6	4.3	0.0004	0.75 ± 0.01	-
Promislow *et al.*[32 (a)]	Magnetic latex	0.6	4.3	0.0020	0.51 ± 0.01	-
Černák *et al.*[6]; Černák[7]	Inverse ferrofluid	0.0114	2.3	0.021	0.786	0.67 ± 0.15
Fraden *et al.*[33]	ER fluid	1.27	15.5	0.009	0.60 ± 0.02	-

(a) In these works concentration was in vol %.

Figure 4a contains typical data corresponding to particle-level simulations. Obviously, in contrast to experimental results, initial aggregation phenomena are not observed and at the initial time, $N_c = N_1$; $S = l$ and $N_a = 0$. Overall, simulation data closely resemble those obtained in experiments (see Figure 3). Again, a power law region is observed and the short time region is better resolved. The simulation results are in very good agreement with Brownian dynamic simulations reported in Dominguez-García *et al.*[8] [see figure 7 in that paper] with the exception of the curve for N_a that in our case goes to zero at the initial times.

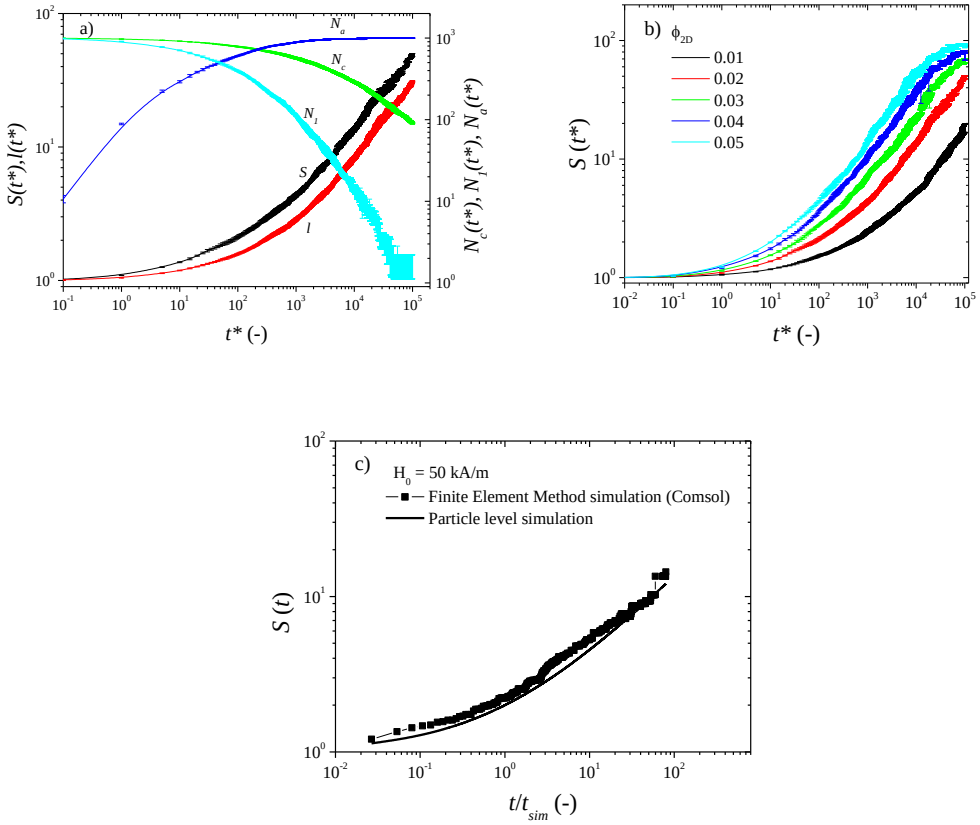

Figure 4. Simulation predictions for the aggregation process in $L_z^* = 100$ microchannels. a) Evolution of the kinetic variables in a typical numerical simulation at $\phi_{2D} = 0.02$, b) Mean cluster size as a function of dimensionless simulation time for different particle surface fractions ϕ_{2D}, c) Mean cluster size as a function of reduced time obtained from Finite Element Method calculations and particle-level simulations. Here, surface fraction is 0.025, $L_z^* = 75$ and $H_0 = 50\ kA/m$.

According to the discussion above, results within these two time regimes should collapse onto a master curve:[19,34]

$$S(t) = S(0)[1 + (t/t_s)^z] \tag{8}$$

Here $S(0)$ is a measure of the initial aggregation state ($S(0) = 1$ in disaggregated suspensions), z is the dynamic exponent and t_s is the scaling time. More precisely, t_s is the characteristic time it takes for two particles to come together. As a result, it should include ϕ and λ effects as these are the dimensionless characteristic numbers under no-flow condition.

Bearing in mind that the λ ratio dependence (i.e. the effect of magnetic field strength) is implicitly included in the linear magnetization assumption behind the simulation model, a vast amount of simulations was then carried out to explore the aggregation kinetics dependence on the other relevant dimensionless number i.e. the particle surface fraction. For this aim we explored particle surface fractions in the range $\phi_{2D} \in [0.01 - 0.05]$ that is accessible from an experimental point of view. Simulation results, shown in Figure 4b, can be scaled with the dimensionless time t^* and ϕ_{2D}. Indeed, using a non-linear least-squares fitting routine, similar to Reynolds *et al.*[12], all the curves reported in Figure 4b were collapsed onto a master curve given by the following expression: $S(t^*) = 1 + at^{*b}\phi_{2D}^c$. The parameters a, b and c obtained from the fitting are 20.2 ± 0.2, 0.55 ± 0.01 and 1.44 ± 0.05, respectively. As observed, the power law exponent b predicted by simulations ($z_{sim} = 0.55 \pm 0.01$) is reasonably close to that obtained in the experiments ($z_{exp} = 0.66 \pm 0.03$, see Table 3).

Rearranging the master curve equation for $S(t^*)$ obtained from the simulation data, the temporal evolution of the mean cluster size can be rewritten as Equation (8) with $S(0) = 1$, $t_s = t_{sim}$ and $z = b$. As a result, the aggregation kinetics is solely explained with two parameters: the kinetic exponent b and the simulation scaling time t_{sim}. Interestingly, t_{sim} can be represented as a function of D, λ and ϕ_{2D} as follows:

$$t_{sim} = \frac{a^2}{165.4D\lambda\phi_{2D}^{2.583}} \tag{9}$$

Here D is the diffusion coefficient for isolated particles: $D = \frac{k_B T}{6\pi\eta a}$. The simulation master curve is represented by the black solid line in Figure 4c.

As expected, our simulation scaling time t_{sim} is very similar to that obtained by See and Doi[23] under a theoretical formalism based on a deterministic aggregation process. Under their deterministic "hierarchical model" the Brownian motion of particles is ignored, all clusters have the same size at a given time and the force between them depends on their respective size. Additionally, the average spacing between the clusters increases during the aggregation process due to phase separation. It is also assumed that under magnetic fields, initially particles associate to form doublets after $t = t_1$, then these doublets continue to form quadruples after $t = t_2$, and so forth. For small particles of size "s" that are relatively separated and aligned with the magnetic field, the interaction energy

was approximated by multiplying s^2 by the inter-particle potential.[12] Furthermore, by taking the friction to be proportional to the cluster size and integrating the equation of motion from an initial position $R_i = R_\phi$ to a final one $R_f = 0$, a deterministic scaling time is obtained:

$$t_{det} = \frac{a^2}{13.72 D \lambda \phi_{2D}^{5/2}} \tag{10}$$

A similar expresion to Equation 10 can be obtained from Liu *et al.*[35] simply replacing the factor 13.72 by 27.44. As observed, both simulations (Equation 9) and theoretical predictions (Equation 10) are in very good aggreement with a power law of exponent 2.5 for the surface fraction ϕ_{2D}. Also, this value is very close to recent experiments by Reynolds *et al.*[12] on non-Brownian latexes that give an exponent of 2.44. It is worth to note here that, as expected, for sufficiently low particle concentrations, of interest in this work, the surface fraction dependence of the deterministic scaling time ($t_{det} \propto \phi_{2D}^{-2.5}$) is different to the surface fraction dependence of the brownian scaling time ($t_B \propto \phi_{2D}^{-1}$) (e.g. $t_B = \frac{a^2}{9.24 D \lambda \phi}$ in See and Doi[22]).

Our simulation data were also validated with Finite Element Method simulations (COMSOL Multiphysics). This allows to track particles position by solving Newton's law of motion (two second order differential equations are solved per particle) using a second-order implicit method. In these simulations, particles are driven by the same forces used in particle-level dynamic simulations (i.e. interparticle dipole-dipole interactions, exponential repulsive forces and Stokes' law; equations 2, 3 and 5) plus inertial forces (particle density was set 7.8 g/cm^3). Initially, a total of 216 particles (diameter 1 μm) were randomly distributed in a rectangular simulation cell of size $L_x = 90$ μm and $L_z = 75$ μm, corresponding to $\phi_{2D} = 0.025$. No-slip boundary conditions were applied, the magnetic field strength was fixed at $H_0 = 50$ kA/m and the viscosity of the dispersing medium was 1 mPa·s. Due to its Newtonian formulation and non-linear pair potential defined between particles, simulations were computationally expensive. As a result we used a small time step (≤ 10^{-8} s), a small number of particles (≤ 300) and the motion of the particles was tracked during only 0.03 s. Results shown in Figure 4c show a good agreement with the scaling time obtained from particle-level simulations. Hence validating our results.

A direct comparison between experiments and simulations is shown in Figure 5. Here we plot the mean cluster size $S(t)$ as a function of the dimensionless time t/t_{sim} for experiments (symbols) and simulations (line). Experiments correspond to carbonyl iron and magnetic latex suspensions at the same particle surface fraction $\phi_{2D} = 0.0239$ under an external magnetic field strength of H_0 = 28.65 kA/m.

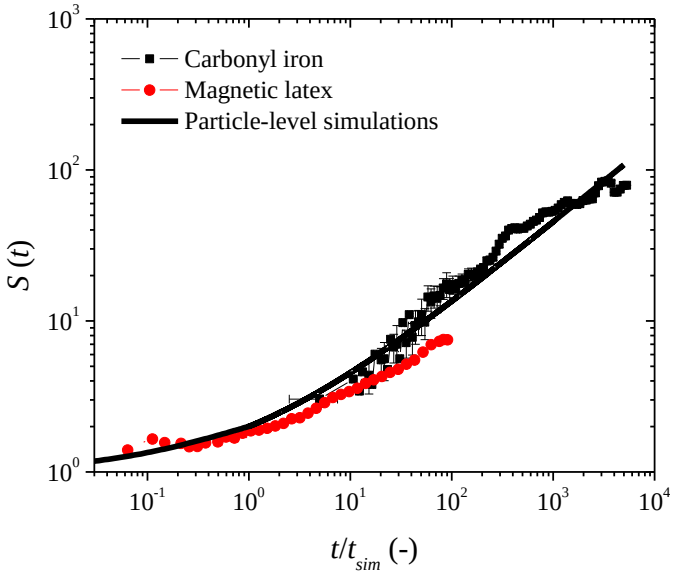

Figure 5. Master curve for carbonyl iron and magnetic latex suspensions using the simulation scaling time t_{sim}. Experiments are averages over at least three curves obtained for a microchannel width of 500 μm, $\phi_{2D} = 0.0239$ and $H_0 = 28.65$ kA/m. Together with experimental data we also plot the simulation predictions (solid line) according to $S(t) = 1 + (t/t_{sim})^b$ with $t_{sim} = \frac{a^2}{165.4D\lambda\phi_{2D}^{2.583}}$ and $b = 0.55$.

The black solid line corresponds to the particle-level simulation results. As observed, experiments and simulations overlap reasonably well.

Data corresponding to the magnetic latex are shifted to the left with respect to the carbonyl iron counterpart and therefore permit the exploration of the short time regime. This was something expected because of the difference in the contrast factor β that is closer to one for carbonyl iron particles. Indeed, in this particular case, for the magnetic field strength employed in the tests, $\beta = 0.65$ for carbonyl iron particles, while $\beta = 0.018$ for magnetic latexes.

To further demonstrate that the λ ratio is truly the governing parameter in the aggregation process, in Figure 6 we also show results for carbonyl iron and magnetic latex for the same value of the λ ratio. In other words, we plot experimental data having the same $R_m/R_\phi \propto \lambda^{1/3}\phi_{2D}^{1/2}$ for a constant ϕ_{2D}. As expected, experimental data overlap now in essentially the same time range and also together with the simulation curve (black line). This finding reinforces our statement that the aggregation process is fully deterministic in both experimental systems explored and that for a constant particle concentration, the governing parameter is solely the λ ratio. At this point it is worth to

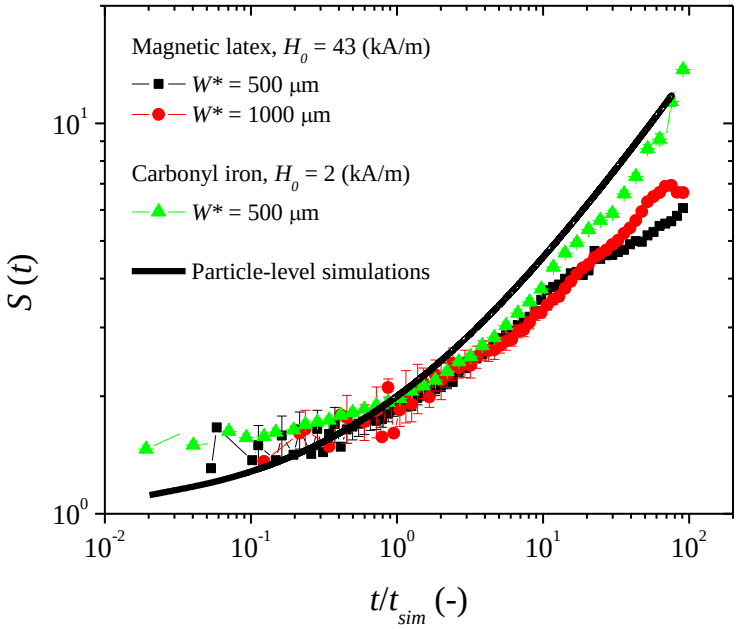

Figure 6. Scaling curve for carbonyl iron particles and magnetic latexes for the same λ ratio ($R_m/R_\phi = 3$) and $\phi_{2D} = 0.0239$. W^* stands for the microchannel width. Solid line corresponds to the particle level simulations data (see description in Figure 5).

remark that the deterministic aggregation process was further demonstrated by the fact that, in contrast to the predictions of the Dynamic Scaling Theory, $s^2 n_s(t)$ does not collapse when plotted against $s/S(t)$ in the power law region. These results are not shown here for brevity.

Finally, the fact that the tip-to-tip mechanism actually dominates the aggregation process is demonstrated by microscopy observations (Figure 7a) and average cluster width calculations (Figure 7b). A typical time sequence for the carbonyl iron particles under a magnetic field is shown in Figure 7a. As time progresses, clusters become longer. However, their thickness remains essentially unchanged suggesting a tip-to-tip aggregation mechanism. This observation was crosschecked calculating the average cluster width from image analysis. For this aim, for every cluster, the two axes of an ellipse placed at its centre of mass, and having the same normalized second central moment, are calculated. The average cluster width plotted in Figure 7b is an average of the minor axes lengths over all clusters at a given time. Interestingly, Figure 7b demonstrates that the average cluster width is essentially constant in time; deviations are less than 25 % reinforcing the fact that aggregation essentially follows a tip-to-tip mechanism and very few defect-driven aggregates are formed.

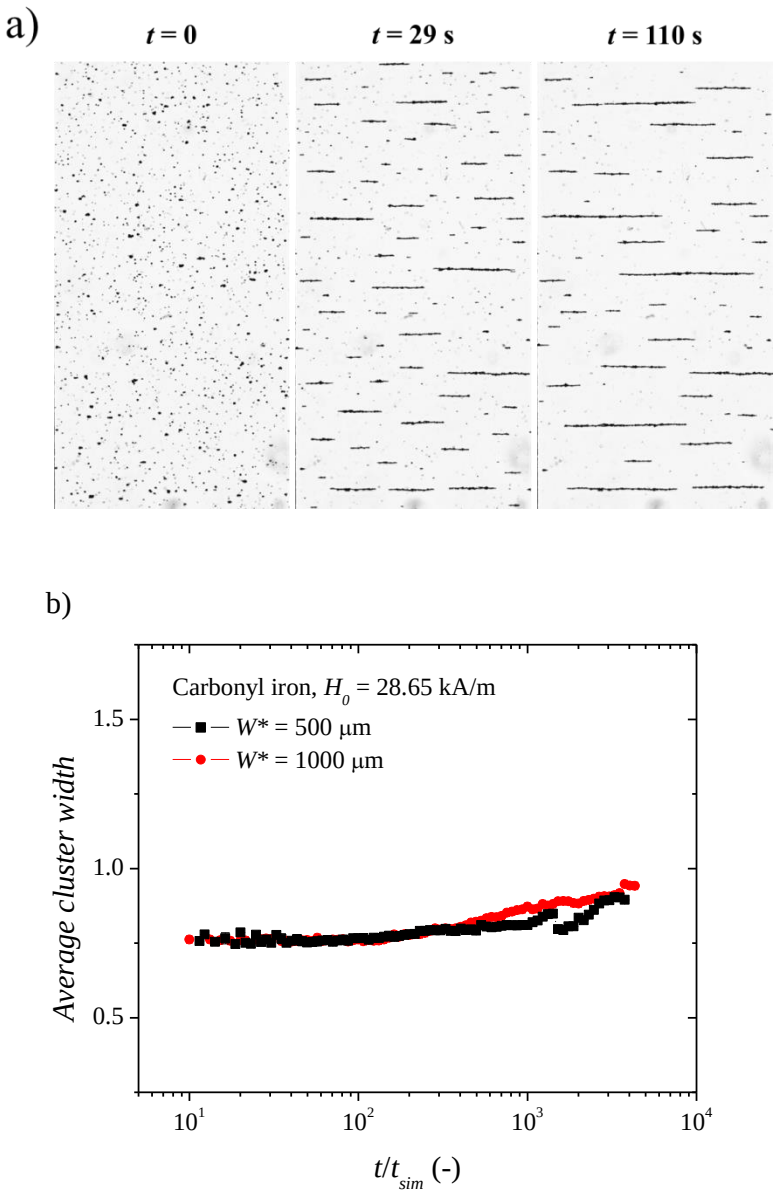

Figure 7. a) Time sequence of micrographs showing the growth of particle chains at several times: a) 0 s, b) 29 s and c) 110 s. Snapshots correspond to carbonyl iron suspensions under fields in a rectangular microchannel of width 500 μm. $\phi_{2D} = 0.0239$. $H_0 = 28.65\,\mathrm{kA/m}$. b) Average cluster width as a function of the reduced time for different channel widths W^* in carbonyl iron suspension.

CONCLUSIONS

We investigated the two-dimensional aggregation kinetics of dilute non-Brownian magnetic suspensions based on carbonyl iron microparticles of interest in magnetorheology using video-microscopy, image analysis and particle-level dynamic simulations. In experiments and simulations, we observed two regions in the evolution of the mean cluster size. First, an essentially constant regime ($S(t) \approx 1$) and then a power law region ($S(t) \propto t^z$) at longer times when the particles aggregate tip-to-tip in the field direction. The results demonstrate that both micronsized carbonyl iron and magnetic latex suspensions follow a deterministic aggregation process. Interestingly, experimental and simulation curves can be collapsed in a master curve when using the time scale $t_{sim} \propto \lambda^{-1}\phi_{2D}^{-2.583}$ obtained from particle-level (non-Brownian) dynamic simulations in agreement with a ballistic aggregation mechanism ($\propto \lambda^{-1}\phi_{2D}^{-2.5}$). By carrying out further experiments on carbonyl iron and magnetic latex suspensions at a fixed λ ratio ($R_m/R_\phi \sim 3$) we found a good collapse onto the master curve constructed using the scaling time t_{sim}. This collapse demonstrates that the λ ratio truly drives the aggregation process. In a future work, we aim to explore the field-induced structuration in more concentrated suspensions and the influence of confinement (e.g. microchannel thickness).

REFERENCES

1 G. Bossis, S. Lacis, A. Meunier and O. Volkova, *J. Magn. Magn. Mater.*, 2002, **252**, 224.

2 J. de Vicente, D. J. Klingenberg and R. Hidalgo-Alvarez, *Soft Matter*, 2011, **7(8)**, 3701.

3 N. Wereley, *Magnetorheology: Advances and Applications*, Royal Society of Chemistry: RSC Smart Materials, London, UK, 2013.

4 G. Helgesen, A. T. Skjeltorp, P. M. Mors, R. Botet and R. Jullien, *Phys. Rev. Lett.*, 1998, **61(15)**, 1736.

5 M. Fermigier and A. P. Gast, *J. Colloid Interface Sci.*, 1992, **154(2)**, 522.

6 J. Černák, P. Macko and M. Kasparkova, *J. Phys. D: Appl. Phys.*, 1991, **24(9)**, 1609.

7 J. Černák, *J. Magn. Magn. Mater.*, 1994, **132(1)**, 258.

8 P. Domínguez-García, S. Melle, J. M. Pastor and M. A. Rubio. *Phys. Rev. E.*, 2007, **76(5)**, 051403.

9 T. Vicsek and F. Family, *Phys. Rev. Lett.*, 1984, **52(19)**, 1669.

10 J. Černák, G. Helgesen and A. T. Skjeltorp, *Phy. Rev. E.*, 2004, **70(3)**, 031504.

11 R. M. Erb, M. D. Krebs, E. Alsberg, B. Samanta, V. M. Rotello and B. B. Yellen. *Phys. Rev. E.*, 2009, ***80*(5)**, 051402.

12 C. P. Reynolds, K. E. Klop, F. A. Lavergne, S. M. Morrow, D. G. Aarts, and R. P. Dullens, *J. Chem. Phys.*, 2015, **143**, 214903.

13 Ruiz-López, J. A., J. C. Fernández-Toledano, R. Hidalgo-Alvarez, and J. de Vicente *Soft Matter*, 2016, **12(5)**, 1468.

14 S. Cutillas, G. Bossis and A. Cebers, *Phys. Rev. E.*, 1998, **57(1)**, 804.

15 G. Pál, F. Kun, I. Varga, D. Sohler and G. Sun, *Phys. Rev. E.*, 2011, **83(6)**, 061504.

16 E. M. Furst and A. P. Gast, *Phys. Rev. Lett.*, 1999, **82(20)**, 4130.

17 J. E. Martin and J. Odinek, *J. Rheol.*, 1995, **39(5)**, 995.

18 M. Mohebi, N. Jamasbi and J. Liu, *Phys. Rev. E.*, 1996, **54(5)**, 5407.

19 D. Sohn, *J. Magn. Magn. Matt.*, 1997, **173(3)**, 305.

20 M. Hagenbüchle and J. Liu, *Appl. Opt.*, 1997, **36**, 7664.

21 S. Melle, M. A. Rubio and G. G. Fuller, *Phys. Rev. Lett.*, 2001, **87(11)**, 115501.

22 P. Domínguez-García, J.M. Pastor and M.A. Rubio, *Eur. Phys. J. E.*, 2011, **34**, 36.

23 H. See and M. Doi, *J. Phys. Soc. Jpn.*, 1991, **60(8),** 2778.

24 A. J. F. Bombard, F. R. Goncalves, K. Shahrivar , A. L Ortiz, J. de Vicente. *Tribo. Int.*, 2015, **81**, 309.

25 Y. Xia and G. M. Whitesides, *Annu. Rev. Mater. Sci.*, 1998, **28**:153.

26 J. R. Morillas, E. Carreón-González and J. de Vicente, *Smart Mater. Struct.*, 2015, **24(12)**, 125005.

27 N. Otsu, *Automatica*, 1975, **11(285-296)**, 23.

28 J. Zhang and J. Hu, Proc. 2008 Int. IEEE Conf. on Computer Science and Software Engineering, 2008, **6**, 105.

29 D. J. Klingenberg, *J. Rheol.*, 1993, **37(2)**, 199.

30 D. Kittipoomwong and D. J. Klingenberg, *Int. J. Mod. Phys. B.*, 2002, **16**, 2732.

31 Z. Wang, K. Shahrivar and J. de Vicente, *J. Rheol.*, 2014, **58(6)**, 1725.

32 J. E. Promislow, A. P. Gast and M. Fermigier, *J. Chem. Phys*., 1995, **102(13)**, 5492.

33 S. Fraden, A. J. Hurd and R. B. Meyer, *Phys. Rev. Lett.*, 1989,**63(21)**, 2373.

34 J. E. Martin, J. Odinek and T. C. Halsey, *Phys. Rev. Lett.*, 1992, **69(10)**, 1524.

35 D. Liu, M. R. Maxey and G. E. Karniadakis, *J. Micromech. Microeng.*, 2005, **15(12)**, 2298.

36 E. Climent, M. R. Maxey and G. E. Karniadakis. *Langmuir*, 2004, **20(2)**,507.

Annex I. Image analysis technique

Raw data obtained from video microscopy analyses provides the contour of the clusters and their area in pixels. In order to calculate statistical parameters (e.g. $S(t)$), it is needed to relate number of particles composing a cluster to its corresponding area. For the aim of counting the number of particles in an aggregate, we explored two pathways:

I. A cluster can have fractional number of particles. According to this, the cluster size is $s = \frac{A_c}{A_P}$, where A_c is the area of a cluster and A_P is the area of a single particle.
II. Each cluster size is an integer number of particles. In this method the cluster size is calculated as follows: $round\left(\frac{A_c}{A_P}\right)$, where $round$ means nearest integer.

Both pathways gave very similar results (see below). Therefore, method II was used along this manuscript.

Additionally, two independent image-processing methods were used to analyse the microscopy pictures. On the one hand we used a commercial software provided by Leica. On the other hand we developed our own software using Matlab subroutines (see text for details).

In the two figures below we compare the mean cluster size $S(t)$ obtained from the two different methods (I & II) using the two different softwares (Leica & Matlab). Results shown below correspond to the aggregation kinetics for two suspensions of carbonyl iron particles and magnetic latex in a microchannel of 500 μm width, $\phi_{2D} = 0.0239$ and $H_0 = 28.65$ kA/m. As observed, the results are very consistent independently of the method, software and particular of suspension.

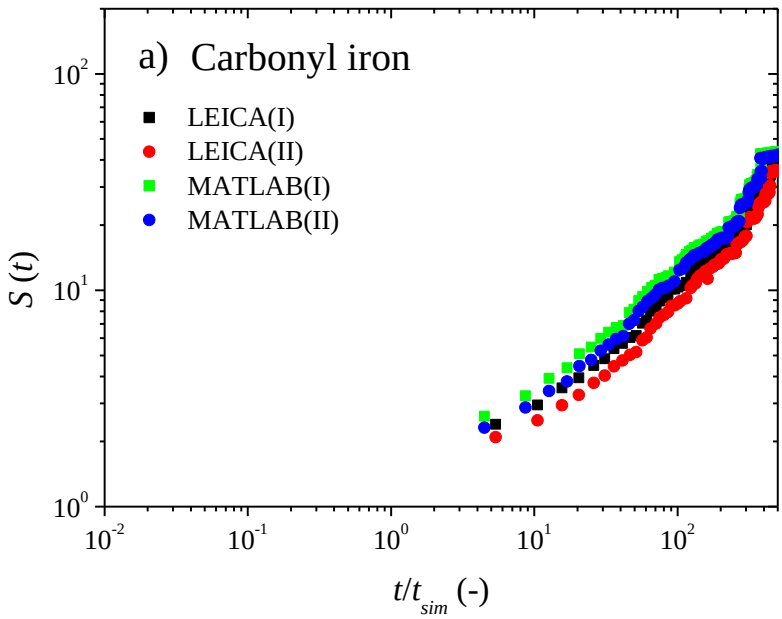
a) Carbonyl iron
LEICA(I)
LEICA(II)
MATLAB(I)
MATLAB(II)
S (t)
t/t_sim (-)

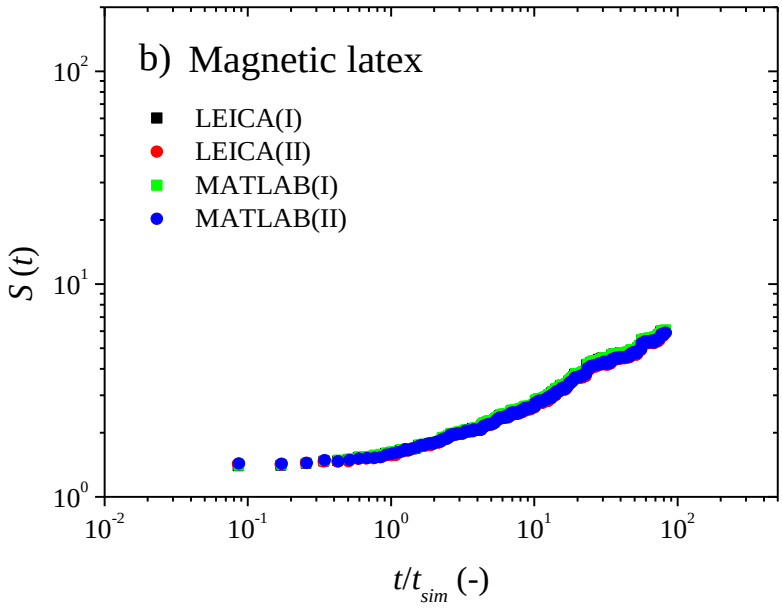
b) Magnetic latex
LEICA(I)
LEICA(II)
MATLAB(I)
MATLAB(II)
S (t)
t/t_sim (-)

CHAPTER 8

Effect of Microchannel Width in the Irreversible Aggregation Kinetics of Carbonyl Iron Suspensions

Keshvad Shahrivar, Elizabeth Carreón-González and Juan de Vicente

Submitted for publication

Abstract

We study the influence of confinement in the aggregation kinetics of dilute carbonyl iron suspensions under strong fields ($\lambda \approx 10^6$) in rectangular microchannels using video-microscopy, image analysis and particle-level dynamic simulations. Channel widths studied are ranged in the interval [75-1000 μm]. In these particular suspensions the experimental and simulation time scales according to: $t_s \propto \lambda^{-1}\phi_{2D}^{-2.614}W^{*-0.227}$, where λ is the Lambda parameter, ϕ_{2D} is the particle surface fraction and W^* is the reduced microchannel width. The effect of channel width is found to be crucial in the dynamic exponent and in the saturation (long time) mean cluster size. On the contrary, it has no effect in the onset of the tip-to-tip aggregation process.

INTRODUCTION

The aggregation of magnetic suspensions (i.e. magnetorheological fluids and inverse ferrofluids) in two dimensions is well described using solely two dimensionless numbers: the particle surface fraction ϕ_{2D} and the Lambda ratio λ (i.e. the magnitude of the magnetic interaction energy between two magnetic moments relative to thermal energy).[1-3]For low enough magnetic field strengths, the λ ratio reads as follows:

$$\lambda = \frac{\pi \mu_0 \mu_{cr} \beta^2 a^3 H_0^2}{2\kappa_B T} \tag{1}$$

where μ_0 is the permeability of vacuum, μ_{cr} is the relative permeability of the continuous phase, $\beta = (\mu_{pr} - \mu_{cr})/(\mu_{pr} + 2\mu_{cr})$ is the contrast factor or coupling parameter, μ_{pr} is the relative permeability of the particles, a is the particle radius and H_0 is the external magnetic field strength.

Generally speaking, dilute magnetic suspensions exhibit two well differentiated regimes: If the field strength is low enough ($\lambda \sim 1$) then aggregation is reversible and elongated structures reach an equilibrium length. However, in the presence of sufficiently large fields aggregation becomes irreversible and structures grow with time following a power law.[4-6.]

It is well known that dilute suspensions of carbonyl iron particles aggregate in 2D following a tip-to-tip mechanism because of the exceedingly large λ ratio whatever the field strength because of the large particle size.[4,5,7] According to this mechanism we expect the elongated structures to indefinitely grow with time in an open container. However, most practical applications require the system to be confined between rigid walls.[8]

Under this scenario, it is interesting to ascertain how these field-induced structures are influenced by the presence of rigid boundaries. In fact, previous works on non-equilibrium structure formation showed that confinement influences the final field-induced structure.[9,10] Recently, Bossis *et al.*[11] studied both theoretically, and also by means of computer simulations, the aggregation kinetics of non-Brownian magnetisable particles. They found a gap-sensitive power-law dependence of the cluster size with time.

In this manuscript we prepare rectangular microchannels using Soft Lithography[12] and having different widths in the range $W \epsilon [75 - 1000]$ microns. Then, the 2D aggregation performance of carbonyl iron suspensions is studied. Additionally, we also

perform particle level simulations for a wide range of reduced microchannel widths $W^*\epsilon\ [25-100]$ where $W^* = W/2a$.

BACKGROUND

The aggregation kinetics is typically described in terms of the time evolution of the number of clusters of size s as a function of time $n_s(t)$ (i.e. basically the cluster size distribution). The most frequently used statistical variable, derived from the cluster size distribution, is the so-called mean cluster size (i.e. weight average cluster size):

$$S(t) = \sum_s s^2 n_s(t) \Big/ \sum_s s n_s(t) \tag{2}$$

The temporal evolution of the cluster-cluster aggregation process is typically given by an initial plateau region followed by a power law time dependence. At short times $S(t)$ data remain constant because of the large inter-particle distance. For longer times, a power law dependence is observed because of the tip-to-tip aggregation.[4,5,13] These two regions are well captured by the following empirical expression:[14]

$$S(t) = S(0)[1 + (t/t_s)^z] \tag{3}$$

Here $S(0)$ is a measure of the initial aggregation state ($S(0) = 1$ in disaggregated suspensions), z is the dynamic exponent and t_s is the scaling time. The scaling time captures the dependence with ϕ and λ.

In general, the aggregation phenomena involve two lengths scales: i) the initial average inter-particle distance: $R_\phi = \sqrt{\pi} a \phi_{2D}^{-1/2}$, and ii) the distance at which the magneto-static dipole-dipole interaction energy is equal to the energy of thermal fluctuations $R_m = 2a\lambda^{1/3}$.[15-17] When $R_\phi > R_m$ the aggregation process is limited by diffusion. On the contrary, when $R_m > R_\phi$ the aggregation process is ballistic.

Scaling time

For the suspensions of interest in this work, $R_m > R_\phi$. In this regime, a scaling time t_s can be derived following the discussion by See and Doi.[18] In their deterministic "hierarchical model" it is assumed that initially the particles are well dispersed, and under the field they associate to form doublets after t_1, then these doublets continue to

form quadruples after t_2, and so forth. For small particles of size "s" that are relatively separated and aligned with the magnetic field, the interaction energy was approximated by multiplying s^2 by the inter-particle potential.[19] Furthermore, by assuming the friction to be proportional to chain size and integrating the equation of motion by taking the initial position $R_i = R_\phi$ and final distance to be zero $R_f = 0$, a scaling time was obtained. This deterministic scaling time can be written as follows:

$$t_{det} = \frac{a^2}{13.72 D \lambda \phi_{2D}^{5/2}} \tag{4}$$

Here D is the diffusion coefficient and η is the shear viscosity. A similar expresion to Equation (4) can be found in Liu *et al.*[20] More recently, particle level simulations and experiments by Shahrivar *et al.*[4] corroborated the deterministic prediction [Equation (4)] for large microchannel widths.

Scaling exponent

The scaling exponent z determines the growth process (c.f. Equation (3)). A number of previous investigations on the aggregation kinetics of magnetic latexes and magnetic holes have been carried out experimentally[15,16,21-25] and by means of computer simulations.[15,20,26] Pioneering simulation work[27,28] considered oriented anisotropic particles with a size-dependent diffusion coefficient ($D(s) \propto s^\gamma$) aggregating into rod-like clusters. These works resulted in a scaling exponent z that was a function of γ according to $z = 1/(1-\gamma)$. In the typical case where friction is proportional to the cluster size ($\gamma = -1$) the scaling exponent becomes $z = 0.5$. However, previous experimental works reported deviations from this theoretical prediction; for instance $0.37 < z < 0.6$,[5] $z = 0.57$,[15] and $0.38 < z < 0.54$.[21] Even though carbonyl iron particles are widely used in the formulation of magnetorheological fluids,[29] there are very few papers describing their aggregation kinetics under field. Just recently, Shahrivar *et al.*[4,13] studied the aggregation of carbonyl iron particles using video microscopy and molecular dynamic simulations in open cavities.

Some previous experiments have shown that, under specific conditions, the scaling exponent deviates from theoretical predictions and/or simulations.[13,21,25] For instance, Černák *et al.*[21] studied the cluster-cluster aggregation of non-magnetic particles in ferrofluids. In the case of Brownian particles ($d < 4\,\mu m$) they found a constant $z = 0.42$ but for non-Brownian particles ($d = 14\,\mu m$) the dynamic exponent showed to be strongly dependent on λ. Erb *et al.*[25] also studied the field-induced assembly of non-Brownian particles in inverse ferrofluids. They found that the dynamic exponent was determined by the particle-particle interaction energy and the particle concentration of both ferrofluid and the nonmagnetic particles. More recently, Shahrivar *et al.*[13] studied

the effect of carrier fluid viscosity and particle-wall interactions by the addition of surfactants to the suspension formulation. They observed that under very strong particle-wall interactions the kinetic exponent sharply decreased and the aggregation was eventually arrested at long times.

EXPERIMENTAL

Carbonyl iron particles (3.0 μm diameter) were obtained from BASF SE (grade EW). The magnetic suspension was prepared by dispersing carbonyl iron particles in glycerol containing 1 wt% sodium dodecyl sulfate. The relationship between 3D and 2D fractions was experimentally obtained to be: $\phi_{2D} = 193.44\phi^{1.18}$. In this particular work, we worked at a low particle concentration (volume fraction $\phi = 5 \times 10^{-4}$, surface fraction ϕ_{2D}=0.02).

Microchannels were prepared using Soft Lithography techniques [e.g. see ref. 12]. Briefly, polydimethylsiloxane PDMS specimens were fabricated from a silicone elastomer kit (Sylgard™ 184, Dow Corning); by mixing the base and curing agent in a mass ratio of 10:1. After manually mixing the two components, the mixture was introduced in a desiccator for degassing. Subsequently, the mixture was poured over a master relief containing the microchannel design, and cured at room temperature for one day. The master for each rectangular microchannel was created on a silicon wafer using an epoxy-based photoresist (SU 8). The final step was to release the elastomer from the master and to seal it onto a glass slide.

Microchannels were later placed on top of an inverted microscope under the presence of DC uniaxial magnetic fields. Images were captured every second to follow the aggregation kinetics. Then images were analysed and statistical variables were calculated. A detailed description of the experimental set-up and image analysis techniques can be found in refs. 4, 13.

PARTICLE LEVEL SIMULATIONS

Particle level simulations were carried out using Klingenberg's technique.[30-32] In this approach, the particles motion is governed by magnetostatic polarization forces, particle/particle and particle/wall short range repulsive forces, and hydrodynamic resistance. It is assumed the point-dipole approximation, Hard Sphere repulsion between the particles and between the particles and the walls, and Stokes' drag force.[4, 30] Briefly, using characteristic length, force and time scales: $l_c = 2a$, $f_c = 9\pi\eta D\lambda$, and $t_c = \frac{4a^2}{3D\lambda}$ the equation of motion is transformed into dimensionless form. Here, the dimensionless variables will be denoted with an asterisk (e.g. $t^* \equiv t/t_c$). Then, the equations of

motion for each particle are integrated numerically using an explicit Euler method with a dimensionless time step $\Delta t^* = 1 \times 10^{-3}$.

Molecular dynamic simulations were performed in a rectangular 2D geometry consisting of two parallel walls positioned at $y^* = 0$ and $y^* = W^*$. Non-slip boundary conditions were applied on these walls. On the other hand, Periodic Boundary Conditions were applied at $x^* = 0$ and $x^* = L^*$, in the direction perpendicular to the magnetic field ($\vec{H} = H\hat{e}_y$). In this geometry, the particle surface fraction is given by $\phi_{2D} = \frac{N\pi}{4W^*L^*}$ where $N = 1000$ is the number of particles.

RESULTS AND DISCUSSION

Representative mean cluster size S versus time t curves are shown in Figure 1a for different microchannel widths. As expected, all experiments begin with $S(0) \neq 1$ due to initial residual interparticle aggregation. When time progresses the mean cluster size continuously grows. As observed, the power law exponent is larger the widest the microchannel. For sufficiently large widths the exponent reaches a constant value. Undoubtedly the most remarkable observation is that the mean cluster size levels off when the microchannel width is small enough.

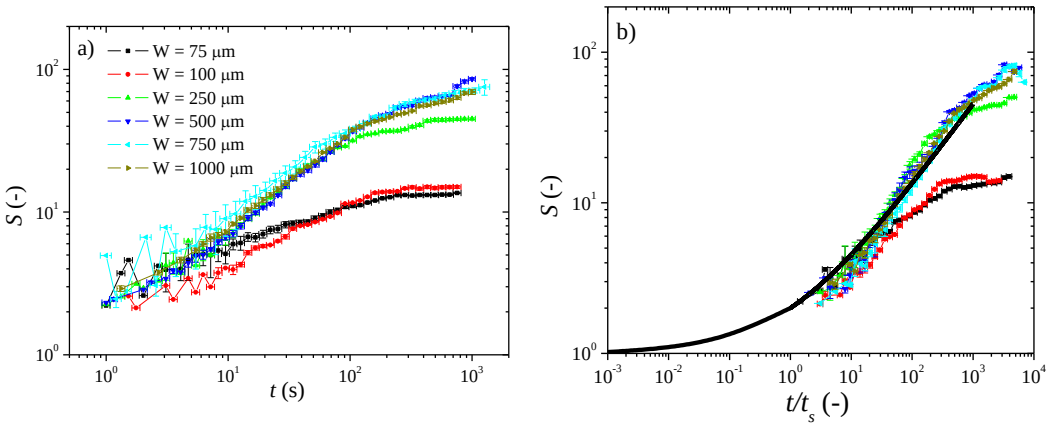

Figure 1. (a) Effect of microchannel width W in the time dependence of the mean cluster size $S(t)$. External magnetic field $H = 28.65\ kA/m$. (b) Master curve for carbonyl iron suspensions using the simulation time scale t_s. Together with experimental data we also plot the simulation predictions (black solid line).

It is also important to remark that the time associated to the onset of the plateau is larger the wider the microchannel and therefore the bigger the aggregates. This suggests that pinning of the particles onto the bottom of the microchannel, because of frictional forces, is not the reason for the onset of the plateau.

A vast amount of simulations were carried out for a wide range of microchannel widths $W^*\epsilon\,[25-100]$ and surface fractions $\phi_{2D}\,\epsilon\,[0.01-0.05]$. Simulation results are shown in Figure 2a for $W^*=25$. Results show a plateau at very short times -$S(t=0)=1$. Then, the mean cluster size grows monotonically with time with a constant slope in log-log scale. This trend is not surprising since experimental, theoretical and simulation works have confirmed the existence of a power-law increase in the mean cluster size in similar magnetic field-responsive suspensions.[5,16,19,21] For the lowest concentration studied ($\phi_{2D}=0.01$), the power-law behavior was observed up to the largest simulation time investigated. However, for higher concentrations ($\phi_{2D}\geq 0.03$) the mean cluster size is observed to level off for the largest times explored. The leveling off occurs at shorter times as the area fraction increases.

Simulation data demonstrate a scaling with $t^*(=t/t_c)$ and W^*. Non-linear least-squares routines were used to fit all the simulation results. Interestingly, all of the curves for the mean cluster size collapse onto a master curve according to $S(t^*)=1+at^{*b}\phi_{2D}^{c}W^{*d}$ in the region where the aggregation follows a power law. The best-fitting parameters a, b, c, and d obtained were 12.045, 0.549, 1.435 and 0.125, respectively. Rearranging the previous master curve expression for $S(t^*)$, we can rewrite the temporal evolution of the mean cluster size to be $S(t)=1+(t/t_s)^b$. Therefore, the aggregation kinetics is explained solely with a reduced time t/t_s and an exponent b. The simulation scaling time, t_s, can be represented as a function of D, λ, ϕ_{2D} and W^* as follows:

$$t_s=\frac{a^2}{69.8D\lambda\phi_{2D}^{2.614}W^{*0.227}} \tag{5}$$

This particular scaling time compares very well with experimental and simulation data from the literature for different λ and ϕ_{2D}.[15,19,20]

Interestingly it demonstrates that the microchannel width W^* does not affect noticeably the onset of the power law region (note the very small W^* exponent 0.227). This was expected because R_ϕ is significantly smaller than the microchannel width W^*. Simulation curves nicely collapse in a single master curve when ploted as a funtion of the reduced time (see Figure 2b). In Figure 1b we show the simulation predictions (master curve from Figure 2b) together with the experimental data. As observed, the scaling time t_s -Equation (5)-, sucessfully collapses experiments and simulations onto a single curve.

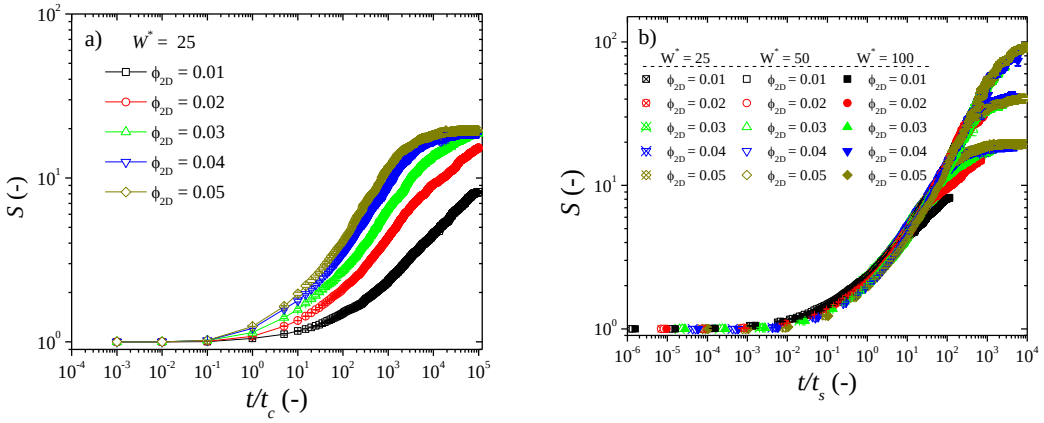

Figure 2. Simulation predictions for the aggregation kinetics corresponding to different microchannel thicknesses. a) Mean cluster size as a function of dimensionless simulation time for a reduced microchannel width of $W^* = 25$ and different particle surface fractions, b) Simulation master curve for different microchannels widths and concentrations.

Power law exponents z are included in Figure 3a as a function of the microchannel width W^*. The kinetic exponent z was calculated by linear regression fitting in log-log scale to the region that follows a power-law. The main feature of Figure 3a is that confinement strongly affects the dynamic exponent z and subsequently the aggregation kinetics. As observed, the dynamic exponent z increases dramatically for narrow channels but then reaches a plateau value for the largest ones. The plateau value around $z = 0.6$ is in good agreement with previously reported values.[5,6,15,21] The results obtained from experiments and simulations are also in reasonably good agreement.

Figure 3b shows the dependence of the maximum mean cluster size S_{max} with the microchannel width W^*. As observed, the simulations predict a linear increase of S_{max} with W^* that is weakly dependent on the particle concentration. In Figure 3b we show simulation results for the only two particle concentrations ($\phi_{2D} = 0.04$ and $\phi_{2D} = 0.05$) where S_{max} is observed for the maximum computational time explored. It is expected that lower concentrations will reach the same value for S_{max}, at a given W^*, but at longer times. Unfortunately, reaching those times is computationally very expensive. Figure 3b demonstrates that there is a reasonably good accordance between experiments and simulations for the smaller W^* data.

Interestingly, experimental data tend to show a saturation in S_{max} above a certain microchannel width (W^*~100) (c.f. Figure 3b), in contrast to simulation predictions for S_{max} that continuously increase with W^*.

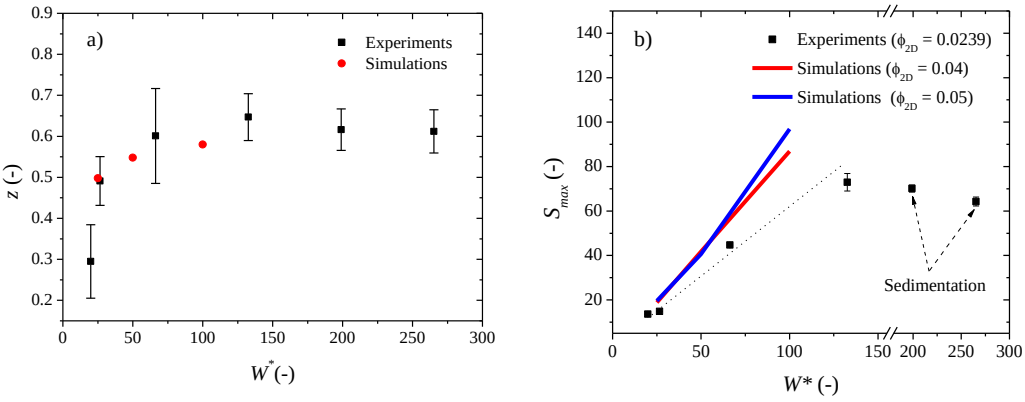

Figure 3. a) Dynamic exponent z for experiments and simulations as a function of dimensionless microchannel width. $\phi_{2D} = 0.02$. $H = 26.85\ kA/m$. b) Maximum mean cluster size as a function of dimensionless microchannel width.

The reason for this is that for the wider microchannels, the clusters may reach a very large size at long times and because of the large density mismatch between the particles and the carrier fluid ($\rho_{CIP}/\rho_f \sim 6.3$), the clusters are expected to sediment pinning to the bottom wall of the microchannel. As a result, the friction between the clusters and the wall may impede the further growth of the clusters resulting in a long time plateau value S_{max}. Obviously, in the absence of friction and for the larger microchannel widths ($W > 500\ \mu m$) it is expected that $S(t)$ will grow indefinitely with time.[18,20,22]

At this point it is worth to stress that the existence of a saturation S_{max} in the number of particles per cluster was predicted in the literature under specific conditions. [23,33,34] Recently, Andreu *et al.*,[33] postulated the existence of a saturation in cluster size at long times for thermodynamically equilibrated systems via simulations and theoretical analyses. They showed that in 3D geometries S_{max} depends only on the λ ratio and particle volume fraction. Darras *et al.*[34] experimentally validated the theory by Faraudo and coworkers[33] in 2D; however, they observed a divergence at a critical value (cluster size of 23 particles). In the present manuscript $\lambda \sim 10^6$ so that thermodynamic equilibrium is precluded.

Reached this point it was important to elucidate whether the sideways coalescence of the chain-like structures occurred because this may also contribute to the appearance of a long time plateau for $S(t)$.[5] Figure 4 reveals the existing structure at the end of the aggregation process in experiments and simulations. In view of these snapshots, aggregates seem to be well separated and lateral coalescence seems to be absent in both experiments and simulations.

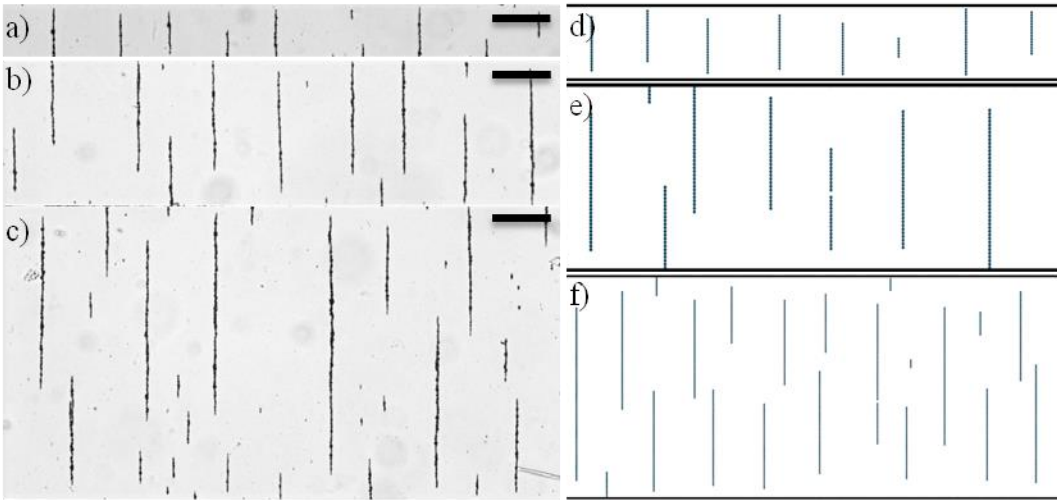

Figure 4. Snapshots corresponding to the suspensions structure at the end of the aggregation experiments and simulations for different microchannel widths: a) W = 100 μm (W^* = 26.5); b) W = 250 μm (W^* = 66.3); c) W =500 μm (W^* = 132.6); d) W^* = 25; e) W^* = 50 and f) W^*= 100. a-c) correspond to experiments. Bar scale = 100 μm. b-f) correspond to simulations.

For quantitative purposes, we also computed the average cluster width, $\langle w \rangle$, and the average cluster spacing, $\langle R \rangle$, to more precisely elucidate whether the sideways coalescence of the chain-like structures occurred. For each cluster, a minor axis length was calculated that is the length of the minor axis of the ellipse that has the same normalized second central moment as the cluster. Next, the average cluster width $\langle w \rangle$ is obtained from the average over all the minor axes lengths. Figure 5a demonstrates that $\langle w \rangle$ remains essentially constant with time (the change is below 25 %) in good agreement with visual observations reported in Figure 4.

The average radial distance between the center of mass of the clusters, $\langle R \rangle$, was calculated as the average distance between nearest neighbour clusters. For this aim, first the center of mass for each cluster was identified and then a Delaunay triangulation[35] was performed on every configuration to determine the nearest neighbour clusters. Results for $\langle R \rangle$, corresponding to different microchannel thicknesses, are contained in Figure 5b. Experiments and simulations reveal that for sufficiently short times $\langle R \rangle$ increases in accordance with clusters that are growing apart. This is easily understood in terms of the existence of repulsive interaction forces between the chain-like structures in good agreement with previous publications.[9,36] In those papers, repulsive forces were theoretically predicted in the case of two parallel finite-size aggregates in an off-registered position depending on their length, lateral and vertical shift.

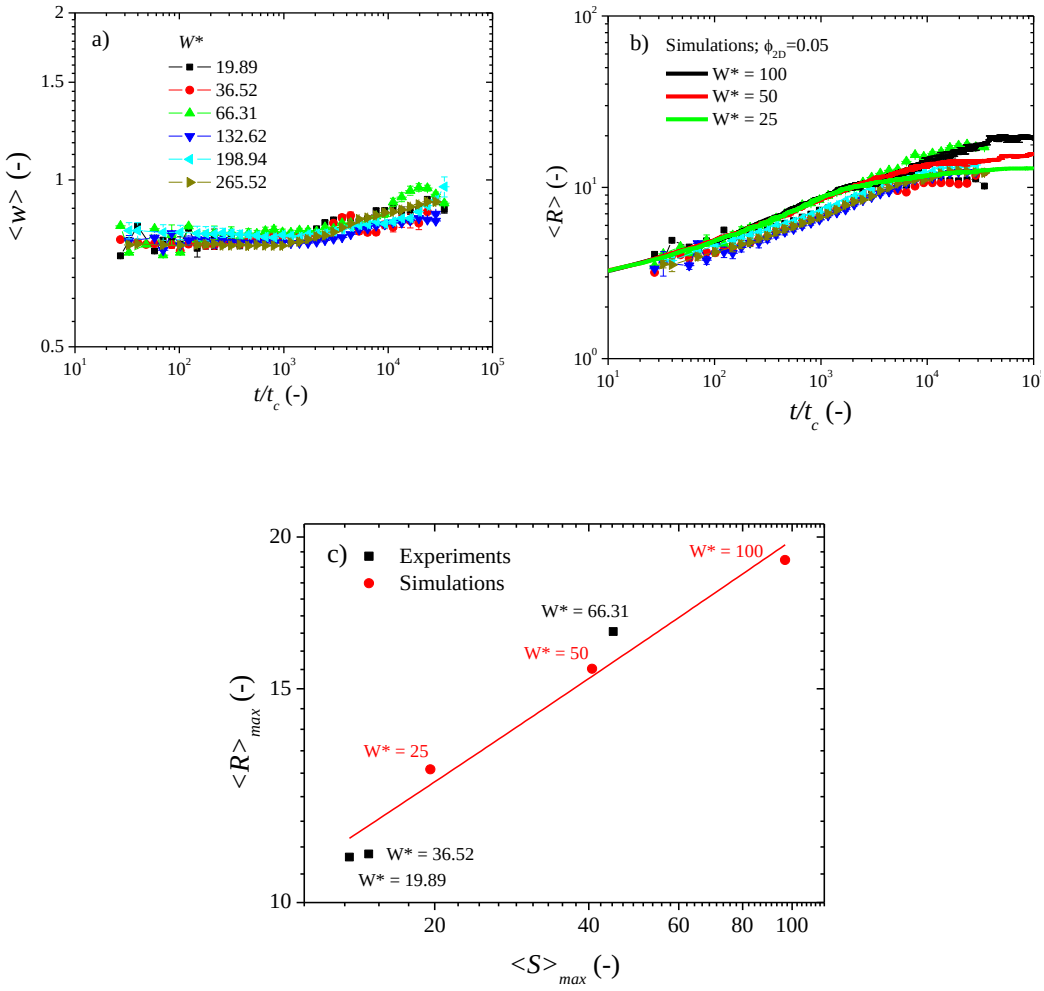

Figure 5. a) Time dependence of the experimental average cluster width $\langle w \rangle$ for different microchannel widths W^*. b) Comparison of the average cluster spacing $\langle R \rangle$ in experiments (symbols) and simulations (line) as a function of dimensionless simulation time for different W^*. c) Maximum cluster spacing $\langle R \rangle_{max}$ versus S_{max} for different microchannel widths in experiments (squares) and simulations (circles): blue solid line is the best fitting result to the equation: $\langle R \rangle_{max} = a{S_{max}}^b$ with $a = 4.7 \pm 0.5$, $b = 0.30 \pm 0.03$ and $R^2 = 0.95725$.

Interestingly, for sufficiently long times $\langle R \rangle$ stabilizes at a constant plateau value that is indicative of a considerable slowing down in the dynamics. This was expected under confinement because the total number of particles is fixed. This was also expected in view of the previous work by Mohebi *et al.*[9] They postulated the existence of a cut-off

distance $\langle R \rangle_c$. When the separation between any two clusters is larger than this cut-off distance, $\langle R \rangle > \langle R \rangle_c$, the two clusters repel each other. This cut-off distance increases with chain length. Bearing in mind that lateral coalescence is not observed (c.f. Figure 4 and 5a) the saturation in the mean cluster size observed for sufficiently narrow microchannels was expected to be due to the repulsion among clusters.

In summary, upon the application of a magnetic field, particles become magnetized and start to aggregate following a tip-to-tip aggregation mechanism. For the particular conditions considered in this work $R_m > R_\phi$, and therefore the aggregation process continues indefinitely with time unless the confining boundaries are close enough. When the boundaries are sufficiently close, the aggregation is hindered and a plateau in the mean cluster size is observed. The onset of this plateau is associated to a critical average cluster spacing where clusters essentially experience repulsive interactions. This is demonstrated in Figure 5c where a correlation exists according to the following the best fitting expression: $\langle R \rangle_{max} = a{S_{max}}^b$ with $a = 4.7 \pm 0.5$ and $b = 0.30 \pm 0.03$ with $R^2 = 0.95725$.

Equation (3) captures reasonably well the aggregation performance of carbonyl iron suspensions under field, at short and medium times, when the microchannel width is large enough. However, it fails when the microchannels are narrow and the mean cluster size levels off for long times. In an attempt to capture the full aggregation curve we propose a semiempirical expression:

$$S(t) = 1 + (S_{max} - 1)(1 + (t/t_d)^\alpha)^\omega \tag{6}$$

Here, t_d is a deviation time corresponding the point where the mean cluster size $S(t)$ levels off to saturation. The parameter α represents the width of the transition region ($t = t_d$): the slope decreases when $|\alpha|$ decreases. Finally, the slope of power-law region is described by ω.

Equation (6) was fitted to the simulation data for a range of particle concentrations and microchannel widths. The resulting best fitting parameters -S_{max}, t_d, α, and ω- as obtained from simulations are included in Table 1. As expected, in view of Table 1, the critical time t_d is strongly dependent on area fraction and dimensionless microchannel width. On the other hand, the slope of $S(t)$ in log-log scale corresponds to the dynamic exponent z. In this case, $z = \alpha\omega = 0.89\phi_{2D}^{0.2}{W^*}^{0.05}$. This result is in good agreement with our observation that z is weakly dependent on the microchannel width for sufficiently wide microchannels but grows with the area fraction.

In Figure 6 we plot the experimental data together with predictions from Equation (6). Interestingly, it is observed a reasonably good collapse between experiments and simulations without any free fitting parameters.

Table 1. Best fitting parameters to the simulation curves using Equation (6):

$$S(t) = 1 + (S_{max} - 1)(1 + (t/t_d)^{\alpha})^{\omega}$$

Parameters	Prediction
S_{max}	$0.97W^* - 5.98$
t_d	$2.3 \times 10^{-4}\phi_{2D}^{-3.2}W^{*1.91}t_c$
α	$-2.4 \times 10^{-2}\phi_{2D}^{-1.05}W^{*0.2}$
ω	$-36.26\phi_{2D}^{1.25}W^{*-0.15}$

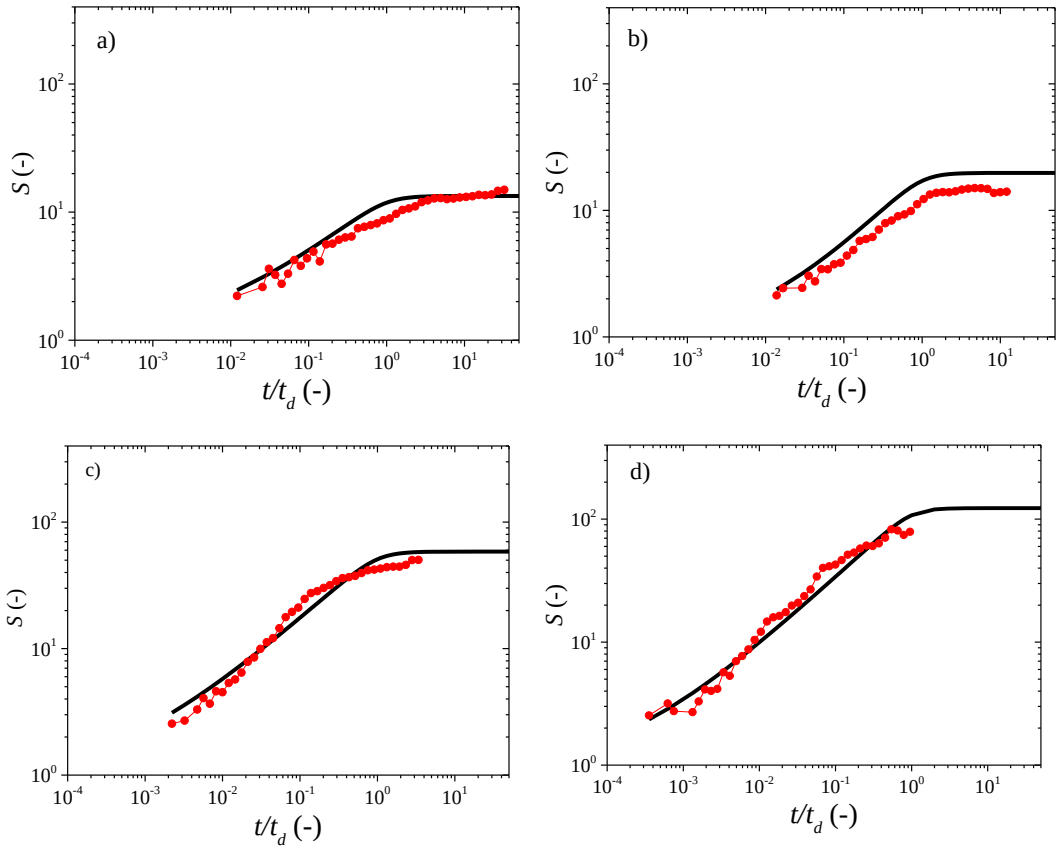

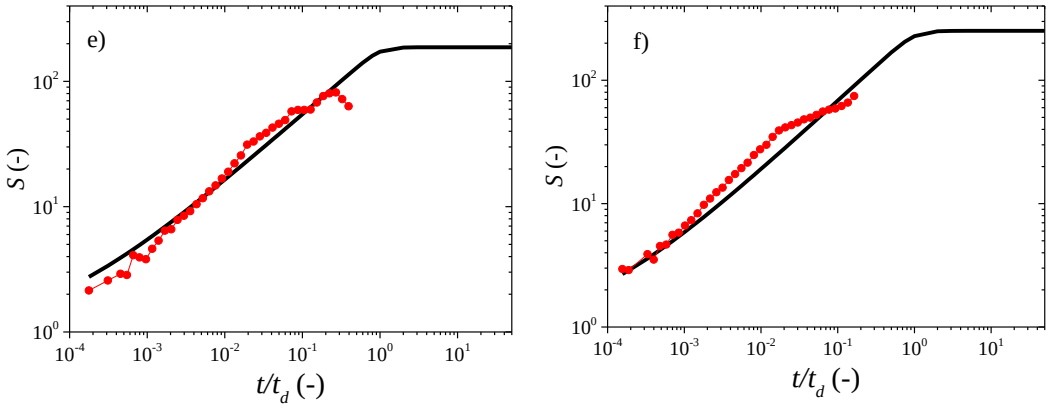

Figure 6. Mean cluster size as a function of reduced time for experiments (symbols) and theoretical prediction (lines): a) $W = 75\mu m$; $W^* = 19.89$, b) $W = 100\ \mu m$; $W^* = 26.52$ c) $W = 250\mu m$; $W^* = 66.31$ d) $W = 500\ \mu m$; $W^* = 132.62$ e) $W = 750\mu m$; $W^* = 198.94$ and f) $W = 1000\ \mu m$; $W^* = 265.25$. The solid line corresponds to Equation (6) with the parameters reported in Table 1.

CONCLUSIONS

We investigated the influence of confinement in the aggregation kinetics of dilute carbonyl iron suspensions in rectangular microchannels of different width using experiments and simulations. We observed three regions in the evolution of mean cluster size. First, a plateau region where particles are isolated and interact very weakly. Next, a power law increase in the mean cluster size when particles start to form single-width particle chains in a tip-to-tip aggregation process. Finally, a plateau region at long times as a result of the arrest of the aggregation kinetics because of the presence of the confining walls. Experimental and simulation curves can be collapsed in a master curve when using the time scale $t_s \propto \lambda^{-1}\phi_{2D}^{-2.614}W^{*-0.227}$, where W^* is the microchannel width. We demonstrate that the long time plateau in the mean cluster size is not due to lateral intercluster aggregation. Instead, the mean cluster size levels off because of predominant repulsive interactions between confined clusters. Experiments and simulations demonstrate that the maximum mean cluster size S_{max} is a power law function of W^* and correlates well with the maximum in the average cluster spacing $\langle R \rangle$. In contrast to the theoretical prediction, experimental data reach a maximum value for large W^* as a result of the pinning of the largest aggregates to the bottom surfaces.

REFERENCES

(1) Fang, F. F.; Liu, Y. D.; Choi, H. J.; Seo, Y. Core–Shell Structured Carbonyl Iron Microspheres Prepared via Dual-Step Functionality Coatings and Their Magnetorheological Response. ACS Appl. Mater. Interfaces, 2011, 3 (9), 3487–3495.

(2) Zhang, W.; Gong. X. L.; Xuan, S. H.; Xu, Y. G. High-performance hybrid magnetorheological materials: preparation and mechanical properties. Ind. Eng. Chem. Res. 2010, 49 (24), 12471–12476.

(3) Carrillo, J. L.; Donado, F.; Mendoza, M. E. Fractal patterns, cluster dynamics, and elastic properties of magnetorheological suspensions. Phys. Rev. E 2003, 68(6), 061509.

(4) Shahrivar, K; Carreón-González, E; Morillas, J. R.; de Vicente, J. Aggregation kinetics of carbonyl iron based magnetic suspensions in 2D. Submitted for publication.

(5) Fermigier, M.; Gast, A. P. Structure evolution in a paramagnetic latex suspension. J. Colloid. Interface Sci. 1992, 152(2), 522-539.

(6) Promislow, J. E.; Gast, A. P.; Fermigier, M. Aggregation kinetics of paramagnetic colloidal particles. J. Chem. Phys. 1995, 102(13), 5492-5498.

(7) Timonen, J. V.; Johans, C.; Kontturi, K.; Walther, A.; Ikkala, O.; Ras, R. H. A facile template-free approach to magnetodriven, multifunctional artificial cilia. ACS Appl. Mater. Interfaces 2010, 2(8), 2226-2230.

(8) Wereley, N. M. (Ed.) Magnetorheology: Advances and applications (Vol. 6). RSC Publ. (2013).

(9) Mohebi, M.; Jamasbi, N.; Liu, J. Simulation of the formation of nonequilibrium structures in magnetorheological fluids subject to an external magnetic field. Phys. Rev. E 1996, 54(5), 5407–5413.

(10) Flores, G. A.; Ivey, M. L; Liu, J.; Mohebi, M.; Jamasbi, N. Field-Induced labyrinthine patterns in ferrofluid emulsions. Int. J. Mod. Phys. A 1996, 10(23n24), 3283-3292.

(11) Bossis, G.; Lançon, P.; Meunier, A.; Iskakova, L.; Kostenko, V.; Zubarev, A. Kinetics of internal structures growth in magnetic suspensions. Phys. A 2013, 392(7), 1567-1576.

(12) Xia, Y.; Whitesides, G. M. Soft lithography. Annu. Rev. Mater. Sci. 1988, 28(1), 153-184.

(13) Shahrivar, K; Carreón-González, E.; de Vicente, J. On the importance of carrier fluid viscosity and particle-wall interactions in magnetic guided assembly of quasi-2D systems. Submitted for publication.

(14) Sohn, D. Kinetic studies of magnetic latex particles' self-assembly under applied magnetic field. J. Mag. Mag. Mater 1997, 173(3), 305-313 .

(15) Domínguez-García, P.; Melle, S.; Pastor, J. M.; Rubio, M. A. Scaling in the aggregation dynamics of a magnetorheological fluid. Phys. Rev. E 2007, 76(5), 051403.

(16) Domínguez-García, P.; Pastor, J. M.; Rubio, M. A. Aggregation and disaggregation dynamics of sedimented and charged superparamagnetic micro-particles in water suspension. Eur. Phys. J. E 2011, 34(4), 1-7.

(17) Melle, S.; Rubio; M. A.; Fuller, G. G. Time scaling regimes in aggregation of magnetic dipolar particles: Scattering dichroism results. Phys. Rev. Lett. 2001, 87(11), 115501.

(18) See, H.; Doi, M. Aggregation kinetics in electro-rheological fluids. J. Phys. Soc. Jpn. 1991, 60(8) 2778-2782.

(19) Reynolds, C. P.; Klop, K. E.; Lavergne, F. A.; Morrow, S. M.; Aarts, D. G.; Dullens, R. P. Deterministic aggregation kinetics of superparamagnetic colloidal particles. J. Chem. Phys. 2015, 143(21), 214903.

(20) Liu, D.; Maxey, M. R.; Karniadakis, G. E. Simulations of dynamic self-assembly of paramagnetic microspheres in confined microgeometries. J. Micromech. Microeng. 2005, 15(12), 2298–2308.

(21) Černák, J.; Helgesen, G.; Skjeltorp, A. T. Aggregation dynamics of nonmagnetic particles in a ferrofluid. Phys. Rev. E 2004, 70(3), 031504.

(22) Climent, E.; Maxey, M. R.; Karniadakis, G. E. Dynamics of Self-Assembled Chaining in Magnetorheological Fluids. Langmuir 2004, 20(2), 507–513.

(23) Koser, A. E.; Keim, N. C.; Arratia, P. E. Structure and dynamics of self-assembling colloidal monolayers in oscillating magnetic fields. Phys. Rev. E 2013, 88(6), 062304.

(24) Laskar, J. M.; Philip, J.; Raj, B. Experimental investigation of magnetic-field-induced aggregation kinetics in nonaqueous ferrofluids. Phys. Rev. E 2010, 82(2), 021402.

(25) Erb, R. M.; Krebs, M. D.; Alsberg, E.; Samanta, B.; Rotello, V. M.; Yellen, B. B. Beyond diffusion-limited aggregation kinetics in microparticle suspensions. Phys. Rev. E 2009, 80(5), 051402.

(26) Miguel, M. C.; Pastor-Satorras, R. Kinetic growth of field-oriented chains in dipolar colloidal solutions. Phys. Rev. E 1998, 59, 826.

(27) Meakin, P; Vicsek, T.; Family, F. Dynamic cluster-size distribution cluster-cluster aggregation: Effect of cluster diffusivity. Phys. Rev. B 1985, 31(1), 564.

(28) Miyazima; S.; Meakin, P.; Family, F. Aggregation of oriented anisotropic particles. Phys. Rev. A 1987, 36(3), 1421.

(29) de Vicente, J.; Klingenberg, D. J.; Hidalgo-Alvarez, R. Magnetorheological fluids: a review. Soft Matter 2011, 7(8), 3701-3710.

(30) Klingenberg, D. J. Simulation of the dynamic oscillatory response of electrorheological suspensions: Demonstration of a relaxation mechanism. J. Rheol. 1993, 37(2), 199-214.

(31) Wang, Z.; Shahrivar, K.; de Vicente, J. Creep and recovery of magnetorheological fluids: Experiments and simulations. J. Rheol. 2014, 58(6), 1725–1750.

(32) Kittipoomwong, D.; Klingenberg, D. J. Simulation of bidisperse magnetorheological fluids. Inter. J. Mod. Phys. B 2002, 16(17n18), 2732–2738.

(33) Andreu, J. S.; Camacho, J.; Faraudo, J. Aggregation of superparamagnetic colloids in magnetic fields: the quest for the equilibrium state. Soft Matter 2011, 7(6), 2336-2339.

(34) Darras, A.; Fiscina, J.; Pakpour, M.; Vandewalle, N.; Lumay, G. Ribbons of superparamagnetic colloids in magnetic field. Eur. Phys. J. E 2016, 39(4), 47.

(35) Haghgooie, R.; Doyle, P. S. Transition from two-dimensional to three-dimensional behavior in the self-assembly of magnetorheological fluids confined in thin slits Phys. Rev. E 2007, 75(6), 061406.

(36) Messina, R.; Spiteri, L. On the interaction of dipolar filaments Eur. Phys. J. E 2016, 39(8), 81.

CONCLUSIONS

In this dissertation, thermoresponsive materials have been used in the formulation of a new class of MRFs. The creep-recovery behavior of MRFs has been investigated experimentally and via Brownian Molecular Dynamic Simulations. Also, the tribological properties of FFs and MRFs have been studied. Furthermore, the aggregation kinetics of carbonyl iron particles was investigated in PDMS microchannels. Main conclusions are summarized as follows:

Thermoresponsive MRFs

1. The use of thermoresponsive materials in the formulation of MRFs constitutes a feasible way to prevent particle sedimentation, but at the same time, retaining a very large MR effect in the excited state.
2. When the carrier operates in the "liquid" phase, the MR composite behaves as a conventional MR fluid. On the contrary, in the "solid" phase, the MR composite behaves as a conventional MR elastomer.
3. Below (above) the sol/gel transition temperature of a concentrated microgel suspension (of a triblock copolymer solution), the MR fluid exhibits a large MR effect as a result of a very low viscosity carrier fluid.
4. Above (below) the sol/gel transition of a concentrated microgel suspension (of a triblock copolymer solution), the dynamics of the iron particles is arrested and sedimentation is inhibited.

Creep-recovery of MRFs

1. Independently of the particle loading, three regimes are observed in the creep curves:
   i) Initial response regime where the systems behave in the viscoelastic region and the average cluster size remains constant.
   ii) Retardation regime where the system behaviour results from the balance between the applied stress and the stress contributions from the particle interactions and viscous flow.
   iii) Long-time steady state where structural parameters reach plateau values. In the case of large enough stress values the system enters in a constant strain rate regime and viscosity bifurcation occurs.
2. The recovery behavior strongly depends on the stress level. For low stress levels, below the bifurcation value, the MR fluid is capable to recover part of the strain. For stresses above the bifurcation value, the recovery is negligible as a result of irreversible structural rearrangements.
3. Long-time creep simulation data are consistent with steady shear flow. Experiments and simulations compare well for $\phi = 0.05$.

4. For $\phi = 0.30$, the agreement between experiments and simulations is not so good because this system is more sensitive to interparticle (remnant magnetization and colloidal) forces.

Tribological properties of FFs and MRFs

1. In the absence of magnetic fields, the tribological behaviour of FFs can be described in terms of a Stribeck curve that closely matches the one obtained for Newtonian fluids.
2. In the presence of magnetic fields, and for sufficiently small loads, friction decreases with respect to the no-field friction coefficient.
3. Friction coefficient can be further decreased when a non-uniform field distribution is displaced towards the inlet of the contact.
4. For the FFs lubrication, the sliding wear occurs mainly by two-body abrasion but in the case of MRFs lubrication the sliding wear occurs by two-body and three-body abrasion.

Aggregation kinetics

1. The carrier fluid viscosity determines the time scale for the aggregation process.
2. When particles interact strongly with the wall, aggregation is hindered and the mean cluster size remains essentially constant at a low value.
3. When friction is reduced the mean cluster size increases following a deterministic aggregation process.
4. Experimental and simulation curves can be collapsed in a master curve, in the power-law region, when using the time scale $t_{sim} \propto \lambda^{-1}\phi_{2D}^{-2.583}$ obtained from particle-level (non-Brownian) dynamic simulations in agreement with a ballistic aggregation mechanism ($\propto \lambda^{-1}\phi_{2D}^{-2.5}$).
5. The plateau region in the mean cluster size distribution at long times is as a result of the arrest of the aggregation kinetics because of the presence of the confining walls.

CONCLUSIONES

En esta tesis doctoral se utilizan materiales poliméricos termosensibles en la formulación de una nueva clase de FMRs. Se investiga el comportamiento en "creep-recovery" de FMRs a través de experimentos y simulaciones de dinámica molecular Browniana. También, se estudian las propiedades tribológicas de FFs y FMRs. Además, se describe la cinética de la agregación de partículas de hierro carbonilo en microcanales de PDMS. A continuación se resumen las principales conclusiones:

FMR termosensibles

1. El uso de materiales termosensibles en la formulación de FMRs permite evitar la sedimentación de las partículas, pero al mismo tiempo, retener un efecto MR muy grande en el estado excitado.
2. Cuando el líquido portador trabaja en la fase "líquida", el compuesto MR se comporta como un fluido MR convencional. Por el contrario, en la fase "sólida", el compuesto MR se comporta como un elastómero MR clásico.
3. Por debajo (o por encima) de la temperatura de transición sol/gel de una suspensión de microgel concentrado (de una disolución de copolímeros tribloque), el FMR presenta un efecto MR grande como resultado de un fluido portador de muy baja viscosidad.
4. Por encima (o por debajo) de la transición sol/gel de una suspensión de microgel concentrado (de una disolución de copolímeros tribloque), las partículas de hierro quedan inmovilizadas y se inhibe por completo la sedimentación.

"Creep-recovery" de FMR

1. Se observan tres regímenes, independientemente de la fracción de volumen de partículas:
   i) Régimen *de respuesta inicial* donde los FMRs se comportan como materiales viscoelásticos y el tamaño promedio de los agregados permanece constante.
   ii) Régimen *de retraso* donde el comportamiento del sistema resulta del balance entre el esfuerzo aplicado y las contribuciones al esfuerzo procedentes de las interacciones entre partículas y el fluido viscoso.
   iii) Estado estacionario (a largos tiempos) donde los parámetros estructurales se estabilizan. Cuando el esfuerzo es suficientemente elevado se entra en un régimen de velocidad de deformación constante y se produce una bifurcación en la viscosidad.
2. El "recovery" depende en gran medida del nivel de esfuerzo. Para esfuerzos pequeños, por debajo del punto de bifurcación, el MRF es capaz de recuperar parcialmente la deformación. Sin embargo, para esfuerzos por encima del punto

de bifurcación, el "recovery" es despreciable como resultado de cambios irreversibles en la microestructura.
3. Los datos de simulación en "creep" a tiempos largos son consistentes con otros de cizalla simple estacionaria. Los experimentos y simulaciones se comparan bien para $\phi = 0.05$.
4. Para $\phi = 0.30$, el acuerdo entre experimentos y simulaciones no es tan bueno porque este sistema es más sensible a las fuerzas existentes entre partículas (magnéticas remanentes y coloidales).

Propiedades tribológicas de FFs y FMRs

1. En ausencia de campos magnéticos, el comportamiento tribológico de los FFs se puede describir en términos de una curva de Stribeck que coincide con la obtenida para fluidos Newtonianos.
2. En presencia de campos magnéticos, y para cargas suficientemente pequeñas, la fricción disminuye con respecto al coeficiente de fricción sin campo.
3. El coeficiente de fricción puede reducirse aún más si la distribución de campo se desplaza hacia la entrada del contacto.
4. En el caso de lubricación por FFs el desgaste por deslizamiento se produce principalmente por abrasión del tipo "dos cuerpos". Sin embargo, en el caso de la lubricación por FMRs, el desgaste por deslizamiento se produce por un mecanismo de abrasión de dos y tres cuerpos.

Cinética de la agregación

1. La viscosidad del fluido portador determina la escala de tiempo para el proceso de agregación.
2. Cuando las partículas interactúan fuertemente con la pared, la agregación se ralentiza (o incluso desaparece) y el tamaño promedio de agregados permanece esencialmente constante en un valor bajo.
3. Cuando la fricción se reduce, el tamaño promedio de agregados aumenta siguiendo un proceso de agregación determinista.
4. Las curvas experimentales y de simulación colapsan en una curva maestra, en la región de la ley de potencia, cuando se utiliza una escala de tiempo $t_{sim} \propto \lambda^{-1}\phi_{2D}^{-2.583}$ obtenida a partir de simulaciones dinámicas moleculares (no Brownianas) de acuerdo con un mecanismo de agregación balístico ($\propto \lambda^{-1}\phi_{2D}^{-2.5}$).
5. El "plateau" en el tamaño medio de agregados a tiempos largos aparece como resultado del confinamiento de las paredes que impide el crecimiento de los mismos.